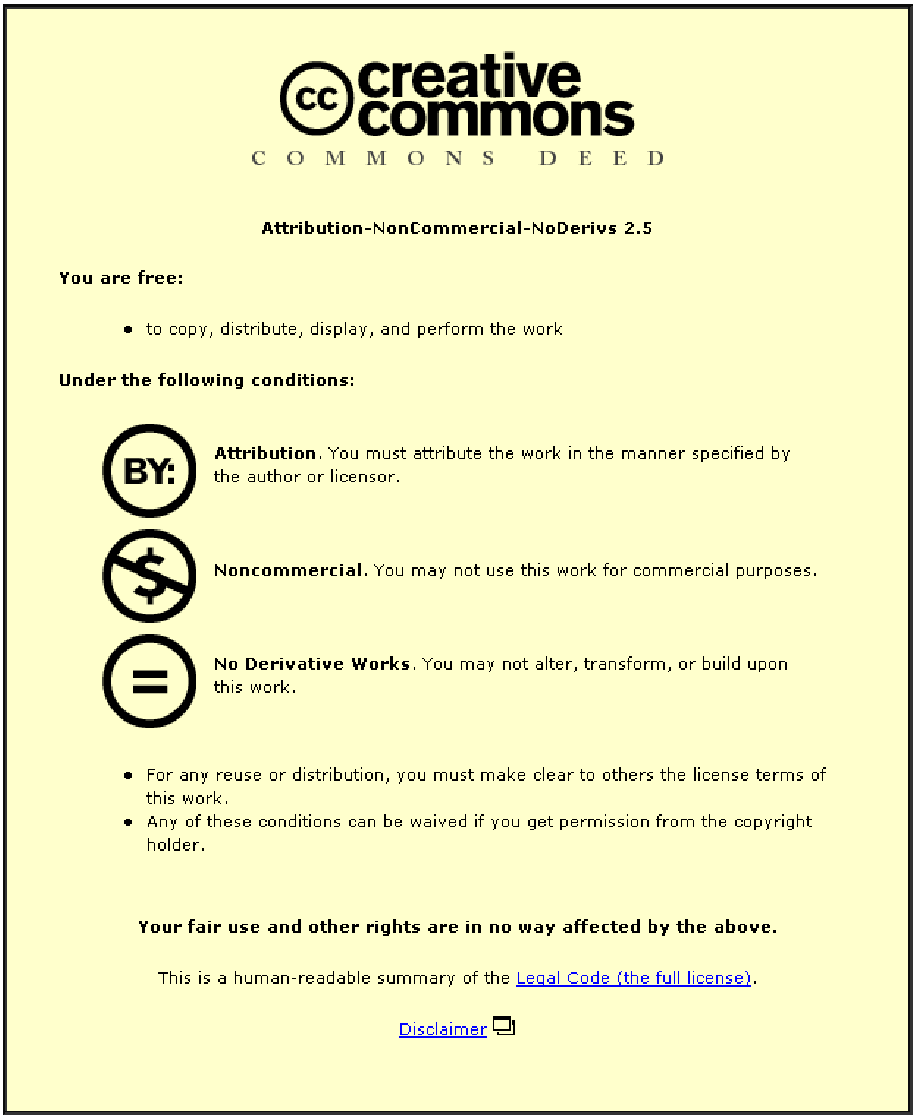

PREPARATION AND CHARACTERISATION OF TRANSPARENT CONDUCTING OXIDES AND THIN FILMS

DONGXIN WANG

A Doctoral Thesis

Submitted in Partial Fulfilment of the Requirements for the Award

of

Doctor of Philosophy

DEPARTMENT OF MATERIALS

LOUGHBOROUGH UNIVERSITY

Dedicated to my wife — Ms Li Zhang
and my baby son

ACKNOWLEDGEMENTS

First of all I would like to express my gratitude to my supervisor Dr. Xujin Bao for his guidance and advice, patient help and dedication throughout my time as a research student at Department of Materials in Loughborough University. With respect and appreciation, I would like to thank my external supervisor Prof. Jingming Zhong for his guidance and advice, care and help, and invaluable support in recent years.

In regards to Loughborough University, I would like to extend my thanks for the studentship and all staff in Department of Materials, special thanks to Mr. John Bates, Dr. David Ross and Mr. Ray Owens for their kind help in characterisation of samples, and also thanks to all members in our research group for their kind help.

In regards to Ningxia Orient Tantalum Co., Ltd., I would like to give my thanks to the financial sponsorship. Particularly, I'd like to thank Prof. Benshuang Sun for supporting these remarkable opportunities bestowed to me and his unyielding support, constant care and suggestions for my studying life in England. Also many thanks go to my colleagues and friends for their kind help and encouragement.

Last but certainly not least, I would like to express my love, respect, and admiration to my family for their unconditional support, understanding and dedication throughout last several decades since I went to primary school, in particularly, to my mother for teaching me how to sort out the things of daily life and making me understand how to turn my weakness into strength, to my father for instructing me to have a clear aim in my life and to keep going, to my sisters and brothers for their help and advice in my study, to my parents-in-law for their understanding and to my wife, Ms Li Zhang, for her love, accompanying me at Loughborough throughout my study time and many sacrifices that words can not describe.

ABSTRACT

Transparent conducting oxide (TCOs) thin films, including non-stoichiometric tin doped indium oxide (ITO) and aluminium doped zinc oxide (AZO), have found considerable applications in various displays, solar cells, and electrochromic devices, due to their unique combination of high electrical conductivity and optical transparency. TCO thin films are normally fabricated by sputtering, thermal vapour deposition and sol-gel methods. Among them, sol-gel processing, which was employed in this project, is no doubt the simplest and cheapest processing method, The main objectives of this project were to produce indium tin oxides (ITO) and zinc aluminium oxides (AZO) nanoparticles with controlled particle size and morphology and to fabricate TCO thin films with high optical transmittance and electrical conductivity.

In this research, hydrothermal method was used to synthesise ITO and AZO nanoparticles. Tin oxides, zinc oxides, ITO and AZO particles with the particle size ranging from 10 nm to several micrometers and different morphologies were synthesised through controlling the starting salts, alkaline solvents and hydrothermal treatment conditions. ITO and AZO thin films were fabricated via sol-gel technique through dip coating method. The effects of the starting salts, alkaline solvents, surfactant additives and coating and calcination conditions on the formation of thin films were investigated.

XRD, TEM, FEG-SEM, DSC-TGA, UV-Vis spectrometer and four-point probe resistance meter were used to characterise the crystallinity, particle size, morphology, optical transmittance and sheet resistance of the particles and thin films. Crack-free thin films with high optical transmittance (>80% at 550 nm) and low sheet resistances (2.11 kΩ for ITO and 26.4 kΩ for AZO) were obtained in optimised processing conditions.

Key words: transparent conducting oxide, ITO, AZO, nanoparticles, hydrothermal method, thin film, sol-gel, dip coating, transmittance, sheet resistance, characterisation

CONTENTS

ABBREVIATIONS

TCO:	Transparent Conducting Oxide
ITO:	Tin doped Indium Oxide
AZO:	Aluminium doped Zinc Oxide
TEM:	Transmission Electronic Microscopy
SEM:	Scanning Electronic Microscopy
XRD:	X-ray Diffraction
EDS:	Energy Disperse Spectrum
TGA:	Thermogravimetric Analysis
DTA:	Differential Thermal Analysis
FTIR:	Fourier Transform Infrared Spectroscopy
UV-VIS:	Ultraviolet and Visible Spectroscopy
BET:	Brunauer-Emmet-Teller
AFM	Atomic Force Microscopy
CRT:	Cathode Ray Tube
FPD:	Flat Panel Display
MRT:	Magnetic Resonance Imaging
LCD:	Liquid Crystal Display
PDP:	Plain Display Panel
OLED:	Organic Liquid Emission Diode
TPD:	Touch Panel Display
bcc:	Body centred cubic
CA :	Citric acid
RF :	Radio frequency
AC :	Alternating current
DC :	Direct current
PEG :	Poly(ethylene glycol)
FWHM :	Full-Width at Half-Maximum

Eq.:	Equation
en:	Enthylenediamine
1D:	One dimension
MEA	Mono-ethanolamine

LIST OF SYMBOLS

E_g:	Energy band gap
E_v:	the valence band
E_c:	the conduction band
$E_g(0)$:	the fitting parameter
q:	the electronic charge
T:	the temperature in Kelvin
E_{vacuum}:	the energy of a free electron outside the crystal
qx:	the electron affinity
sq:	square
Ω:	the resistance (ohm)
h:	hour
$a_{0:}$	lattice constant
Å:	angstrom
D:	crystal size
λ :	the wavelength of X-rays
B :	the measured broadening of the diffraction line peak at an angle of 2θ
d:	the average grain size of particle
A:	the surface area of the powder
ρ :	the theoretical density of tested material.
V:	voltage
t :	the thickness of a thin film
ρ:	the thin film resistivity
s :	interprobe spacing.
I :	current
S :	the cross section area of sample
L :	the length between two points of measuring voltage.

LIST OF FIGURES

LIST OF TABLES

Chapter 1 INTRODUCTION

1.1 Background

The first report of a transparent conducting oxide (TCO) was published in 1907 [1], when Badeker found that CdO thin films could be prepared by a thermal oxidation of sputtered cadmium and became transparent while remaining electrically conducting. From then on, the commercial value of TCO films has been recognised and much research work has been done. At present, transparent conducting oxides (TCOs), including non-stoichiometric tin doped indium oxide (ITO) and aluminum or alumina doped zinc oxide (AZO), have been developed and have found considerable applications in active and passive electronic and opto-electronic devices ranging from aircraft window heaters to charge-coupled imaging devices, due to their unique combination of high electrical conductivity and optical transparency [2]. TCOs exhibit high transmittance in the visible spectral region, high reflectance in the IR region and nearly metallic conductivity [3]. The most well-known and widely used TCO material is ITO, which has been in use since the 1960s [4]. There has also been much interest in recent years in the research on alternative, cheaper semiconducting materials, such as AZO, which presents similar properties to ITO but is much cheaper than ITO.

In the nanomaterials field, it is well known that nanomaterials have novel electrical, mechanical, chemical and optical properties that differ from both molecules and bulk properties [5]. For example, the transmittance of nanoparticles increases simultaneously as the nanoparticle size is reduced, and varying shape of the nanoparticles also induces novel optical properties [5]. Hence, it is possible to manipulate the chemical and physical properties of materials through the control of nanoparticle size and shape. Although there are many methods can be used to control the particle size, such as calcination at different temperatures and duration time or using different synthesis methods, for instance, co-precipitation and hydrothermal synthesis, there are essentially two ways to control the particle shape and size: growth directed syntheses and template directed synthesis [6]. In this project, the hydrothermal synthesis method was employed to synthesise TCO particles with controlled particle size and morphology via changing the synthetic parameters. The effects of starting salts, alkaline solvents, hydrothermal treatment temperature and ripening time, concentration of starting salt and additive on the formation of nanoparticles were investigated.

Normally, TCO thin films are fabricated by sputtering, thermal vapour deposition and sol-gel methods [7]. Among them, sputtering is the most common method to fabricate ITO thin films whose the highest optical transmittance is over 95% and minimum electrical resistivity is less than 4×10^{-5} Ω·cm [8]. However, the sputtering instrument, especially for the instrument with a large chamber, is extremely expensive. In addition, only a flat substrate and a solid target can be used. Therefore, industries are looking for the low-cost methods to prepare TCOs thin films. Among the available techniques for fabricating thin films, the sol-gel process is undoubtedly the simplest and the cheapest one. It is also easy to coat the large and different shaped substrates. This method is based on the phase transformation of a sol (obtained from metallic alkoxides or organometallic precursors) to a wet gel (a three-dimensional network structure) through, normally, hydrolysis and polymerisation at low temperature. The wet gel is then converted to an inorganic product by thermal treatment. In a sol-gel process, the fabrication parameters (withdrawal speed, the number of deposit layer, heat treatment temperature and time, etc.) are important elements, which will affect the properties of coated film as well as the properties of colloid itself such as dispersion, concentration and stability, etc. [6]. For example, particle size in colloid affects transmission of thin film since it has an effect on the thickness and the electrical conductivity of the thin film due to the different contact resistance between particles. In this project, the effects of the properties of ITO and AZO sols (concentration and amount of dopant, etc.) and the fabricating parameters including heat treatment condition, withdrawal speed and the number of deposit layer on the properties (optical transmittance and conductivity) of ITO and AZO thin films via sol-gel technique will be investigated.

1.2 General aims & objectives

The aims of the project are:

(1) scientifically understanding the reaction mechanisms and the effects of synthesis conditions on formation of indium hydroxide and oxide, tin hydroxide and oxide, zinc hydroxide and oxide, ITO and AZO particles with controlled morphology, particle size and size distribution;

(2) understanding the reaction mechanism of preparation sols and formation film processes of ITO and AZO, and to fabricate ITO and AZO thin films with high optical transmittance and electrical conductivity using sol-gel technique via dip coating.

Indium oxide, tin oxide, indium tin oxide, zinc oxide and aluminium zinc oxide particles, and their corresponding hydroxide, will be synthesised by the hydrothermal method. The morphology and particle size of particles synthesised will be modified by controlling the reaction conditions including starting salt and alkaline type, and the hydrothermal conditions such as hydrothermal temperature, ripening time and the solvent.

ITO and AZO thin films are fabricated by using the sol-gel technique by dip coating approach. The properties of the ITO and AZO sols (for example, concentration of sol, amount of dopant and additive) and the fabrication technique including withdrawal speed and the number of deposit layer, which affect the properties (optical transmittance and conductivity) of thin films, are studied. The effect of annealing variables on the properties of the thin films will also be investigated.

Various instruments are employed in characterising the particles and transparent conducting thin films of ITO and AZO. The size and morphology of particles and the microstructures of thin films of ITO and AZO are observed using TEM and SEM. The optical transmittance of thin film is measured by a UV-Vis spectrophotometer, and the electrical conductivity of thin film is tested by a four-point resistance meter. Of course, the crystal structures of all samples prepared in this project are characterised by XRD.

1.3 Layout of the thesis

Six chapters are included in this thesis. The first chapter is introduction r, in which the background, aims and objectives and layout of the thesis are described.

In chapter 2, the background knowledge and the relevant literature review are presented. The structures, properties and application of ITO and AZO are reviewed. The synthesis methods of particles, the fabrication methods of transparent conducting oxide thin film, such as sputtering method, thermal evaporation method and sol-gel technique, and the literatures related to fabrication of ITO and AZO thin films are covered.

Chapter 3 presents the chemicals used in the experiment and the experimental details involved in the synthesis of nanoparticles and fabrication of thin films. Characteistion equipments and the details of characterisation are also included in this chapter.

Synthesis of the particles using the hydrothermal method is included in chapter 4. The details of the effects of synthesis conditions including starting salt, alkaline solvent, hydrothermal temperature and ripening time, etc., on the morphology and size of particles synthesised is investigated and the reaction mechanism is discussed.

Chapter 5 illustrated the fabrication of ITO and AZO thin films. The effects of sol concentration, amount of dopant, heat treatment conditions and fabrication technique on the properties of thin films are investigated. The factors influencing fabrication of thin films are analysed and discussed as well.

Finally, the conclusions and a list of suggestions for future work are presented in chapter 6.

Chapter 2 LITERATURE REVIEW

2.1 Nanomaterials

In traditional materials, their grain sizes vary from hundreds of microns to centimetres. However, some materials, termed nanomaterials, have grains in the nanoscale size (1 nm = 10^{-9} m). Pierret defined that "nanomaterials are whose characteristic length scale lie within the nanometric rang, i.e., in the range between one and one hundred of nanometres."[9] Nanomaterials normally include nanoparticles, thin films and bulk materials with nanosized grains, which constitute a bridge between molecules and micromaterials. The properties of nanomaterials are significantly different from those of atoms, molecules or micromaterials with the same chemical composition due to the size effect [10]. Suitable control of the properties of nanometer-scale structures can lead to the materials having new properties, which can be developed into new products, devices and technologies [11].

In general, nanomaterials can be prepared by chemical or physical methods. The main methods are listed below [12].

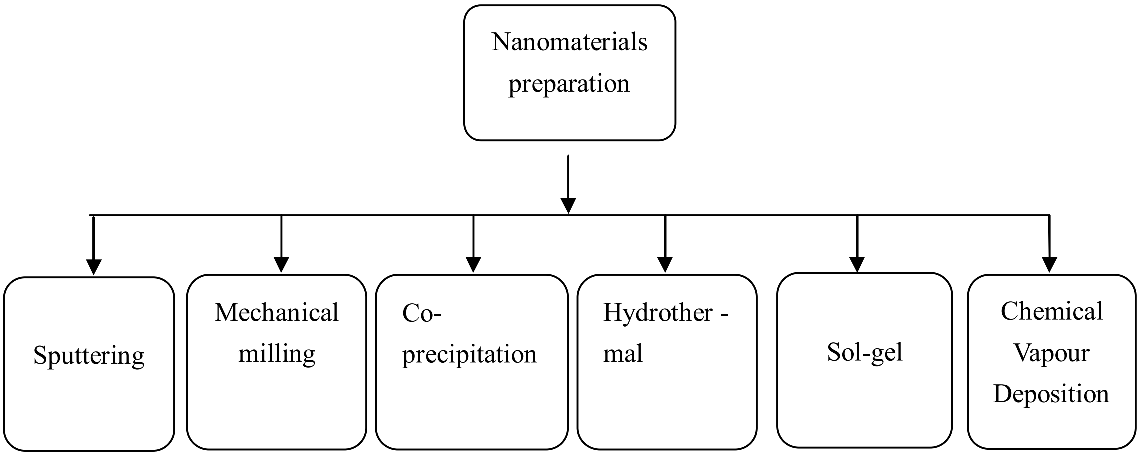

The applications of nanomaterials are determined by their mechanical, physical and chemical properties. Current applications include, but are not limited to the following [12]:

Applications of nanomaterials

① Insulation materials, such as “smart” window, etc.
② Machine tools, such as cutting tools and drills, etc.
③ Phosphors, such as using for CRT and FPD (Flat Panel Display), etc.
④ Batteries, such as Nickel metal hydride batteries, etc.
⑤ High power magnets, such as Magnetic Resonance Imaging (MRI) in medical diagnostics, automobile alternators, etc.
⑥ Motor vehicles and aircraft, as a coating material for the engine cylinders ,etc.
⑦ Medical implants
⑧ Other medical uses, such as used in DNA separations, etc.

The science and technology of nanomaterials has created great excitement and expectations in the last decades. Many types of nanomaterials were developed. Among them, transparent conducting metal oxides are fundamental to development of smart and function materials, which are candidates for optics, optoelectronic, and chemical, biochemical and environmental sensors as well as transducers[13], because they have two unique structure features: switchable and/or mixed cation valences, and adjustable oxygen deficiency. Metal oxide nanoparticles and their thin films showed enhanced physical and chemical properties [13] and attracted considerable interest in the scientific understanding and practical application in the fields of synthesis of nanoparticles and fabrication of thin films.

2.2 Semiconducting materials

A semiconducting material is either crystalline or amorphous material whose conductivity falls intermediate between that of insulation, 10^{-22} to 10^{-10} ohm^{-1} cm^{-1}, and that of metals, 10^4 to 10^6 $ohm^{-1} \cdot cm^{-1}$. The conductivity of a material increases with the increase of temperature or concentration of impurities or by illumination with light [14,15]. The transparent semiconducting material is also sensitive to visible light but reflective in the infrared range [16].

Electricity can be conducted through solids by ionic or electronic and electronic conduction is the common way of transfer of electricity. For semiconductors, the principle of conduction can be described by the energy-band theory, i.e., electronic migration between a band gap (E_g) within the material. In the ground state, the band gap is determined by separation of the valence band (E_v) and the conduction band (E_c). When sufficient energy is supplied to a semiconducting material, the electrons within the valence band become excited and pass to the conduction band, which is called excitation. This process of excitation leaves holes in the valence band which creates electron-hole pairs. When an external electric field is made available, the electron and its paired hole begin to migrate in opposite directions in the conduction and valence bands, respectively. An energy band diagram is shown in **Figure 2.1**.

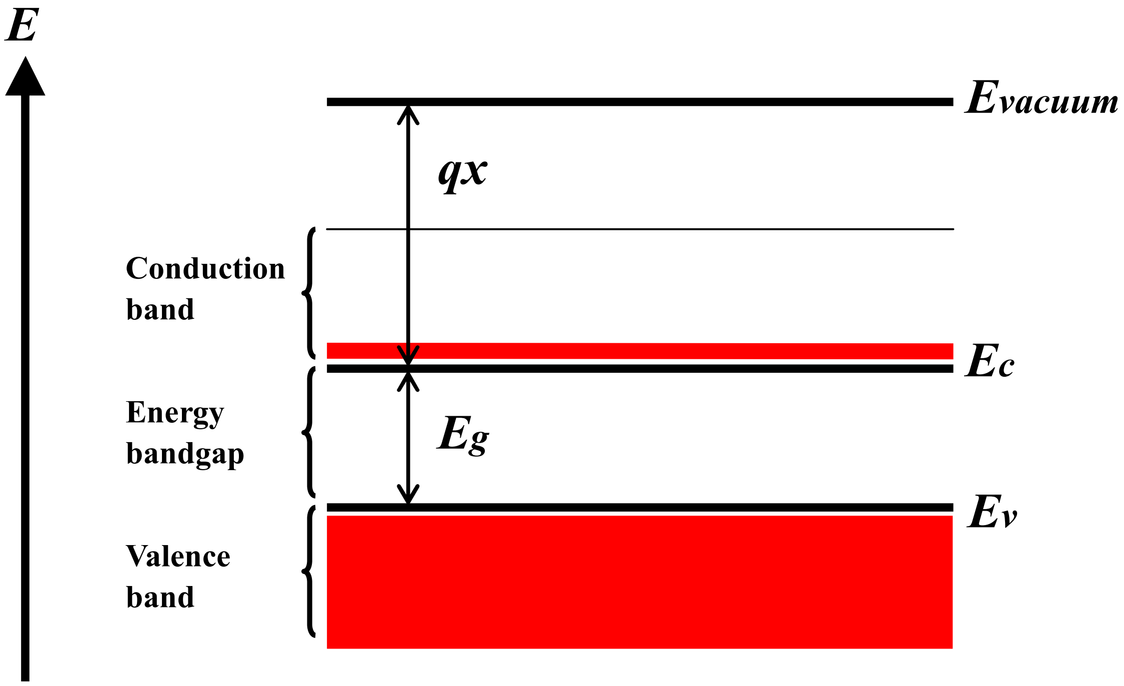

Figure 2.1 Simplified energy band diagram used to describe semiconductors. band gap, Eg, the valence band edge, E_v, and the conduction band edge, E_c. The vacuum level, E_{vacuum} (the energy of a free electron outside the crystal), and the electron affinity, qx, are also indicated on the diagram [17].

There are two types of semiconducting materials, n-type and p-type. They are based on different carriers. In the semiconducting materials, the presence of imperfections or defects–foreign impurities dissolved in the host material or irregularities in the orderly geometric array of the host crystal lattice—can create isolated centres in a solid which can ionise and thereby contribute electrons to the conduction band of the material. Such defects are called donor centres or donors since they donate conduction electrons to the semiconductor. When these negatively charged electrons are the majority charge carries, the material is called an n-type semiconductor. Other crystal defect types create acceptor centres or acceptors, which remove (or accept) electrons from the chemical bands of the semiconductor, producing electron vacancies. These vacancies, or holes as they are called, behave as positive charge carriers, located in the valence band. A p-type semiconductor results when holes are the majority charge carriers.

2.3 Transparent conducting metal oxides nanoparticles

Transparent conducting metal oxide nanoparticles, in general, are used as functional materials and the particle size and shape are important aspects related to the properties of nanoparticles [11], such as thermodynamic, electronic, spectroscopic, electromagnetic and chemical properties [18]. The size effect can be classified into two types: specific size effect (e.g. magic numbers (a number of nucleons (either protons or neutrons) such that they are arranged into complete shells within the atomic nucleus) of atoms in metal clusters, quantum mechanical effects at small sizes) and size-scaling effect applicable to relatively larger nanostructures. Control of the nanoparticles size normally involves three steps: nucleation, growth and termination [19, 20]. Though the reaction temperature and reagent concentrations provide a basic control of these three steps, it is often impossible to control them independently and hence the obtained nanoparticles (nanocrystal) usually exhibit a distribution in size [18].

The shape of nanoparticles also affects the properties of nanoparticles. It was found that the properties of nanoparticles follow from the confinement of the electrons to the physical dimensions of the nanoparticles [21], and predicted that light emitted from a nano-rod would be linearly polarized along the growth-axis [22]. Hence, smarter synthetic schemes have been designed which selectively produce nanoparticles in the form of rods, elongated spheres, cubes and hexagons by careful control of reaction conditions for different purposes [18].

2.4 Transparent conducting metal oxides thin films

The transparent conducting metal oxide (TCO) thin films require high optical transparency (more than 80%) in the visible light spectrum and high electrical conductivity (about 10^3 Ω^{-1}cm^{-1} or high) simultaneously, which is not possible in an intrinsic stoichiometric material [7]. Partial transparency and fairly good conductivity may be obtained in thin films of a variety of metals. TCO thin films have semiconducting properties with a large band gap, providing spectrally selective characteristics. Visible light is a form of electromagnetic radiation with wavelengths in the range of 400 nm to 700 nm corresponding to an energy range of 3.1 to 1.8 electron volts (eV). When light strikes an object it may be transmitted, absorbed, or reflected. Materials with band gap energies less than 1.8 eV will be opaque owing to all visible light will be absorbed by electron transitions from the valence to the conduction band. Materials with band gap energies greater than 3.1 eV will not absorb light in the visible range and will appear transparent and colourless, but this kind of materials has no or little conductivity due to large band gap. Therefore, the way to obtain good transparent conducting thin film is to create electron degeneracy in a wide band gap (greater than 3 eV) oxide by controllably introducing non-stoichiometry and/or appropriate dopants. ITO and AZO are this kind of transparent conducting materials because they have wide band gaps which are more than 3.1 eV and also have high valence elements, tin (+4) and aluminum (+3), used as dopants, respectively. The optical and electrical properties of transparent conductive oxide thin film are related closely to preparation parameters and dependent on the composition, crystallinity, defect density and dopant concentration of the film [23].

2.5 Structures of ITO and AZO

2.5.1 Structure of ITO

ITO has the same two crystal structures as pure In_2O_3: the bixbyite structure (bcc structure, a=10.117 Å) and the corundum structure (rhombohedron structure, a=5.487Å, c=14.510 Å), as illustrated in **Figure 2.2** and **Figure 2.3**, respectively. The bixbyite crystal has a unit cell containing 40 atoms and two non-equivalent cation sites. **Figure 2.2** shows the structure where one fourth of the anions are missing. Indium cations are located in two different six-fold-coordinated sites. One fourth of the cations are located in trigonally compressed octahedra (b site). The remaining three-fourths are located in highly distorted octahedral (d site). Each cationic site can be described as a cube where two anion sites are empty at opposite vertices for b sites and along one diagonal of a face for d sites. The structural oxygen vacancies are located along the four <111> axes [24]. And in this structure, ITO is essentially formed by substitutional doping of In_2O_3 with Sn^{4+} which replaces the In^{3+} ion from the cubic bixbyte structure of indium oxide [25]. The corundum structure ITO is a high-pressure phase, which is always prepared under conditions of high pressure (~10×10^4 MPa), high temperature (≥ 800°C), or the both [26]. ITO, depending on how much Sn doped, has a lattice parameter which is positioned in the range 10.12 Å to 10.31 Å. This lattice parameter is near to that of In_2O_3 [27].

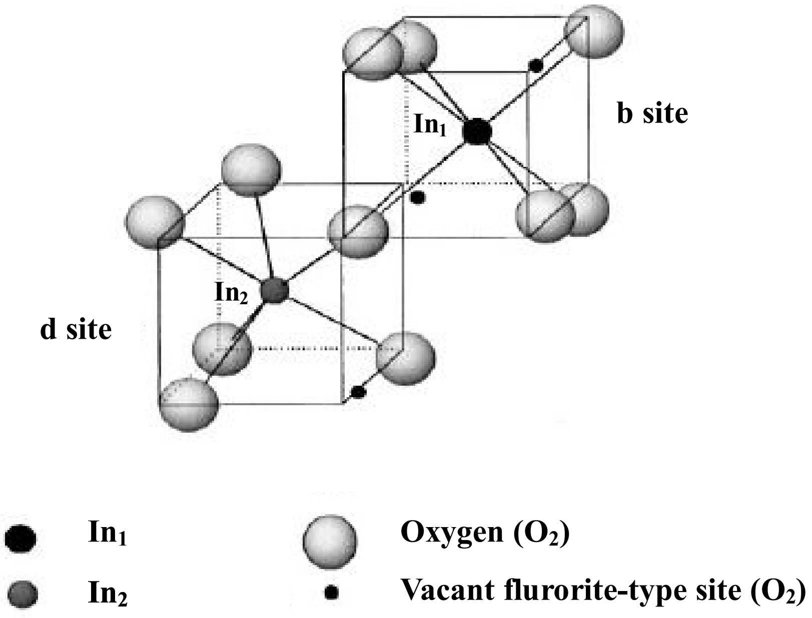

Figure 2.2 The bixbyite structure of In_2O_3 [24].

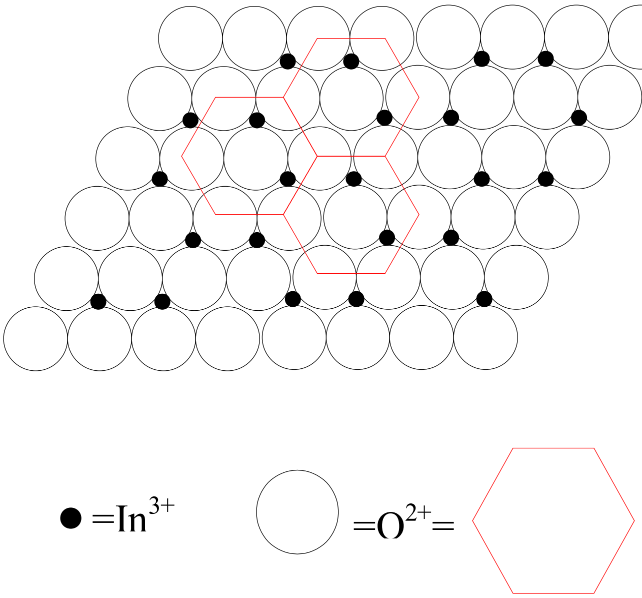

Figure 2.3 The corundum structure of In_2O_3 [26].

2.5.2 Structure of AZO

The structure of AZO is similar to that of zinc oxide which is a hexagonal close-packed structure (**Figure 2.4**). As Al atom is doped into the lattice of ZnO, the site of Zn atom will be replaced by Al. The replacement affects only the lattice parameter and does not change the structure of ZnO.

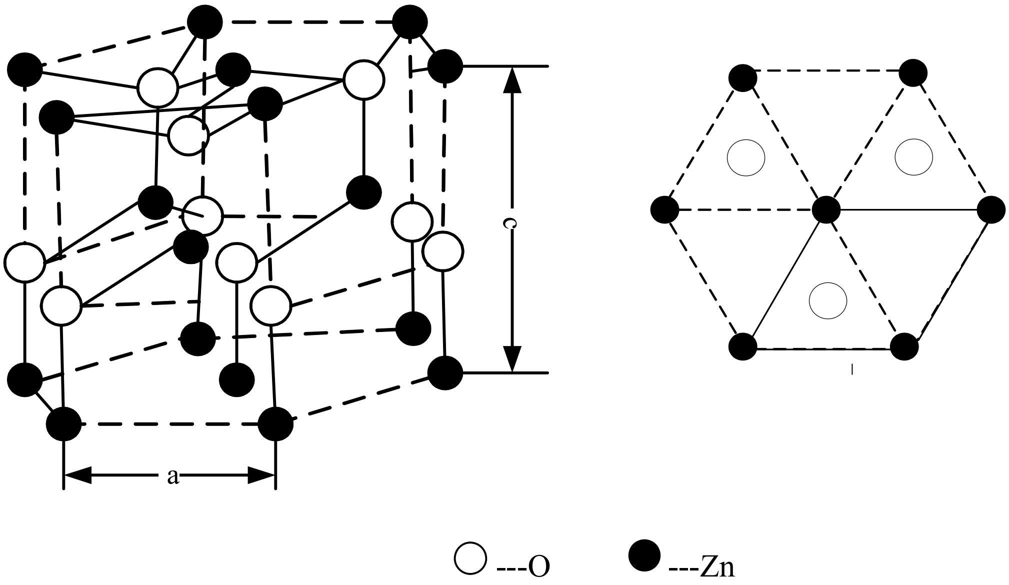

Figure 2.4 Structure of ZnO.

2.6 Properties of ITO and AZO

The optical and electrical properties are the very important properties for ITO and AZO thin films used as transparent conducting materials [28].

2.6.1 Optical and electrical properties of ITO

Indium oxide is an n-type semiconductor with wide energy gap of 3.5 ~ 4.3 eV. As Sn is doped into In_2O_3, SnO or SnO_2 is formed which has a valence of +2 or +4, respectively. This valence status has a direct effect on the final conductivity of indium tin oxide (ITO). The lower valence state (Sn^{2+}) causes a net reduction in carrier concentration since a hole is created which acts as a trap and reduces conductivity. Conversely, a tetravalent cation (Sn^{4+}) is doped which results in n-type donor providing an electron to the conduction band. Once the substitution is done, an electron charge-compensation will be formed as a result of different valences of Sn^{4+} and In^{3+} as represented below:

$$xIn_2O_3 + xSn^{4+} \rightarrow In_{2-x}^{3+}\left(Sn^{4+} \bullet e\right)_x O_3 + xIn^{3+} \tag{2-1}$$

Substitutional Sn contribution makes the narrowed energy gap in ITO (**Figure 2.5**). Hence, the electrical conductivity of ITO increases with the increase of Sn^{4+} concentration. However, only limited doped Sn is available because of the limitation of the solubility of Sn in In_2O_3, which is about 6–8 at% [29,30]. On the other hand, the oxygen vacancies act as doubly ionised donors and contribute a maximum of two electrons to the electrical conductivity as shown in the following equation [31]:

$$O_0 \rightarrow V_0^{\bullet\bullet} + \frac{1}{2}O_2(g) + 2e^- \tag{2-2}$$

Therefore, oxygen is also important to control the electrical conductivity of ITO, and the ITO can be described as $In_{2-x}Sn_xO_{3-2x}$ [27].

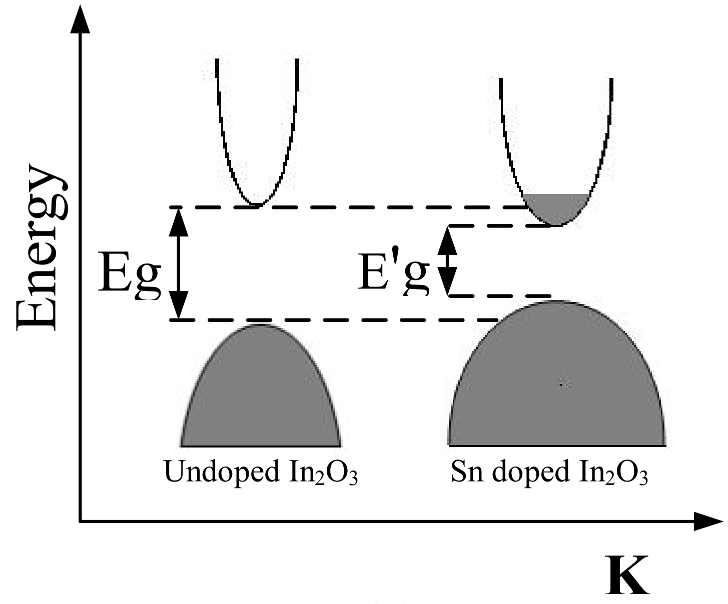

Figure 2.5 The energy band structure of ITO [32].

ITO is transparent in the visible light range and reflective in the infrared spectral regions due to its wide optical energy gap [33]. The ITO film with high transmittance (85-98%) in the visible range was prepared using oxygen ion-beam assisted deposition [34]. It can be seen that transmission decreased from 98% to 85% at 550 nm with the thickness increased from 84 nm to 250 nm, because the absorption increased with the thickness (**Figure 2.6**).

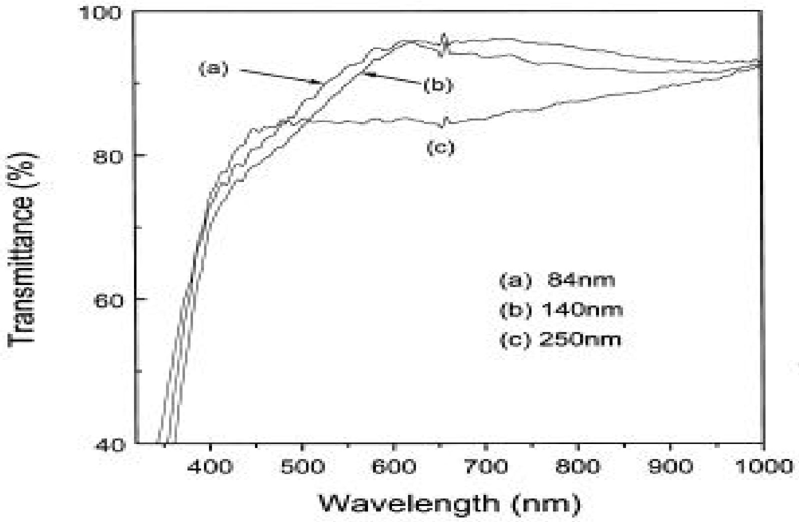

Figure 2.6 Variations of the optical transmittance of ITO thin films as a function of thickness [34].

The optical and electronic properties of ITO films are highly dependent on the deposition parameters and the starting composition of evaporation material used. The deposited film layer must contain a high density of charge carriers for it to conduct. These carriers are free electron and oxygen vacancies. High conductivity (or low sheet resistance) is balanced against high transmittance in the visible region. Sheet resistance can be less than 10 Ω/sq. with a visible transmittance of >80%. To obtain transmittance near 90%, sheet resistance must be >100 Ω/sq. At longer wavelengths, the film becomes reflecting, and the IR reflectance is related to the sheet resistance of the film; sheet resistance must be <30 Ω/sq. to obtain IR reflectance >80% [35].

2.6.2 Optical and electrical properties of AZO

Zinc oxide is also an n-type semiconductor with a wide direct band gap of 3.3 eV and its conductivity can be controlled by thermal treatment or by adequate doping [36]. The doping of ZnO with the group III elements can increase the conductivity of the films. In comparison with other elements, Al and Ga are the best dopants because their ionic radii are similar to that of Zn^{2+} [37]. When Al is doped into ZnO, the band gap decreases. The electrical conductivity of the AZO depends mainly on the carrier concentration. The carrier concentration increases with the increase of doping concentration, as substitutional doping of Al^{3+} at the Zn^{2+} lattice site creating one extra free carrier in the process, resulting in the increase of conductivity of AZO. However, the dopant atoms in the crystal grain and grain boundaries tend to be saturated after 0.8 at.% of Al doping in the AZO [38].

AZO is an excellent transparent conducting oxide material in the visible light range since it has wide energy gap. Al doping level and the microstructure of the films affect the transmittance. Ma et al.[39] reported that over 80% of optical transmittance was observed from ZnO and AZO films (**Figure 2.7**). AZO thin films with high transmittance of 90% in the visible light range at temperature ranged from 90 °C to 350 °C was reported by Lee et al.[40].

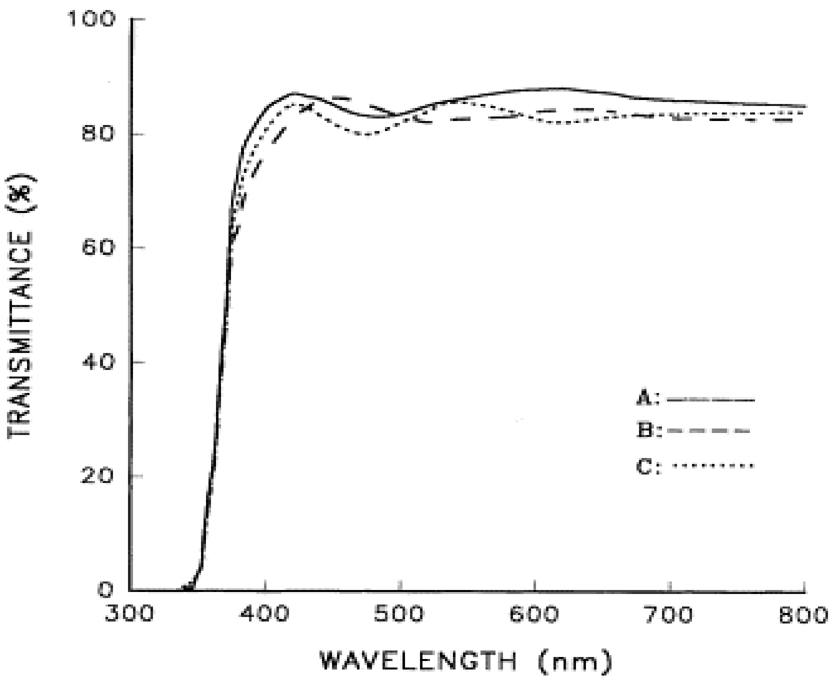

Figure 2.7 Optical transmission of the ZnO and ZnO:Al films as a function of wavelength; film thickness 350nm. (A) as-deposited ZnO film; (B) annealed ZnO Film; (C) ZnO:Al film with Al/Zn 0.9 at% [39].

2.7 Applications of ITO and AZO

As ITO thin films have excellent optical transparency and electrical conductivity, they have found many applications in contemporary and emerging technology, such as in various displays (**Figure 2.8**), solar cells, electrochromic devices, and heatable glass [41]. They are also used for prevention of radiative cooling, thermal insulation of widows, etc., if they have low thermal emittance and high conductivity. The main applications of Al doped ZnO films are used as transparent conducting electrode in photovoltaics, and as the replacement for the expensive ITO in displays due to its low cost of starting materials and comparable low resistivity with ITO [23].

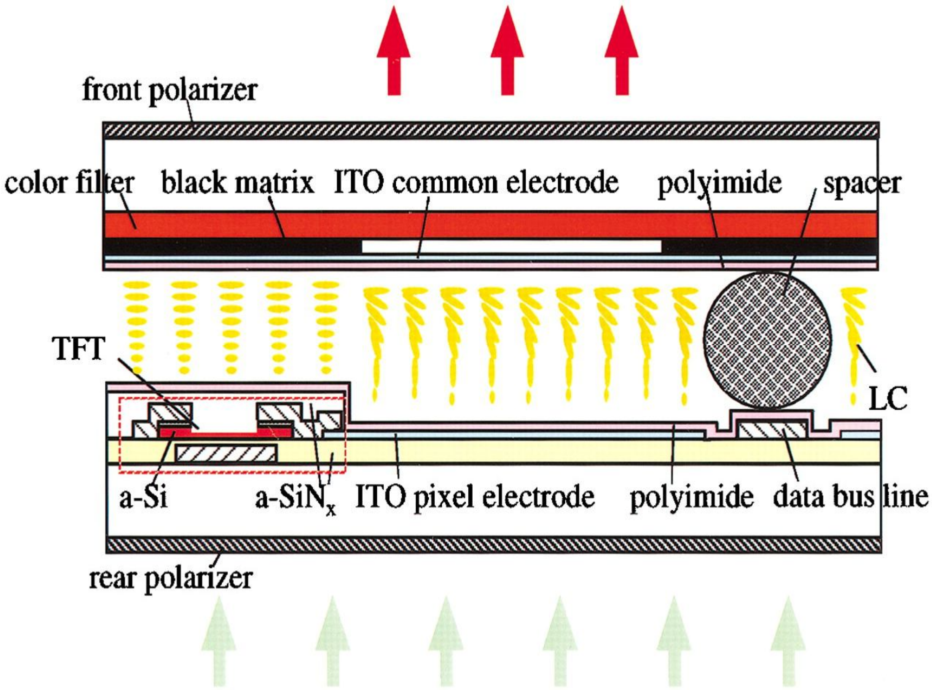

Figure 2.8 ITO thin film used as electrode in LCD display [42].

2.8 Synthesis of ITO and AZO nanoparticles

Generally, there are two approaches which are “top-down” and “bottom-up” can be conducted to prepare nanomaterials [12]. “Top-down” method can be defined as the modification of larger objects to achieve smaller-scale structures. It is similar to sculpt a picture from a piece of bulk materials. This approach, including lithography techniques (e.g., electron or ion-beam, scanning probe, optical near field), film deposition and growth [43], laser-beam processing [44], and mechanical techniques (e.g., machining, grinding, and polishing) [45], has been applied in the industrial scale. A practical disadvantage of top-down techniques is the particle size that is larger than that of bottom-up techniques [5]. “Bottom-up” method means that smaller units (such as atoms and molecules) are built into larger objects or more complex substance via chemical, physical, and biological procedures, which can provide access to extremely fine features and structures [46].

Many methods have been useing in production of ITO and AZO nanoparticles. Co-precipitation and hydrothermal synthesis are the most commonly used ones [47], which are both “bottom-up” approaches. The hydroxides prepared by co-precipitation normally are amorphous [48]. After high temperature heat-treatment, the hydroxides lose water and transform into oxides, while changing the structures from the amorphous to the crystalline phase [49].

TGA and DTA were used to analysise the phase transformation of indium tin hydroxides to oxides of indium (III) and tin (IV), as shown in **Figure 2.9**. It can be seen from the TG curve that indium tin hydroxide converted to ITO completely at 314.7 °C. The differential thermal analysis (DTA) showed a series of endothermic and exothermic reactions. A sharp peak temperature of 288.5 °C was an endothermic reaction of 10 at% tin doped indium hydroxide, e.g., the temperature of transformation between indium tin hydroxide and ITO.

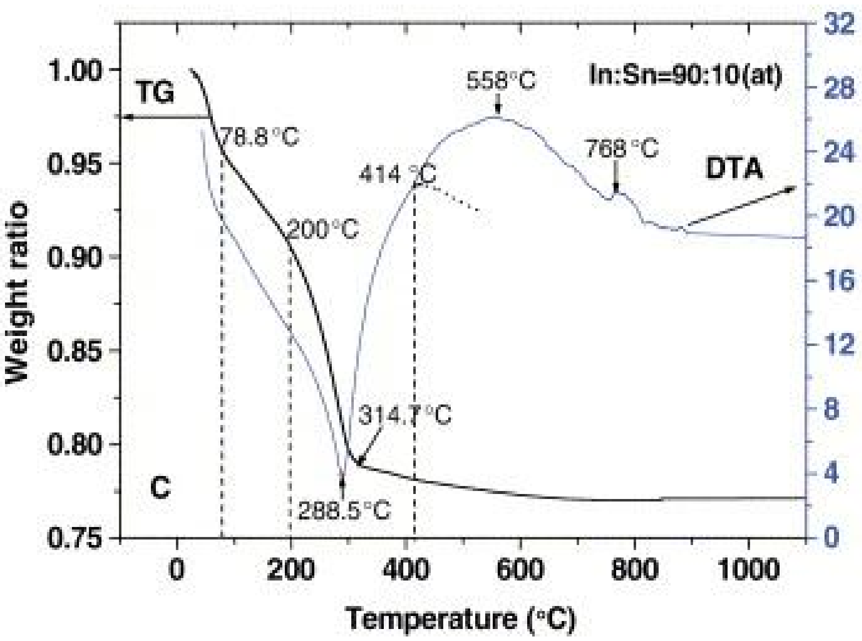

Figure 2.9 Thermal analysis of the ITO precursor sample with thermal temperature [50].

2.8.1 Co-precipitation synthesis method

Co-precipitation is the method to produce solid precipitates via mixing two or more chemical solutions under certain reaction conditions. Desired materials will be obtained after filtering, washing and drying. In many cases, the precipitates need to be calcined at certain temperature to produce the desired chemical composition and crystalline phase [51]. Co-precipitation method has some advantages in synthesis of particles:

- Simple and rapid synthesis.
- Easy control of particle size and composition.
- Various possibilities to modify the particle surface state and overall homogeneity.

The method has been used to synthesise advanced ceramics, including ITO and AZO. Reaction parameters including pH value, reaction temperature, thermal oxidation temperature, alkaline solution and composition affect size and morphology of the particles synthesised [52].

ITO plate-shaped particles with 60 nm in size were produced via co-precipitation when the solution has pH 6.75, which was changed to spherical shape when pH value increased from 6.75 to 9.75 after adding more ammonia [52]. Li et al.[50] found that the ammonium salt acted as a “template” in the formation inorganic compound and greatly affected the orientation of crystals. The metal cations, generally, are linked together by means of single bridge of hydroxo group to produce [In^{3+}–OH–In^{3+}] backbone. However, the “template” $In(NH_3)_4^{3+}$ can prevent [In^{3+}–OH–In^{3+}] backbones growing in other directions except [100] direction, $In(OH)_3$ octahedral nuclei in the cubic structure cell will mainly stack along the closest plane (100). On the other hand, the seeds cannot grow along sectional diameter and form rods with smaller sizes compared to spherical shape. Hence, the rod-like particles formed.

The reaction temperature and the heat treatment temperature will affect the particle size and morphology of indium tin hydroxide and indium tin oxide. It was found that indium tin hydroxide particles prepared at 40 °C were mainly spherical with size range 260–610 nm. The particles prepared at 100 °C showed rod-like and elliptical shapes with size distributions in sectional diameter and in axial length were 120–220 nm and 300–800 nm, respectively. After calcination at 800 °C, ITO particles inherited the shape of ITO precursor powders and the shapes were slightly varied, e.g., the calcination temperature did not change the shape of the particles [50]. Some researches reported that size of ITO particle was increased with the increase of the calcination temperature, and the particle shape was easily changed, even at 400 °C, the particle shape becoming spherical [52, 53].

Tin content was a factor that affected the particle size and morphology as well. The particle size was decreased from 40-50 nm to 10-20 nm as tin content was increased from 3.18 to 21.11 at% shown in **Figure 2.10**[52]. For comparison, the same precursor's samples were calcined at 600 °C in air. It was found that bar or elliptical type of particles with 20–30 nm size were synthesised in low tin content. As tin content increased, the shape of large particles became irregular and size decreased less than 10 nm. It indicated that tin content had the effects on the particle size and morphology.

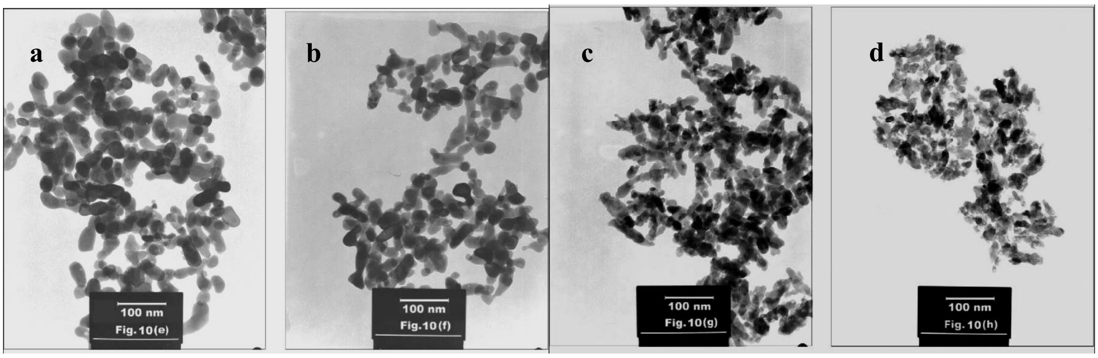

Figure 2.10 TEM micrographs of produced ITO particles with at% Sn/In in precursor: (a) 3.18, (b) 6.30, (c) 15.93 and (d) 21.11 at.% Sn/In [52].

Furthermore, ITO powder also produced by calcining precipitates with different Sn contents at 600 °C for 1h in air and the particle sizes are presented in **Table 2-1**. It can be seen that the size of the particles is between 22 nm and 26 nm regardless of the Sn contents from 0% to 12% [29].

Table 2-1 Particle sizes ITO with different Sn contents.

Sn content (at.%)	Particle size (nm)
0	26 ± 5
4	20 ± 4
8	24 ± 3
12	22 ± 4

2.8.2 Hydrothermal and solvethermal synthesis methods

The hydrothermal method or solvethermal method is one of the most important tools for advanced materials processing, particularly owing to its advantages in the processing of nanostructural materials for a wide variety of technological applications such as electronics, optoelectronics, catalysis, ceramics, biomedical, biophotonics, etc[54]. Hydrothermal/solvethermal process can be defined as any heterogeneous reaction in the presence of aqueous solvents or mineralisers under high pressure of 0.1 MPa and temperature above 100 °C to dissolve and recrystallise materials that are relatively insoluble under ordinary conditions [55]. This is a method to prepare crystalline oxide materials using water or solvent above its boiling point in an enclosed vessel that produces high autogenous pressure.

The hydrothermal method has attracted much attention since particles with the desired characteristics can be prepared with this technique by controlling the solution pH, reaction temperature, reaction time, solute concentration and the types of solvent conditional in a particular application [54,56]. The major advantages of hydrothermal synthesis are related to homogeneous nucleation processes, attributed to the possibility of elimination of the calcination step to produce very small grain-sized crystal particles with narrow size distribution, good chemical homogeneity and high purity powders [51,57].

Indium tin oxide nanoparticles were prepared through the hydrothermal method [31,58,59]. It was found that ITO powders with a single cubic phase could not be produced by the conventional hydrothermal process as it did not have enough energy to break the bonds among the precursor molecules under the supercritical condition [31]. Therefore, organic solvent, such as ethylene glycol ($C_2H_6O_2$), polyethylene glycol 600 ($H(OC_2H_4)_nOH$) and ethanol (C_2H_5OH), was substituted for the medium of water. It was found that the solvent viscosity in the hydrothermal process strongly influenced both electrical and optical properties of ITO materials. The size of synthesised ITO particles increased with increasing solvent viscosity due to steric hindrance. At the same time the shape became square-like with increasing solvent viscosity, because the preferred orientation of ITO materials for crystallisation was the fastest in the <1 0 0> direction. However, hydrothermal treatment temperature was another key factor to synthesise pure cubic phase ITO (**Figure 2.11**). It was observed that 250 °C was the critical temperature for forming a single oxide phase.

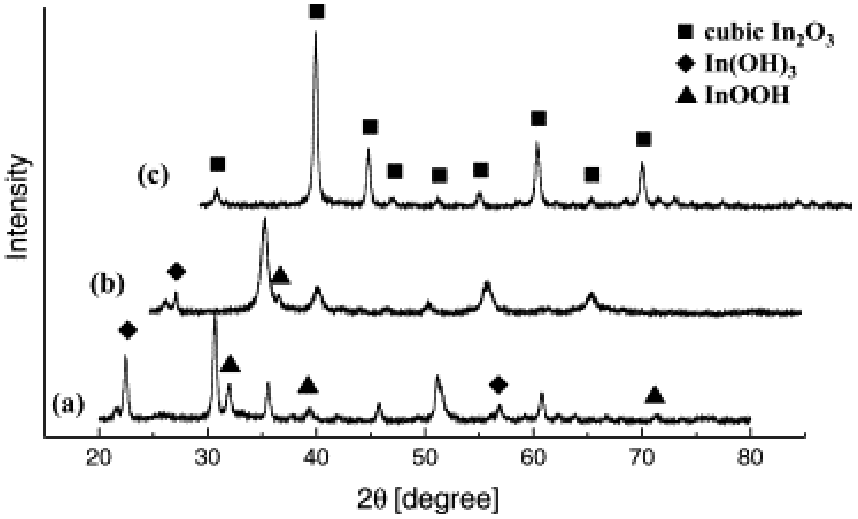

Figure 2.11 XRD patterns of ITO powders synthesised by the solvethermal process with ethylene glycol as the solvent at different tenperatures for 6 h: (a) 210°C, (b) 230°C, and (c) 250°C [31].

For the preparation of zinc oxide, Liu et. al.[60] reported that cluster and rod-like ZnO whiskers were fabricated successfully by hydrothermal processing using the solution of zinc salts and hydrazine hydrate in the presence of sodium succinate hexahydrate used as a dispersant and complex in the process. The size of cluster whiskers formed was ranged between 200-800 nm in diameter and 12 μm in length The reaction of the formation of ZnO was suggested by decomposition of the $Zn(OH)_4^{2-}$ precursor as following:

$$N_2H_4 + H_2O \rightarrow N_2H_5^+ + OH^-$$
$$Zn^{2+} + 2OH^- \rightarrow Zn(OH)_2$$
$$Zn(OH)_2 + 2OH^- \rightarrow Zn(OH)_4^{2-}$$
$$Zn(OH)_4^{2-} \rightarrow ZnO + H_2O + 2OH^-$$

Furthermore, citric acid (CA) was also used to assist the hydrothermal process [61]. It was found that the growth habit of ZnO was mainly determined by its structure. However, the pH value, temperature and the molar ratio of Zn^{2+} and CA had a significant influence on the morphology of ZnO nanostructures. For example, pH value can greatly affect the quantity of ZnO nuclei and of growth units. Disk-like, flower-like and nanorod flower-like ZnO nanoparticles with hexagonal structure were prepared by changing different reaction conditions. The nanorod flower-like ZnO particles were synthesised at higher pH value (about 13.5), which can be attributed to the pH value improved the anisotropic growth of ZnO because the anions could be absorbed on the different crystal planes. In contrast, the disk-like morphology of ZnO nanostructure was prepared in the lower pH due to existence a large amount of negatively charged $[Zn(C_6H_5O_7)_4^{-12}]^{-10}$ which was favourite to adsorb on the positive polar plane (0001) and decreased the growth rate of (0001).

It has been known that a modifying agent is the important factor that affects the zinc oxide particle size and morphology in the hydrothermal process [62]. Some modifying agents such as polyethylene glycol (PEG) [63,64,65,66,67], cetyltrimethylammonium bromide (CTAB) [68,69] and amines [70, 71] were applied to synthesise zinc oxide particles with different morphologies and particle sizes.

The effect of PEG with different molecular weights was investigated on the formation of zinc oxide. The single-crystalline hexagonal prism ZnO nanorods with diameters ranging from 60 to 120 nm and lengths of hundreds of nanometers were synthesised with a PEG400-assisted hydrothermal process at 140 °C [63]. Liu and Huang [72] reported that synthesis of ZnO nanotubes and tubular whiskers by using $Zn(NO_3)_2 \cdot 6H2O$, $NH_3 \cdot H_2O$ as the starting materials in the presence of PEG2000 at ambient pressure and low temperature of 70 °C. It was found that the morphology of nanorods was changed when the PEG 4000 was used as the additive [66].

ZnO particles were prepared from the decomposition of soluble $[Zn(OH)_4]^{2-}$ precursor in water at 280 °C in the presence of cetyltrimethylammonium bromide (CTAB). The results demonstrated that ZnO nanorods were synthesised [68]. But Sun [69] reported that rod-like zinc oxide particles were synthesised using zinc powder and CTAB at 180 °C. In the synthesis process, CTAB acts as a surfactant, which can reduce the surface tension and guide the growth of zinc oxide.

Well-defined flower-like ZnO microstructures with different sizes were successfully synthesised using a simple aqueous solution with zinc chloride and sodium hydroxide as the reactants, triethanolamine (TEA) as the modifying agent [70]. Other amines such as tributylamine, cyclohexylamine and ethanolamine [71] were applied to produce the different shaped zinc oxide and the rod-like, spindle-like, sheet-like and polyhedral-shaped zinc oxide particles formed respectively at 160 °C for 5 hours.

Different solvents are also used in the process of synthesis of zinc oxide. Xu et al.[73] prepared zinc oxide powders with various morphologies by hydrothermal treatment of zinc acetate in pure water, KOH or ammonia aqueous solution. It was found that the selected solvents play a different role in controlling the morphologies of the obtained powders. In pure water, the pencil-like ZnO particles are obtained. Upon using KOH solutions of different concentrations as the solvents, the morphologies of the ZnO powders such as twinned pyramidal, shortened prismatic, sheet and prismatic-like are obtained. If ammonia solutions of different concentrations are employed as the solvents, the shapes of the ZnO particles are ellipsoidal and long prismatic-like. Another researcher[74] synthesised the zinc oxide nanowires in the NaOH aqueous solution at 80 °C for various durations of time. He found the average length of ZnO nanowires was increased with the increase of reaction time from 12 h to 24 h .

2.8.3 Comparison of coprecipitation method and hydrothermal method

The comparison of coprecipitation method and hydrothermal method is listed in **Table 2-2**.

Table 2-2 The comparison of coprecipitation method and hydrothermal method [75].

	Coprecipitation method	Hydrothermal method
Size of particle (nm)	> 10	> 5
Homogeneity	Good	Very good
Purity	Very good	Very good
Temperature of calcination (°C)	500-1000	80-374
Agglomeration	High	Low
Costs	Moderate	Moderate

2.9 Fabrication of transparent conducting oxide thin film

Various thin film deposition techniques have been developed to prepare transparent conducting oxide (TCO) thin films: wet chemical method (spraying, dipping and spinning using liquid precursors), sputtering method and thermal evaporation method (chemical vapour deposition and physical vapour deposition) [12]. The electrical and optical transport of the films depend strongly on their microstructure, stoichiometry, the nature of the impurities presented and the deposition technique used [7].

2.9.1 Sputtering method

Sputtering method is a very common technique to fabricate semiconducting thin films. The sputtering process takes place in an evacuated chamber. The principle of this method is that argon is introduced, then ionised in the chamber which contains the substrate and the target of the film material to be sputtered. The target is maintained at a negative potential relative to the positively charged argon ions. The positive ion is accelerated towards the negatively charged target, striking the target with sufficient force to remove the material. If a chemical reaction occurs during the transfer from the target to the substrate, the process is referred to as reactive sputtering (**Figure 2.12**). In general, most sputter sources are compound targets such as ITO and AZO targets. The sputtering can be achieved in many ways including radio frequency (R.F.) magnetron sputtering [76], pulsed magnetron sputtering [77], alternating current (AC) magnetron sputtering [78] and direct current (DC) magnetron sputtering [79]. The advantage of sputtering deposition is that even materials with very high melting temperature are easily sputtered to form thin film and the deposited films have the same composition as the source material. Sputtered films also have a better adhesion to the substrate.

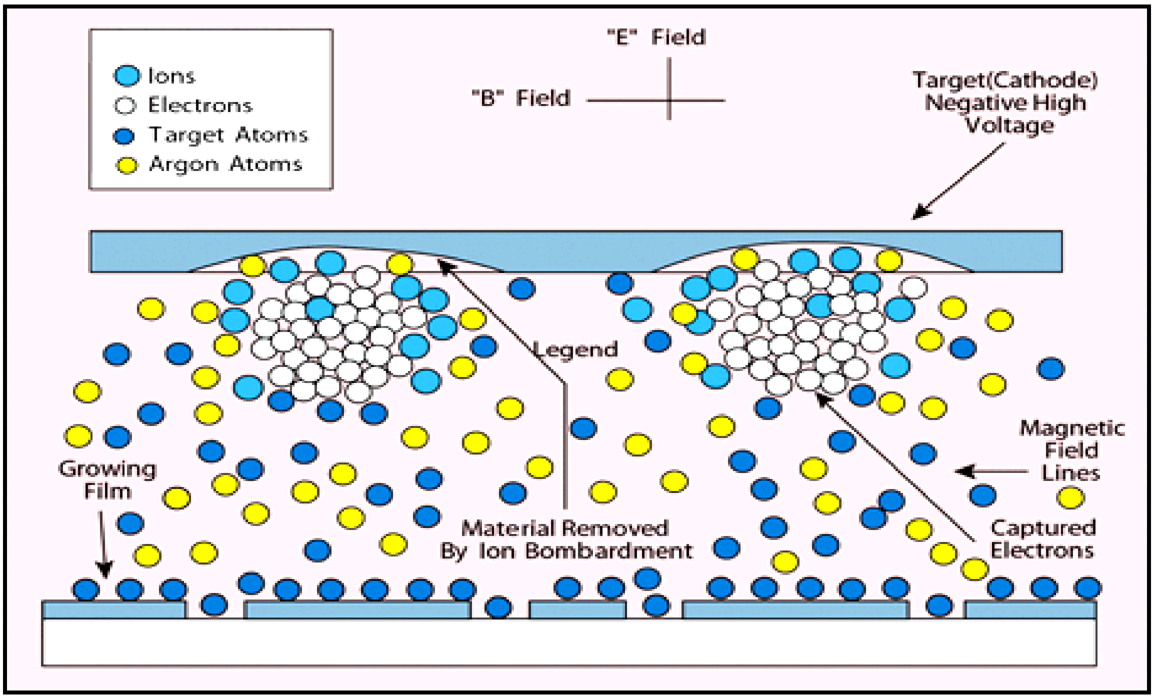

Figure 2.12 The sketch of principle of sputtering [80].

ITO thin films (0.3 μm thick) with a doping level of 28 mol% SnO_2 were prepared by a R.F. magnetron sputtering method using a composite target [81]. It was found that the sputtered film showed amorphous structure, but the films annealed at 350 °C and 510 °C exhibited crystalline structures with grain sizes of 0.12 μm and 0.14 μm, respectively. Gheidari, et al.[33] found that the electrical resistivity was dependent on the annealing temperature of ITO thin film. A maximum resistivity was obtained for the annealing temperature of 400°C. Additionally, AZO thin films were also prepared by sputtering method, including R.F. magnetron sputtering [82,83,84] and DC magnetron sputtering [79].

2.9.2 Thermal evaporation method

Thermal evaporation includes chemical and physical vapour deposition, which involve vapourising a solid by heating the material to high temperature and recondensing it on a cooler substrate. The high temperature can be achieved by resistively heating or by firing an electron or ion beam at the boat containing the material to be evaporated. In this process, alloy is usually used as the source. Evaporation takes place in a vacuum, i.e. vapours other than the source material are almost entirely removed before the process begins. In high vacuum, evaporated particles can travel directly to the deposition target without colliding with the background gas. ITO thin film properties strongly depend on oxygen partial pressure and film thickness [85], deposition rate, substrate temperature and tin concentration [86]. Reports of substrate temperatures being raised incrementally from 300 °C to 450 °C during evaporation in order to enhance conductivity and transmittance are available in the literature [87]. Takafumi Seto et al. [88] reported that AZO thin film was produced by thermal evaporation and found that Al-doped ZnO particles by aluminum acetate had high electrical conductivity (the order of 10^2 $\Omega^{-1}\cdot cm^{-1}$). The electrical conductivity could be controlled by the amount of aluminum source vapour. However, Al-doped particles by $AlCl_3$ had low electrical conductivity of the order of 10^{-8} to 10^{-6} $\Omega^{-1}\cdot cm^{-1}$ because of generation of high resistivity $Zn_5(OH)_8Cl_2$.

2.9.3 Sol-gel method

The sol-gel method has provided a very important means of preparing complex oxides with a low temperature synthesis route [89] and complex functional oxide nanostructures [48]. It is a wet chemical method and a multistep process involving both chemical and physical processes such as hydrolysis, polymerisation, drying and densification [90]. The sol-gel method, which can be used for formation of thin films, is a precursor-based solution deposition process [12]. Generally, a post-deposition high temperature anneal (normally more than 500-600 °C) is required to convert the dried gel into a desired phase. Basically a required sol is prepared and the template is dipped into the sol for a certain period of time (generally for half an hour or an hour). After the template is withdrawn from the sol, it is dried and then heat-treated at a certain temperature to obtain the desired phase. The schematic of the sol-gel route is shown in **Figure 2.13**.

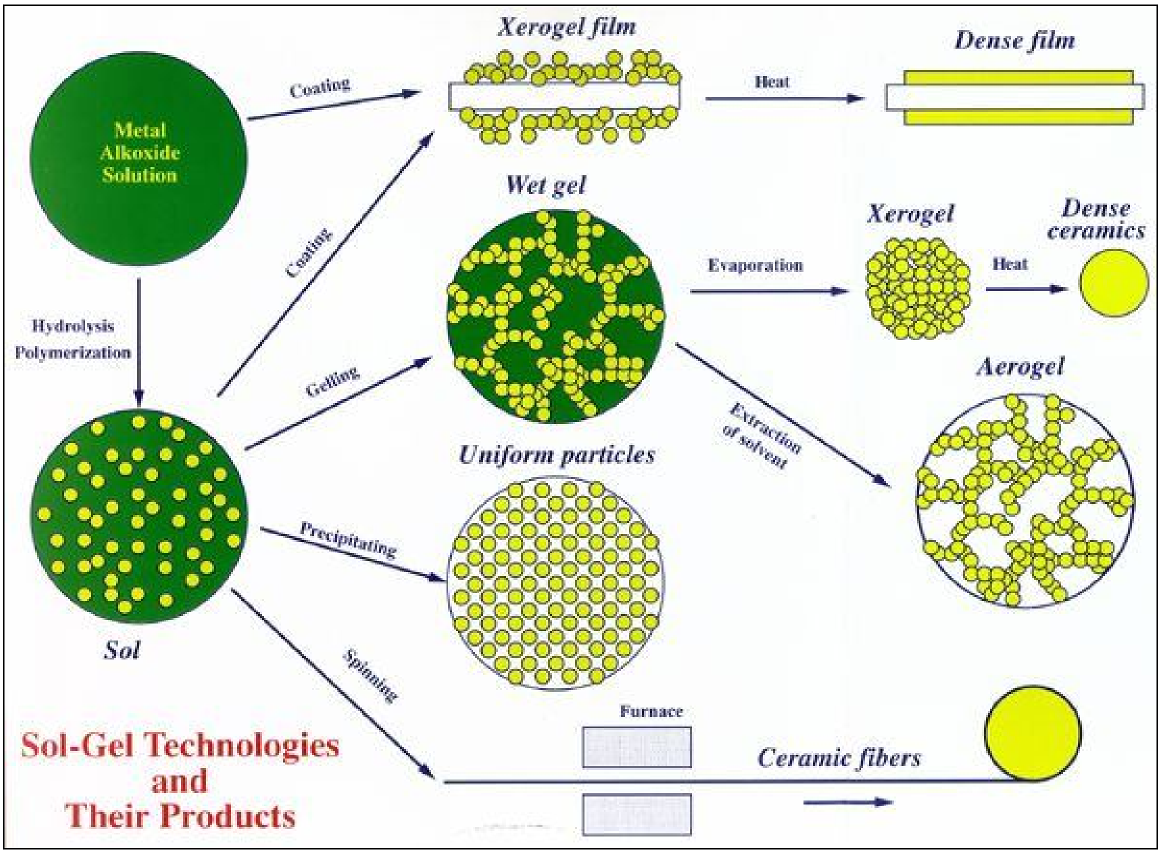

Figure 2.13 Summary of sol-gel process [91].

The coating approach by sol-gel process usually involves three steps:

(1) Preparation of a precursor solution or sol, which involves homogeneous nucleation and growth in a solution of designed chemistry.

(2) Coating the precursor solution/sol onto the substrate surface by dip or spin coating techniques.

(3) High temperature drying and processing (calcination or sintering).

One of the advantages of using the sol-gel technique for producing multicomponent inorganic materials is the ability to control precisely the microstructure, high purity and all at relatively low processing temperatures. There are three methods used to coat thin film on the different substrates: dip coating, spin coating and spray coating.

2.9.3.1 Dip coating

Dip coating is the method first developed in thin film production and has been commercialised about fifty years. Dip coating refers to immersing a substrate into a coating bath containing coating material, removing the substrate from the bath and allowing it to drain. The dip coating process can be, generally, divided into three stages as shown in **Figure 2.14**.

a) Immersion: the substrate is immersed in the solution of the coating material at a constant speed.
b) Dwell time: the substrate remains fully immersed and motionless to allow for the coating material to apply itself to the substrate.
c) Withdrawal: the substrate is withdrawn, again at a constant speed to avoid any shake.

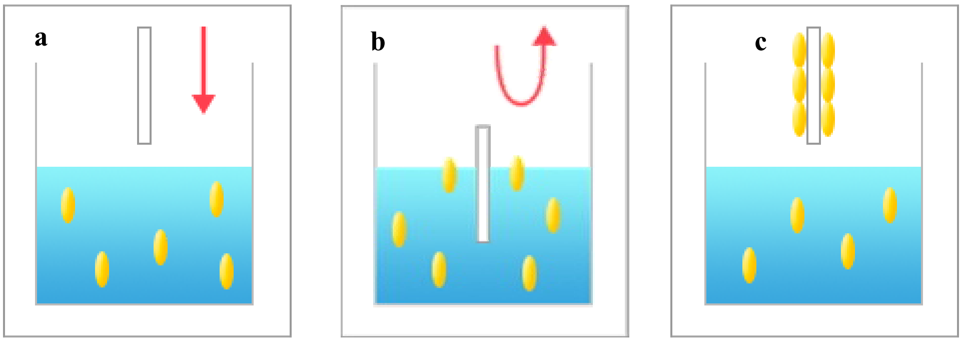

Figure 2.14 Summary of the dip coating process: a) immersion, b) dwelling and c) withdrawal.

The whole coating system consists of a liquid container for sol solutions and a motor-driven wire with a clip connected to substrates. Containers will be well cleaned before filling with prepared sols to minimise possible contaminations from the outside environment. Withdrawal speed of the motor is controlled by computer; therefore different thickness can be achieved by adjusting the properties of sol and the parameters of the dip coater. The relationship between the withdrawal speed and the thickness of thin film can be expressed by the following equation by Landau and Levich [92].

$$h_0 = 0.944 \frac{(\eta u_0)^{2/3}}{\sigma^{1/6} (\rho g)^{1/2}} = 0.944 (Ca)^{1/6} \left(\frac{\eta u_0}{\rho g}\right)^{1/2} \qquad (2\text{-}3)$$

where, h_o, u_o, η, ρ, and σ is the limiting film thickness, the withdrawal speed, the solution viscosity, the solution density and the solution surface tension, respectively. Ca (= $\eta u_o/\sigma$) is a capillary number.

If the viscosity and density of sol solution are maintained constantly, the equation can be simplified to:

$$\text{Thickness} \propto [\text{withdrawal speed}]^{1/2} \qquad (2\text{-}4)$$

The film thickness can be varied by changing the withdrawal speed. The faster the speed is, the thicker the film layers will be. The more constant the withdrawal speed is, the more uniform the thickness is. Other factors like viscosity and liquid density can also be kept constant by sealing the liquid container after preparation of sol solution. Therefore, variations in film thickness can be minimised within the same sol system.

There are some advantages of dip coating over other coating methods including:

- Any size or shape substrate can be coated;
- Simple method which can be set up at relatively low cost;
- Easy to keep contamination at a minimum;
- Easy to operate in controlled atmosphere if required.

There are however some limitations in using dip coating: a big container may be required if the substrate is very large in size, i.e. large amount of solution has to be prepared before coating, which is not economical for expensive starting materials like indium oxide. Secondly, it is not the best method to do multilayer coating because careful operation should be taken after each time, cross contaminations can also occur. Thirdly, it is even more inconvenient if only one side of the substrate needs to be coated.

2.9.3.2 Spin coating

Spin-coating differs from dip-coating in that centrifugal draining and evaporation are used in depositing thin films. Spin coating is the preferred method for application of thin, uniform films on flat substrates. The process includes four stages: deposition, spin-up, spin-off and evaporation [93]. An excess amount of sol is placed on the substrate. The substrate is then rotated at high speed in order to spread the sol by centrifugal force. Rotation is continued for some time, with sol being spun off the edges of the substrate, until the desired film thickness is achieved. One drop will be used to coat one layer so multilayers can be done by continues dropping with a certain time interval. There are only two parameters, i.e. the solution viscosity and the spinning speed, that strongly influence the deposit layer formation. Therefore, the process optimisation focuses only on these two parameters. Spinning speed is controlled by computer. The solvent is usually volatile, providing for its simultaneous evaporation. Compared with dip coating, spin coating is much more suitable for multilayer coating on a single sided substrate.

One of the advantages of spin coating is a uniformly thick coating during spin-off, provided that the viscosity is not shear-dependent and does not vary over the substrate [92]. This tendency is due to the balance between the viscous force (friction), which acts radially inward, and centrifugal force, which drives flow radially outward. The thickness of an initially uniform film during spin-off can be expressed as:

$$h(t) = h_0/(1+4\rho\omega^2 h_0^2 t/3\eta)^{1/2} \quad (2\text{-}5)$$

where, h_0 , t, ρ and ω is the initial thickness, time, the density, and the angular velocity, respectively.

If the viscosity and density of sol solution are kept constant, film thickness can be expressed as proportional to spinning rate by:

$$h(t) \propto 1/\omega \tag{2-6}$$

It can be seen that the thickness of a deposit layer can also be varied by changing the spinning rate from the equation (2-6). The faster the spinning rate, the larger centrifugal force will be and the thinner deposit layer can be obtained. Also, solution concentration can affect deposit layer thickness. Hence comprehensive considerations should be taken before estimating deposit layer thickness. As the spin rate is normally very fast (required to be >3000 rpm) to produce the thin film coatings on the substrate, a uniform thickness of the coatings can be achieved only when the diameter of a regular shaped round substrate is smaller than 0.2 m [93].

2.9.3.3 Spray coating

Spray coating is used extensively for a wide range of industrial applications and applied to substrates that are not suitable for either dip coating or spin coating [94]. Sol solutions in this case are sprayed onto surfaces of target substrates; however, the qualities of the coatings produced are inferior to the others. The solid content of the sol solution, the scanning speed and the spray pressure are the key parameters affecting the quality of the deposit layer. Coated layers can be porous, less dense and rougher. With respect to the film thickness, the spray method can offer much thicker deposit layers on a larger substrate compared with the other two methods. Also, the porous structure of the coatings can be achieved for some specific applications, such as antireflective and contrast enhancing coatings.

2.9.4 Preparation of precursor sol solution

The properties of precursor sol solution, which affect the properties of fabricated thin film, is high related to its forming conditions including starting materials, dopant, additive and sol concentration, etc.

2.9.4.1 Starting materials

Two main groups of salts, the metallic salts (M_mX_n, where M is the metal, X is an anionic group, and m and n stoichiometric coeffients) and the alkoxides (their general formula is $M(OR)_n$) which are miscible, can be used as starting materials in sol-gel process [95]. In aqueous or organic solvents, these compounds are hydrolysed and condensed to form inorganic polymers composed of M-O-M bonds [96]. Metal alkoxides are often used as starting materials in the sol–gel process, but many of the alkoxides are very difficult to obtain and deal with because of the high sensitivity to the atmospheric moisture. However, because metal salts are very useful, cheaper and easier to handle than metal alkoxides, they are good alternatives. For metal salts, hydrolysis proceeds by the removal of a proton from an aquoion $[MO_NH_{2N}]^{Z+}$ to form a hydroxo (M-OH) or oxo (M=O) ligand. Condensation reactions involving the hydroxo ligands result in inorganic polymers in which metal centers are bridged by oxygens or hydroxyls [96]. Some metal salts include chlorides, acetates, nitrates and sulfides. Chlorides, nitrates and sulfides have high solubility in water or organic solvents. In some cases, acetates have lower solubility in water or organic solvents than other metal salts. However, acetate ions can stabilise the metal ions in solutions through coordination by C=O groups [95]. For AZO thin film fabrication, many zinc salts have been used, such as zinc acetate dihydrate [97], zinc acetyl acetonate [98], zinc sulphate, zinc chloride and zinc nitrite [99].

When selecting solvents for preparing sol solutions, many solvents can be chosen, such as ethanol, methanol, isopropanol, acetyl acetonate [98], dehydrated isopropyl alcohol [97], 2-methoxyethanol [100]. Different solvents have different solubility to precursors and also have different rates of volatility rate when exposed in air, which will affect concentrations. Different combinations between precursors and solvents have different influences on TCO thin film qualities. Lee [100] suggested the use of 2-methoxyethanol as solvent because of its high boiling point (124.5 °C). Organic precursors, especially those with relatively long C-C chains could help to “tailor” and easily synthesise network structures. Some residual “R” reactant groups at the end or branches along backbones can also offer poly-additional reactions, which make new synthetic structures in sol-gel chemistry. Various physical properties such as optical transmittance, refractive index, as well as magnetic and mechanical features can be designed based on those network reactions [96].

Concentration of precursor sol solution affects the properties of thin film due to sol viscosity with respect to precursor concentrations. Some researchers have chosen the sol solution with various concentrations to study their effects on the properties of thin films. It was found that different concentrations may result in different pore sizes and surface morphologies after drying when the concentration of zinc acetate varied from 0.2 mol/L to 1.0 mol/L [97]. Dutta et al.[101] found that the thickness increased almost linearly from 36 nm to 247 nm with increase of the concentration from 0.03 mol/L to 0.1 mol/L when zinc acetate was used as starting salt (Error! Reference source not found.). In addition, the SEM micrographs of the films showed that the grain size increased with the increase of sol concentration (**Figure 2.16**). As the sol concentration increases, the amount of solute (i.e. zinc acetate) increases in the sol solution and therefore the electrostatic interaction between the solute particles becomes larger thereby increasing the probability of more solute to be gathered together forming a grain. Thus as the concentration increases, grain size also increases.

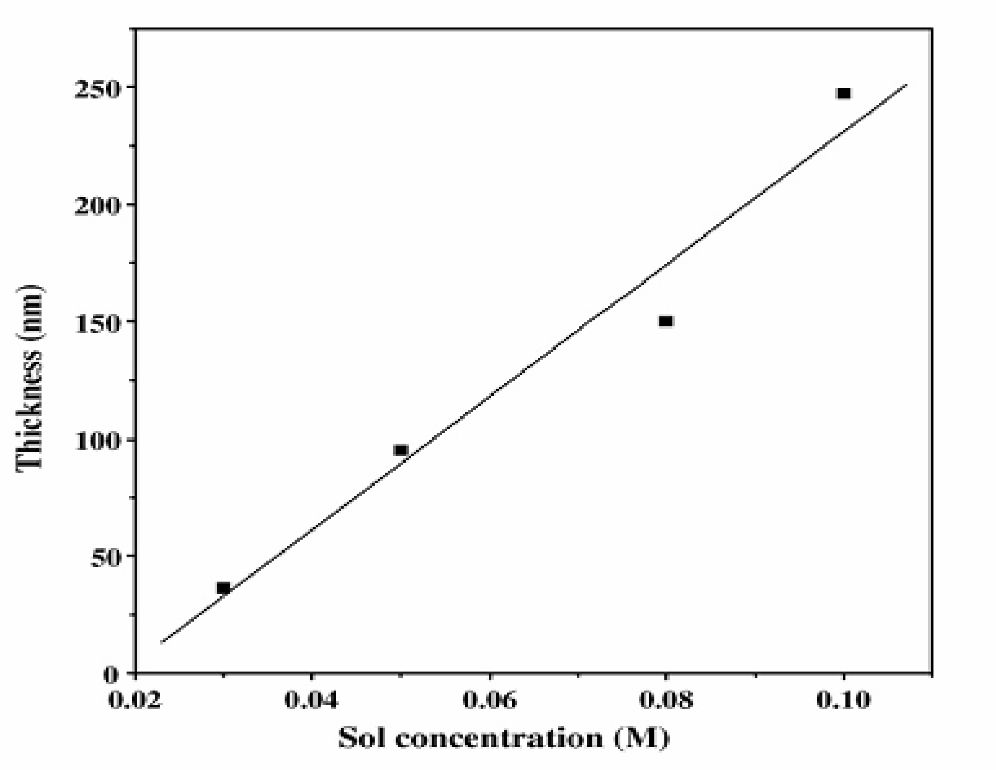

Figure 2.15 Variation of thickness of ZnO films with sol concentration [101].

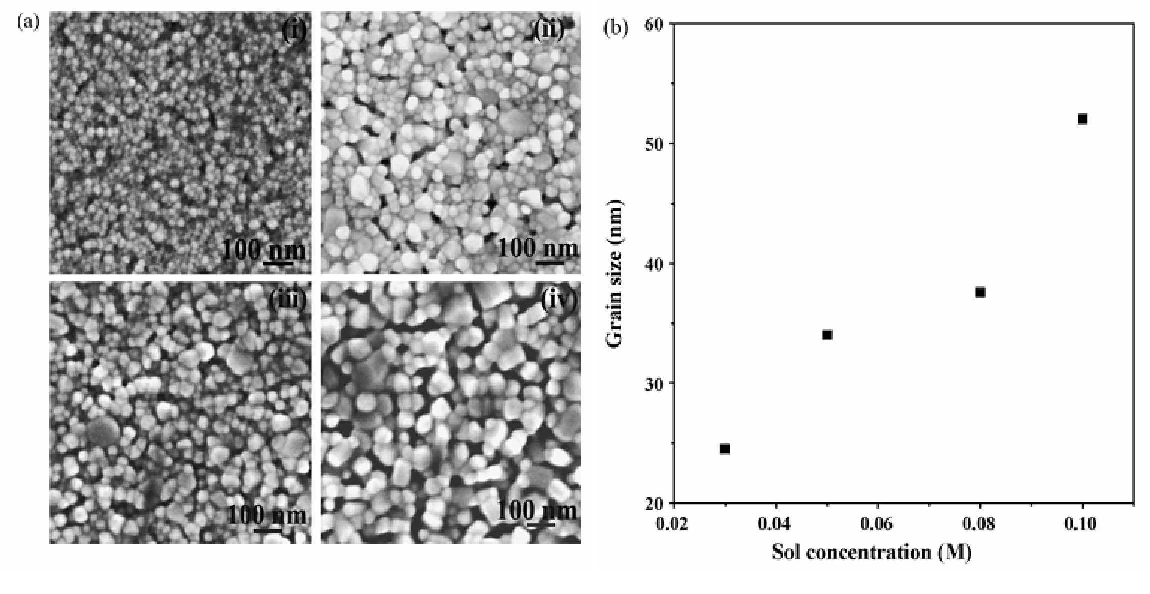

Figure 2.16 SEM micrographs of the films for sol concentrations of (i) 0.03 mol/L, (ii) 0.05 mol/L, (iii) 0.08 mol/L and (iv) 0.1 mol/L. (b) Variation of grain size with sol concentration [101].

2.9.4.2 Additives

Additives can be used in a sol solution to control both pH values and stability of the sols. Some organic precursors, such as zinc acetate dihydrate, dissolve slowly in many solvents. Additives such as diethanolamine (DEA) and monoethanolamine (MEA) can assist precursors to dissolve quickly at room temperature and make solutions stable for a long time without precipitation [97,100]. They themselves are stable during hydrolysis-polymerisation reactions and can help form uniform and dense oxide films without affecting qualities of TCO thin films.

The amount of DEA or MEA can also affect pH values in sol solutions. Parmod Sagar, et al.[102] found the pH values varied with the weight ratio "*r*" (MEA/ZnAc) ranging from 0 to 1.0 in the steps of 0.25. They found that pH values increased from 6.4 to 10.6 with the increase of the weight ratio "*r*" as shown in **Figure 2.17**. It was also found that MEA can improve the homogeneity and stability of the sols when increasing pH value within a suitable range. In the other word, increasing additives such as MEA or DEA, resulted in increasing the alkaline nature of the prepared sols, smooth microstructure, large grain size and low surface roughness. Therefore, additives are important in controlling hydrolysis-polymerisation reactions and yield good quality thin films [102].

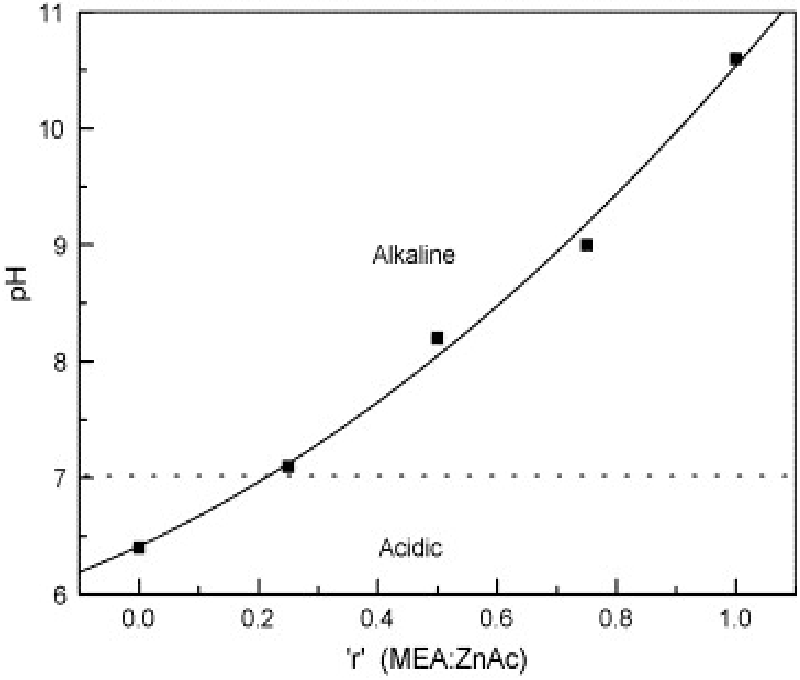

Figure 2.17 Variation of pH of sols for different value of '*r*' (MEA:ZnAc)[102].

Besides additives such as DEA and MEA, there were other additives that once used in preparation of sols: triethanolamine [103] and acetylacetone [104] have also been used as proton acceptors and improve film homogeneity of TCO thin films.

2.9.4.3 Dopant and concentration

A dopant, also called doping agent, is an impurity chemical element added to a crystal lattice in low concentrations in order to alter the optical/electrical properties of the pure semiconductor material [17]. Through doping, a semiconductor material may acquire a surplus of positive charge carriers and become a p-type semiconductor or a surplus of negative charge carriers and become an n-type semiconductor.

For improving the properties of indium oxide thin films, dopant materials including tin [27, 29, 30, 81], titanium [7], molybdenum [105] and fluorine [106] etc. have been studied in indium oxide films. Among them, tin is the one most used as dopant to fabricate ITO thin films. X. Zhang et al.[107] studied the resistivity of ITO thin films, which were fabricated using starting solution prepared by mixing indium chloride and tin chloride dissolved in ethanol via dip coating method, as a function of Sn doping concentration in the solution as shown in **Figure 2.18**. It was found that the resistivity of the thin films first decreased and reached the bottom when the content of Sn was 10 mol% (In:Sn = 9:1), and then increased. When thin films were fabricated with dip coating, the starting solution was prepared by mixing indium chloride in acetylacetone and tin chloride in ethanol[104, 108]. Similarly, the resistivity of the film decreased from 6.1×10^{-3} $\Omega\cdot$cm to 1.5×10^{-3} $\Omega\cdot$cm with the increase of Sn content up to 10 wt.%, and after that the resistivity started to increase to 4.0×10^{-3} $\Omega\cdot$cm while Sn content increased to 20 wt.%. The reason is that the Sn doping is a type of donor doping, when Sn substituting In and occupying its position in the crystal lattice, there appear unpaired electrons owing to the mismatch of stoichiometric ratio. These electrons are bounded by weak force; therefore, they can move freely and form free carriers. As the Sn doping concentration increased, the free carriers increase and improve the electrical conductivity of ITO. However, when the Sn doping concentration continuously increased, on the contrary, the electrical conductivity decreased. The increase in the resistivity of the ITO thin films with increase in Sn doping concentration beyond a critical value (10 mol%

in this present case) has been associated with segregation of the dopant ion components at the grain boundaries [109,110, 111]. Many reports [104, 109, 112] have investigated the influence of the Sn doping concentration on the conductance of ITO thin films and suggested the optimal concentration was 8–10 mol%, which is close to the theoretical value [29, 30]. Therefore, doping is an important method to improve the electrical conductivity of ITO, but doping concentration must match the experimental conditions in order to obtain satisfying results.

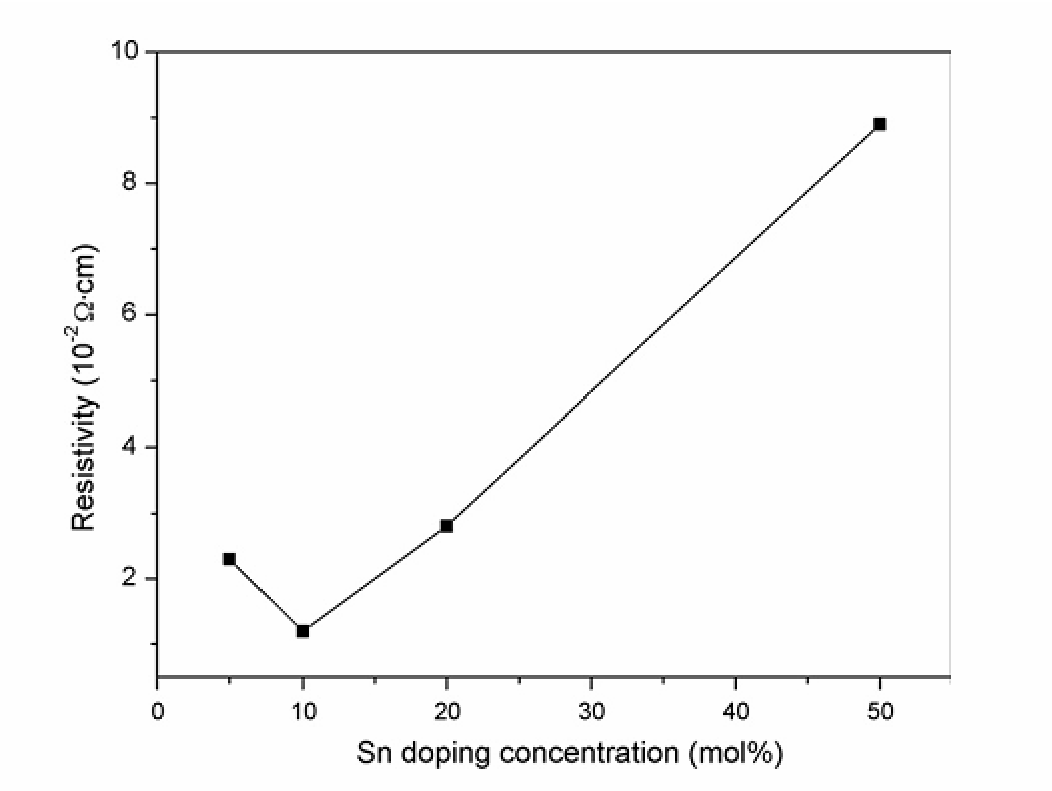

Figure 2.18 Resistivity of ITO thin films with various Sn doping concentrations [107].

In regard to fabricating ZnO films, dopant materials can be Al, In and Sn [100], and Mn [113], which affect the microstructure of thin films. When doping the same level of Al, In and Sn, particle sizes and film thicknesses are different; surface morphologies of Al dopant are better than the other two. When changing concentrations of these dopants, the change of particle size is more rapid with aluminium dopant due to the largest difference in ionic radii between aluminium and zinc than the other dopants [100]. To fabricate AZO thin films, the sources of aluminium dopant come from aluminium chloride, aluminium nitride [97], aluminium isopropoxide [114], aluminium pentanedionate [115] and so on. They can be divided into organic and inorganic systems. Aluminium dopant concentration was found effective in changing surface morphologies of AZO thin films fabricated via sol-gel method by the chemical spray technique [115]. When the ratio of [Al/Zn] in sol solutions is between 2.0 at% to 3.0 at%, smooth, uniform and compact surface morphology was obtained. The grains were also changed from small rounded particles to larger and elongated ones (**Figure 2.19**). It can be considered that beyond a certain critical [Al/Zn] ratio, the Al tends to segregate at the grain boundaries, hindering the development of longer grains. Moreover, the high resistivity (>4.3 $\times 10^{-3}$ Ωcm) measured in this film indirectly confirms the presence of a highly resistive aluminum oxide phase in the grain boundaries, although at a concentration lower than the limit of resolution of the X-ray diffractometer used, since according to the spectra obtained no aluminum or aluminum oxide phases were detected.

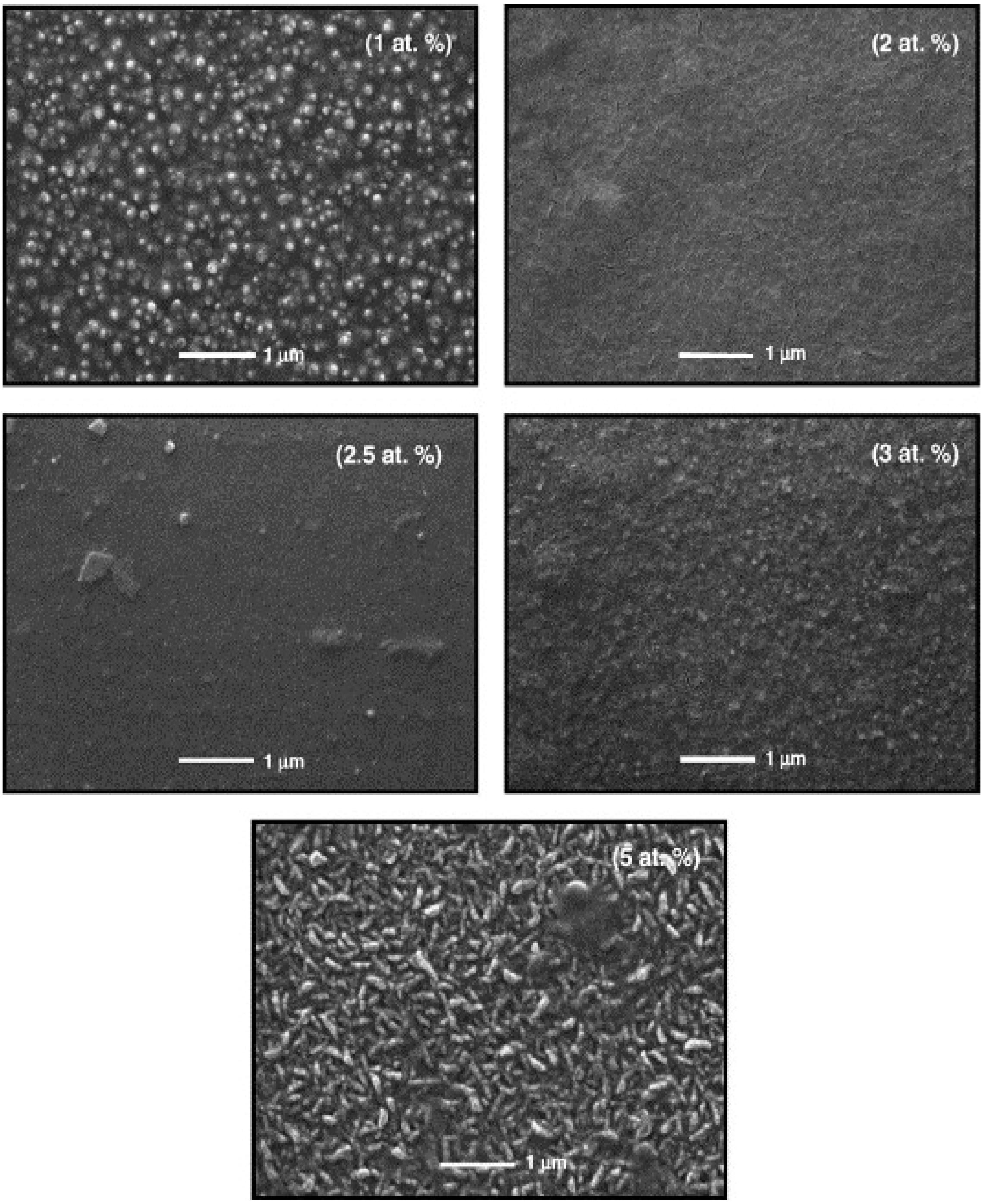

Figure 2.19 SEM micrographs for annealed AZO thin films deposited at 500 °C from starting solutions with different [Al/Zn] ratios:1 at.%, 2 at.%, 2.5 at.%, 3 at.%, and 5 at.% [110].

Transparent AZO films were also prepared by using zinc acetate-2-hydrate [$Zn(CH_3COO)_2 \cdot H_2O$] and aluminum nitrate nonahydrate [$Al(NO_3)_3 \cdot 9H_2O$] as the starting materials, and alcoholic solution as the solvent by dip coating method [116]. It was found that doping concentration had influences on the microstructures of AZO films. Compared with undoped and 5 mol% Al-doped AZO thin film, the smaller grain size was observed for the aluminium doped AZO. This can be attributed to the tendency of the dopant aluminium to create more nucleation centers during the deposition process [117]. The similar results were also observed by Lee [100] and Bandyopadhyay et al. [118]. The particle size reduced with the increase of the doping concentration of aluminium. The results showed that the film doped with 1 at% of aluminium had particles of approximately 80 nm and exhibited a porous structure. When the doping concentration was 2 at%, particle size was decreased and the microstructure of the film became denser. The 3 at% doped film consisted of small particles forming a matrix and large ones lying on the matrix.

2.9.5 Processing conditions of fabrication thin films

Processing conditions of fabrication thin films including coating rate, deposit layer and heat treatment are the important factors which affect the qualities of TCO thin film, such as surface morphology, thickness, grain size, microstructure, optical and electrical properties of the thin film.

2.9.5.1 Coating rate

Coating rate, i.e. withdrawal speed of substrate in dip coating process, has a relationship with film thickness, which can be estimated by equation 2-4, i.e. thickness $\propto$ [withdrawal speed]$^{1/2}$. The equation works only under constant liquid viscosity and concentration. Ota et al. [119] have studied this theory in fabricating ITO thin films. It was found that the thickness increased with the increase of the withdrawal rate (withdrawal speed), u, during the dip coating. The experimental result is consistent with the equation 2-4, i.e. thickness of the ITO film was approximately proportional to the square root of the withdrawal speed.

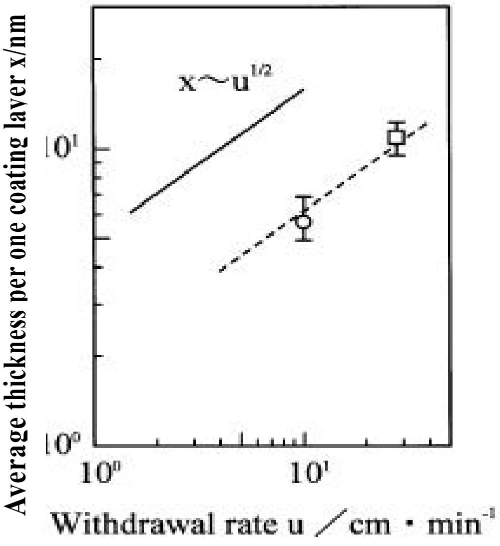

Figure 2.20 Average thickness per one coating layer of ITO films deposited by dip coating vs the withdrawal rate [119].

Conductivity and transparency of thin films are known to be strongly interrelated, leading to a certain trade-off between the two. Park and Mackenzie [120] studied the relationship of sheet resistivity and optical transparency with thickness of tin oxide thin films prepared by dip coating method. The results showed that both sheet resistivity and optical transparency decreased significantly with increasing film thickness (**Figure 2.21**). The reason can be attributed to both the sheet resistivity (Rs) and optical transparency (Tr) of thin film are related closely to the film thickness. Sheet resistivity can be expressed as: $Rs = \rho_{(t)}/t$, where $\rho_{(t)}$ is resistivity, and t is thickness of thin film. The sheet resistance is decreased with the increase of the thickness of thin film. Optical transparency (Tr) can be calculated from the eqation [121]: $Tr = e^{-a \cdot t}$, where a is absorption coefficient, and t is thickness of thin film.

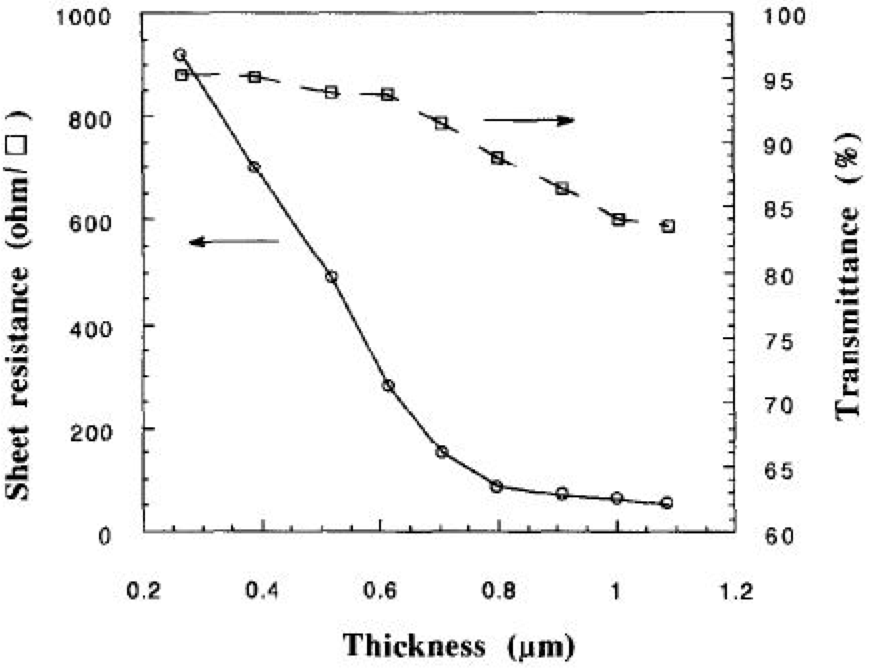

Figure 2.21 Variation in the sheet resistance *Rs,* and average visible transmittance *T* with thickness for multi-dipped tin oxide thin films [120].

2.9.5.2 Effect of multiple deposition layers

It is known that the increase of both the withdrawal speed and the number of deposited layer leads to increase of the film thickness. On the other word, the more layers coated onto substrates, the thicker of TCO films will be. The thickness of AZO films varied with the number of deposited layer has been investigated by Lin and Tsai [122] as shown in **Figure 2.22**. It can be seen that the thickness of thin film increased with the increase of the number of deposited layer, and there was a linear relationship between the film thickness and the number of deposit layer. They also found that the number of deposited layer affected surface morphologies of AZO thin films. SEM micrographs in **Figure 2.23** shows surface morphologies of AZO thin films with number of deposited layer from 1 to 5. When the film with single layer, it can be observed that the film exhibited many pores and rough surface morphology, which is possibly due to the evaporation of solvents and decomposition of partially hydrolysed and condensed precursor materials. With further increases in the number of deposit layer, the pores and roughness of thin film decreased. It was believed that pores of the first layer were filled when the second layer was deposited. This filling of pores and the repeated coating of the films seemed to result in decreasing pores and surface roughness [123]. Therefore, suitable number of deposit layer could prevent surface defects of thin film such as pores or cracks, and help to obtain the thin films with smooth surface with minimum roughness.

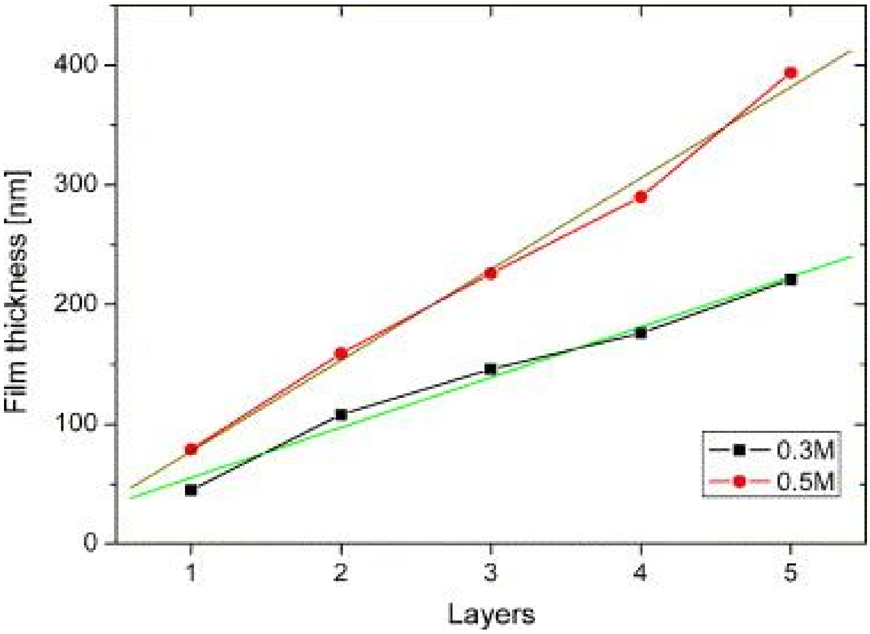

Figure 2.22 Thickness of AZO thin films varied with numbers of deposit layer [122].

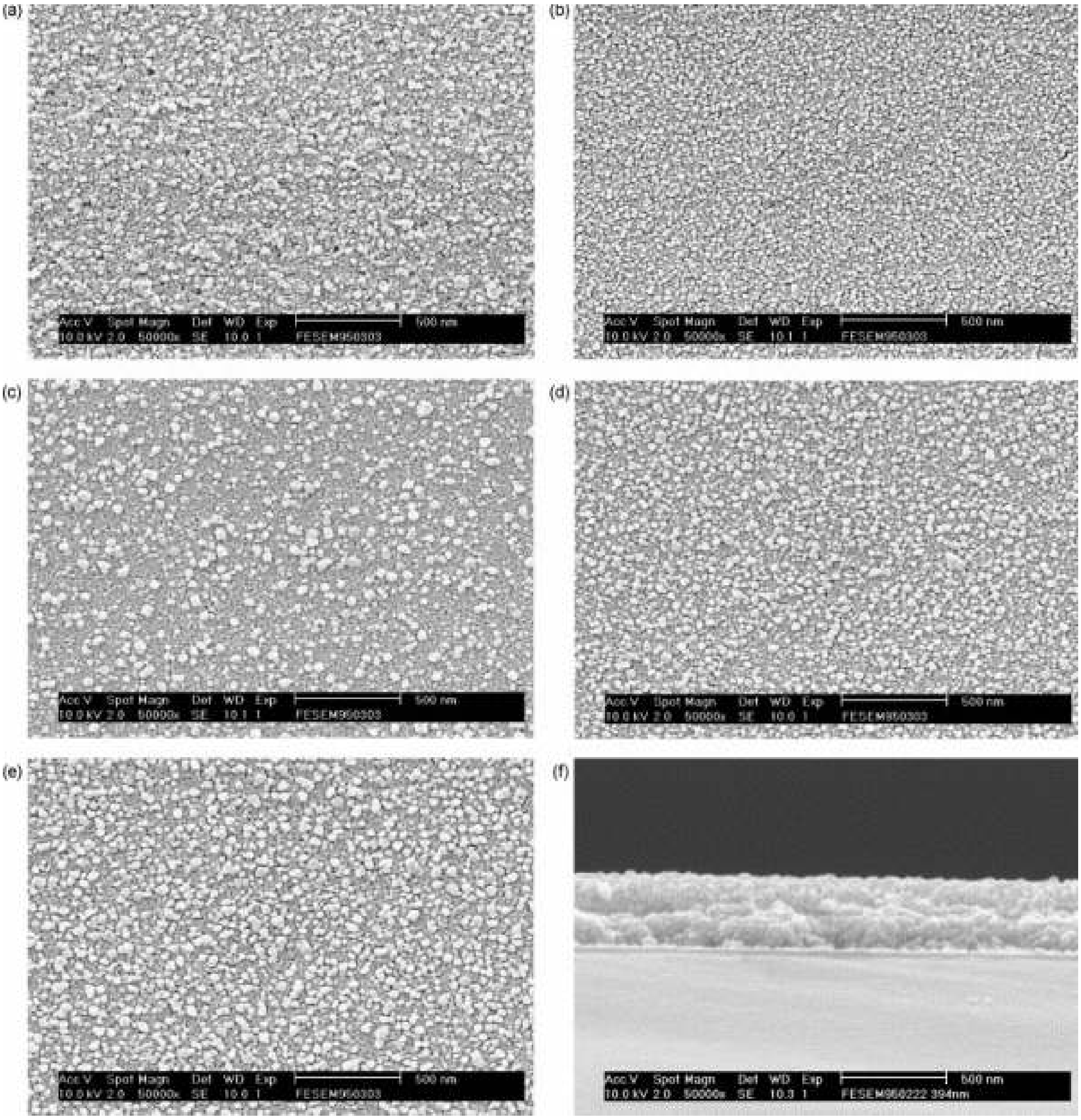

Figure 2.23 Surface morphology of AZO films, 0.5M, Al/Zn=2at.%, pre-heated at 600°C in air, and post-heated at 600°C under vacuum: (a–e) present layer number 1–5, respectively; (f) gives the cross-section of the five layers film [122].

The influence of the number of deposit layer on the sheet resistance of ITO thin films on quartz-glass substrate at the withdrawal speed of 8 cm/min was studied by Li et al.[124]. The result showed that the sheet resistance of the films decreased with the increase of the number of deposit layer (**Figure 2.24**). It was found that the relationship between the sheet resistance of the film and the number of deposit layer is not linear. Higher sheet resistance of the monolayer film can be explained by the discontinuous nature of the film, i.e. insufficient coverage of the substrate or many pores existed and poor crystal growth. The thickness of thin films increased with the number of deposit layer can be owing to the followed coating is formed on the first one and the sol has better wetting ability on the coating than that on the substrate, which resulting in that the followed coating has more thicker thickness and much higher density [124]. The reduced sheet resistance with the increase of thickness of thin films is attributed to the improved crystallinity and increased crystalline sizes that weaken inter-crystallite boundary scattering and increase carrier lifetime, which consequently, increase the mobility for carrier with the increased thickness of thin films [125]. Another reason that sheet resistance decreased with the number of deposit layer was found to be that the relative density of thin film increased from 65% to 87% as the number of deposit layers increased from 1 to 5 [126]. The increase of the density of the film with the increase in the number of layer can be attributed to two factors：the first factor is the process of the sol filling the pores of the previously deposited layers (except for the last one); the second factor is connected to pore elimination during re-crystallisation.

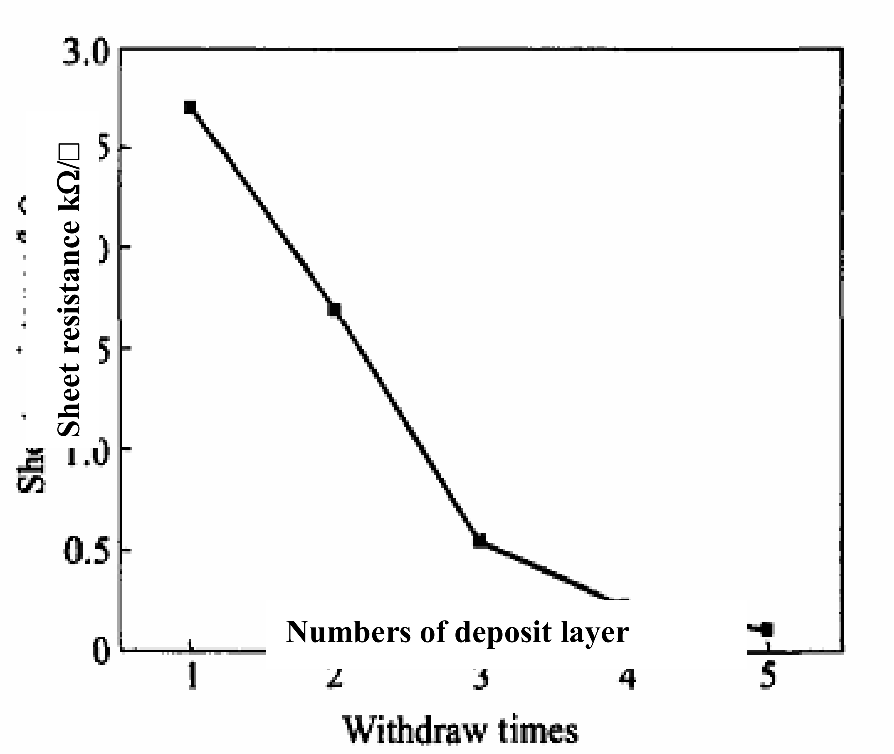

Figure 2.24 Sheet resistance of ITO thin films varied with numbers of deposit layer [124].

The influence of the number of deposited layer on the transmittance of AZO thin film, i.e., the influence of thickness on the transmittance of thin film is shown in **Figure 2.25**. The transmittance of thin films was decreased from 92% to 83% while the thickness of the AZO films increased from 400 nm to 1600 nm [125], which can be attributed to the optical absorption of the thickness discussed in previous section.

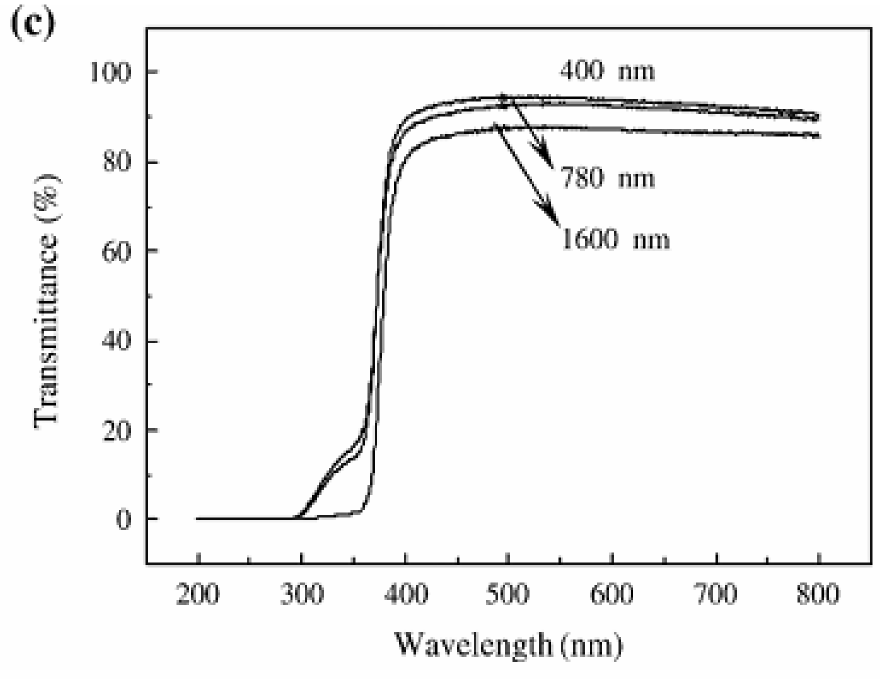

Figure 2.25 The influence of numbers of deposit layer on the transmittance of AZO thin film [125].

2.9.5.3 Heat treatment

Heat treatment process, either annealing temperature or annealing time, will affect crystal growth, surface morphologies, and so on. In the sol-gel process, particle-stack a porous structure within TCO thin films is formed in the microstructure point of view, since the evaporation of organic components during heat treatments. For evenly distributed pores within these films, they normally have different electrical conductivity [127]:

$$\ln\sigma_r = V_g \ln\sigma_g + V_s \ln\sigma_s \qquad (2\text{-}7)$$

where, σ_r, σ_g and σ_s represent conductivities of whole material, gas and solid state; V_g and V_s are volumetric proportions of gas and solid phases. It is obvious that the holes have great influence on the conductivity of the whole film material. On the other hand, electrical and optical properties of TCO thin film are also affected by grain growth during heat treatment process because the grain growth is proportional to the square root of the annealing time [128].

Various studies have reported the effect of heat treatment on such materials， for example, indium tin oxide thin films were fabricated by dip coating using the starting solution prepared by mixing indium chloride dissolved in acetylacetone and tin chloride dissolved in ethanol [104, 129] (**Figure 2.26**). It was found that the heat treatment temperature significantly affected the resistivity of 10 wt.% Sn-doped ITO films. The resistivity decreased considerably as the heat treatment temperature raised to 600 °C in air (**Figure 2.27**). This can be attributed to two reasons: one is that the higher treatment temperatures enhance the crystallisation of ITO films, resulting in the increase of the carrier mobility; the other is that the formation possibility of the oxygen-ionic vacancies increases with the temperature, resulting in the increase of the conductivity [124]. However, the resistivity increased with the increasing temperature when the treatment temperature was higher than 600 °C. Because SnO_2 may be reduced to SnO, i.e. the valence of the Sn ion transforms from +4 to +2 at higher temperatures, the ionic conductivity decreases. On the other hand, at the higher temperatures, oxygen will diffuse into the ITO lattice, reducing the number of oxygen vacancies and leading to a decrease in charge carrier concentration [130].

In other work[131, 132], the optical transmittance of ITO film in the visible region improved with increasing heat treatment temperature with the maximum transmittance at 900 nm of 80% for 400 °C annealed film, which increased to 88% for 500 °C and further increased to 93% after treatment at 600 °C (**Figure 2.28**). The optical properties of ITO films prepared by sol–gel process using inorganic metal salts (anhydrous indium trichloride and hydrous tin (IV) chloride) with polymer poly(ethylene glycol) (PEG) as the additive were investigated. An increase of optical transmittance (3% to 5%) in wavelength 350–700 nm was observed by addition of PEG as it improved the surface quality of thin film.

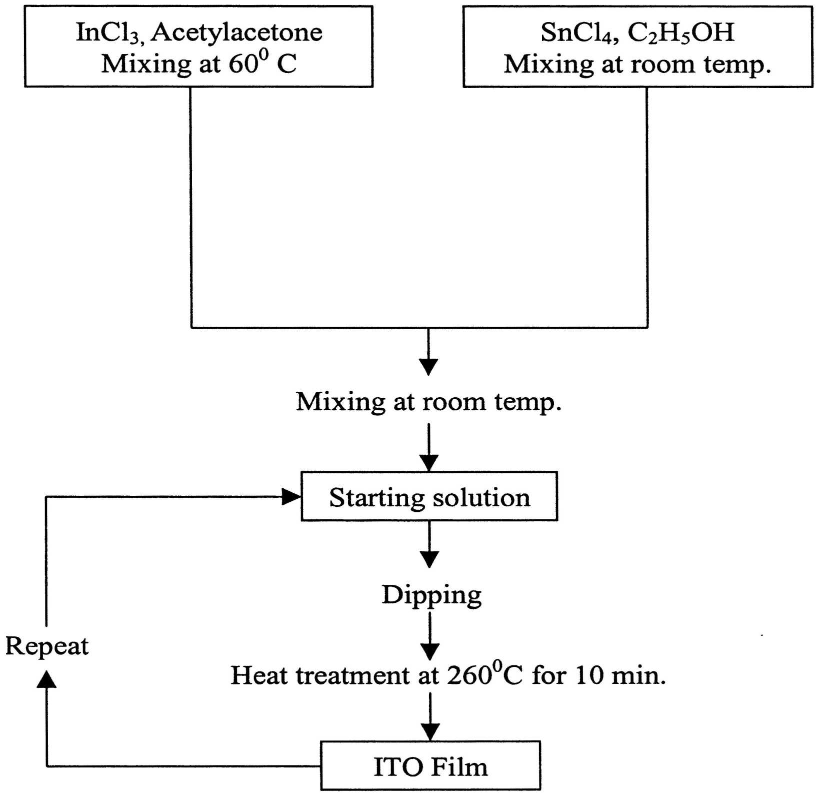

Figure 2.26 Preparation procedure of ITO thin film by sol-gel process [104].

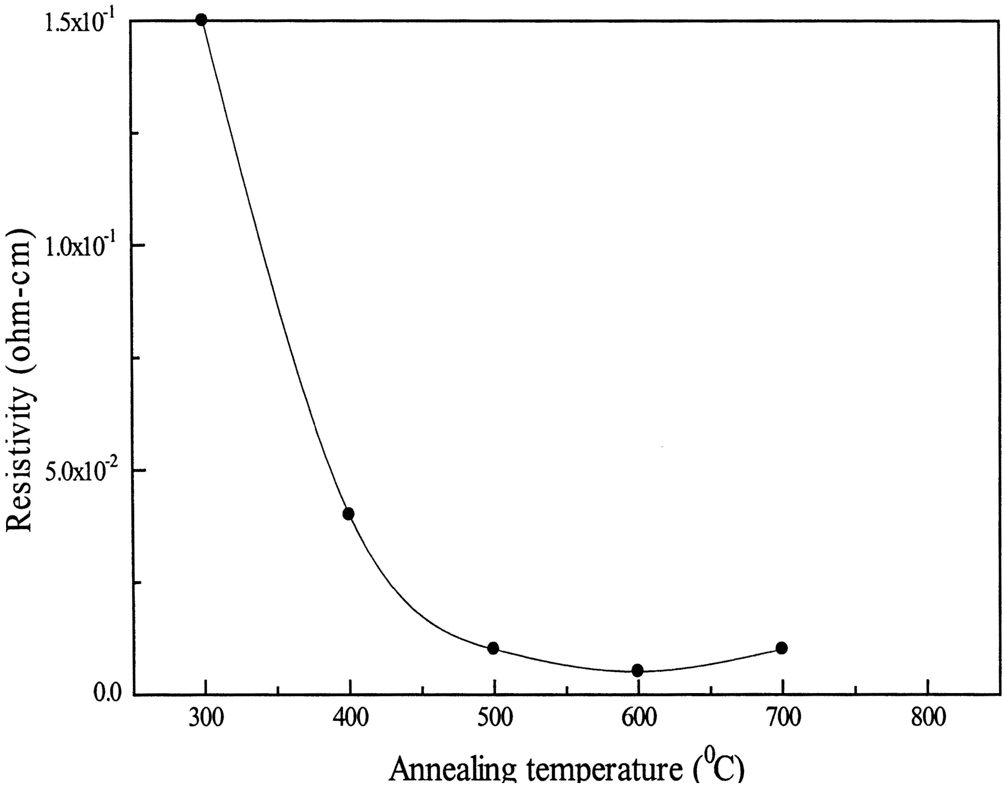

Figure 2.27 Resistivity of the ITO thin films as a function of annealing temperature [129].

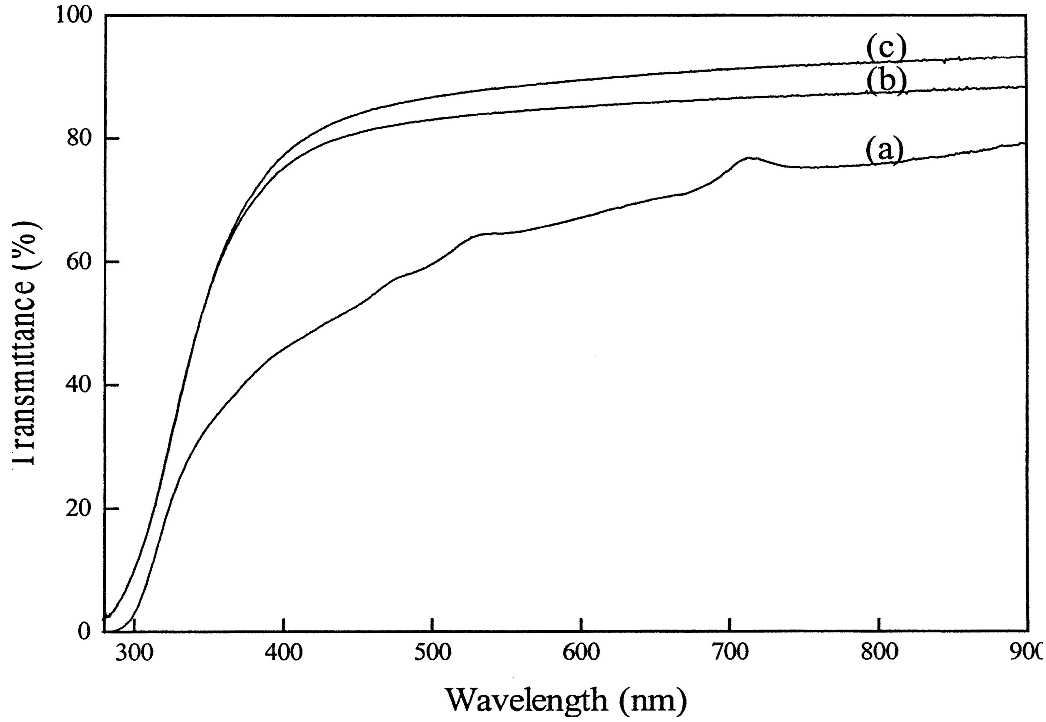

Figure 2.28 Optical transmission spectra of ITO films (250 nm) with various annealing temperature (a) 400 °C, (b)500 °C and (c) 600 °C [104].

The influence of heat treatment temperature on the grain growth of ITO thin film, which is prepared using solutions of 2,4-pentanedione, ethanol, indium and tin salts by dip-coating process on silica substrates, was investigated by Beaurain et al [133]. The result showed that the grain sizes increased from 8 nm to 90 nm with the increase of heat treatment temperatures from 350 °C to 550 °C. The study indicated a correlation between the resistivity and the size of ITO crystallites, i.e., the smaller the size of ITO crystallites is, the higher the resistivity is. The lowest sheet resistance (or resistivity =1.6×10^{-2} $\Omega\cdot$cm) was obtained at annealing temperature of 550 °C. In another case, transparent AZO films were prepared by using zinc acetate-2-hydrate and aluminum nitrate nonahydrate as the starting materials, and alcoholic solution as the solvent [117,134,135]. It was found that annealing temperature had influences on the grain size of AZO films. The results showed both undoped and 5 mol% Al-doped AZO thin films, the grain size was increased with the increase of annealing temperature (**Figure 2.29**). The similar results were also observed by Lee [100] and Bandyopadhyay et al.[136].

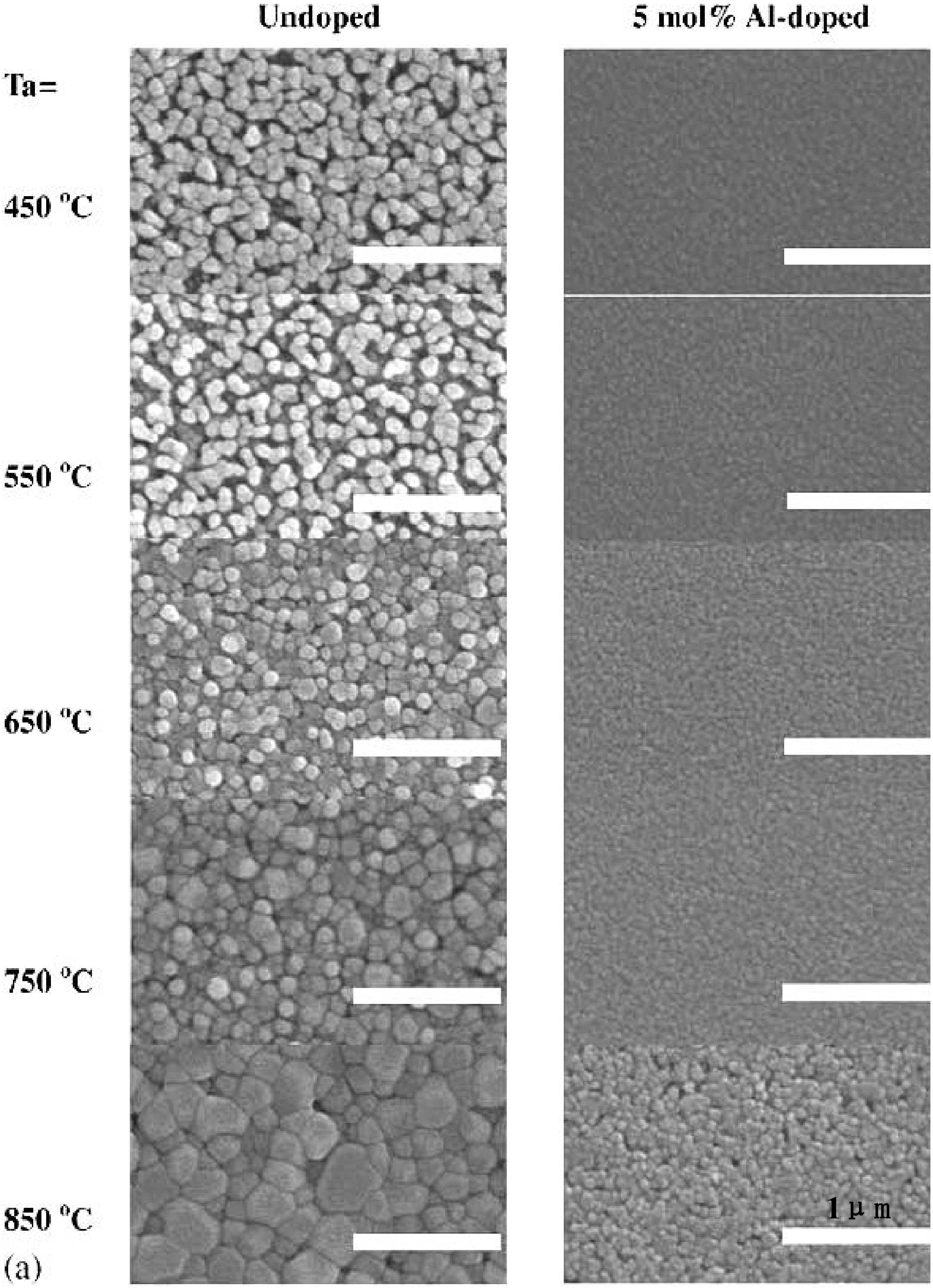

Figure 2.29 SEM micrographs of undoped and 5 mol% Al-doped ZnO thin films annealed at various temperatures from 450 °C to 850 °C [134].

Kim and Tai [137] studied the influence of heating temperatures on the qualities of AZO thin films, which were fabricated using zinc acetate-aluminium chloride system and annealed at the temperatures ranged from 500 °C to 700 °C at an interval of 50 °C. They suggested the reason to control crystal growth by heating temperatures can change thin film surface morphologies, i.e., the pores within films can also be minimised at chosen temperatures and a uniform dense microstructure can be obtained. From SEM micrographs as shown in **Figure 2.30**, it can be observed that uniform and dense microstructures were obtained at 600 °C and 650 °C. At lower temperatures, sizes of crystals are not uniform and films are not as dense as those at higher temperatures are. But when the temperature went up to 700 °C, big pores were found although the film was denser. The pores result from the decomposition reaction of precursors at high heating temperatures and the evaporation of residual organics in gels. Furthermore, microvoids can then coalesce to form bigger pores [138]. On the other hand, the electrical resistivity of the AZO thin films was decreased from 73 to 22 Ω·cm as the heating temperature increased up to 650 °C; however, the resistivity of the film annealed at 700 °C increased greatly to 580 Ω·cm (**Figure 2.31**). The optical transmittance of the films annealed below 650 °C was over 86%, but it decreased to < 80% at 700 °C (Error! Reference source not found.). The decreases of electrical and optical properties in the AZO films annealed at 700 °C seemed to be due to the segregation of Al_2O_3 at grain boundaries and partially pores [137], which decreased carrier mobility in the films. Another reason is probably due to $ZnAl_2O_4$ cubic phase was formed after annealing at 700 °C, which also reduces the conductivity of AZO thin films [134].

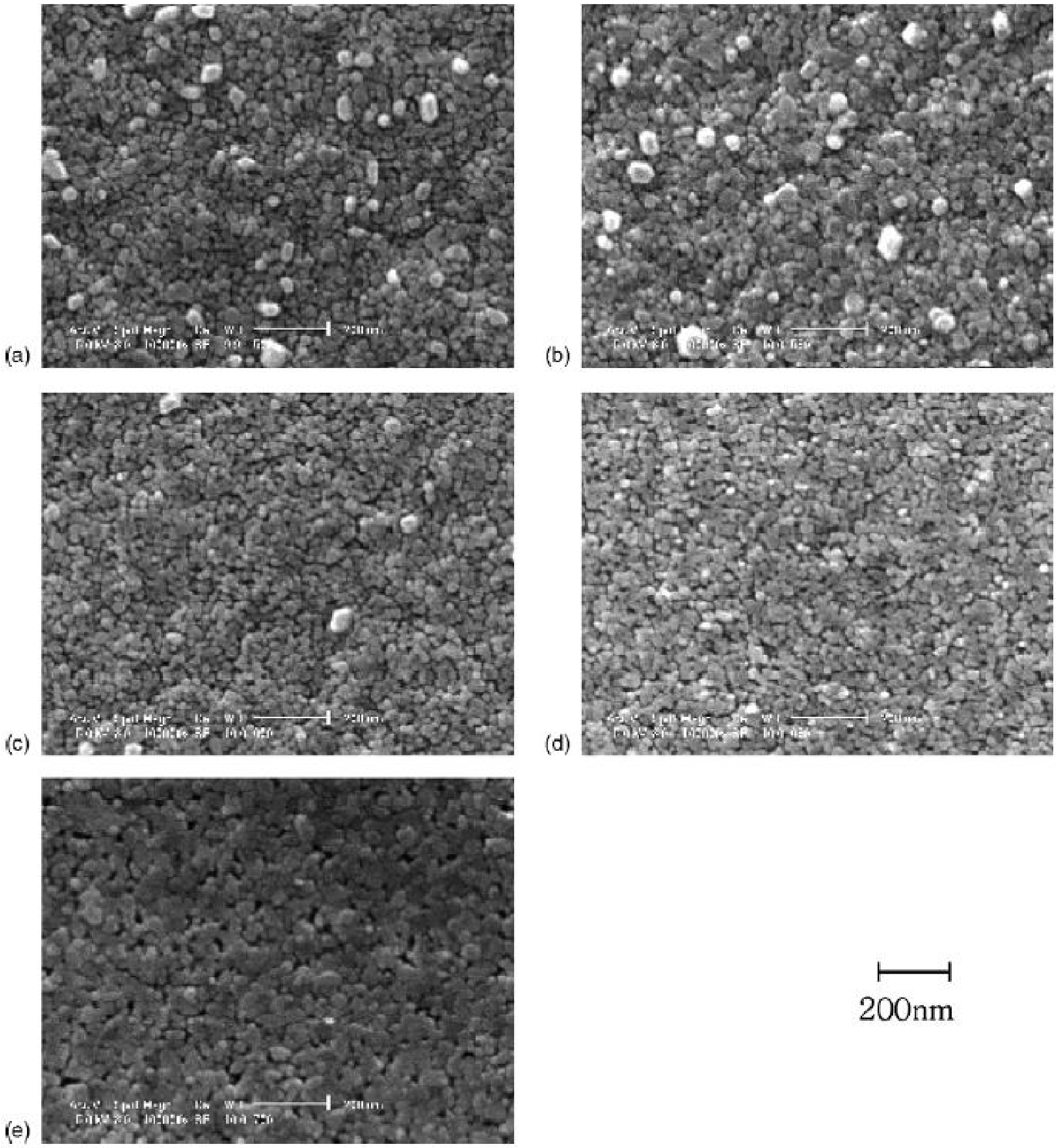

Figure 2.30 SEM micrographs of Al-doped ZnO films postheated at various temperatures of (a) 500 °C, (b) 550 °C, (c) 600 °C, (d) 650 °C and (e) 700 °C [137].

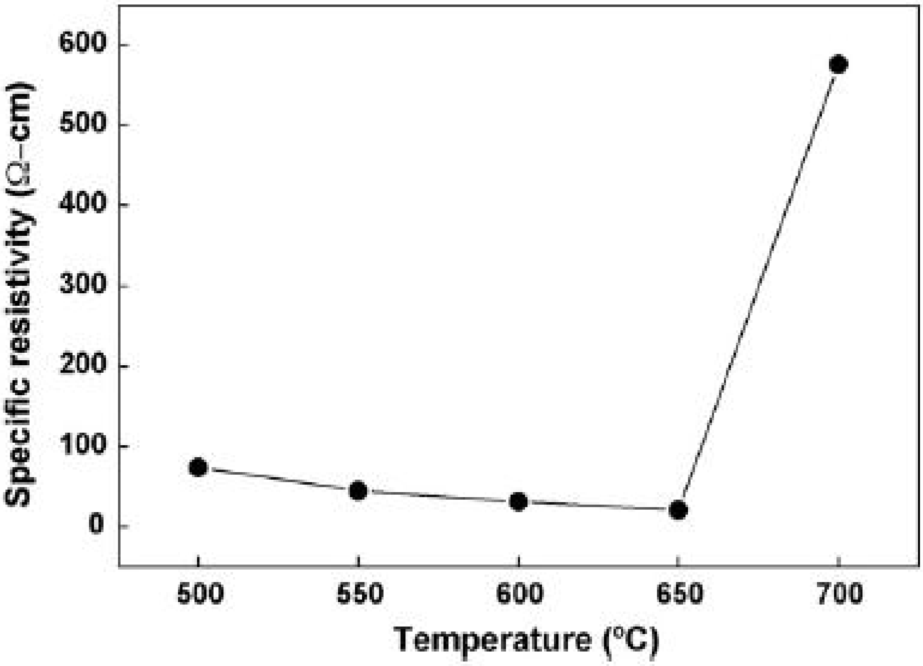

Figure 2.31 Resistivity varied with annealing temperature[137].

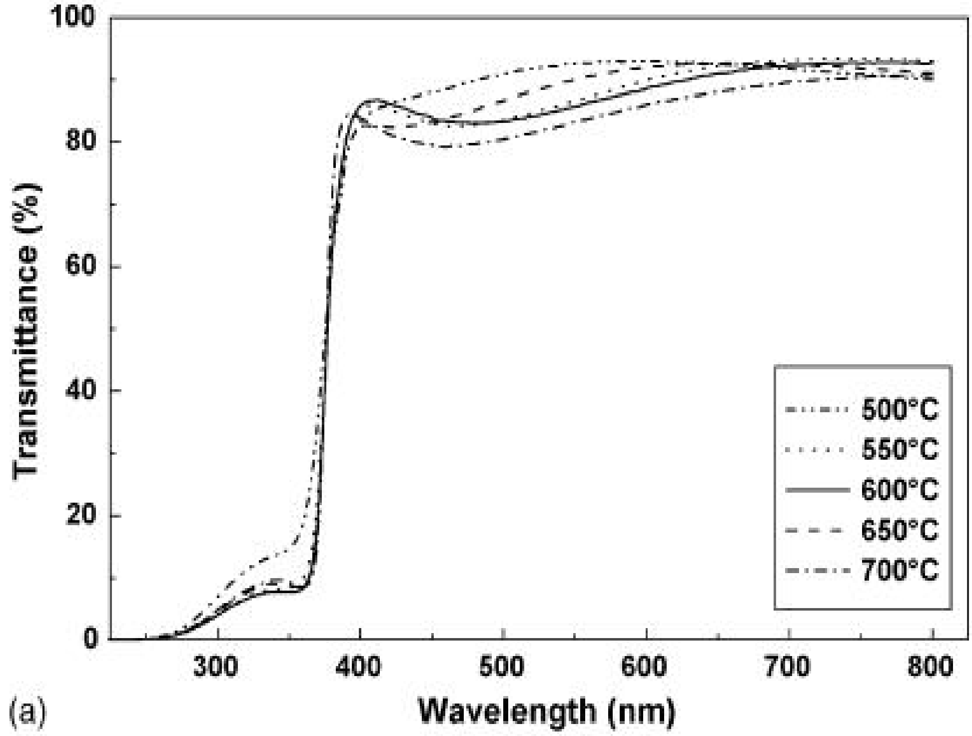

Figure 2.32 Transmittance varied with annealing temperatures[137].

Chapter 3 EXPERIMENTAL DETAILS

3.1 Materials

The chemicals and materials used in this project are listed in **Table 3-1**:

Table 3-1 List of chemicals

Chemicals	FW （g/mol）	Purity (%)	Manufacturer
Indium metal (In)	114.82	99.99	Ningxia Orient Tantalum Industry Co., Ltd, China
Stannic chloride pentahydrate ($SnCl_4·5H_2O$)	350.58	99	Rugao Chemical Company, China
Zinc nitrate hexahydrate ($Zn(NO_3)_2·6H_2O$)	297.47	97	Fisher Scientific, UK
Zinc chloride ($ZnCl_2$)	136.29	98.3	Fisher Scientific, UK
Zinc sulfate heptahydrate ($ZnSO_4·7H_2O$)	287.54	99	Fisher Scientific, UK
Zinc acetate dihydrate ($Zn(C_2H_3O_2)_2·2H_2O$)	219.5	98+	Sigma-Aldrich Co., Ltd, USA
Indium sulfate ($In_2(SO_4)_3$)	517.64	99	Jonson Matthey Company, UK
Aluminum nitrate nonahydrate ($Al(NO_3)_3·9H_2O$)	375.13	98	Fisher Scientific, UK
Ammonium hydrogen carbonate (NH_4HCO_3)	79.06	Assay: 100.14	Fisher Scientific, UK
Silver nitrate ($AgNO_3$)	169.87	99.99	Sigma-Aldrich Co., Ltd, USA

Sodium hydroxide (NaOH)	40	97+	Sigma-Aldrich Co., Ltd, USA
Poly(ethylene glycol) $H(OCH_2CH_2)_nOH$	400	---	Sigma-Aldrich Co., Ltd, USA
Poly(ethylene glycol) $H(OCH_2CH_2)_nOH$	1000	---	Sigma-Aldrich Co., Ltd, USA
Poly(ethylene glycol) $H(OCH_2CH_2)_nOH$	3400	---	Sigma-Aldrich Co., Ltd, USA
Poly(ethylene glycol) $H(OCH_2CH_2)_nOH$	8000	---	Sigma-Aldrich Co., Ltd, USA
Ammonia solution (NH_4OH, d=0.91g/cm^3, 25%)	35	---	Fisher Scientific, UK
Hydrochloric acid (HCl, d=1.16 g/cm^3, 32%)	36.5	---	Fisher Scientific, UK
Nitric acid (HNO_3, d=1.42 g/cm^3, 70%)	63	---	Fisher Scientific, UK
Ethanol (CH_2CH_2OH)	45	98	Sigma-Aldrich Co., Ltd, USA
2-Methoxyethanol ($CH_3CH_2OCH_2CH_2OH$)	76.10	99	Sigma-Aldrich Co., Ltd, USA
Mono-ethanolamine(MEA) ($H_2NCH_2CH_2OH$)	61.08	99	Sigma-Aldrich Co., Ltd, USA
Ethylenediamine ($H_2NCH_2CH_2NH_2$)	60.10	99	Sigma-Aldrich Co., Ltd, USA

$InCl_3$ and $In(NO_3)_3$ were obtained by stirring the In-metal ingots with concentrated HCl and HNO_3, respectively for 6-10 h at 80 °C, and then evaporation at 100 °C until the solid salts formed.

3.2 Synthesis of TCO nanoparticles

The hydrothermal method is employed to synthesise transparent conducting oxide (TCO) nanoparticles including tin oxides, indium oxides, indium tin oxides (ITO), zinc oxides, aluminum oxides and aluminum zinc oxides (AZO).

3.2.1 Hydrothermal method

A flow chart of synthesis of TCOs nanoparticles by hydrothermal method is shown in **Figure 3.1**:

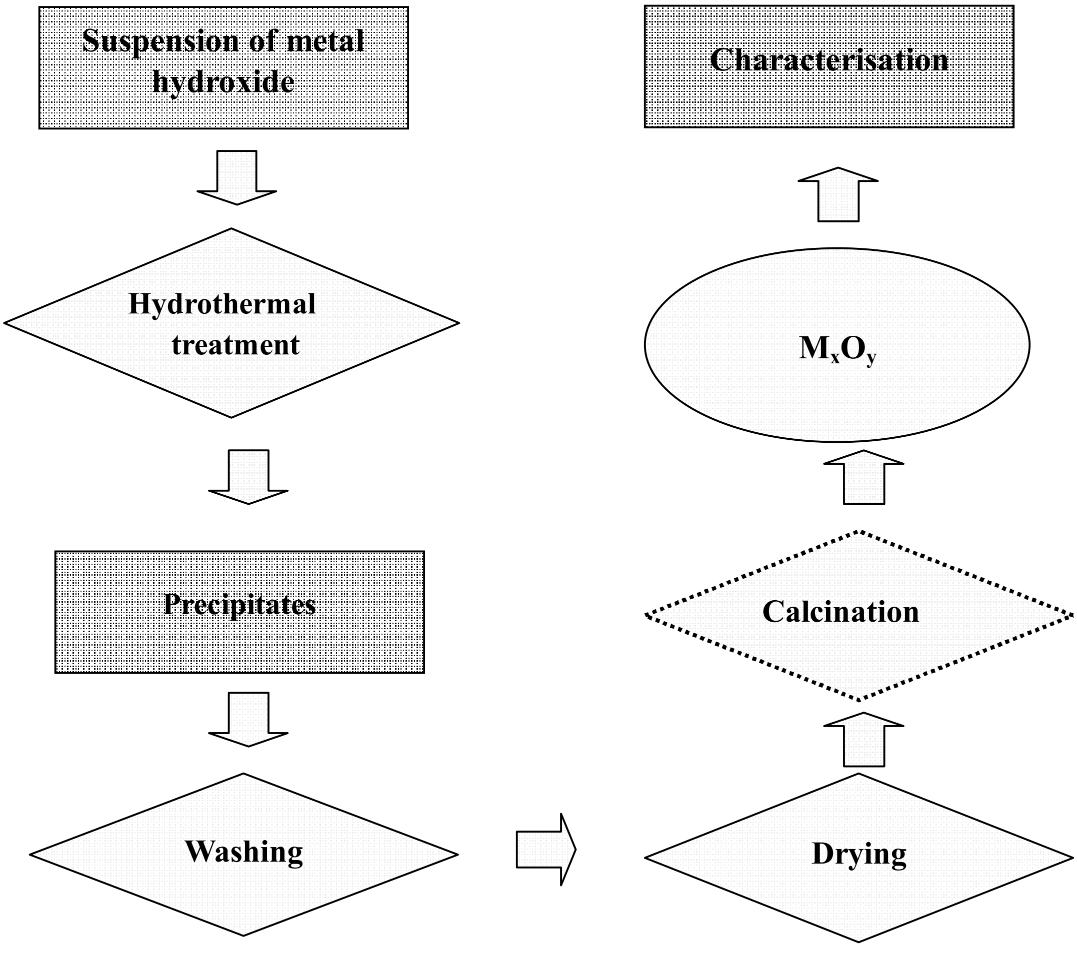

Figure 3.1 A general flow chart of synthesis of nanoparticles by hydrothermal processing.

3.2.1.1 Synthesis of indium hydroxides and indium oxides

Indium hydroxides were synthesised using different indium salts including $InCl_3$, $In(NO_3)_3$ and $In_2(SO_4)_3$ as the starting materials. Different alkaline solvents were also used in the synthesis to investigate the effect of solvent on the properties of particles synthesised. The details of variable are given in **Table 3-2**.

Table 3-2 The synthesis of $In(OH)_3$ using different starting salts and solvents at 200 °C for 24 h.

Starting salts	Solvent
$InCl_3$	NH_4OH
	NaOH
	NH_4HCO_3
$In(NO_3)_3$	NH_4OH
	NaOH
	NH_4HCO_3
$In_2(SO_4)_3$	NH_4OH
	NaOH
	NH_4HCO_3

First, 0.01 mol of starting salt was dissolved in 2 mL of deionised water, then 19 mL of an alkaline solution (NH_4OH, NaOH and NH_4HCO_3) (pH was fixed at 11) was introduced by stirring for about 5 min to form a suspension. The 21 mL of mixed suspension was transferred into an autoclave, which was heated at 200 °C for 24 h, then was cooled down to room temperature naturally. White precipitates were collected by filtration and washed with deionised water several times using a centrifuge, followed by drying at 60 °C overnight and then at 100 °C for 24 h.

3.2.1.2 Synthesis of tin oxides

In order to investigate the effects of the above factors on the properties of particles, the SnO_2 nanoparticles were prepared by hydrothermal method under various conditions. The heated temperature may change from 160,180, 200 to 220 ºC at 48h, the ripening time from 3, 6, 12, 24, 48, 72 to 120h at 200 ºC in various concentrations of the starting materials (i.e. 0.25, 0.5, 1.0, 1.5, 2.0 and 4.0 mol/L). $SnCl_4{\cdot}5H_2O$ was used as the starting material and was dissolved in deionised water to produce the precursors solution. Ammonia (25%) was mixed with deionised water for preparing ammonia solution with pH value of 11. The ammonia solution and $SnCl_4{\cdot}5H_2O$ solution were mixed completely by stirring for 5 minutes at room temperature. Subsequently, the mixed solution (21 mL) transferred into an autoclave, which was sealed and put into an oven with a set reaction temperature for a fixed time. After cooling down to room temperature naturally, the SnO_2 precipitates were collected then washed by deionised water for 5 times followed by a centrifuge treatment to remove the chloride ions. The obtained precipitates were dried at 60 ºC overnight and then at 100 ºC for 24 h.

Different alkaline solvents with a fixed pH value of 11 were also used in the synthesis of SnO_2 as shown in **Table 3-3**.

Table 3-3 Synthesis of SnO_2 using different solvents at 200 °C for 24 h.

Starting salt	Solvent
$SnCl_4{\cdot}5\ H_2O$	NH_4HCO_3
	NH_4OH
	NaOH

3.2.1.3 Synthesis of indium tin hydroxides and indium tin oxides (ITO)

The synthesis process of ITO particle was carried out by dissolving indium chloride (0.01 mol) and tin chloride with the molar ratio of In:Sn of 9:1 in 2 mL of deionised water with stirring. Then 19 mL of ammonia solution (pH = 11) was added into the solution with mixing for 5 min at room temperature. The mixed solution was transferred into an autoclave and kept at 200 ºC for 24 h. After the autoclave was cooled down to room temperature naturally, the precipitates were filtered and washed using deionised water for 5 times until the pH was ~ 7. The obtained precipitates were dried at 60 ºC overnight and then at 100 ºC for 24 h. In some cases, NH_4HCO_3 or NaOH (pH=11) was also used to synthesise indium tin hydroxides.

Indium tin hydroxides prepared were heat treated at 800 ºC for 2 h at the heating rate of 2 ºC/min in a cabinet carbolite furnace to produce ITO.

3.2.1.4 Synthesis of zinc oxides

In this section, different starting salts, alkaline solvents and various synthesis conditions were undertook to synthesise ZnO powders. The process performed to prepare the zinc oxide powders via hydrothermal method was described as follows.

0.01 mol of zinc salts, $ZnSO_4 \cdot 7H_2O$, or $ZnCl_2$ or $Zn(NO_3)_2 \cdot 6H_2O$, was dissolved in 21 mL of aqueous ammonia solution (pH=11) by stirring for 5 min to obtain the suspension, which was then put in an autoclave. The hydrothermal treatment was carried out in a pre-heated oven at 200 °C for 24 h then cooled down to room temperature. The precipitates were filtered then washed by deionised water for several times. Finally the powders were dried at 60 °C overnight and then at 100 ºC for 24 h in air. In some cases, 0.2g of PEG 400, or PEG 1000, or PEG 3400 or PEG 8000 was added to investigate the effect of PEG on the properties of particles synthesised. Different amounts of PEG 8000 from 0.1 g to 0.6 g were also added into the mixed solution to investigate the effect of PEG content on the properties of particles.

3.2.1.5 Synthesis of zinc aluminum hydroxides and AZO

0.5 mol/L of zinc aluminum solution (21 mL) was prepared by mixing the starting salt of $ZnCl_2$ (0.01 mol) and the dopant of $Al(NO_3)_3$ with the mole fraction of Al to Zn of 1.0%, 3.0%, 5.0% and 10.0%, respectively. Then 25% ammonia solution was added drop-wise into the solution until pH around 11. The mixed solution transferred to a 30mL autoclave and heated at 200 °C for 24 h in an oven.

3.2.2 Other experimental treatments

Several experimental treatment processes, such as washing, drying and calcination, wire also employed in the synthesis of the particles.

3.2.2.1 Washing

A centrifuge (Biofuge Primo, Heraeus Instruments) was used for separation of solid precipitates from the suspensions. The precipitates were washed by deionised water to remove both ammonia added as a reactant and other components such as NH_4Cl produced in the reaction. The centrifuge condition is at 4500 rpm for 5 min. The precipitates were washed more than 5 times until the pH was around 7 which was measured using pH indicator paper.

3.2.2.2 Drying

All samples after washing were dried in an oven (UT-6, Heraeus Instruments) at 60 °C overnight then at 100 °C for 24 h to remove residual water.

3.2.2.3 Calcination

Calcination of powders was conducted in a normal cabinet carbolite furnace (RFH 16/3, Carbolite, UK). The samples were heated to a pre-determined temperature at the heating rate of 2 °C/min and dwell time of 2 h for calcination.

3.3 Fabrication of TCOs thin film by sol-gel technique

TCOs thin films including indium tin oxide (ITO) and aluminum doped zinc oxide (AZO) thin films were prepared under different conditions using sol-gel technique by dip-coating method. Properties of the thin films, including the surface morphology, optical transmittance and electrical conductivity were characterised.

3.3.1 Preparation of ITO sol

Normally, the starting materials for sol–gel are the class of materials known as organo-metallic compounds. However, the indium or tin organic compounds are very difficult to obtain due to the preparation problems, unavailability or too high cost. Therefore, inorganic metal salts such as indium trichloride and tin (IV) chloride with appropriate organic solvent were used as the alternative starting materials for the preparation of the sol of the ITO thin films. The details of the preparation of ITO sol are as follows.

Initially, 0.024 mol of $InCl_3$ was dissolved in 40 mL of 2-methoxyethanol (CH_3-O-CH_2-CH_2-OH) and then 0.024 mol of monoethanolamine (MEA, HO-CH_2-CH_2-NH_2) was added into the solution with stirring for 30 min. Finally, 0.0024 mol of tin chloride ($SnCl_4 \cdot 5H_2O$, Sn to In = 10 to 90, in molar ratio) was added to form the ITO precursor sol. The sol obtained (**Figure 3.2**) was further stirred for 6 h, and then aged for at least 24 h at room temperature before the preparation of the thin film.

The sols were prepared using different conditions as shown in **Table 3-4** to **Table 3-6**.

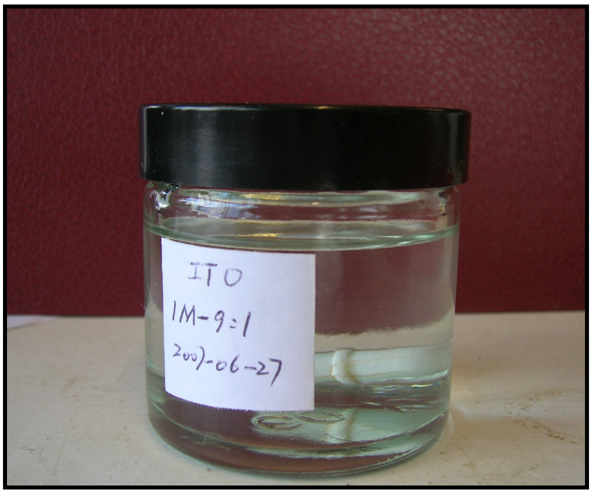

Figure 3.2 An ITO sol.

Table 3-4 ITO sols prepared using different concentrations of starting salt and 10 at.% of tin (Sn/(Sn+In)).

Variable parameters		Fixed parameters	
		Solvent	$MEA/InCl_3$ (in molar ratio)
Concentrations of starting salt (mol/L)	0.1	2-Methoxyethanol	1:1
	0.3		
	0.6		
	1.0		
	2.0		

Table 3-5 ITO sols prepared using different contents of Sn and 0.6 mol/L starting salt.

Variable parameters		Fixed parameters	
		Solvent	$MEA/InCl_3$ (in molar ratio)
Sn / (In+Sn) (at.%)	1.0	2-Methoxyethanol	1:1
	3.0		
	5.0		
	10.0		
	15.0		
	20.0		

Table 3-6 ITO sols prepared using different contents of MEA and 0.6 mol/L starting salt.

Variable parameters		Fixed parameters	
		Solvent	Sn /(In+ Sn) (at.%)
$MEA/InCl_3$ (in molar ratio)	0.1	2-Methoxyethanol	10.0
	0.5		
	1.0		
	2.0		
	5.0		

3.3.2 Preparation of AZO sol

Typically, the precursor sols of AZO were prepared by dissolving 0.024 mol of zinc acetate [$Zn(C_2H_4O_2)_2 \cdot 2H_2O$] in 40 mL of 2-methoxyethanol by stirring at room temperature until all solid salt was dissolved. Then MEA (monoethanolamine, used as the stabiliser) was added into the solution. The molar ratio of MEA to zinc acetate was kept at 1.0 and the concentration of zinc nitrate was 0.6 mol/L. Finally, 1mol% of dopant (aluminum nitrate nonahydrate, $Al(NO_3)_3 \cdot 9H_2O$, [Al/Zn]) was added into the mixed solution to form AZO sol for coating. The sol (**Figure 3.3**) was kept aging for at least 24 h at room temperature before using.

Figure 3.3 An AZO sol.

In order to investigate the effects of the sol properties on the performance of the thin film fabricated, the different sols were prepared by varying the conditions of preparation, which were listed in the Tables **3-7**, **3-8** and **3-9**.

Table 3-7 AZO sols using different concentrations of starting salt and 1.0 at.% of Al.

Variable parameters		Fixed parameters	
		Solvent	$MEA/Zn(AC)_2$ (in molar ratio)
Concentrations of starting salt (mol/L)	0.1	2-Methoxyethanol	1:1
	0.3		
	0.6		
	1.0		
	2.0		

Table 3-8 AZO sols using different contents of dopant and 0.3 mol/L starting salt.

Variable parameters		Fixed parameters	
		Solvent	$MEA/Zn(AC)_2$ (in molar ratio)
Al , at.%	0.5	2-Methoxyethanol	1:1
	1.0		
	3.0		
	5.0		
	10.0		
	15.0		

Table 3-9 AZO sols using different contents of MEA and 0.3 mol/L starting salt

Variable parameters		Fixed parameters	
		Solvent	Al (at.%)
$MEA /Zn(AC)_2$ (in molar ratio)	0.5	2-Methoxyethanol	1.0
	1.0		
	2.0		
	5.0		

3.3.3 Fabrication of ITO and AZO thin films

A flow chart of preparation of TCOs thin film by sol-gel technique is shown in **Figure 3.4**.

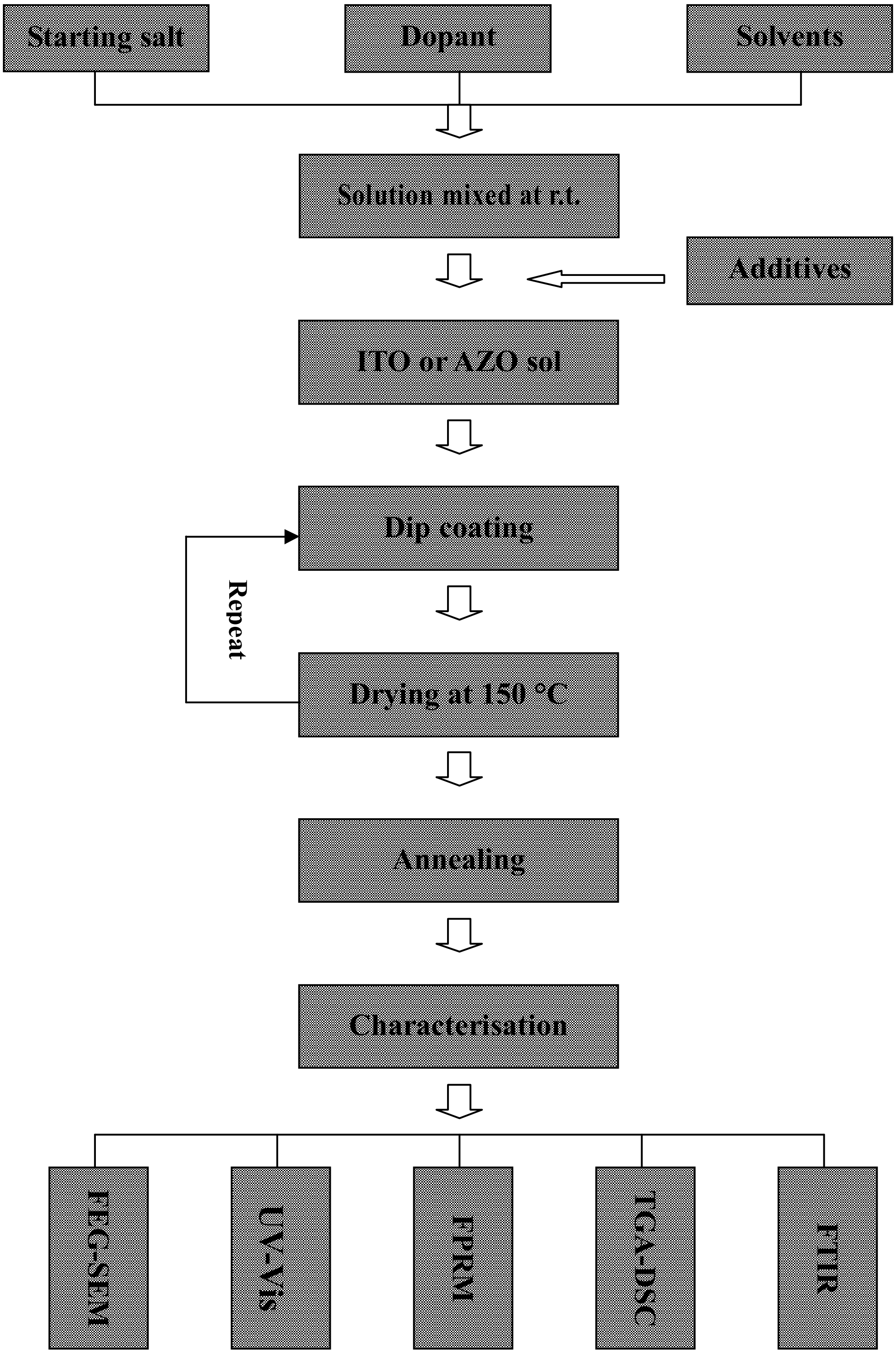

Figure 3.4 Fabrication of TCOs thin films using sol-gel technique by dip-coating.

The depositions of the ITO and AZO thin films on the Corning glass substrate (22mm × 22mm × 0.16 ~ 0.19 mm) were performed by dip coating method using the sol prepared in the section of 3.3.1 and 3.3.2. In order to prevent the composition of Corning glass to diffuse into the film, Corning glass should be coated with a silicon layer. The viscosities of the sols were kept at 4-20 mPa•s. Firstly, the Corning glass substrates were cleaned ultrasonically for 30 min in 5% ~ 10% sodium hydroxide solution and rinsed several times with deionised water. Then the glass substrate was washed using acetone or absolute ethanol. After the glass substrate was dried at room temperature, it was dipped into the coating solutions for 1~2 min and pulled out at the withdrawal speed, which varied from 1.2 cm/min to 12 cm/min. After coating, the films were put into an oven horizontally, then dried at 150 °C for 20 min. The coating process was repeated from 1 to 10 times in order to achieve different thickness of thin film. Finally, the samples were annealed in a cabinet carbolite furnace with air. The annealing temperatures were various from 400 to 600°C and the annealing time varied from 30 to 240 min.

3.2.3.2 Fabrication of ITO thin films

The variable fabrication conditions including withdrawal speed, the number of deposit layer, annealing temperature and time, were carried out to investigate the relationship between the process conditions and the properties of the thin films. The details of the processing conditions are shown in **Table 3-10**.

Table 3-10 The fabrication conditions of ITO thin films by dip coating

		Concentrations of starting salt (mol/L)					The atom percentage of dopant (Sn, at%)						solvent	MEA/InCl$_3$ (in molar ratio)				
		0.1	0.3	0.6	1.0	2.0	1.0	3.0	5.0	10	15	20	Meth.	0.1	0.5	1.0	2.0	5.0
Withdrawal speeds (cm/min)	1.2			√						√			√			√		
	2.4	√	√	√	√	√	√	√	√	√	√	√	√	√	√	√	√	√
	5.0			√						√			√			√		
	7.5			√						√			√			√		
	12			√						√			√			√		
Annealing temp.(C)	400			√						√			√			√		
	450			√						√			√			√		
	500			√						√			√			√		
	550			√						√			√			√		
	600	√	√	√	√	√	√	√	√	√	√	√	√	√	√	√	√	√
Annealing time (min)	30			√						√			√			√		
	60	√	√	√	√	√	√	√	√	√	√	√	√	√	√	√	√	√
	120			√						√			√			√		
	240			√						√			√			√		
The number of deposit layer	1	√	√	√	√	√				√			√			√		
	2			√						√			√			√		
	3			√			√	√	√	√	√	√	√	√	√	√	√	√
	5			√						√			√			√		
	10			√						√			√			√		

3.3.3.2 Fabrication of AZO thin films

The AZO thin films were fabricated by different conditions including the withdrawal speed, concentrations of starting salt, the amount of dopant, annealing temperature and time and the number of deposit layer, etc., in order to investigate the effect of the fabrication conditions on the properties of thin films. The fabrication conditions of AZO thin films are listed in **Table 3-11**.

Table 3-11 The fabrication conditions of AZO thin films.

		Concentrations of starting salt (mol/L)					The atom percentage of dopant (Al, at.%)						solvent	MEA/ZnCl$_2$ (in molar ratio)			
		0.1	0.3	0.6	1.0	2.0	0.5	1.0	3.0	5.0	10.0	15.0	Meth	0.5	1.0	2.0	5.0
Withdrawal speeds (cm/min)	1.2		√					√					√		√		
	2.4	√	√	√	√	√	√	√	√	√	√	√	√	√	√	√	√
	5.0		√					√					√		√		
	7.5		√					√					√		√		
	12		√					√					√		√		
Annealing temp.(C)	400		√					√					√		√		
	450		√					√					√		√		
	500	√	√	√	√	√	√	√	√	√	√	√	√	√	√	√	√
	550		√					√					√		√		
	600		√					√					√		√		
Annealing time (mins)	30		√					√					√		√		
	60	√	√	√	√	√	√	√	√	√	√	√	√	√	√	√	√
	120		√					√					√		√		
	240		√					√					√		√		
The number of deposit layer	1	√	√	√	√	√		√					√		√		
	2		√					√					√		√		
	3		√				√	√	√	√	√	√	√	√	√	√	√
	5		√					√					√		√		
	10		√					√					√		√		

3.4 Characterisation

Many characterisation techniques including TEM, SEM, XRD, AFM and TGA-DSC, etc., were employed to characterise the properties of particles and thin films. The details are desribed as follows.

3.4.1 Transmission electron microscopy

Transmission electron microscopy (TEM) is a microscopy technique whereby a beam of electrons transmittes through an ultra thin specimen, interacting with the specimen as it passes through it. An image is formed from the electrons transmitted through the specimen, magnified and focused by a set of lenses and appears on an imaging screen, a fluorescent screen in most TEMs, plus a monitor, or on a layer of photographic film, or to be detected by a sensor such as a CCD camera. TEM is widely used to characterise the morphology, defects, and phase structure of various materials, especially for those in nanometer scales. TEM can be used to characterise nanoparticles due to its high magnification and high resolution. The particle size and morphology can be observed exactly by TEM. It can also be used to analyse the structure of powders by analysis diffraction patterns.

In this project, particle size and morphology were performed on a JEOL-2000FX TEM operated at an accelerating voltage of 200 kV. The size and morphology of powders were investigated from the micrographs. The samples were prepared by producing a suspension of the nanoparticles in ethanol, through ultrasonic dispersion. Then a drop of the suspension was spread on a carbon film coated brass grid for TEM observation.

3.4.2 Scanning electron microscopy

The scanning electron microscopy (SEM) is a type of electron microscope that creates various images by focusing a high energy beam of electrons onto the surface of a sample and detecting signals from the interaction of the incident electrons with the sample's surface. In a typical SEM, electrons are thermionically emitted from a tungsten or lanthanum hexaboride (LaB_6) cathode and are accelerated towards an anode, alternatively, electrons can be emitted via field emission (FE). The type of signals gathered in a SEM varies and can include secondary electrons, characteristic x-rays, and back scattered electrons. The SEM is capable of producing high-resolution images of a sample surface in its primary use mode, secondary electron imaging. Due to the manner in which this image is created, SEM images have great depth of field yielding a characteristic three-dimensional appearance useful for understanding the surface structure of a sample.

Field Emission Gun-Scanning Electron Microscopy (FEG-SEM, LEO 1530VP) with the resolution of 1.0 nm and the magnification up to 900K was used to investigate the surface morphologies of ITO and AZO thin films and bulk materials. It is also used to measure the thickness by observing the cross-section of thin films. The samples were mounted on sample holders with double sided carbon tape or silver gel to conduct away any charge generated by electron beam. The nanoparticles and thin films were made more conductive by sputtering a thin layer of gold in argon gas.

3.4.3 X-ray diffraction meter

X-ray diffraction (XRD) techniques are a family of non-destructive analytical techniques which reveal information about the crystallographic structure, chemical composition, and physical properties of materials and thin films. These techniques are based on observing the scattered intensity of an x-ray beam hitting a sample as a function of incident and scattered angle, polarisation, and wavelength or energy. X-ray diffraction meter is one of the most important characterisation tools used in solid-state chemistry and materials science. It has been in use in two main areas, for the identification characterisation of crystalline materials and the determination of their structure. Each crystalline solid has its unique characteristic X-ray powder diffraction pattern which is used as a “fingerprint” for its identification. Once the material has been identified, X-ray crystallography can be used to determine its structure, i.e. how the atoms pack together in the crystalline state and what the interatomic distance and angle are. The information of XRD pattern can also be used to measure the crystallite size (*D*) of materials. It is based on the Scherrer's formula:

$$D = 0.9\lambda/B\cos\theta \qquad (3\text{-}1)$$

where, λ - the wavelength of X-rays

B- the measured broadening of the diffraction line peak at an angle of 2θ, at full-width half maximum intensity (FWHM) in radian

θ- incidence angle

The crystallite size, crystallinity and phase analysis of samples synthesised were carried out with Bruker D8 X-ray diffraction, with an accelerating potential of 40 kV and a current of 40 mA, using Cu Ka radiation (1.5406 Å). Data was acquired over 2θ range 10–90° with the step of 0.02° per second at room temperature.

3.4.4 Four-point probe resistance meter

Four-point probe resistance meter is a common instrument for measuring sheet resistivity of thin film, as well as bulk material. Four-point probe resistance meter used in the project consists of a set of four probe tips, power supply (0-30 V, 0-3 A) and multimeter (model TTi-1604 digital multimeter).

The four-point probe, as the measure principle shown in **Figure 3.5**, contains four thin collinear tungsten wires which are made to contact the sample under test. Current I is made to flow between P_1 and P_4 probe, and voltage V is measured between P_2 and P_3 probe, ideally without drawing any current. If the sample is of semi-infinite volume and if the interprobe spacings are $s_1 = s_2 = s_3 = s$, then it can be shown that the sheet resistance of the semi-infinite volume is given by

$$R_S = 4.53 V/I \quad (\Omega/\square) \quad \text{for } t/s \leq 0.5 \qquad (3\text{-}2)$$

Where, t is the thickness of thin film and s the interprobe spacing.

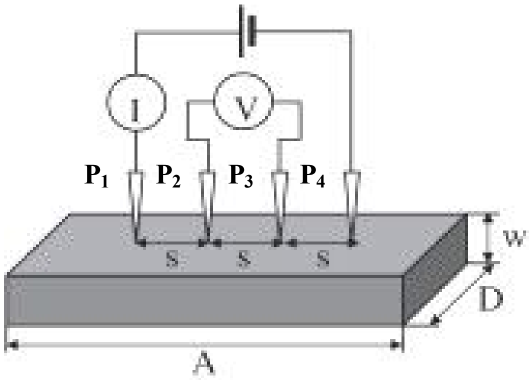

Figure 3.5 Diagram of four-point probe.

3.4.5 UV-Vis spectrometer

UV/Vis spectrometer with the wavelength normally ranged from 200 nm to 1100 nm is routinely used in the quantitative determination of some chemical species. It measures the intensity of light passing through a sample (I), and compares it to the intensity of light before it passes through the sample (I_o). The ratio I / I_o is called the transmittance, and is usually expressed as a percentage (%T). The sample tested normally is solution, but the solid sample, such as the thin film coated on the glass substrate, can also be tested under certain conditions.

The optical transmittance of thin film was measured by UV-visible spectrophotometer (Perkin Elmer Lambda – 2 UV/VIS) in wavelength range from 300 nm to 800 nm. The bare glass substrate was used as a reference.

3.4.6 Fourier transform infrared spectrometer

Fourier transform infrared spectrometer has been a useful instrument for materials analysis in the laboratory. An infrared spectrum represents a fingerprint of a sample with absorption peaks which correspond to the frequencies of vibrations between the bonds of the atoms making up the material. Because each different material is a unique combination of atoms, no two compounds produce the exact same infrared spectrum. Therefore, FTIR can be used to identify unknown materials, to determine the quality of a sample and the amount of components in a mixture.

The components of ITO and AZO thin films were measured by Fourier transform infrared spectrometer. The samples of ITO and AZO were prepared by coating the sols onto KBr pellets with a pipette and annealed at different conditions which as same as those of ITO and AZO thin film prepared. The samples to be tested were kept in a desiccator at room temperature.

3.4.7 Differential scanning calorimetry-thermogravimetry analyser

Thermogravimetry (TG) is a technique by which the change in sample mass is monitored as a function of temperature and time. Differential scanning calorimetry (DSC) is a thermoanalytical technique in which the difference in the amount of heat required to increase the temperature of a sample and reference are measured as a function of temperature and time. Both the sample and reference are maintained at nearly the same temperature throughout the experiment. The samples were tested using a TA instrument (Model SDT –2960) for simultaneous TGA-DSC measurement at the heating rate of 5 °C/min. The measurements can be performed in controlled atmospheres (Ar, N_2, O_2, air) and the temperature range in which the SDT 2960 can be used is from room temperature to 1500 °C. The TGA has a sensitivity of 0.1 μg and accuracy of ±1%.

Chapter 4 Synthesis of Nanoparticles

4.1 Synthesis of ITO and AZO nanoparticles by hydrothermal method

The effects of starting salts, solvents and hydrothermal treatment conditions on the particle size and shape of indium hydroxide, tin oxide, indium tin hydroxide, zinc oxide, etc., using hydrothermal method were investigated. The particles synthesised were characterised by SEM, TEM and XRD.

4.1.1 Synthesis of indium hydroxides

The particles synthesised using different starting salts and solvents via hydrothermal at 200 °C for 24 h were examed by XRD. The XRD peaks at $2\theta = 22.3^o, 31.7^o, 39.1^o, 45.5^o, 51.2^o$ and 56.5^o refer to the crystal plane (200), (220), (222), (400), (420) and (422), respectively, indicating the formation of indium hydroxide (**Figure 4.1**). The results of the effect of ammonia solution with different starting salts on the formation of $In(OH)_3$ (**Figure 4.2**) shows that, the $In(OH)_3$ particles with cubic shape and large particle size (about 200-1000 nm) were synthesised when $InCl_3$ and $In(NO_3)_3$ were used as the starting salts. However, the cubic particles of about 50 nm in size were obtained when $In_2(SO_4)_3$ was used as the starting salt.

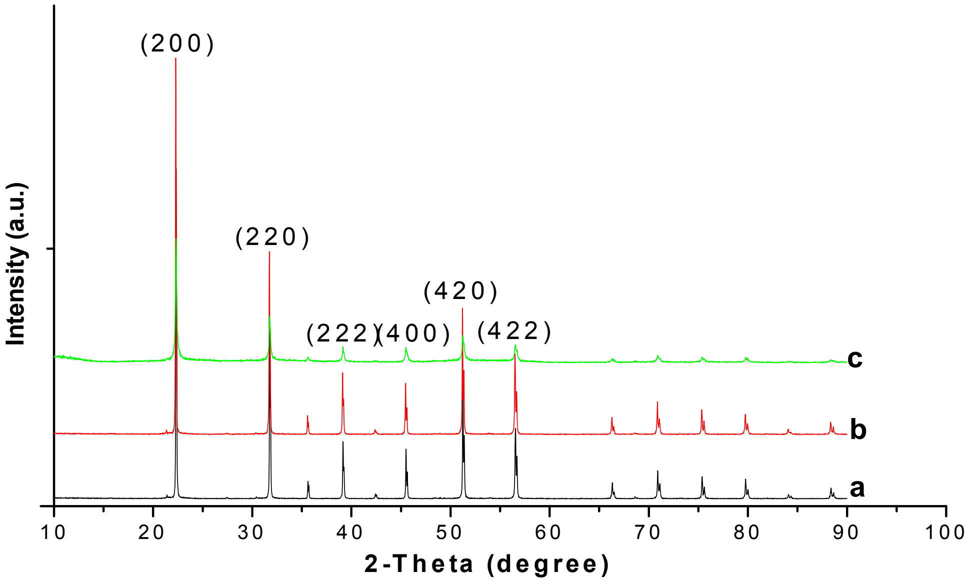

Figure 4.1 XRD results of In(OH)$_3$ synthesised using ammonia with (a) InCl$_3$, (b) In(NO$_3$)$_3$ and (c) In$_2$(SO$_4$)$_3$, respectively.

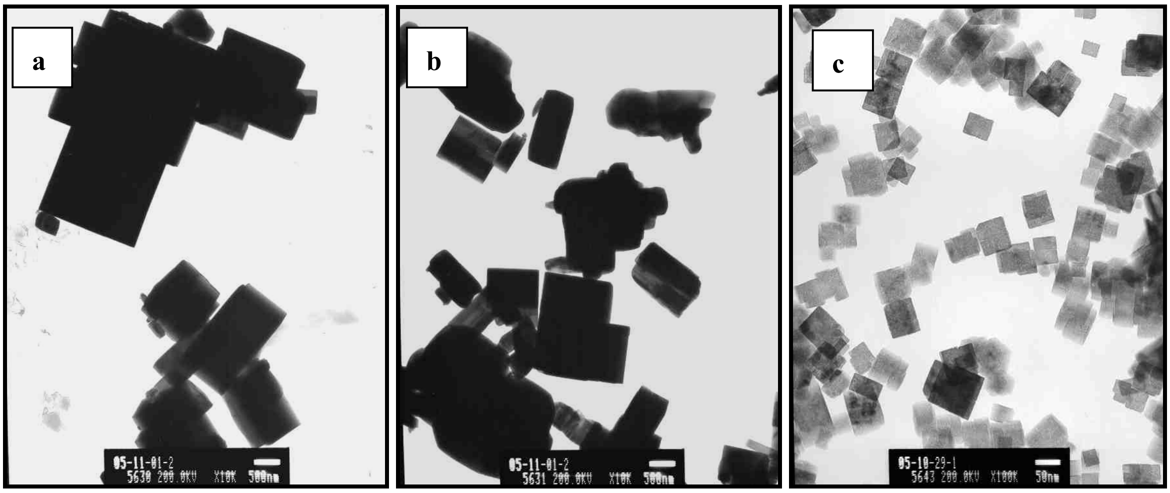

Figure 4.2 TEM micrographs of In(OH)$_3$ synthesised using NH$_4$OH (pH=11) solution and different salts: (a) InCl$_3$, (b) In(NO$_3$)$_3$ and (c) In$_2$(SO$_4$)$_3$, respectively.

The effect of NH$_4$HCO$_3$ used as the alkaline solution with different starting salts on In(OH)$_3$ was shown in **Figure 4.3**. The TEM micrographs show that large cubic shaped particles of 100-200 nm in size were formed when InCl$_3$ was used as the starting salt, and the cubic particle of 20 nm and 10 nm when In(NO$_3$)$_3$ and In$_2$(SO$_4$)$_3$ were used as the starting salts, respectively.

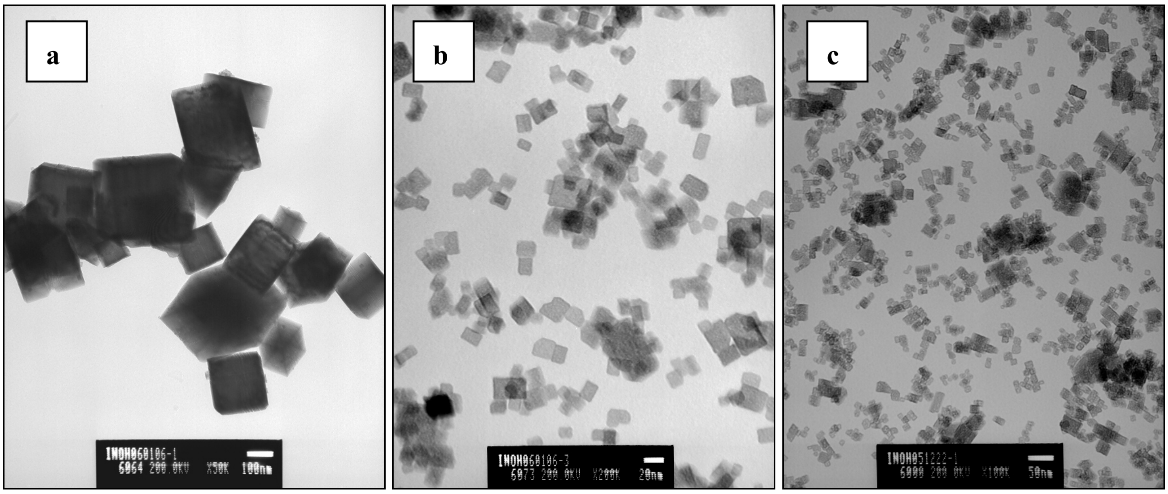

Figure 4.3 TEM micrographs of $In(OH)_3$ synthesised using NH_4HCO_3 (pH=11) solution and different salts: (a) $InCl_3$, (b) $In(NO_3)_3$, (c) $In_2(SO_4)_3$, respectively.

The TEM micrographs of $In(OH)_3$ particles with spherical (about 10 nm) and very tiny spherical aggregations (less than 5 nm) synthesised using NaOH with different salts were shown in **Figure 4.4**. All results mentioned above were summarised in **Table 4-1**.

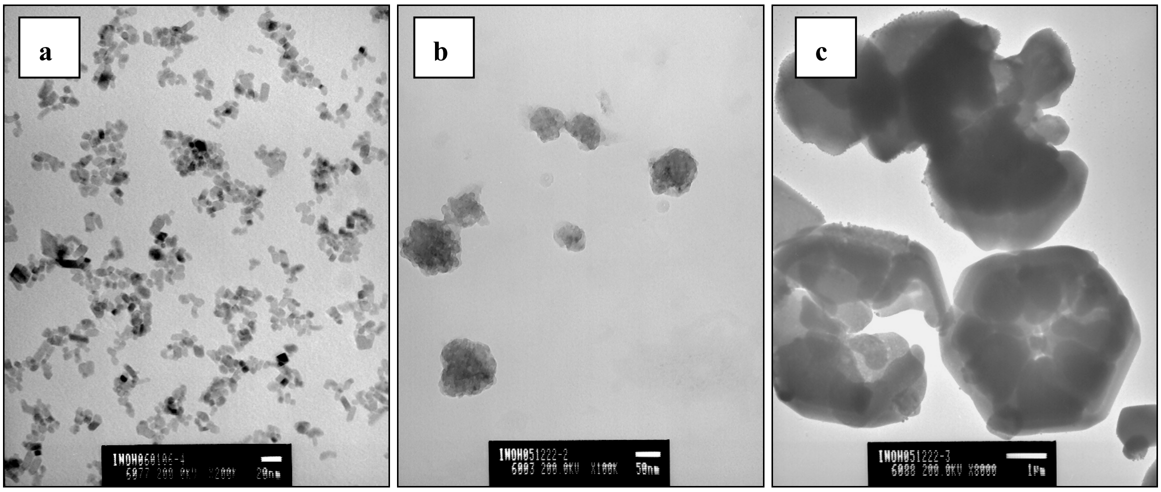

Figure 4.4 TEM micrographs of $In(OH)_3$ synthesised using NaOH (pH=11) solution and different salts: (a) $InCl_3$, (b) $In(NO_3)_3$, (c) $In_2(SO_4)_3$, respectively.

Table 4-1 The effects of different solvents with different starting salts on $In(OH)_3$.

Solvent	Starting salt	Particle description	Size (nm, TEM)
NH_4OH (pH=11)	$InCl_3$	cubic	1000
	$In(NO_3)_3$	cubic	200-500
	$In_2(SO_4)_3$	cubic	50
NH_4HCO_3 (pH=11)	$InCl_3$	cubic	100-200
	$In(NO_3)_3$	cubic	20
	$In_2(SO_4)_3$	cubic	10
NaOH (pH=11)	$InCl_3$	spherical	20
	$In(NO_3)_3$	agglomerated	--
	$In_2(SO_4)_3$	agglomerated	--

4.1.2 Synthesis of tin oxides (SnO2)

Tin oxide was prepared under various synthesis conditions by the hydrothermal method. The effects of temperature, treatment time, starting salt concentration and different solvents on the size and morphology of the particles synthesised were investigated.

4.1.2.1 Effect of hydrothermal temperature

The XRD results (**Figure 4.5**) show that the crystal structures of all samples synthesised at the temperatures from 160 °C to 220 °C for 48 h are tin oxide [139]. The size of particles was increased from about 10 nm to 110 nm with the increase of treatment temperatures from 160 °C to 220 °C (**Figure 4.6**).

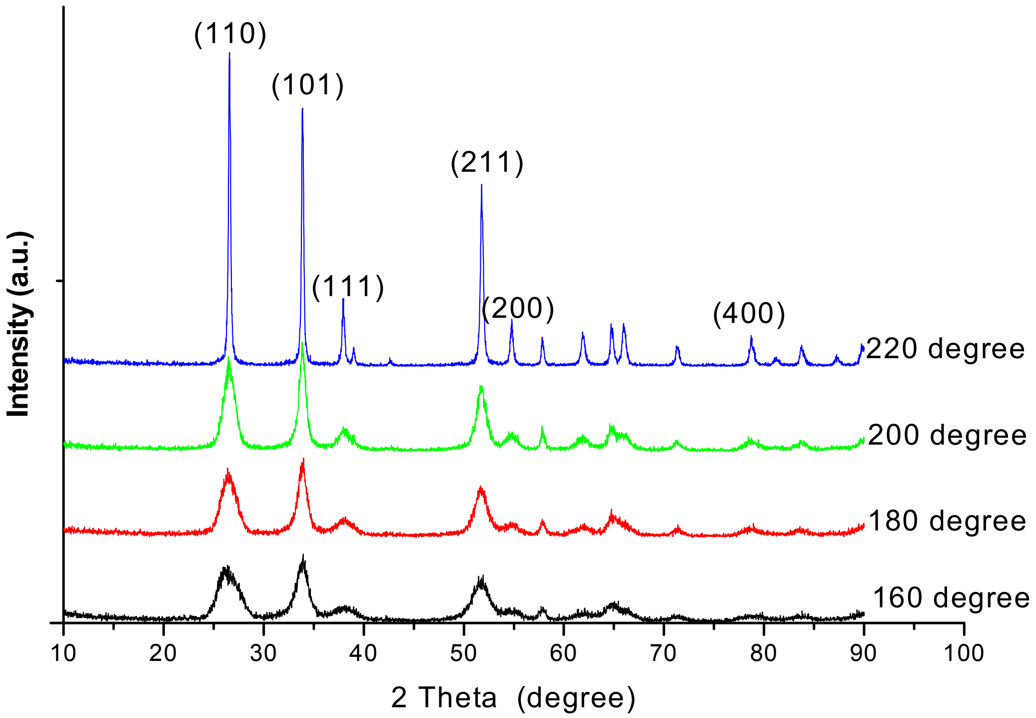

Figure 4.5 XRD results of SnO_2 synthesised at different hydrothermal treatment temperatures:160 °C, 180 °C, 200 °C and 220 °C for 48 h.

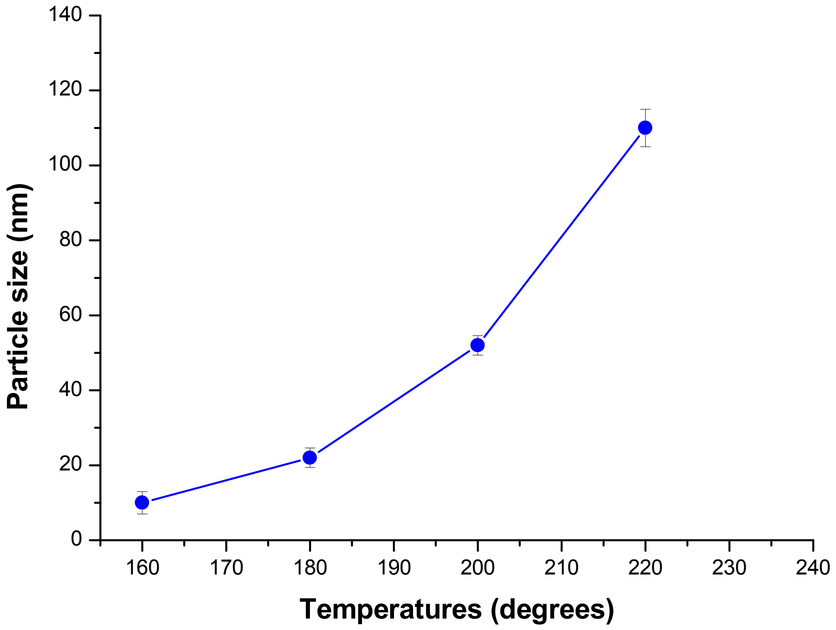

Figure 4.6 The particle size of SnO_2 varied with the hydrothermal temperatures.

Figure 4.7 (a, b and c) shows the TEM micrographs of SnO_2 syntheisised at different hydrothermal temperatures. The particle morphology was rod-like shape at 160 °C, 180 °C, and 200 °C for 48 h, but a mixture of rod-like and polygon shape at 220°C for 48 h was observed (**Figure 4.7** (d)).

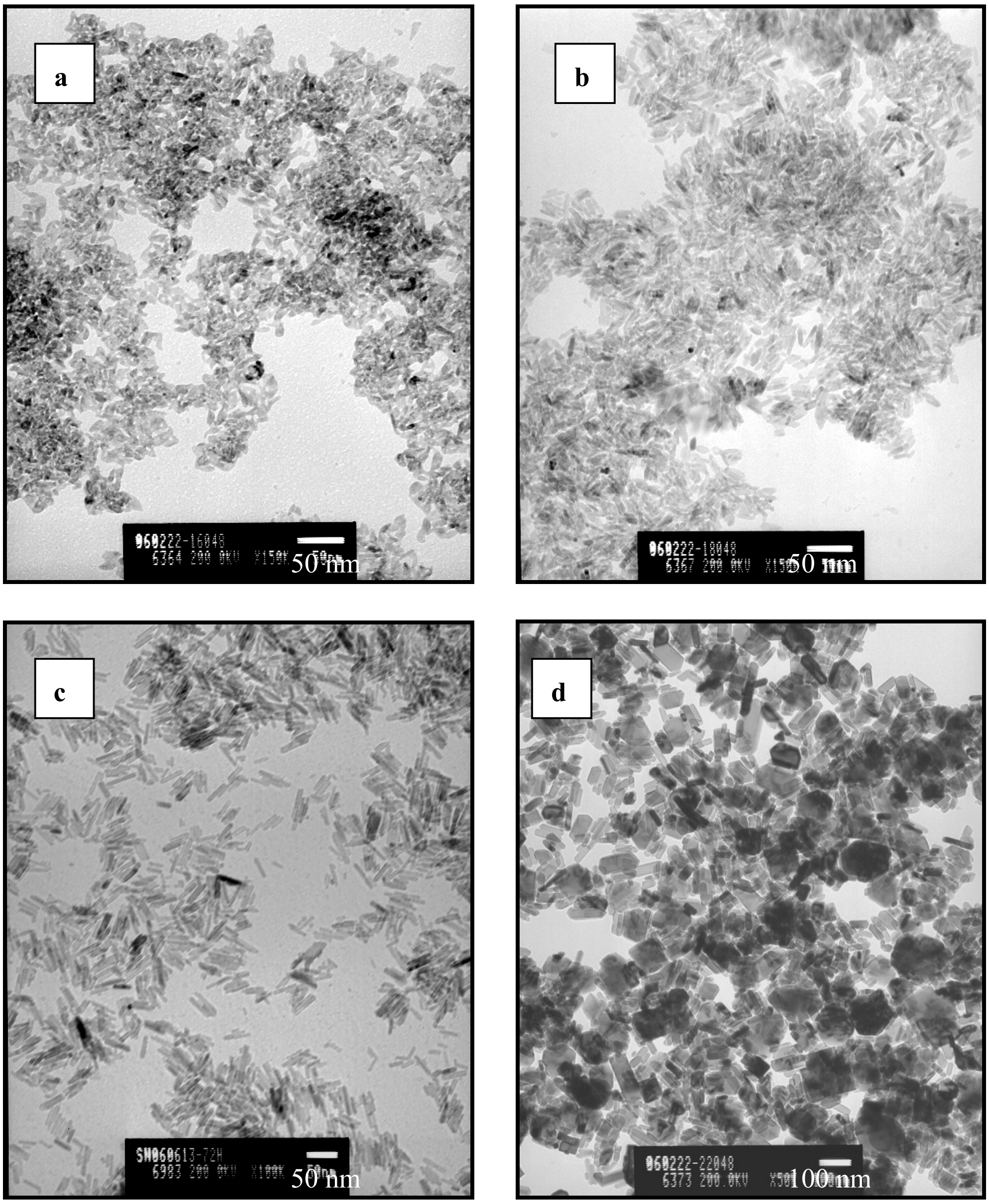

Figure 4.7 TEM micrographs of SnO_2 prepared at different hydrothermal temperatures: (a) 160 °C, (b) 180 °C, (c) 200 °C and (d) 220 °C, respectively.

4.1.2.2 Effect of hydrothermal ripening time

The samples synthesised at 200 °C for the ripening time from 6 h to 48 h showed rod-like shaped morphology with different particle sizes (**Figure 4.8**). The particle size was increased from around 12 nm for 6 h to 55 nm for 48 h. The results were summarised in **Table 4-2.** XRD results (**Figure 4.9**) also show the phase of the particles was with SnO_2 structure [139].

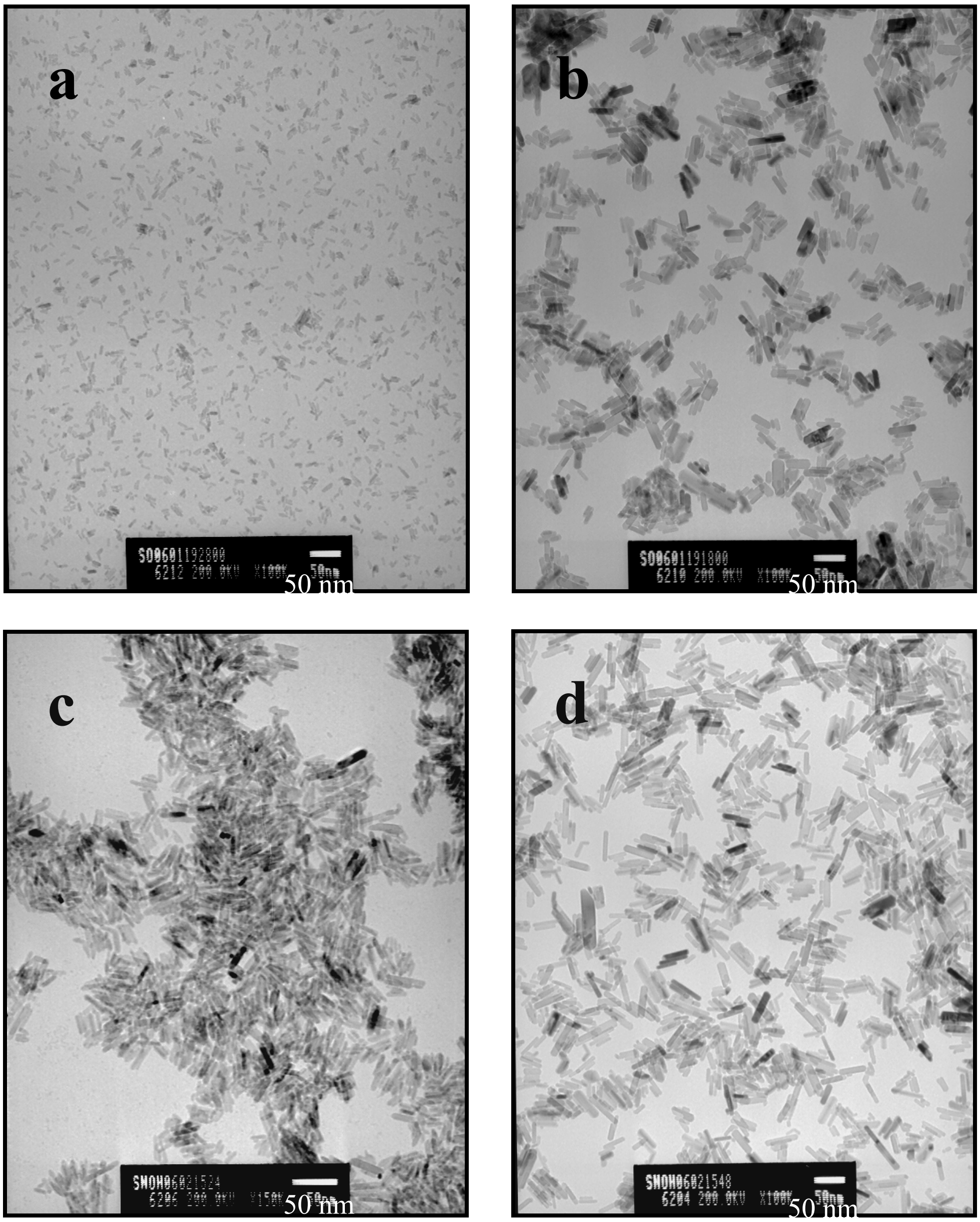

Figure 4.8 TEM micrographs of SnO_2 nanoparticles synthesised at 200 °C for different hydrothermal ripening time: (a) 6 h, (b) 12 h, (c) 24 h, and (d) 48 h, respectively.

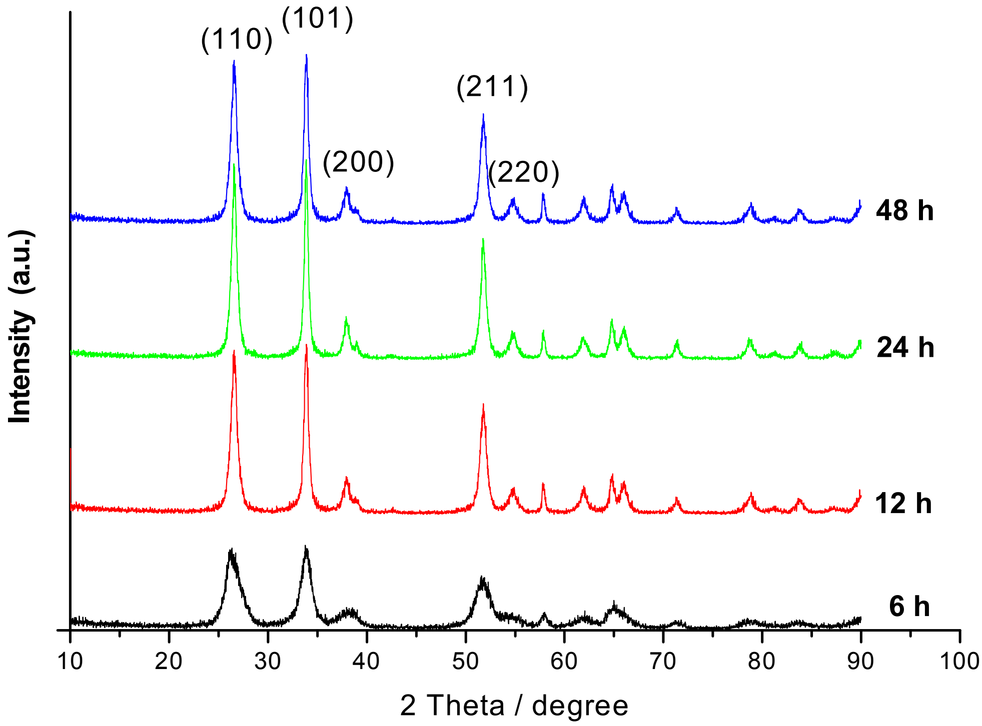

Figure 4.9 XRD patterns of SnO_2 synthesised at 200 °C for different ripening time with 6 h, 12 h, 24 h and 120 h, respectively.

Table 4-2 Summary of the effect of hydrothermal ripening time on the size and morphology of SnO_2.

$SnCl_4 \cdot 5H_2O$ (mol/L)	Solvent (pH=11)	Temp. (°C)	Time (h)	Phase	Particle description	Size (TEM, nm)
0.5	NH_4OH	200	6	SnO_2	rod-like	12×2
			12			23×5
			24			32×7.5
			48			55×12

4.1.2.3 Effect of the concentration of tin chloride solution

The different tin chloride concentrations (0.25 mol/L, 0.5 mol/L, 1.0 mol/L, 1.5 mol/L, 2.0 mol/L and 4.0 mol/L) were used to study the influence of starting salt concentration on the properties of the particles. No particle was found from 0.25 mol/L of tin chloride, which was probably due to the concentration of 0.25 mol/L lower than that of nucleation threshold. The XRD results of particles synthesised by using different concentrations of $SnCl_4$ solution (from 0.5 to 4.0 mol/L) at 200°C for 48h, as shown in **Figure 4.10**, indicated the formation of tin oxide phase. **Figure 4.11** shows TEM micrographs of SnO_2 particles. As shown in **Figure 4.11**(b to e), the particle shape was changed from the rod-like to oval shape when $SnCl_4$ concentration increased from 1.0 to 4.0 mol/L. As shown in **Figure 4.12**, the particle size increased from 22 to 30 nm when the $SnCl_4$ concentration increased from 0.5 to 1.0mol/L, subsequently decreased to 14 nm where the $SnCl_4$ concentration was 4.0mol/L.

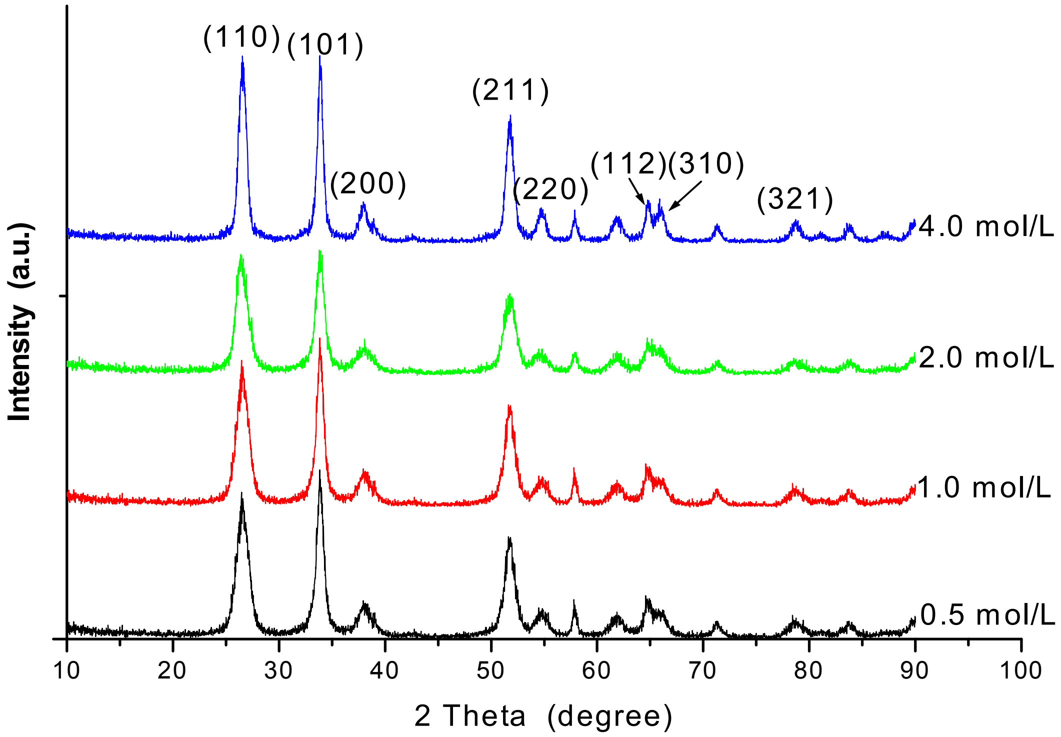

Figure 4.10 XRD patterns of SnO_2 synthesised using different concentrations of tin chloride: 0.5, 1.0, 2.0 and 4.0mol/L, respectively.

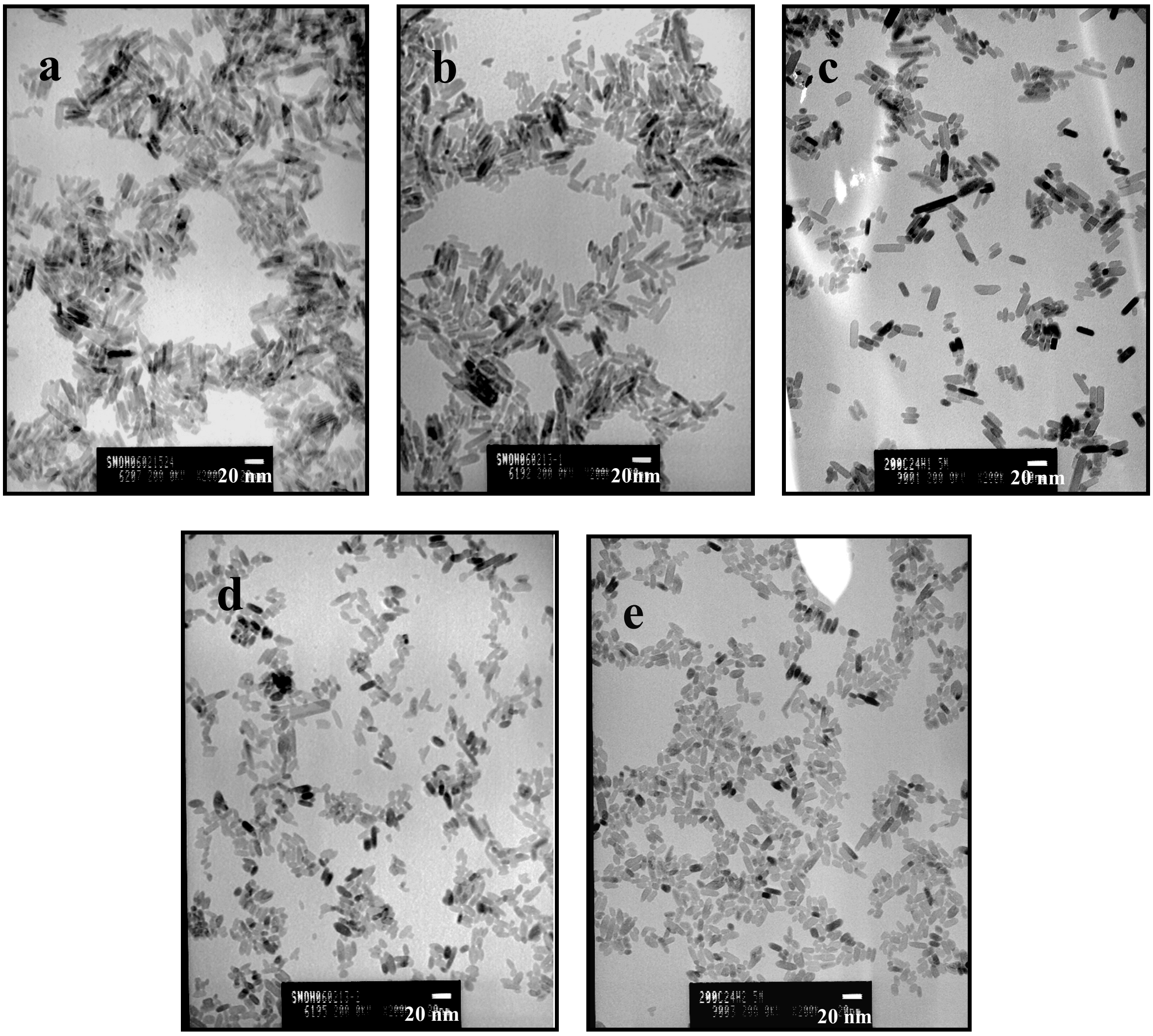

Figure 4.11 The morphologies of SnO_2 nanoparticles synthesised using different concentrations of $SnCl_4 \cdot 5H_2O$: (a) 0.5 mol/L, (b) 1.0 mol/L, (c) 1.5 mol/L, (d) 2.0 mol/L, and (e) 4.0 mol/L.

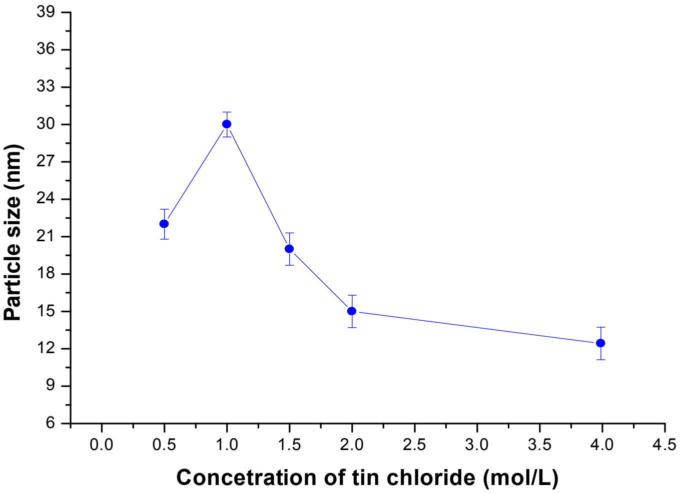

Figure 4.12 The SnO_2 particle sizes varied with the concentrations of $SnCl_4 \cdot 5H_2O$.

4.1.2.4 Effect of alkaline solvents

Different alkaline solvents were used to prepare tin oxide powders to investigate their effects on the size and shape of particles. The synthesis process was conducted at 200°C for 24 h using $SnCl_4{\cdot}5H_2O$ as the starting salt with different alkaline solvents. **Figure 4.13** shows the TEM micrographs of tin oxides synthesised. Short rod-like and rod-like shaped nanoparticles were produced when ammonia or ammonia hydrogen carbonate solution was used, but spherical shaped tin oxide particles were obtained when sodium hydroxide was used. The particle size of the nanoparticles synthesized was summarised in **Table 4-3**. The smaller particle size of around 10 nm was obtained by using sodium hydroxide solution as the solvent. However, the bigger particles of 20~60 nm in size were obtained while ammonia solution was used.

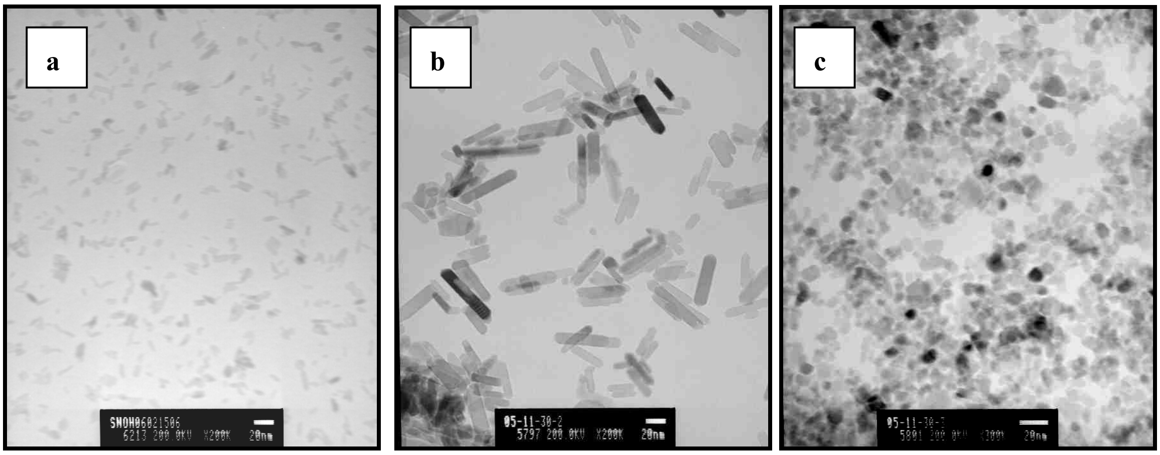

Figure 4.13 The micrographs of SnO_2 prepared using different solvents: (a) $NH_4HCO_3^{pH=11}$, (b) $NH_4OH^{pH=11}$ and (c) $NaOH^{pH=11}$, respectively.

Table 4-3 Summary of SnO_2 synthesised using different solvents.

Starting salt	Solvent	Particle description	Size (nm, TEM)
$SnCl_4{\cdot}5H_2O$	$NH_4HCO_3^{pH=11}$	short rod-like	10-20
	$NH_4OH^{pH=11}$	rod-like	20-60
	$NaOH^{pH=11}$	spherical	~10

4.1.3 Synthesis of indium tin hydroxides and indium tin oxides (ITO)

XRD results show that that the particles synthesised using indium chloride and tin chloride with the molar ratio of In:Sn of 9:1 at 200 °C for 24 h are indium hydroxide (**Figure 4.14**), which implies that ITO particles can not be obtained directly under this hydrothermal condition. The morphology of indium tin hydroxides was examined by TEM. **Figure 4.15** (a, b and c) shows the morphologies of indium tin hydroxides particles were different when different solvents were used. It can be also seen that the morphology of particles had a little change while different alkaline solvents were used. **Figure 4.15**(e, f and g) shows the micrographs of ITO particles, which were obtained by calcination of samples (a), (b) and (c) at 800 °C for 2 h.

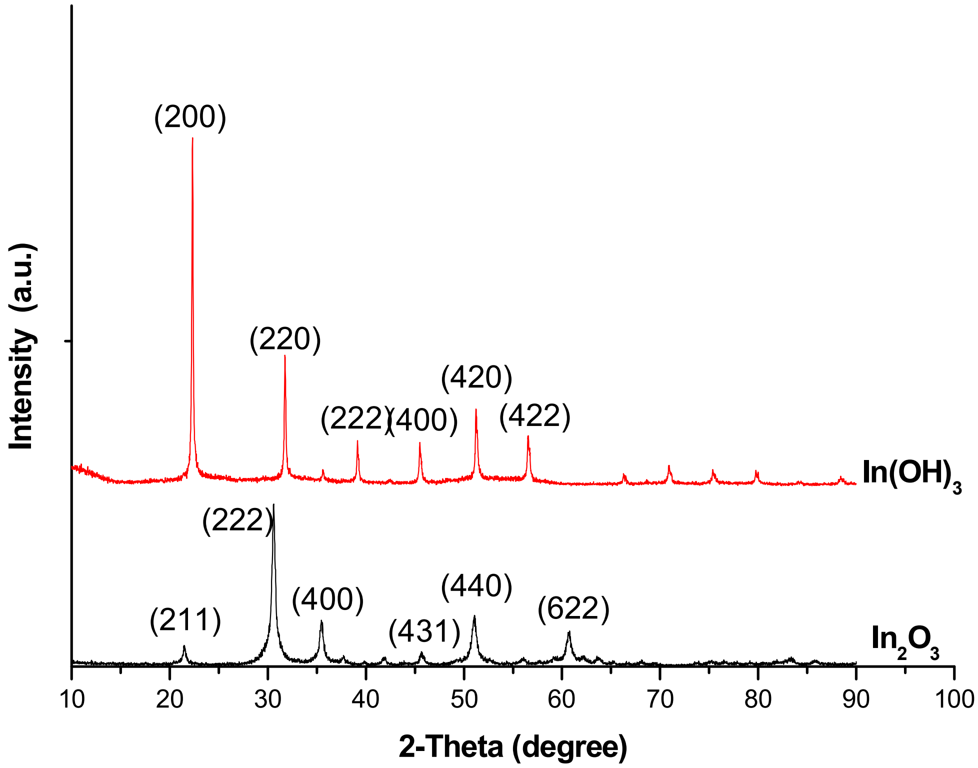

Figure 4.14 XRD results of indium tin hydroxide prepared using indium chloride and tin chloride (the molar ratio of In:Sn is 9:1) with ammonia solution and corresponding ITO particles calcined at 800 °C for 2 h.

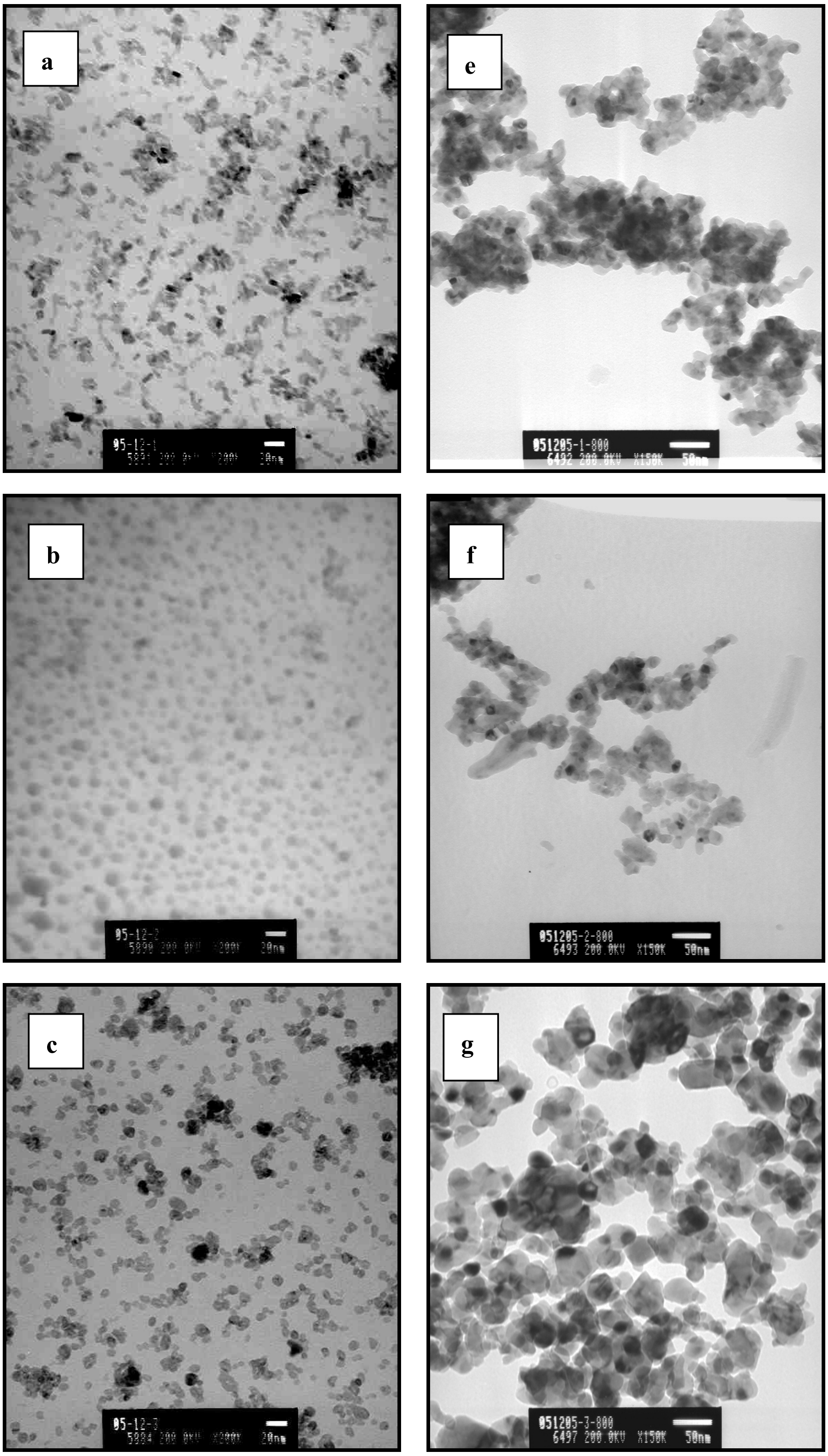

Figure 4.15 The TEM micrographs of indium tin hydroxides (the molar ratio of In:Sn is 9:1) prepared using different solvents: a) NH_4OH, b) NaOH, c) NH_4HCO_3, respectively and corresponding ITO e), f) and g) after calcining a), b) and c) at 800 °C for 2 h.

4.1.4 Synthesis of zinc oxides (ZnO)

Different salts including $ZnCl_2$, $Zn(NO_3)_2$ and $ZnSO_4$ and different synthesis conditions such as temperature and ripening time were used to investigate their effects on the particle size and morphology of zinc oxide. The effects of surfactant (polyethylene glycol (PEG)) and pH value on the properties of particle synthesised were investigated as well.

4.1.4.1 Effect of starting salts

The morphologies of $Zn(OH)_2$ produced using $ZnCl_2$, $Zn(NO_3)_2$ and $ZnSO_4$ as salts with ammonia solution (the final pH value was around 9 in order to obtain the pricipitates) were shown in **Figure 4.16** (a), (b) and (c), respectively. Large particles with the size of 2 μm in diameter and about 5 μm in length were formed when $ZnCl_2$ was used as the starting salt (**Figure 4.16** (a)). Sheet-like (**Figure 4.16** (b)) and the very tiny spherical (**Figure 4.16** (c)) particles were obtained when $Zn(NO_3)_2$ and $ZnSO_4$ were used as the starting salts, respectively.

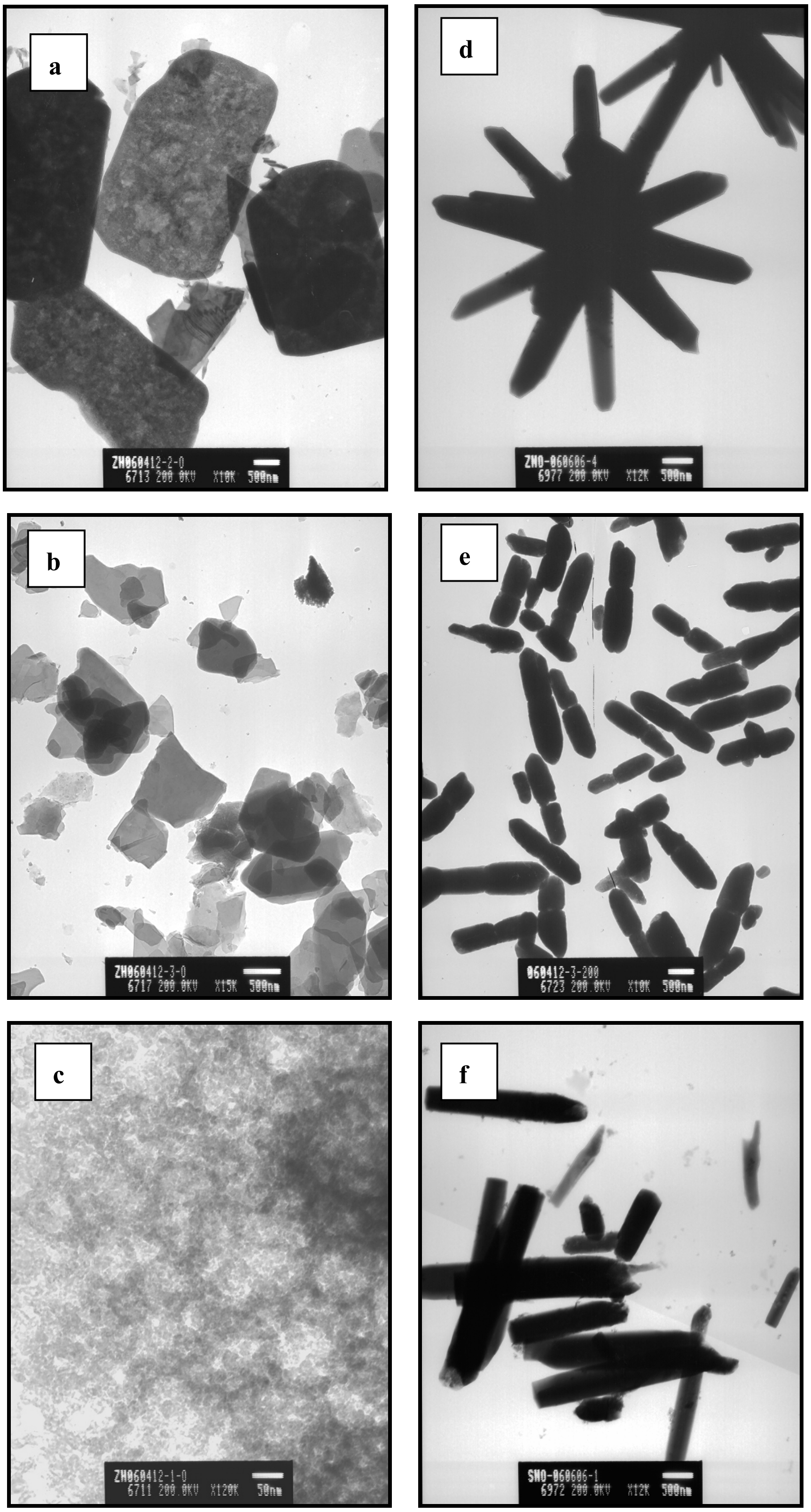

Figure 4.16 The TEM micrographs of $Zn(OH)_2$ particles obtained using (a) $ZnCl_2$, (b) $Zn(NO_3)_2$ and (c) $ZnSO_4$, respectively and corresponding ZnOs obtained using (d) $ZnCl_2$, (e) $Zn(NO_3)_2$ and (f) $ZnSO_4$ as salts by hydrothermal treatment at 200 °C for 24 h.

The ZnO particles were prepared by hydrothermal treatment at 200 °C for 24 h and examined by XRD (**Figure 4.17**). **Figure 4.16** (c), (d) and (e) show the micrographs of ZnO particles synthesised using $ZnCl_2$, $Zn(NO_3)_2$ and $ZnSO_4$, respectively. It was found that flower–like ZnO particles (the morphology of single particle is rod-like shape with a tip) of 200-500 nm in diameter and about 2-3 μm in length were formed when $ZnCl_2$ was used. But ZnO particles with spindle-like morphology and the particle size about 500 nm in diameter and 1.5-2 μm in length and rod-like ZnO with the particle size about 100-500 nm in diameter and 2-3 μm in length were obtained when $Zn(NO_3)_2$ and $ZnSO_4$ were used, respectively.

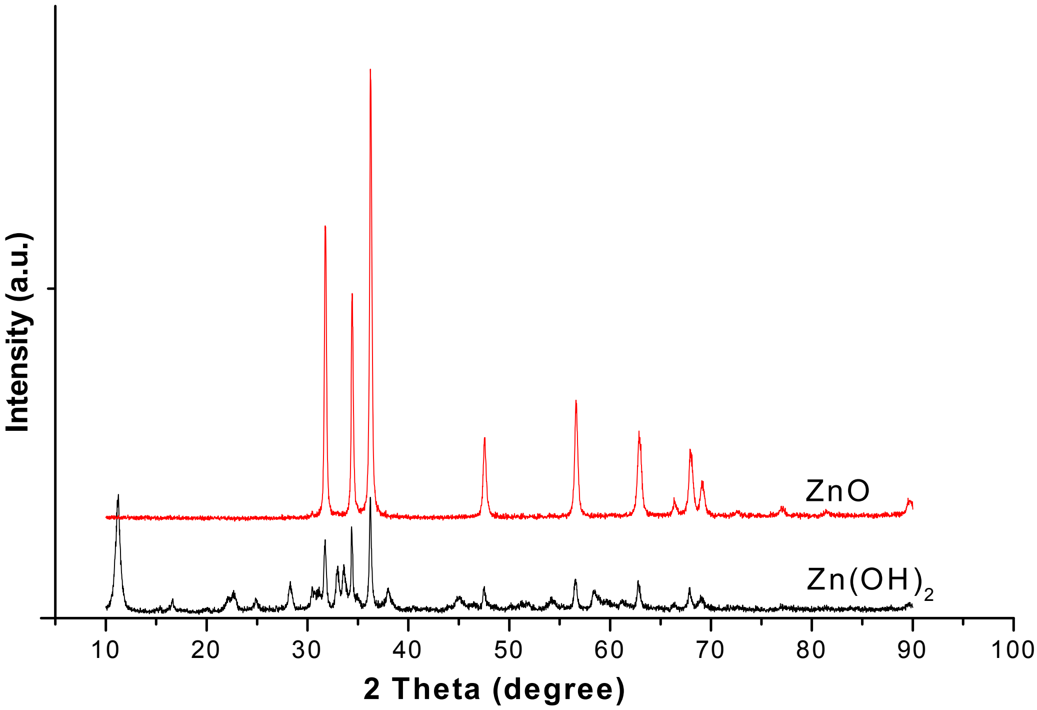

Figure 4.17 XRD results of ZnO and $Zn(OH)_2$ prepared using $ZnCl_2$.

4.1.4.2 Effect of surfactant (PEG)

The XRD results (in **Figure 4.18**) show that ZnO particles were obtained at 200 °C for 24 h by using zinc chloride and ammonia solution (pH=11) with adding 0.2 g of PEG with different molecular weight of 400, 1000, 3400 and 8000, respectively.

Figure 4.19 shows the morphologies changed with different PEG used. For example, the rod-like particles were achieved by using PEG 400 (**Figure 4.19**a), the spindle-like shape with rough surfaces (**Figure 4.19**b) by using PEG 1000, the mixture of discs and short rods (**Figure 4.19**c) by using PEG 3400, whilst the completely disc-like shaped particles (**Figure 4.19**d) when PEG 8000 was used. Moreover, the particle size decreased from several micrometers to around 300 nm while the molecular weight of PEG increased from 400 to 8000. This is because the molecular chain increased with the increase of molecular weight of PEG, which adsorbed on the surface and affected the growth of zinc oxides.

In order to study the effect of PEG content on the properties of zinc oxide particles, 0.1, 0.2, 0.4 and 0.6 g of PEG 8000 was added into the precursor solution, respectively. The results show that particles with thin disc-like morphology had little change in the range of 0.1 g to 0.6 g of PEG 8000 content (in **Figure 4.20**).

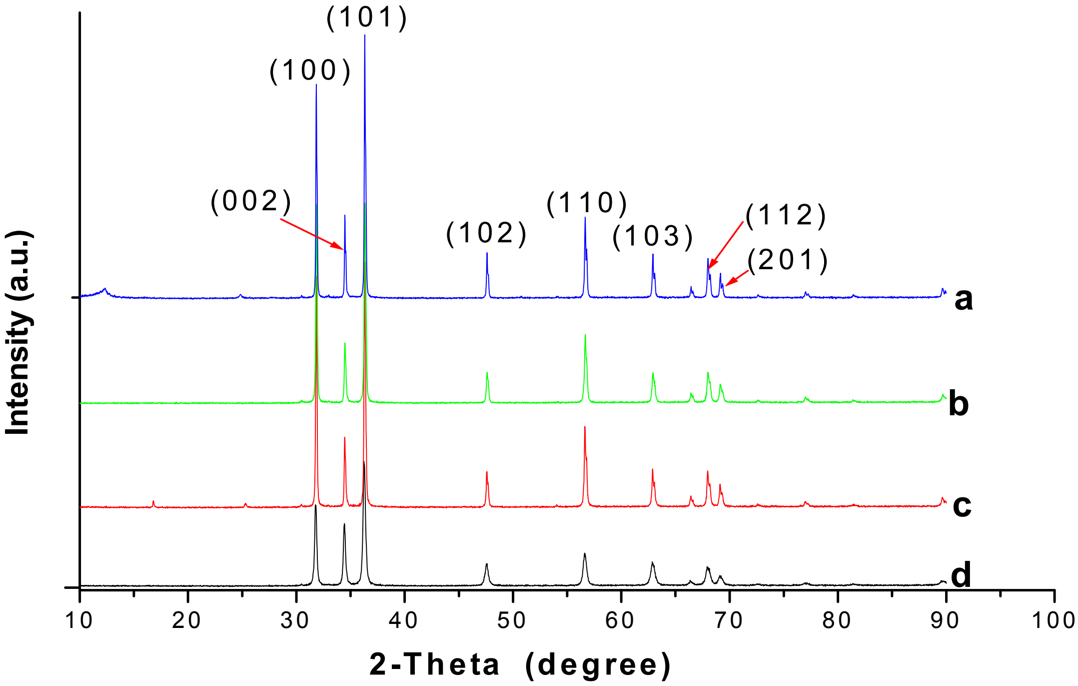

Figure 4.18 XRD results of ZnO particles synthesised using PEG with different molecular weight: a) 400 g/mol, b) 1000 g/mol, c) 3400 g/mol and d) 8000 g/mol at 200 °C for 24 h.

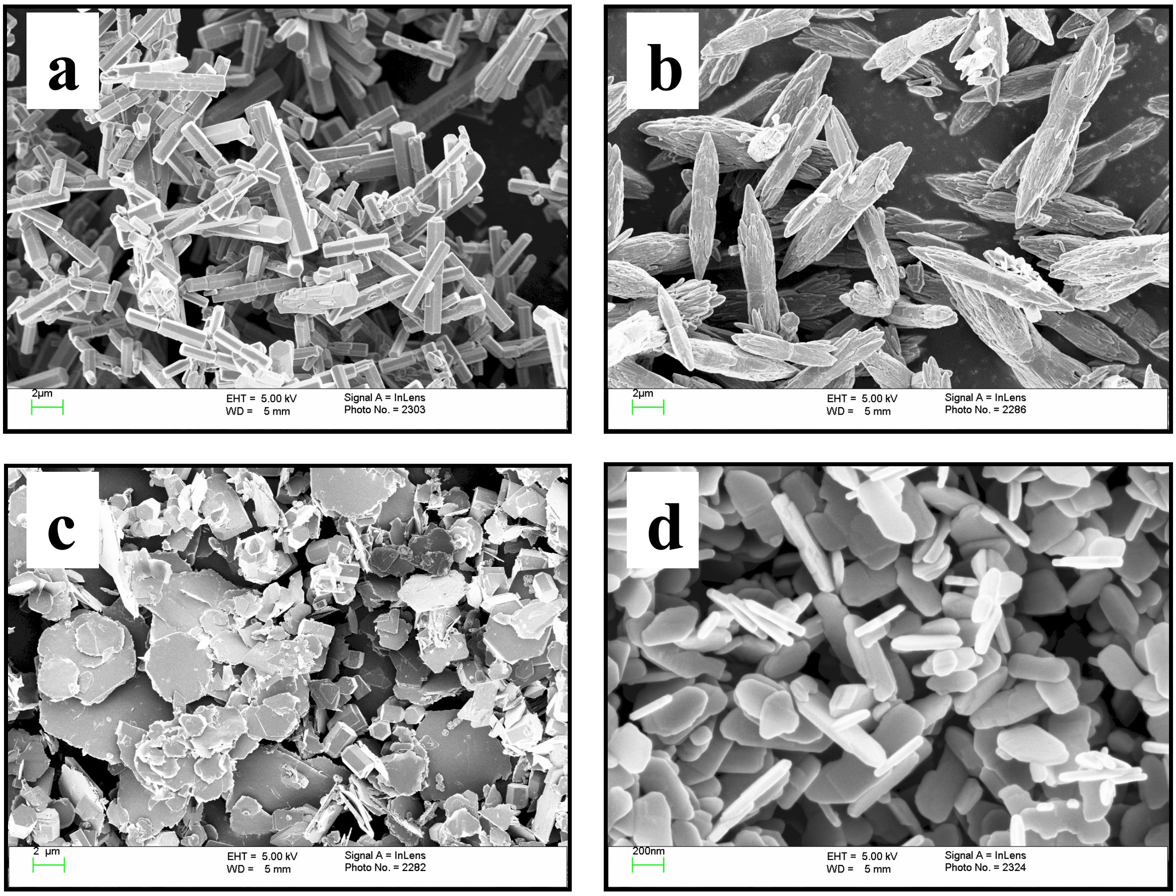

Figure 4.19 SEM micrographs of ZnO paerticles synthesised using PEG with different molecular weight: a) 400 g/mol, b) 1000 g/mol, c) 3400 g/mol and d) 8000 g/mol, respectively.

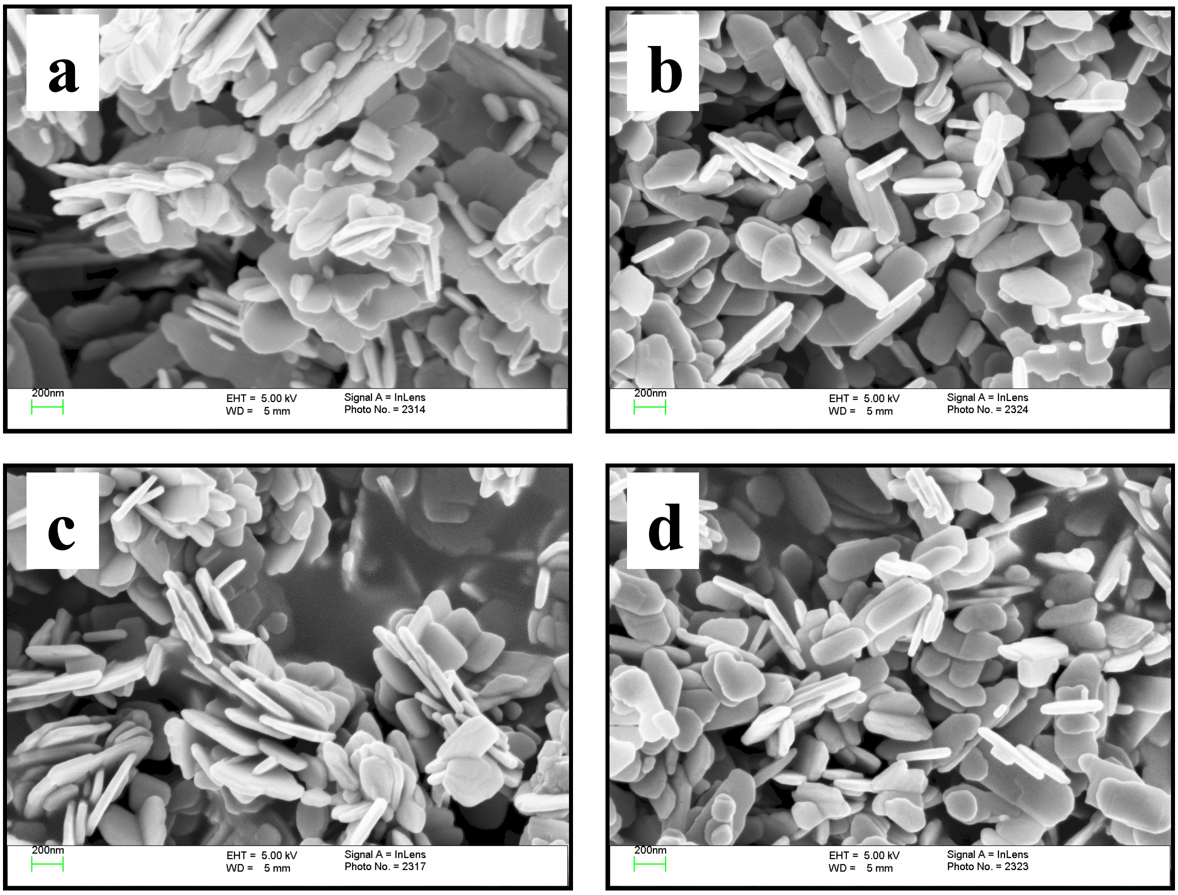

Figure 4.20 SEM micrographs of ZnO particles synthesised using PEG 8000 with different PEG concentration: a) 0.1 g, b) 0.2 g, c) 0.4 g and d) 0.6 g, respectively.

4.1.4.3 Effect of pH value

The pH value was generally set as a constant of 11 in the hydrothermal process of this project. However, In order to understand the influence of pH of starting solution on the properties of synthesised particles, the pH value of solution was varied from 9 to 12 and the hydrothermal treatment condition was kept at 200 °C for 24 h. It was observed that the white precipitates were formed while pH value was reached at 9. After further increase of the pH value to 10, the precipitates started to partly dissolve into solution, and they were dissolved completely while the pH value reached 11. The reason can be attributed to the amphoteric property of the precursor-zinc hydroxide. **Figure 4.21** shows the morphologies of zinc oxide particles with different pH value. The corresponding XRD results are shown in **Figure 4.22**. It can be seen that the particles with round shaped morphology were formed when pH value was 9, and the morphology of the particles were changed to mixed round and rod-like shape at pH=10, which was further changed to rod-like when pH value was increased to 11. However, no particles were collected when pH value was 12.

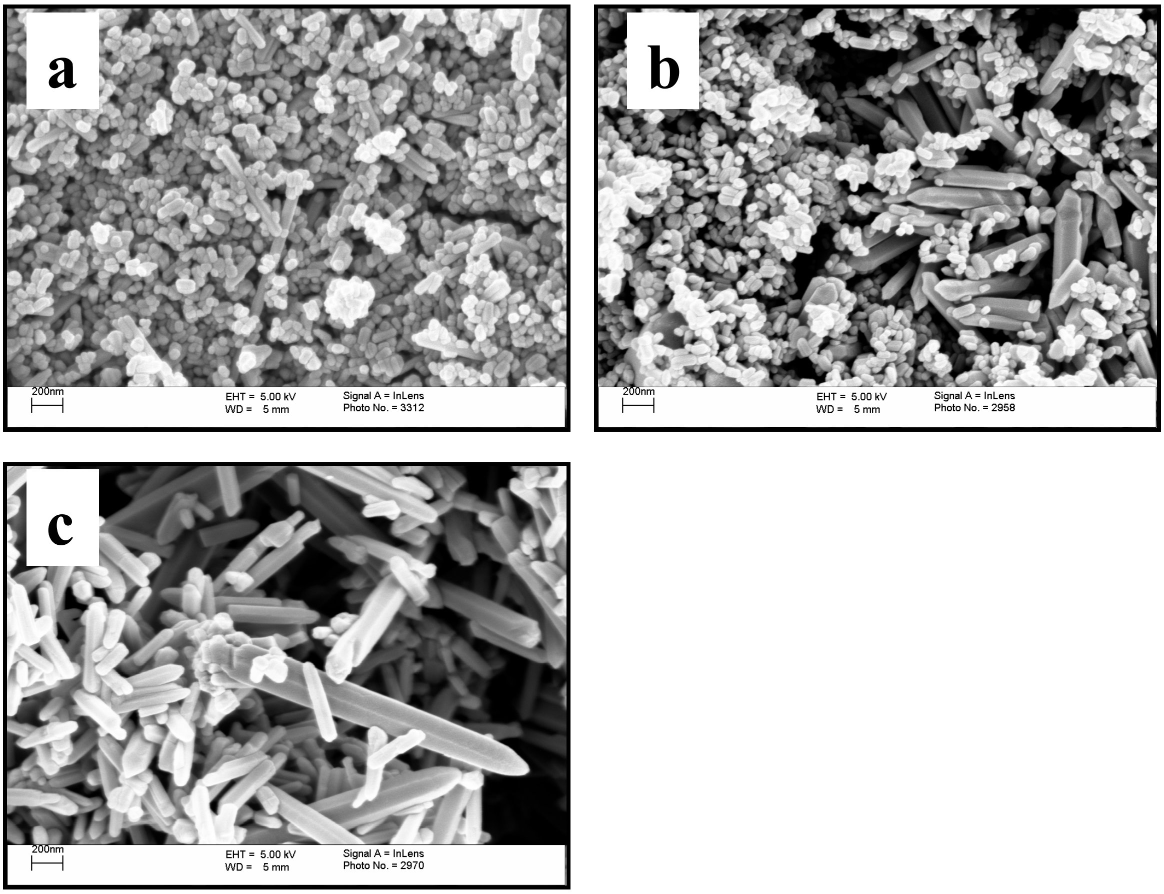

Figure 4.21 SEM micrographs of zinc oxides synthesised with the pH value of, a) 9, b)10 and c) 11 at 200 °C for 24 h.

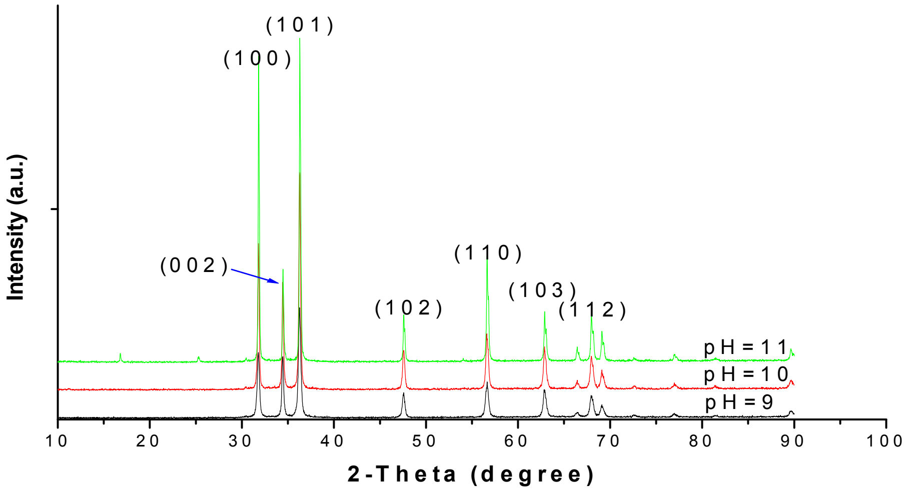

Figure 4.22 XRD results of ZnO synthesised with varying pH values at 200 °C for 24 h.

4.1.5 Synthesis of zinc aluminum oxides (AZO)

The AZO particles were synthesised at 200 °C for 24 h by mixing the starting salt of $ZnCl_2$ and the dopant of $Al(NO_3)_3$, which were mixed with the mole fraction of Al to Zn of 1.0%, 3.0%, 5.0% and 10.0%, respectively. XRD results show that zinc aluminum oxides were formed (**Figure 4.23**). It can be observed that the AZO particles with different contents of dopant were spherical (**Figure 4.24**, a, b, c, d) and the particle sizes decreased from about 200 nm to 50 nm as the percentages of Al increased (**Figure 4.25**).

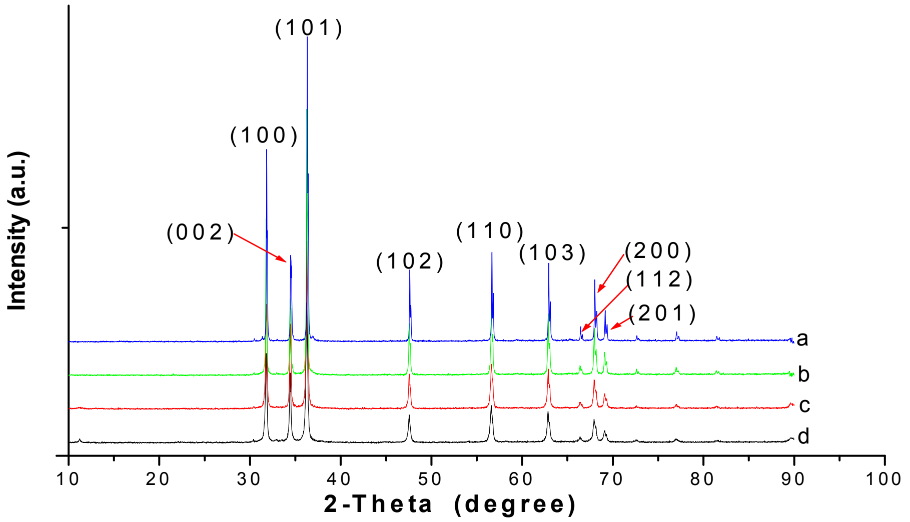

Figure 4.23 XRD results of AZO particles synthesised using different aluminium contents at 200 °C for 24 h: a) 1.0 at%, b) 3.0 at%, c) 5.0 at% and 10.0 at%, respectively.

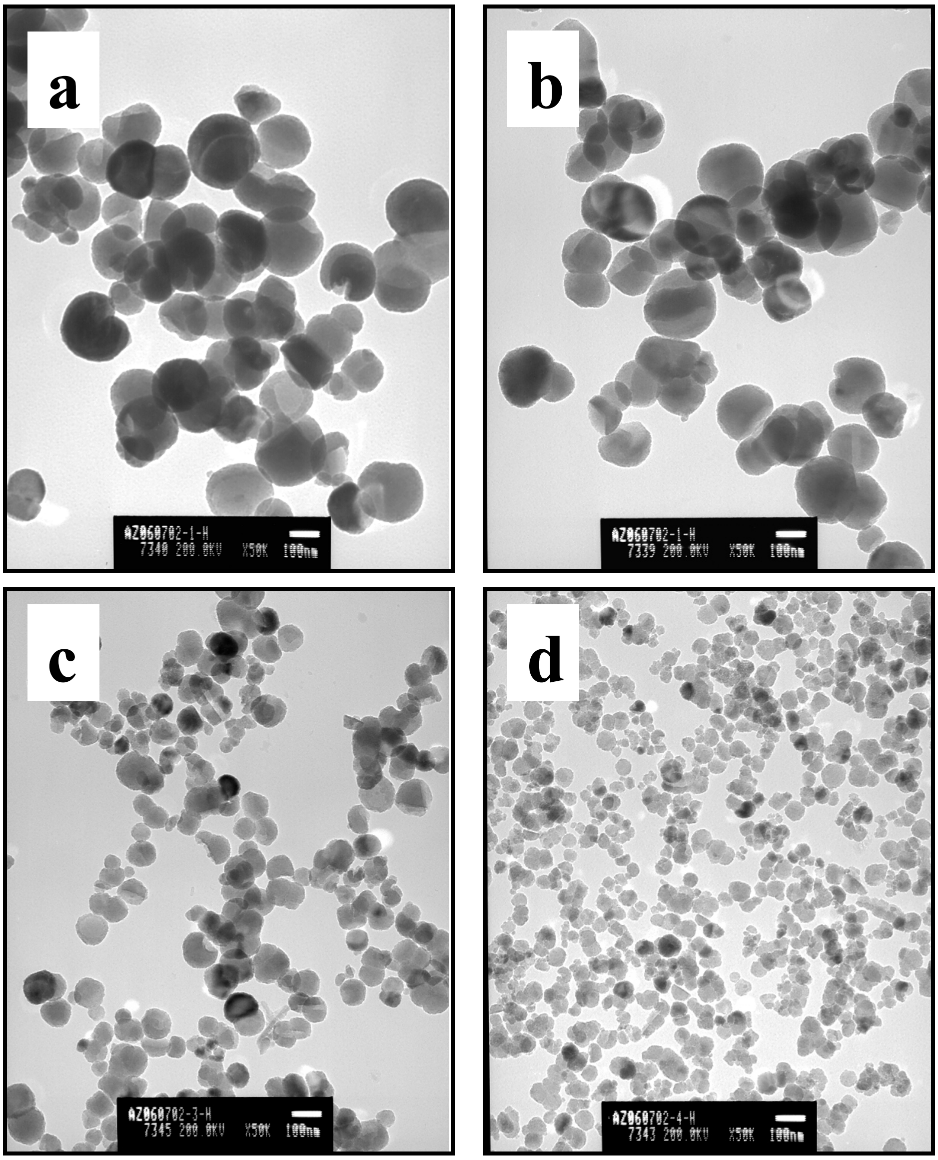

Figure 4.24 TEM micrographs of AZO particles with various contents of dopant prepared at 200 °C for 24 h: (a) 1.0 at%, (b)3.0 at%, (c) 5.0 at% and (d) 10.0 at%, respectively.

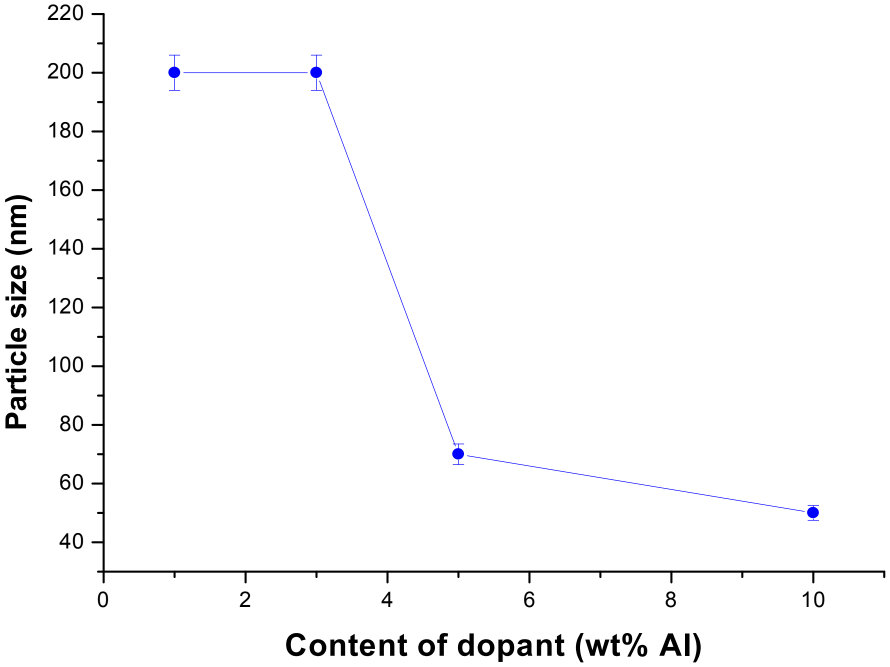

Figure 4.25 Particle size of AZO various with the contents of dopant

4.2 Discussion

Hydrothermal synthesis is a potentially useful method for low cost production of advanced metal oxides because the suspended precursor is not dried and calcined but instead heated in an autoclave with a certain pressure until the precursor has crystallised [54]. The processing of metal oxides under hydrothermal conditions constitutes an important aspect of hydrothermal processing of materials because of its advantages in the preparation of highly monodispersed nanoparticles with a controlled morphology and size [140]. Therefore, the hydrothermal method has been widely used to synthesise ceramic particles with different size and morphology [141,142,143,144,145], which can be controlled by modifying the hydrothermal conditions, such as solute concentration, solvent, pH value, additive, type of starting salt, and hydrothermal temperature and ripening time, which will be discussed in following sections.

4.2.1 Effect of starting salts

Zinc oxides were prepared using different salts (zinc chloride, zinc nitrate and zinc sulfate) with ammonia solution by hydrothermal method. The zinc oxide morphologies of flower-like, spindle-like and rod-like with varying particle size were obtained (Error! Reference source not found.). In synthesis of metal oxides using different salts, there were different anions existed in the precursor solutions, and they have different chemical properties. Although growth of particles from a solution is determined mainly by its instinctive structure, external factors also have an effect on it [146]. The results mentioned above indicated that different anions had influence on not only the particle shape, but also the particle size, because particle growth is a surface phenomenon. Different anions have different properties and selectively absorb on the surface of crystal faces to change energy distribution of the surface and affect the growth behaviour of those crystal faces and thus changing the morphology [52,147].

4.2.2 Effect of alkaline solvent

Hydrothermal synthesis, usually operated as a closed system with a high temperature and pressure, is a straightforward equilibrium reaction for synthesis of powders [148,149]. These powders are insoluble under room temperature, but they dissolve and form the crystalline phase under hydrothermal conditions. In the reaction process, solvent plays a very important role. In generally, pure water, which is often used in the hydrothermal process, serves two different functions: on one hand, it is the solvent, but it is not sufficient to dissolve certain substances for crystallisation, even at high temperature. Therefore, it is necessary to add a mineraliser such as alkaline solvents or alkali salts of weak acids, which when is added to the aqueous solution, speeds up crystallisation, and it usually works by increasing the solubility of the solute through the formation of soluble species that would not normally be present in the water [150]. In our project, ammonia, ammonium hydrogen carbonate, and sodium hydroxide solutions were used as the mineralisers. On the other hand, they are also the pressure-transmitting medium [150]. Hence, the pVT-data (p: pressure, V: volume, T: temperature) of water at high temperatures and pressures are of significant importance. **Figure 4.26** shows the V-T diagram (the pressure-temperature relations of water at constant volume) of water (volume is replaced by the density).

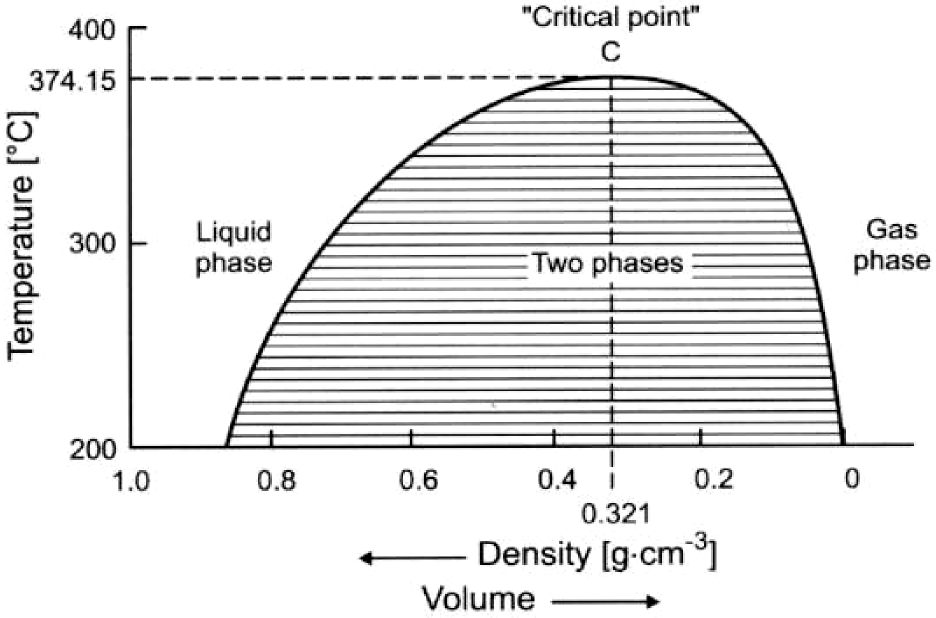

Figure 4.26 Volume (density)/temperature-dependence of water [150].

The diagram shows a closed, two-phase section, in which the liquid and the gaseous phase are in equilibrium, which means they exist at same time. The density of the two phases at a given temperature is given by the two intersections of a horizontal line through the two-phase region with the equilibrium curve. The density of the liquid water decreases as the density of the corresponding gas phase increases when the temperature is increased. At the critical point C, the densities of both phases are the same. This means that the difference between liquid and gaseous phases has disappeared. Above the critical temperature only one phase (the fluid or supercritical phase) exists.

In practical applications, the diagram of P-T varied with the different volume ratios of water put into the reaction container is more useful (**Figure 4.27**). The curve between the triple point (Tr) where the gas, liquid and solid phase coexist and the critical point (C) represents the saturated steam curve at which the liquid and gas phases coexist. The isochors (solid lines) can be used to estimate the pressure that is developed inside a closed container which is partially filled with water and heated to a certain temperature. In other words, the pressure under working conditions is determined by the degree of fill, i.e. by the volume of the reaction vessel that was originally filled with solvent. In our project, the volume ratio of water filled in the autoclave was fixed at 70%. It can be seen that liquid phase and gas phase coexisted and the pressure was estimated about 7-10 MPa in the 70% volume ratio of water at 200 °C (**Figure 4.27**).

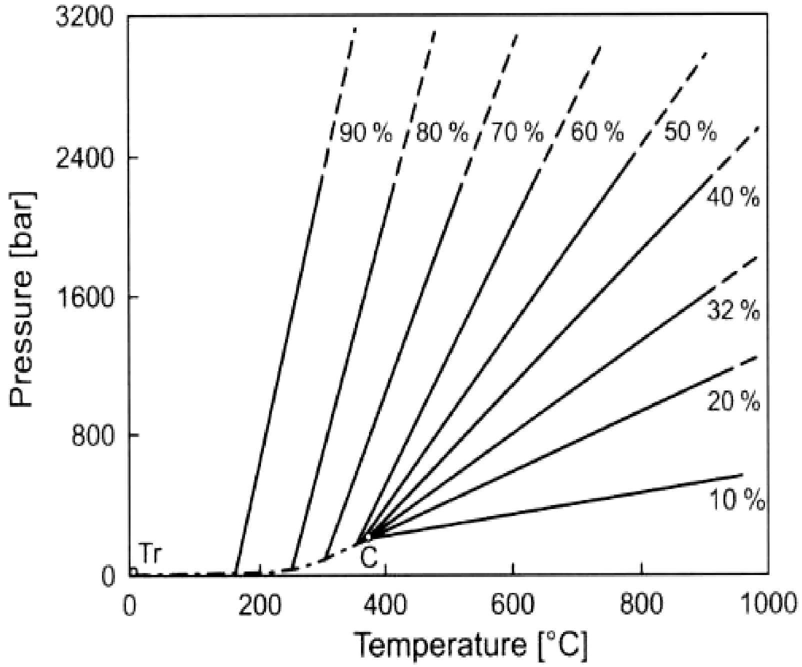

Figure 4.27 Pressure/temperature varied with water for different ratios of filling of the reaction container [150].

Under the synthesis conditions mentioned above, it was found that the particles synthesised via the hydrothermal process were indium hydroxides and no indium oxide observed at 200 °C for 24 h (**Figure 4.1**). This is probably because the hydrothermal process did not have enough energy to break the bonds of the $In(OH)_3$ precursors under this synthesis condition [31]. However, tin oxides, zinc oxides and zinc aluminum oxides were obtained at the same reaction conditions, which was possibly due to the different decomposition process among them [151].

Ammonia solution was used to form indium hydroxide, tin oxide and indium tin hydroxide particles in order to investigate the effect of solvent on the particles synthesised. It was found that cubic shaped $In(OH)_3$ particles with different particle size (**Figure 4.2** and **Figure 4.3**) and rod-like tin oxide particles (**Figure 4.13** b) were formed. When tin was doped into indium hydroxide to form indium tin hydroxide, the spherical shaped particles were formed (**Figure 4.15** a). It could be explained that the effect of tin on the formation of indium hydroxide morphology was more than that of ammonia cation. Under the same experimental conditions, the cubic shaped particles were also obtained when NH_4HCO_3 was used as the solvent (**Figure 4.3**). The formation of rod-like indium hydroxide particles using ammonia and ammonium hydrogen carbonate normally because the ammonium salt could play a "template" role in the formation of nanoparticles [152,153]. A proposed model of rod development is shown in **Figure 4.28**.

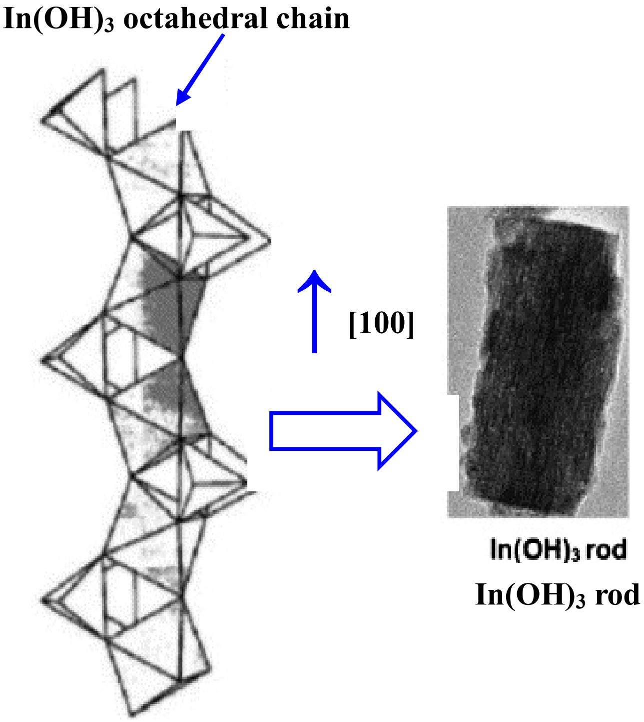

Figure 4.28 Section of an growing chain in $In(OH)_3$, viewed in a direction perpendicular [1 0 0] [50].

The mechanism of involvement of the ammonia in the formation of indium hydroxide crystals is as follows:

$$NH_3+H_2O \rightleftharpoons NH_3 \cdot H_2O \rightleftharpoons NH_4^+ + OH^- \qquad (4\text{-}1)$$

$$In^{3+}+NH_3 \rightarrow In(NH_3)_4^{3+} \qquad (4\text{-}2)$$

NH_4^+ in solution has great effect on the orientation of crystals [140,152,153,154]. NH_4^+ not only adjusts the pH of the reaction and the concentration of $In(NH_3)_4^{3+}$, but also has great guiding effect on the formation of $In(OH)_3$ nuclei in solution[50]. The concentration of $In(NH_3)_4^{3+}$ was found to be condensed and the pH of the solution decreased because the reaction in eq. 4-1 moved to the left. This growth morphology can be simply explained by the "lowest energy" thoery, i.e., the (100) plane of $In(OH)_3$ is the closest packed plane in the crystal, and stacking along the [100] direction therefore becomes energetically favourable[50]. Another reason is the metal cations are linked together by means of a single bridge of hydroxo group to produce the $[In^{3+}–OH^-–In^{3+}]$ backbone [50]. Because the "template", $In(NH_3)_4^{3+}$ can prevent $[In^{3+}–OH^-–In^{3+}]$ backbones growing in other directions except [100] direction, $In(OH)_3$ octahedral nuclei in the cubic structure cell will stack mainly along the closest plane (100).

Sodium hydroxide solution was used to produce $In(OH)_3$ particles with different salts， tin oxide and indium tin oxide particles as well. It was found that particles with spherical shape and about 10 nm in size (**Figure 4.4** a) were formed for $InCl_3$ and aggregated morphology (**Figure 4.4** b and c) were produced for $In(NO_3)_3$ and $In_2(SO_4)_3$. Tin oxide particles of 10 nm with spherical shape (**Figure 4.13** c) and aggregated indium tin hydroxide particles (**Figure 4.15** b) were also synthesised. The mechanism of the effect of NaOH on the size and morphology of particles possibly can be explained by the fact that NaOH solvent provided the higher hydroxyls concentration due to its complete dissociation of hydroxyl group. Thus, a large number of particles were formed within the same liquid volume [155] and the particles were kept in a small size with high surface energy resulting in a decrease in the total surface area by an aggregation-agglomeration process [156]. On the other hand, during wet-chemical synthesis, if a high concentration of hydroxyl existed, surface hydroxyl groups would bond particles via hydroxyl bridge bonds and cause severe particles aggregation[157].

4.2.3 Effect of concentration of starting salt

Synthesis of particles in solution involves two important processes: nucleation and growth from a supersaturated solution [147, 158]. The main features may be explained in terms of the La Mer's diagram [150] (**Figure 4.29**). When a chemical was added to the solution, the concentration of the solute was increased to the saturation concentration, C_s, where no precipitation took place. When the minimum concentration for nucleation, C_0, reached after some time t_1, nucleation occurred. After that, the concentration of the solute kept increasing to the critical supersaturation concentration (C_{ss}) when a large amount of the solute was added, where nucleation was extremely rapid. After that, the concentration decreased again due to the consumption of solute by nucleation and precipitation of particles. Once the concentration of solute decreased to C_0 again after a time t_2, no new nuclei was formed. Generally, the nucleation occurs in the first few hours [159], i.e., nucleation time ($t_1 \sim t_2$) was very short. After the initial fast rate of growth of these nuclei reduces the concentration below the minimum nucleation concentration (C_0) rapidly, the growth of crystals at the eventual slow rate of growth leading to a growth period longer than the nucleation period is undergoing until the concentration reaches C_s. Then, the growth mechanism of the crystals is determined by Ostwald ripening process [158].

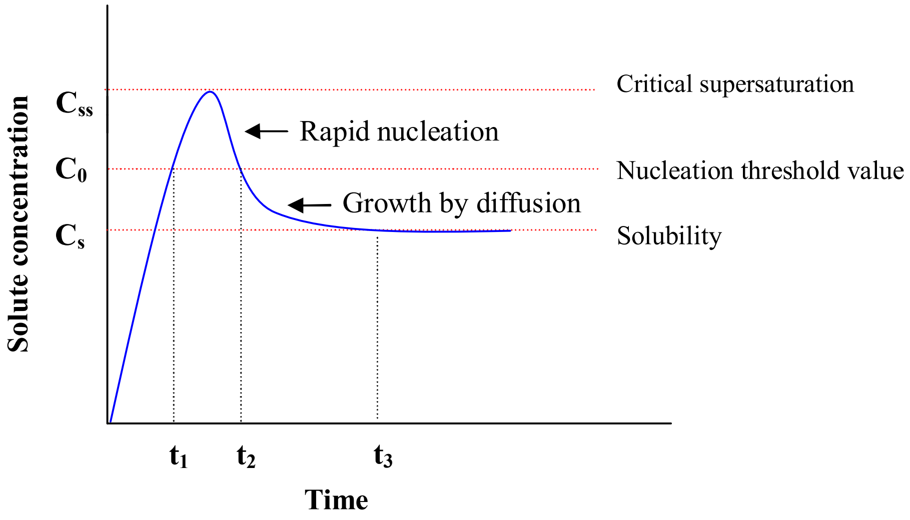

Figure 4.29 Schematic diagram illustrating La Mer's condition for nucleation and growth of crystals.

According to the theory of La Mer, the concentration is an important factor affecting the properties of particles synthesised in solution. In this project, the influence of starting salt concentrations varied from 0.25 mol/L to 3.0 mol/L on the size and morphology of tin oxide particles prepared using ammonia solution by hydrothermal method was investigated. The hydrothermal synthesis was carried out at 200 °C for 48 h. There were no particles collected when 0.25 mol/L of tin chloride was used, which is probably owing to the concentration was not reached the concentration of nucleation (C_0) and resulted in no tin oxide particles formed. However, it was observed that both the particle morphology and size were different using various concentrations of $SnCl_4$ solutions from 0.5 mol/L to 4.0 mol/L (**Figure 4.11** and **Figure 4.12**). When the concentration of $SnCl_4$ solution was reached at 0.5 mol/L and 1.0 mol/L, rod-like shaped nanoparticles with particle sizes of 22 nm and 30 nm were formed, respectively (**Figure 4.11** a and b). However, with a further increase of the concentration of $SnCl_4$ solution to 4.0 mol/L, not only was the morphology of the particle changed from rod-like to oval shape, but the particle size was decreased from 30 nm to 14 nm (**Figure 4.11** b and e). Actually, in the solution, nucleation is either heterogeneous (catalytic formation of a nucleus around an impurity or on the container wall) or homogeneous (spontaneous formation of a nucleus consisting of pure molecules of solute)[160]. At low supersaturations, heterogeneous nucleation is dominative therefore the number of formed crystals is determined by the number of active heteronulei in the solution [146]. Nucleation is followed by crystal growth and the mechanism of which largely determines the crystal shape. Under the condition mentioned above, if the growth rate is pronouncedly anisotropic, elongated shapes such as needles, rods and plates maybe formed. For example, Pleskach and Chirkova successfully prepared the plate-like shaped $BaSO_4$ crystals by controlling the solution concentration at a low supersaturation condition [161]. In the process of synthesis of tin oxides, the rod-like particles were formed while the concentrations of starting salt were 0.5 mol/L and 1.0 mol/L.

When the concentration of tin chloride further increased from 1.0 mol/L to 4.0 mol/L, the concentration of the solution would be at high supersateration. At the high supersaterations, homogeneous nucleation becomes important and this results in a sudden increase in the number of particles formed, i.e., the higher nucleation will occur within a short burst of time [146]. As the result, the particle size is decreased and the morphologies tend to be more isometric [146]. Hence, the morphologies of tin oxides were changed form rod-like to oval shaped and the particle size decreased from 30 nm to 14 nm when the concentration of tin chloride increased from 1.0 to 4.0mol/L.

4.2.4 Effect of hydrothermal temperature and time

Hydrothermal temperature is an important factor, which influences the size and morphology of particles synthesised. Tin oxides were synthesised at different temperatures including 160, 180, 200 and 220°C for 48 h.

XRD results (**Figure 4.5**) showed that all particles synthesised were tin oxide at the temperature from 160 °C to 220 °C for 48 h. Rod-like shaped particles were obtained at the temperature below 200°C, which were changed to a mixture of rod-like and polygon shapes at 220 °C (**Figure 4.7**). The average particle size of tin oxide also increased from 10 nm to 110 nm when the temperature increased from 160 °C to 220 °C (**Figure 4.6**). This change can be explained by the fact that the smaller particles are more soluble than larger particles under higher temperature and higher pressure, due to curvature effects [162]. On the other hand, the increase of particle size with the increase of hydrothermal temperature can also be explained by kinetic ripening mechanism [163]. Increasing of temperature introduces higher solubility and redissolution of all crystals until a new solubility limit reached in the solution. Hence, small crystals will completely redissolve in the solution, whereas the large ones will only slightly reduce in size. A reverse decrease of temperature will restore the original solubility and the solute in excess in the solution will deposit on the surface of the remaining particles, resulting in the formation of larger particles with the increase of hydrothermal treatment temperature.

Hydrothermal ripening time is another important parameter, which will affect the size and morphology of tin oxide particles. Rod-like shaped tin oxide particles with the particle size increased from 12 to 55 nm (**Table 4-2**) were observed for the samples synthesised at varied ripening time from 6 to 48h with fixed heating temperature at 200°C. The results which indicated that ripening time greatly affected not only the morphology (**Figure 4.8**), but also the particle size of tin oxide, can be explained by the mechanism of crystal growth in solution. Regarding the growth process, the mechanism of particle growth can be termed as Ostwald ripening process [158, 164] (**Figure 4.30**). In general, the small particle has a quite high ratio of surface to volume. Because of the large surface area present, it is observed that surface excess energy becomes more important in very small particles, constituting a non-negligible percentage of the total energy. Hence, when the thermodynamic equilibrium for a solution does not reach initially, large particles will be formed at the cost of smaller particles in order to reduce the surface energy. On the other hand, in the aspect of diffusion mechanism, for a solid species present at a solid/liquid interface, the chemical potential of a particle increases with the decrease of particle size, the equilibrium solute concentration for a small particle is much higher than that for a large particle, as described by the Gibbs-Thompson equation [158]. The resulting concentration gradients lead to transport of the solute from the small particles to the large particles, resulting in the dissolvation of the small particles and the formation of the large particles with increase of the ripening time.

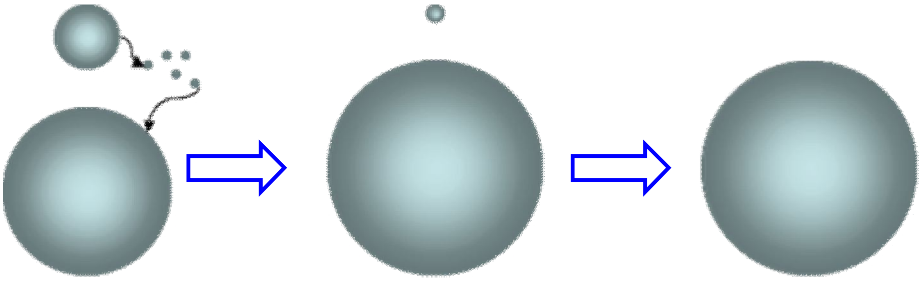

Figure 4.30 Basic schematic of the Ostwald ripening process.

4.2.5 Effect of PEG

Polyethylene glycol (PEG) is a water-soluble linear polyether, which is available over a wide range of molecular weights from 300 g/mol to 10,000,000 g/mol. The larger the molecular weight is, the larger the molecular chain is. In this project, the effects of molecular weight and concentration of PEG on the properties of particles synthesised were investigated. There are many factors which influence the shape and size of metal oxide particles synthesised in solution, which can be categorised into two aspects: the inherent structure of crystal itself and outside physical chemistry conditions [68]. For comparison, zinc oxide particles were also synthesised without the use of any additives.

Zinc oxide particles with rod-like morphology were formed using zinc chloride with ammonia solution (pH =11) by hydrothermal treatment at 200 °C for 24 h (**Figure 4.16**, d). It was reported that the growth habit of ZnO prepared without additive was mainly determined by the internal structure during the hydrothermal process [165, 166]. In general, a ZnO crystal is a polar crystal whose positive polar plane is rich in Zn and the negative polar plane is rich in O. In the hydrothermal process under the condition of ammonia solution (pH=11), the mechanism of formation of ZnO is usually accepted as follows [66]:

$$NH_3+H_2O \leftrightarrow NH_3 \cdot H_2O \leftrightarrow NH_4^+ + OH^- \quad (4\text{-}3)$$

$$Zn^{2+}+2OH^- \rightarrow Zn(OH)_2 \quad (4\text{-}4)$$

$$Zn(OH)_2+2OH^- \rightarrow Zn(OH)_4^{2-} \quad (4\text{-}5)$$

$$Zn(OH)_4^{2-} \rightarrow ZnO+H_2O+2OH^- \quad (4\text{-}6)$$

In the presence of the OH^- ions in the solvent at high temperature and pressure, OH^- was first introduced into Zn^{2+} aqueous solution, and then $Zn(OH)_2$ colloids were formed. The further reaction of between $Zn(OH)_2$ and OH^- was to form a $Zn(OH)_4^{2-}$ unit, which was finally decomposed to ZnO. It can be seen that ZnO nuclei were obtained by the dehydration of $Zn(OH)_4^{2-}$. Finally, these ZnO species formed ZnO seeds, which were agglomerated to form a hexagonal planar nucleus. In the structure of wurtzite ZnO, it is known that Zn atoms are tetrahedrally coordinated with four oxygen atoms. Thus one face of the hexagonal sheet is Zn rich and forms the (0001) plane whereas the opposite face is the $(000\bar{1})$ plane. The ZnO crystals are polar in nature and the Zn rich positive (0001) surface being more reactive than the oxygen rich negative $(000\bar{1})$ surface can attract new ZnO species or the opposite ionic species to its surface[167]. From the crystal habits of wurtzite ZnO, it is well known that the growth rate of the different family of planes follows the sequence (0001)> (01 $\bar{1}$ $\bar{1}$)> (01 $\bar{1}$ 0)> (01 $\bar{1}$ 1) > (000 $\bar{1}$)[166, 168]. As it is known, the faster the growth rate, the earlier the disappearance of the plane. Hence, the (0001) plane, the most rapid growth rate plane with the lowest density of surface free energy (9.9 eV/nm^2) [169], disappears in the hydrothermal process, which results in the pointed shape at an end of the c-axis ([0001]) as shown in **Figure 4.31**. In contrast, the (000$\bar{1}$) plane, the slowest growth rate plane, is maintained in the hydrothermal process, which leads to the plain shape in another end of the c-axis.

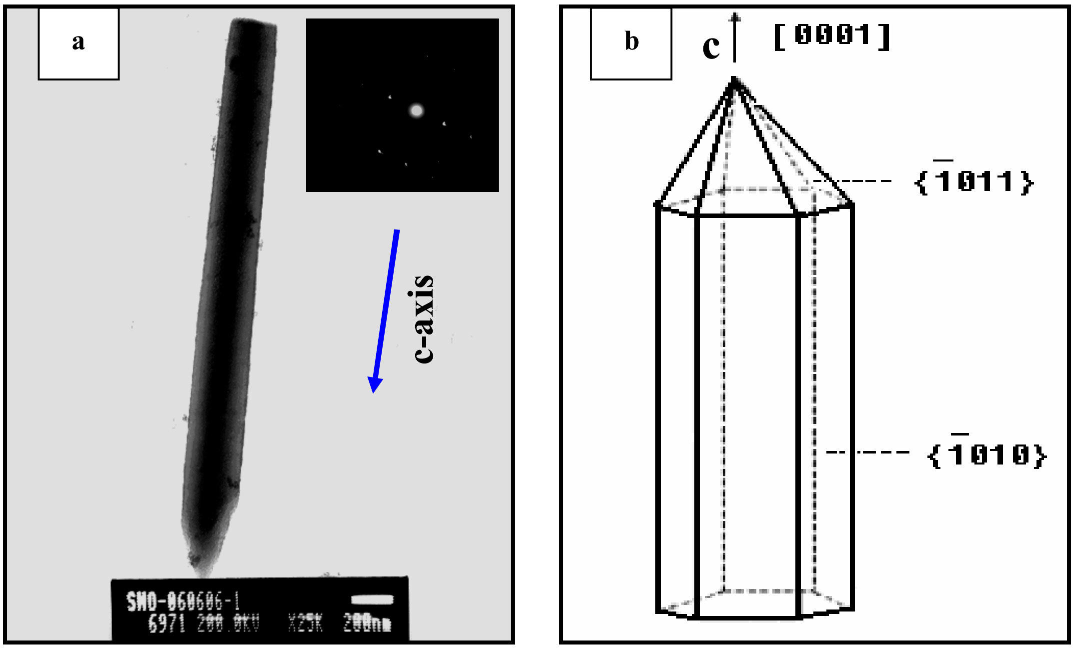

Figure 4.31 (a) A single particle of ZnO, (b) Growth sketch of a ZnO crystal.

When 0.2 g of PEG 400, PEG 1000, PEG 3400 and PEG 8000 were added into the solution, respectively, the morphology of ZnO particles was changed greatly. As shown in **Figure 4.19,** the shape of ZnO particles is rod-like when PEG 400 was used (**Figure 4.19** a). With the increasing of molecular weight of PEG, the shape changed to spindle-like (**Figure 4.19** b) for PEG 1000, mixture of disc and short rod-like (**Figure 4.19** c) for PEG 3400 and entirely disc-like shape (**Figure 4.19** d) for PEG 8000, respectively.

There has not yet been an adequate mechanism, except the adsorption mechanism, which reasonably account for the effect of additives on morphology and size of the crystal[70]. In order to investigate the role of PEG in the hydrothermal process, it is necessary to discuss its molecular structure. PEG, a non-ionic polymer, has a long molecular chain of $HO\text{-}CH_2\text{-}(\text{-}CH_2\text{-}O\text{-}CH_2\text{-})_n\text{-}CH_2\text{-}OH$. It can be seen that PEG has hydrophilic –O– and hydrophobic –CH_2–CH_2– on the long chains [170]. In the presence of PEG, growth units $Zn(OH)_4^{2-}$ are easily adsorbed by the atom O in the chain of C–O–C (hydrophilic head) [171]. When PEG 400 is added into the solution, it can fully extend its molecular chains due to the short linear chain of PEG 400. Hence, $Zn(OH)_4^{2-}$ adsorbed on the chain can be carried and transformed into ZnO crystalline particles and grow on active sites around the surface of ZnO nuclei, which results in the formation of the rod-like shaped ZnO particles. The PEG 400 acts as soft templates to direct growth of the crystals. However, PEG will show its characteristic intertwisting nature when their molecular chain increases with the increase of molecular weight [171]. When the high molecular weight of PEG was used, such as PEG 1000, 3400 and 8000, it adsorbed on the surface of ZnO particles by hydrogen bonding, which was formed between PEG and the –OH group of the surface of ZnO nanoparticles [65]. In the meantime, the long molecular chains wrapped around the ZnO nanoparticles and the thickness of the adsorption layer increased with the increase of molecular weight [172, 173]. Thus, with the increase of molecular weight, more surfaces of ZnO particles were confined. From the view of kinetics of crystal growth, if the crystal adsorbs the polymer on some area of its surface, the growth rate of the crystals in some certain direction will be confined and results in the changes of the morphologies of the particles with PEG with different molecular weight.

The effect of concentration of PEG 8000 on the size and morphology of zinc oxide particles was also investigated. Though it was reported that the concentration of PEG has great influence on the morphology and size of particles synthesised [65], ZnO particles with thin disc-like shape and 200 nm -400 nm in size had changed very little while 0.1 g, 0.2 g, 0.4 g and 0.6 g of PEG 8000 was added into the solution (**Figure 4.20**). This is probably because the variation of PEG 8000 in the range of 0.1 g to 0.6 g can not obviously affect the surface property of ZnO particles.

4.2.6 Effect of pH value

The morphology of zinc oxides varied with the pH value was probably due to: as pH value was less than 11, the zinc hydroxide precursors were partially dissolved and zinc oxide particles were nucleated in a heterogeneous system. As pH=11, all zinc hydroxide precursors were dissolved and a clear solution was formed, hence zinc oxide particles were nucleated in a homogeneous solution, i.e., the nucleation mechanism is different when the pH value of solution is different. Generally, the possibility of nucleation in the homogeneous solution is lower than that in heterogeneous solution [162]. Thus, the number of formed nuclei at pH=11 is less than that at pH=9 or 10. The zinc ions present in the homogeneous solution have a large freedom to move and array themselves to a more stable energy state when homogeneous nucleation occurs. Moreover, zinc oxide crystal has a positively charged Zn-(0001) surface with chemically active and a negatively charged O-$(000\bar{1})$ surface with relatively inert, which results in a growth along [0001] direction [68]. Thus, the rod-like shaped particles formed. It also can be observed that particle size of zinc oxides was increased with the increase of pH value. This is ascribed to the increase in the zinc ion concentration in solution when more zinc hydroxide precursors were dissolved when the pH value of solutions increased and more zinc atoms were supplied to zinc oxide nuclei, which resulted in an increase in the particle size of formed particles. However, zinc oxide is also an amphoteric oxide [71], which will be dissolved in strong alkaline solution (pH value is more than 12).

4.2.7 Effect of dopant

It is well known that substitutional doping can improve the property of semiconductor metal oxide [174], and it can also affect the morphology and size of particles [52, 175]. The particle size of AZO nanoparticles decreased significantly with the increase of aluminium content from 200 nm for 1.0 at% of aluminium to 50 nm for 10.0 at% of aluminium by the hydrothermal method (**Figure 4.24** and **Figure 4.25**). It could be attributed to the dopant of aluminium atoms act as an impurity in the synthesis process, which may influence the size and morphology of a given particle by participating in the nucleation and growth, and the nucleation rate could be increased with the increase of aluminium content [177]; on the other hand, the particle growth during processing was prevented by resistance of the motion of grain boundaries via the secondary phase such as Al_2O_3, which might occur at more than 1.0 at% of aluminium because the limitation of solubility of Al in zinc oxide is 0.8 at% [38]. When the moving boundaries were obstructed, the secondary phase gave a retarding force on the boundaries and this force opposed the driving force of grain growth, hence the crystallite size decreased [176]. It can also be seen that the morphology of zinc oxides synthesised using the hydrothermal method was changed from rod-like shape to spherical shape with addition of aluminium dopant, which is probably because aluminium atoms adsorb on the surface of crystal faces and modify the relative energy of the different crystal faces, thus resulting in the crystal morphology changed [177, 178].

Chapter 5 FABRICATION OF THIN FILMS

The ITO and AZO thin films were prepared via sol-gel technique by dip coating method. The effects of fabrication conditions including different sols, which were prepared using various starting salt concentrations, solvent, additive and dopant contents, different withdrawal speeds and number of deposit layer, different heat treatment temperatures and time, on the quality and properties of thin films produced were investigated.

5.1 Fabrication of ITO thin films

5.1.1 Effect of annealing temperatures

Thermal behaviour of the precursor sol consisting of indium chloride and tin chloride dissolved in 2-methoxyetbanol based solvent was presented as plots of TG-DSC results in **Figure 5.1**.

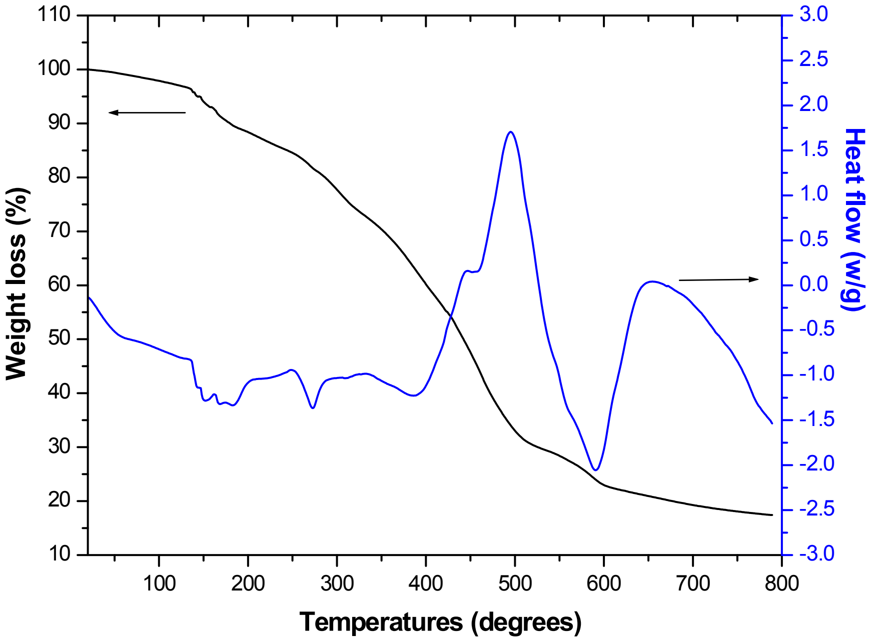

Figure 5.1 TG-DSC curves of ITO thin films.

The wide endothermic peak was observed between 144 °C and 192 °C, and the weight loss of the sol was around 10% at 190 °C, which was attributed to the evaporation of residual water and solvent. Another endothermic peak at 272.5 °C was presented, accompanied with another 10% weight loss, which was owing to the thermal decomposition of the organic component in the sol. When the temperature reached 500°C, a further weight loss of 50% was observed, together with an exothermic peak at 500 °C. This was attributed to the crystallisation of indium tin oxide. Moreover, there was an endothermic peak detected at 589 °C with weight loss of 5% at 600 °C, which was possibly due to residual organic component being burnt out.

The crystallinity of the thin films after heat treatment at different temperatures was characterised using X-ray diffraction. The XRD results are shown in **Figure 5.2**.

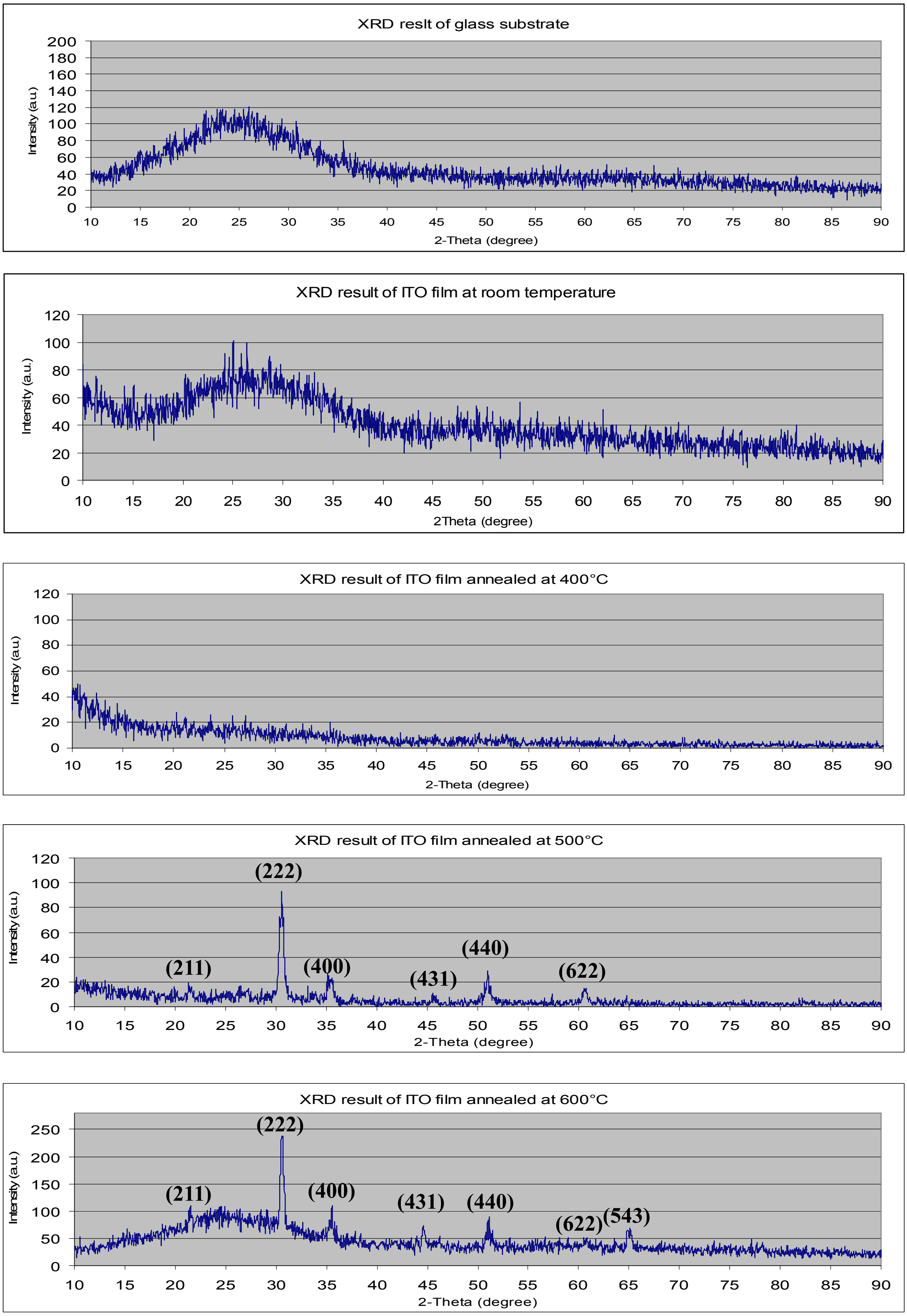

Figure 5.2 XRD results of the ITO thin films annealed at different temperatures.

For comparison, a bare glass substrate sample was also analysed and shown in **Figure 5.2**. It can be seen that there was no diffraction peak detected for the bare glass substrate and the ITO thin film samples until the temperature reached 500 °C. The analysis of X-ray patterns of the thin films revealed that the detected peak at $2\theta = 30.6°$, $35.6°$ and $51.1°$ corresponded with those of ITO standard pattern[179], i.e., three intense peaks were found at (222), (400) and (440). It was also observed that the intensities of these peaks were increased slightly after heat treatment at 600 °C, probably resulting from a slight increase of the crystallinity of the ITO thin film.

The transmittance of 3-layered ITO thin films annealed at different temperature ranging from 400 °C to 600 °C for 60 min in air was shown in **Figure 5.3**. It can be seen that, in the range of visible light (wavelength: 400 nm – 700 nm), the transmittance of the ITO thin films increased with the increase of annealing temperature. At 550 nm, the transmittance of thin film was 81.5% for annealed at 400 °C, 83.7% for 450 °C, 85.8% for 500 °C, 87.1% for 550 °C and 88.3% for 600 °C, respectively. The increase in optical transmittance with annealing temperature is mainly attributed to the increase of structural homogeneity and crystallinity of ITO in the film.

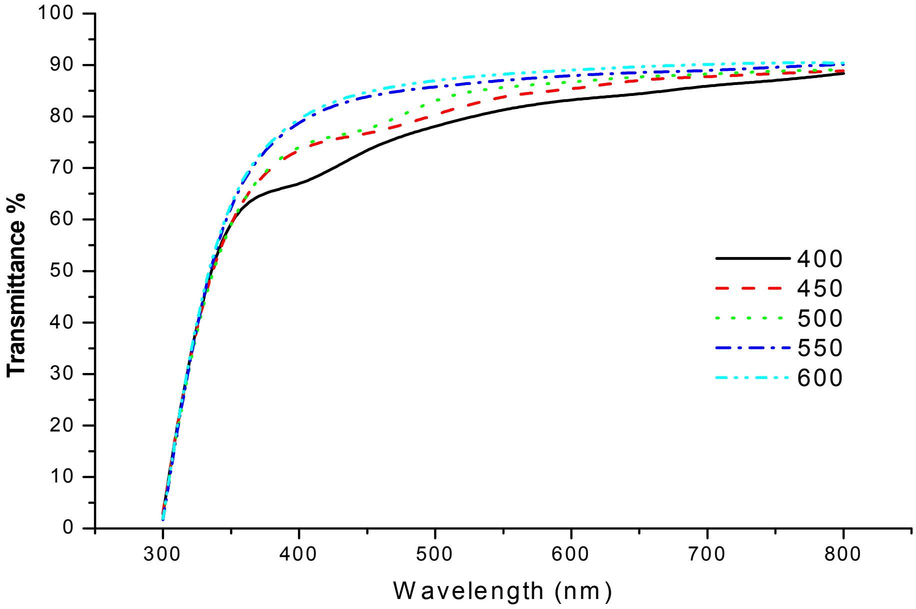

Figure 5.3 Transmittance of ITO thin film annealed at different temperatures.

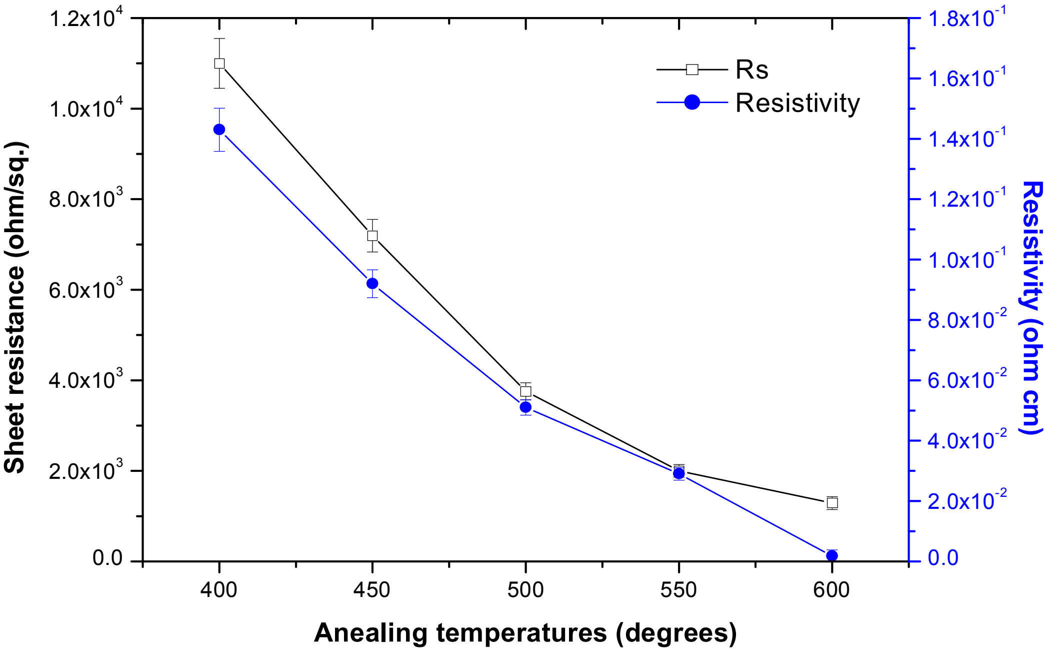

Figure 5.4 Sheet resistance and resistivity of ITO thin films annealed at different temperatures.

Figure 5.4 shows the sheet resistances and resistivities of ITO films as a function of annealing temperatures. It was observed that the sheet resistance of ITO thin films decreased from 110 kΩ/□ to 3.77 kΩ/□ as the annealing temperature increased from 400 °C to 500 °C, which decreased further to 1.33 kΩ/□ when the annealing temperature was up to 600 °C. The resistivity of ITO thin films decreased from 1.43×10^{-1} Ω•cm to 1.80×10^{-3} Ω•cm when the annealing temperature increased from 400 °C to 600 °C. The decrease in sheet resistance and resistivity with the increase of the annealing temperature probably due to may the increase of the grain size of ITO thin films with increasing annealing temperature (**Table 5-1**), leading to the reduction of the grain boundary scattering and enhancing conductivity[180].

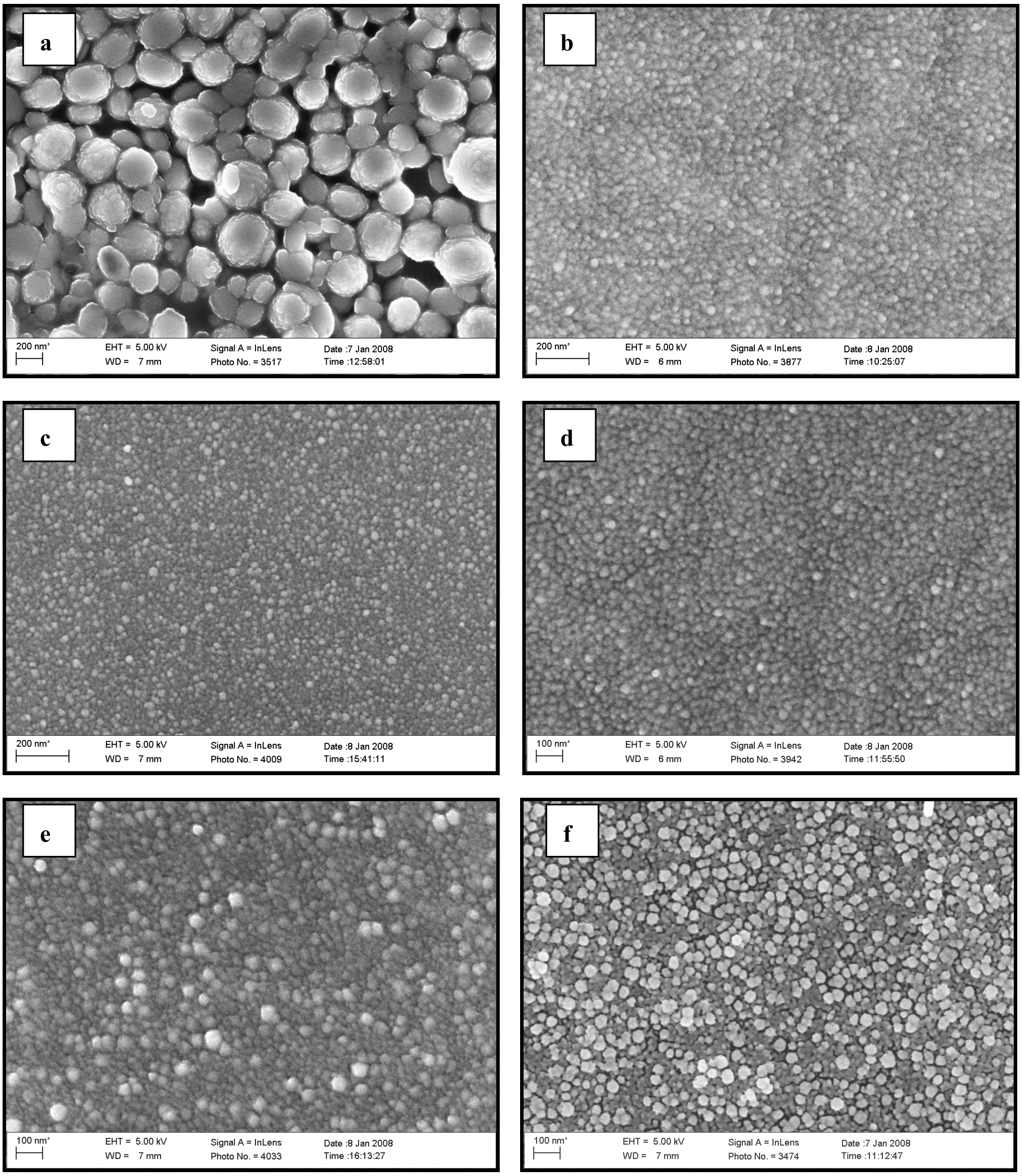

Figure 5.5 SEM micrographs of ITO films annealed at varying temperatures: a) RT, b) 400 °C, c) 450 °C, d) 500 °C e) 550 °C and f) 600 °C.

Table 5-1 Grain size of ITO thin films annealed at different temperatures.

Temperature (°C)	400	450	500	550	600
Grain size (nm)	23	22	31	39	44

5.1.2 Effect of annealing time

The transmittance and the sheet resistance/resistivity of 3-layered thin films annealed at 600°C for varying annealing time (from 0 min to 240 min) were measured and shown in **Figure 5.6** and **Figure 5.7**, respectively. The transmittance of the thin film without heat treatment was around 90% in the visible region. The highest transmittance of 91% at 550 nm was measured as the annealing time was set for 30 min. Then, the transmittance decreased to 85% when the annealing time was 60 min. However, further increase of the annealing time to 240 min, the transmittance increased to 89.3% at 550 nm. The sheet resistance of ITO thin films (**Figure 5.7**) decreased significantly from 9.71 kΩ/□ to 1.75 kΩ/□ for annealing time from 30 to 60 min. But it increased to 4.43 kΩ/□ when the annealing time was up to 240 min. The similar tendency was observed for the resistivity varied with annealing time. It appears that the sheet resistance and the resistivity of the thin films were related to the heat treatment conditions and the optimum time for annealing ITO thin film at 600 °C was 60 min. The grain size vaired with the annealing time was summarised in **Table 5-2.** It can be seen that grain size was increased from 26 nm to 50 nm when the annealing time was increased from 30 min to 240 min.

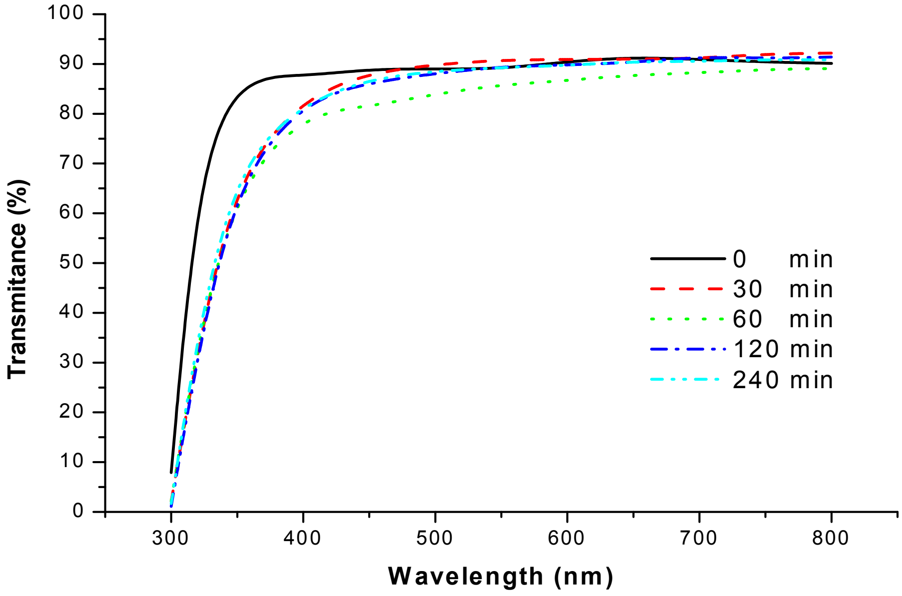

Figure 5.6 Transmittance of ITO thin films annealed for different durations

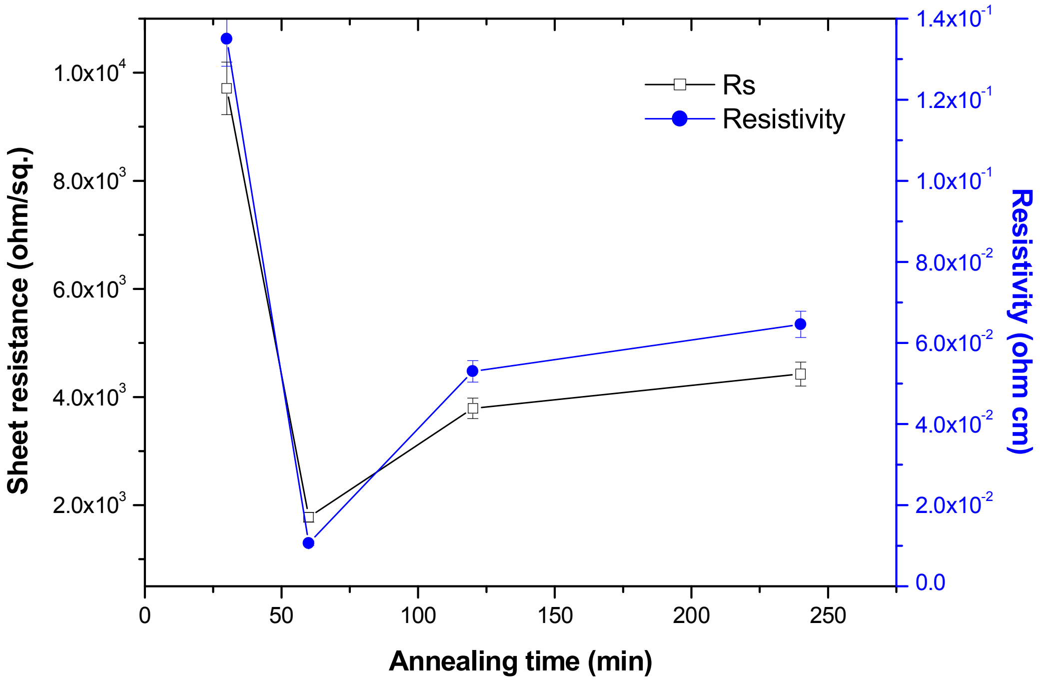

Figure 5.7 Sheet resistance and resistivity of ITO thin films annealed for different durations

Table 5-2 The summary of grain size varied with annealing time

Time (min)	30	60	120	240
Grain size (nm)	26	44	46	50

5.1.3 Effect of starting salt concentration

The effects of starting salt concentrations (0.3 mol/L, 0.6 mol/L, 1.0 mol/L and 2.0 mol/L) on the transmittance, sheet resistance and resistivity of single-layer ITO thin films annealed at 600 °C for 60 min were shown in **Figure 5.8** and **Figure 5.9**. It can be seen that both the transmittance and the sheet resistance of the thin films were decreased with the increase of the concentration of the starting salt. The transmittance of film was 84.7% at 550 nm at 0.3 mol /L sol, which was decreased to 48.5% at 2.0 mol/L. The sheet resistance and the resistivity were also decreased from 5.49 kΩ/□ for 0.3 mol /L to 0.41 kΩ/□ for 2.0 mol /L, from 3.5×10^{-2} Ω•cm for 0.3 mol /L to 9.3×10^{-3} Ω•cm for 2.0 mol /L, respectively. This could have resulted from the increase of thickness of the thin films from 65 nm for 0.3 mol /L to 227 nm for 2.0 mol /L (**Table 5-3**). The surface morphology was also changed when the concentration of starting salt was changed (**Figure 5.10**). Therefore, in order to get the ITO films with high transparency and low sheet resistance, the concentration of starting salt is suggested to be less than 1.0 mol/L.

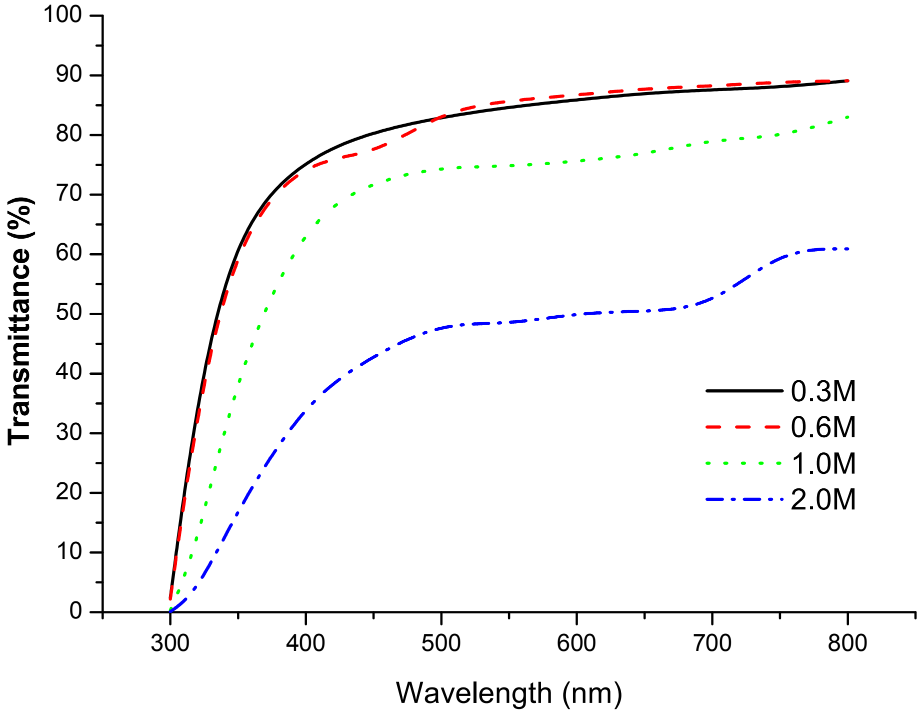

Figure 5.8 Transmittance of ITO thin films prepared using different concentrations of starting salt

Table 5-3 The thickness of ITO thin films prepared using different concentrations of starting salt

Concentration of starting salt (mol/L)	0.3	0.6	1.0	2.0
Thickness (nm)	65	89	117	227

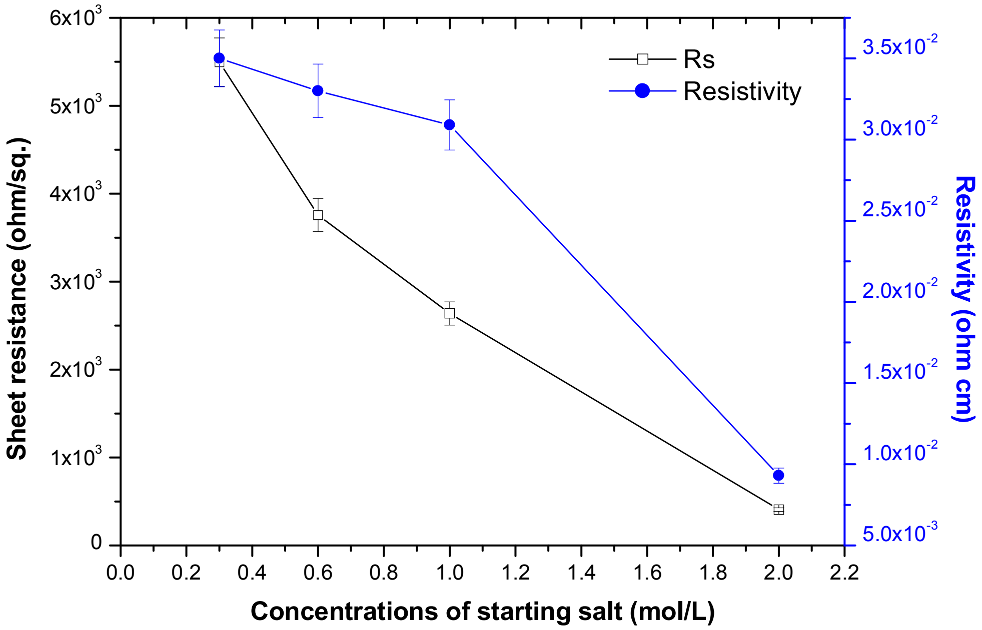

Figure 5.9 Sheet resistance and resistivity of ITO thin films prepared using different concentrations of starting salt

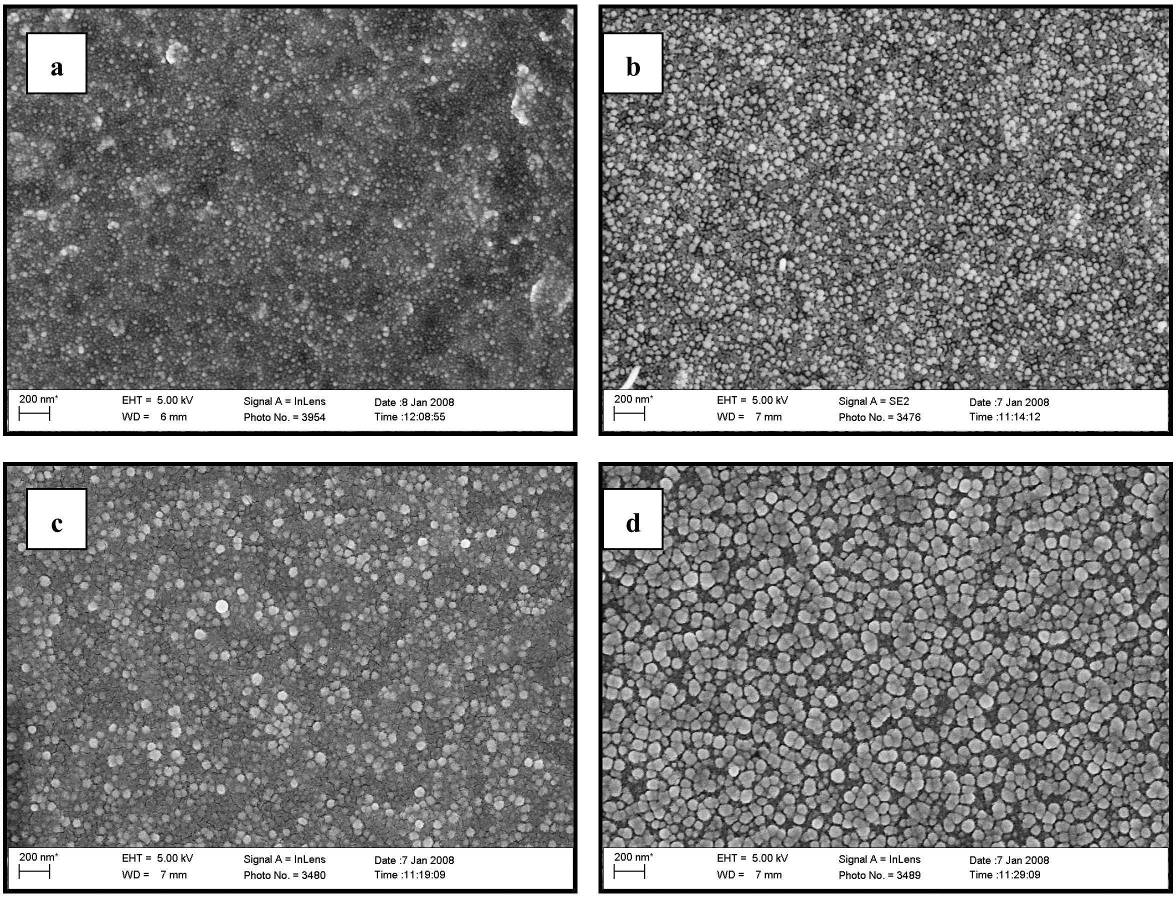

Figure 5.10 SEM micrographs of ITO films fabricated using varying concentrations of starting salt: a) 0.3 mol/L, b) 0.6 mol/L, c) 1.0 mol/L and d) 2.0 mol/L.

5.1.4 Effect of MEA content

Additives such as monoethanolamine (MEA) can assist precursors to dissolve quickly at room temperature and make solutions stable for a long time without precipitation [97,100]. They themselves are stable during hydrolysis-polymerisation reactions and can help form uniform and dense oxide films without affecting qualities of TCO thin films. The molar ratios (r) of MEA to $InCl_3$ were set at 0.1, 0.5, 1.0, 2.0 and 5.0 to study the effect of MEA content on the properties of thin films. **Figure 5.11** shows the variation of transmittance of three-layered thin film with the content of MEA. The lower transmittance of 81.6% at 550 nm was observed while $r = 0.1$ and it reached the maximum value (89.8%) when r was increased to 0.5, and then decreased to 86.9% and 85.7% when $r = 1.0$ and 2.0, respectively. The transmittance was little improved as $r = 5.0$. For sheet resistance of thin films, it was decreased from 12.35 kΩ/□ to 2.74 kΩ/□ when r was increased from 0.1 to 1.0, and the lowest sheet resistance was achieved as $r = 1.0$ (**Figure 5.12**). However, the sheet resistance was increased to 3.44 kΩ/□ while r further increased to 5.0. The change of the resistivity with the MEA content was similar to that of the sheet resistance. The variations of transmittance and sheet resistance of thin film with different contents of MEA could be attributed to the changes of the microstructures of these thin films, as shown in **Figure 5.13**. It can be observed that many pores located between the small particles when r was 0.1, which could be scattered the visible light and increased the contact resistance and resulted in the very low transmittance and the higher sheet resistance and resistivity (**Figure 5.13**, a). Compared to the sample with $r = 0.1$, the transmittance was little improved and the sheet resistance and resistivity were decreased sharply, which was attributed to the pores decreased significantly (**Figure 5.13**, b) while r was increased to 0.5. Then the particles in the thin film were grown up and the lowest sheet resistance and resistivity were achieved as the $r = 1.0$. However, when further increasing of MEA ($r = 2.0$ and 5.0), the sheet resistance and resistivity were increased. It can be considered that more organic compounds existed in the thin films during fabrication, which was removed in the heat treatment and left more pores when the film annealed at high temperature, as shown in the SEM micrographs shown in **Figure 5.13** d and e.

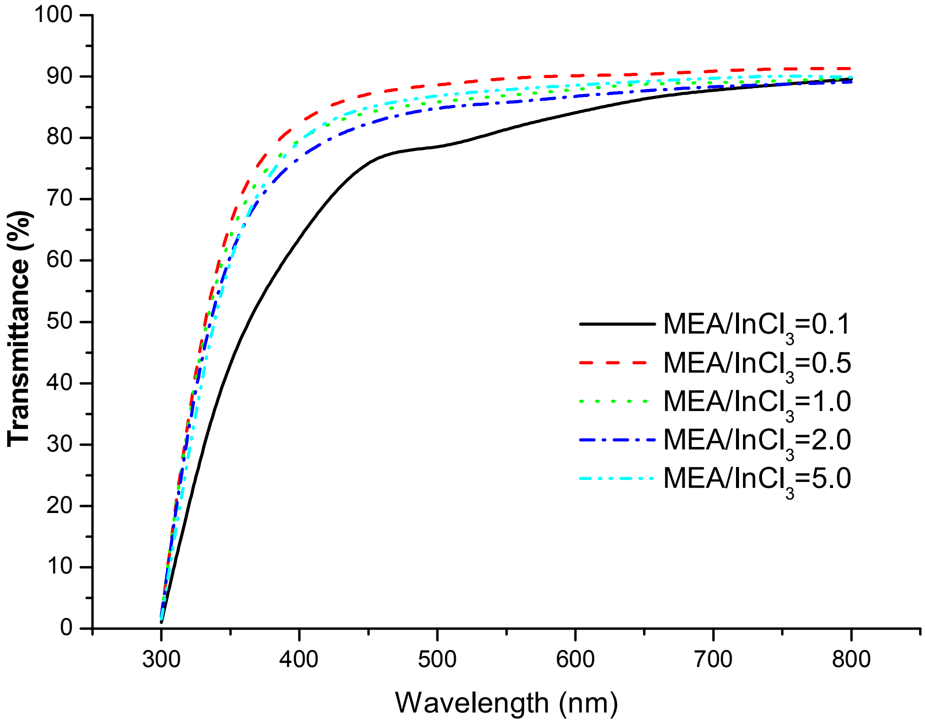

Figure 5.11 Transmittance of ITO thin films prepared with different molar ratios of MEA to $InCl_3$.

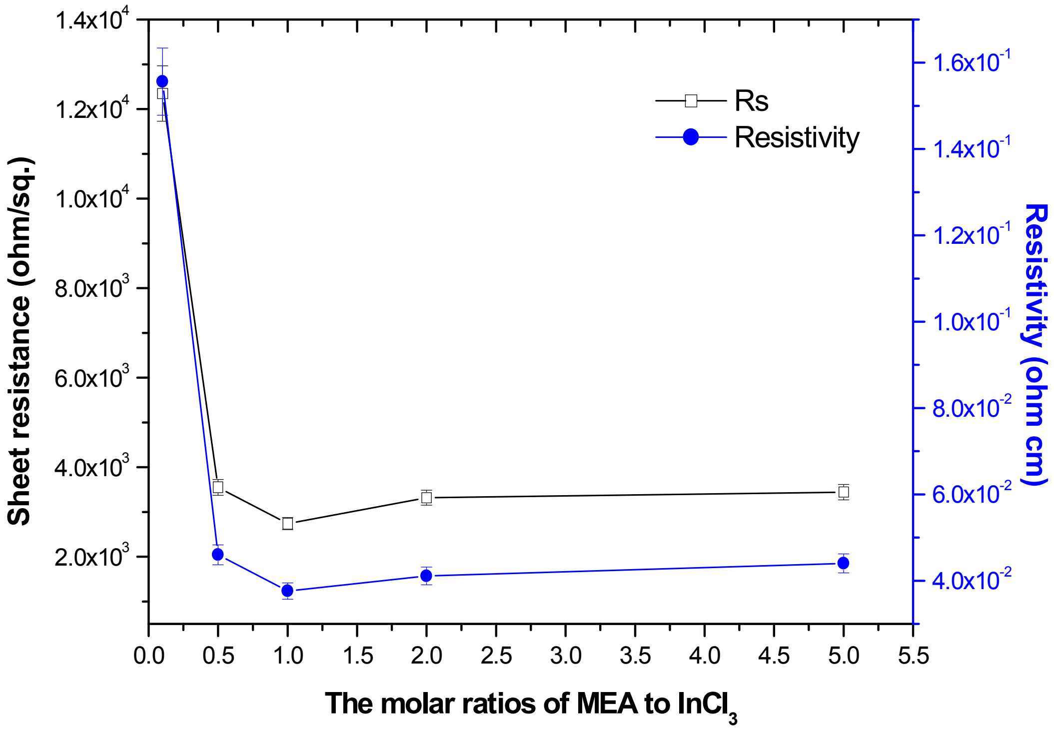

Figure 5.12 Sheet resistance and resistivity of ITO thin films prepared using different molar ratios of MEA to $InCl_3$

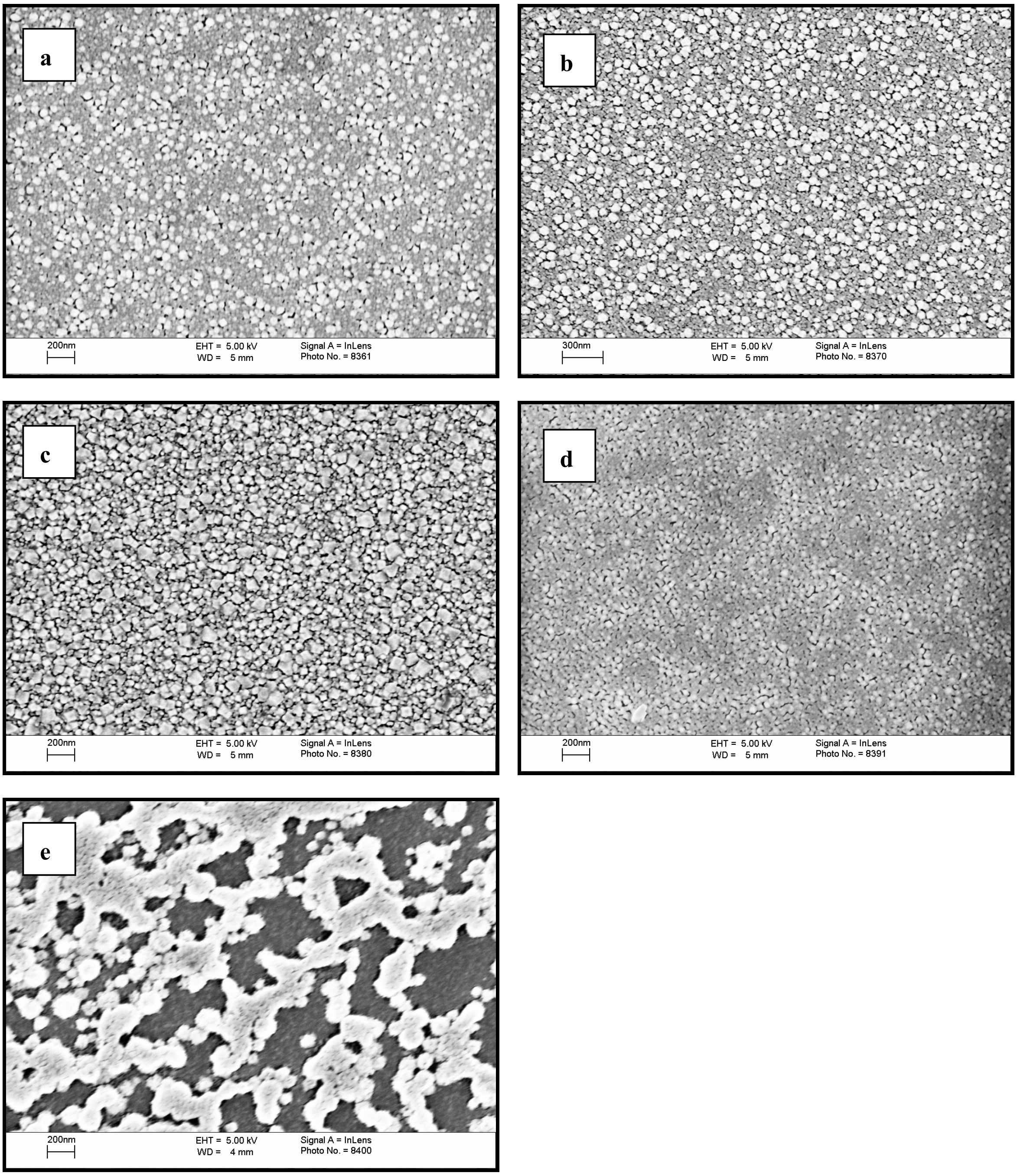

Figure 5.13 SEM micrographs of ITO thin films with varying contents of MEA (MEA/$InCl_3$ in molar ratio): a) 0.1, b) 0.5, c) 1.0, d) 2.0 and e) 5.0, respectively.

5.1.5 Effect of dopant content

The effect of dopant content (Sn) on the properties of the ITO thin films was investigated using the 3-layered thin films and annealed at 600°C for 60 min. The transmittance was varied with the dopant content for the ITO thin films shown in **Figure 5.14**. The transmittance increased from 85.8% to 91.3% at 550 nm as the dopant content of Sn was increased from 1.0 at% to 5.0 at%. However, for heavily doped samples, 10.0 at%, 15.0 at% and 20.0 at%, the transmittance was decreased from 88.0% to 81.1% at 550 nm.

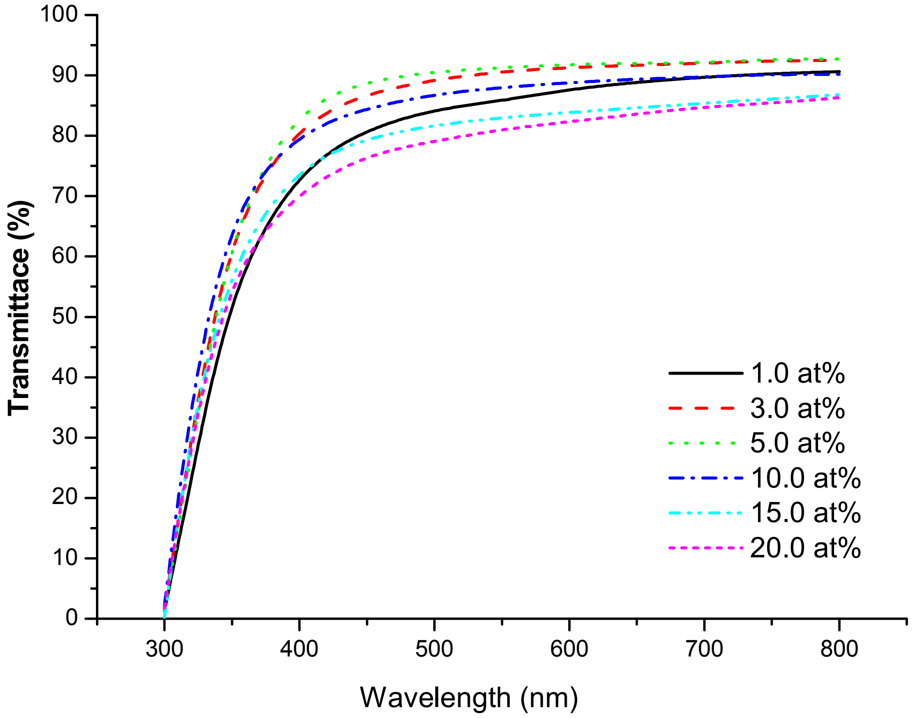

Figure 5.14 Transmittance of ITO thin films prepared with different contents of Sn

Figure 5.15 shows that the sheet resistance and resistivity of ITO thin films varied with Sn dopant contents. The result showed that the sheet resistance and resistivity had a similar shaped curve when the content of dopant was changed from 1.0 at% to 20.0 at%. The sheet resistance of the film was 19.01kΩ/□ with the Sn content of 1.0 at%, and decreased with Sn content increasing up to 10 at%, in which the sheet resistance of the ITO tin films reached the lowest value of 2.11kΩ/□. The sheet resistance started to increase again while the Sn content was further increased and reached 9.06kΩ/□ at Sn content of 20.0 at%.

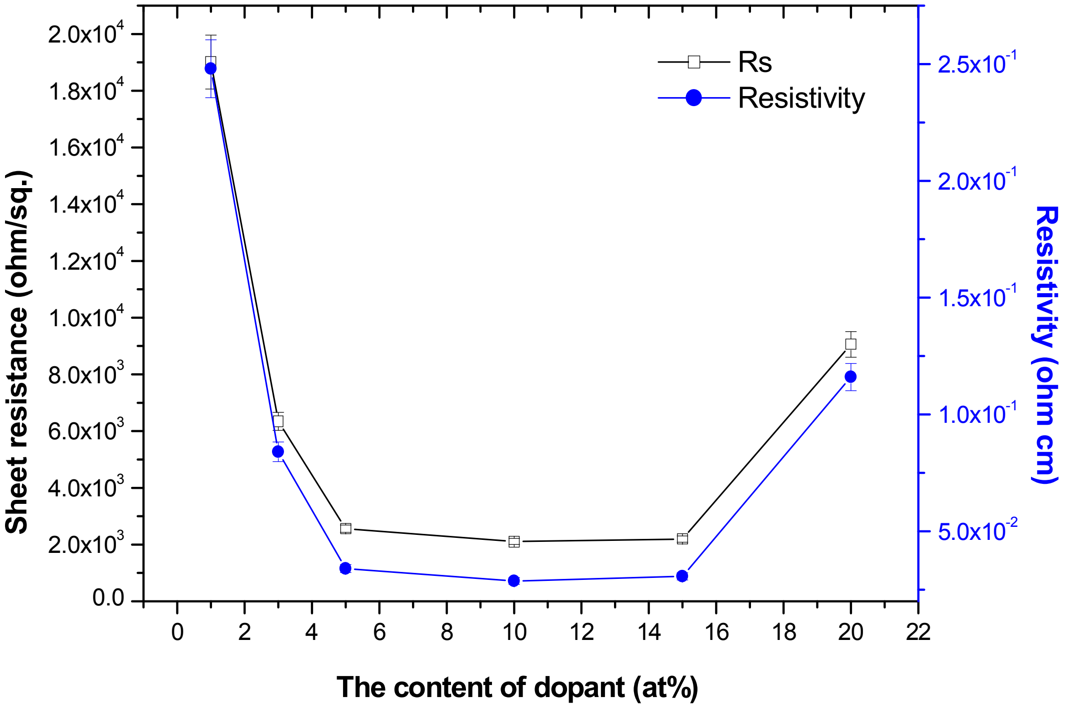

Figure 5.15 Sheet resistance and resistivity of ITO thin films with different contents of Sn

The SEM micrographs of the thin film with different content of Sn dopant were shown in **Figure 5.16**. It can be seen that all the ITO films showed uniform and consist of well-defined crystallites. The grain size of the ITO films increased as the doping level increased from 1.0 to 10 at%, which resulted in the decrease of the sheet resistance and the increase of the transmittance of the thin films (summarised in **Table 5-4**). However, with a further increase of the content of Sn to 20.0 at%, the grain size was decreased to the smallest (about 29 nm). This phenomenon can be attributed to the nucleation mechanism of the indium oxide phase. Generally, the increasing of the tin concentration will enhance the nucleation of the indium oxide phase and consequently result in the smaller crystallite size [122]. Together with the decrease of the transmittance, it may be due to the increase of scattering of photons by crystal defects created by doping and effect of grain boundaries.

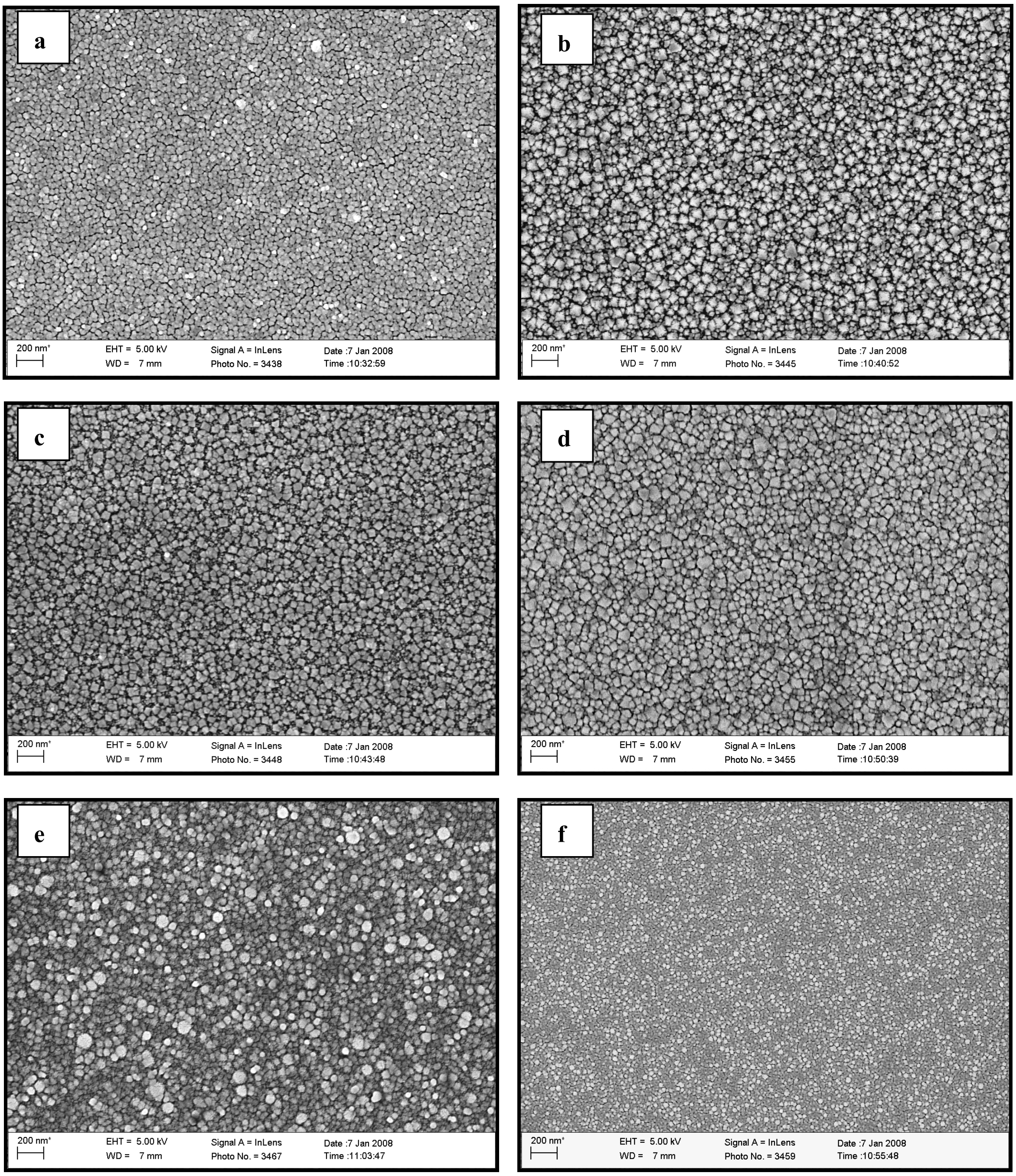

Figure 5.16 SEM micrographs of ITO thin films with different contents of Sn: (a) 1.0 at%, (b) 3.0 at%, (c) 5.0 at%, (d) 10.0 at%, (e) 15.0 at% and (f) 20.0 at%, respectively.

Table 5-4 Smmary of grain size varied with the content of dopant

The content of dopant (at%)	1.0	3.0	5.0	10.0	15.0	20.0
Grain size (nm)	47	64	64	71	57	29

5.1.6 Effect of withdrawal speed

The withdrawal speed is a factor that could affect the properties of thin films owing to the change of the thickness of the thin films.

Figure 5.17 shows the transmittance of thin films changed with the changes of withdrawal speed from 1.2 cm/min to 12.0 cm/min. The transmittance increased from 85.4% at 550 nm for 1.2 cm/min to 86.3% for 2.4 cm/min and reached the highest value of 87.3% for 5.0 cm/min. Subsequently, a decrease of the transmittance 75.8% for 12.0 cm/min was observed with the further increase of the withdrawal speed.

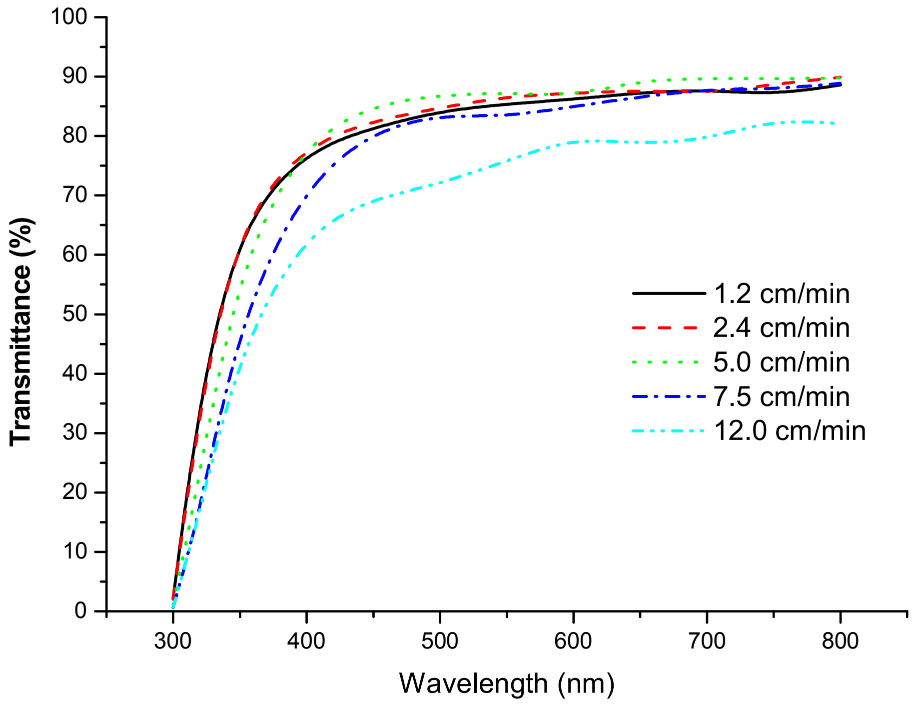

Figure 5.17 Transmittance of ITO thin films prepared with different withdrawal speeds

On the other hand, the sheet resistance and resistivity of the thin films decreased continuously when the withdrawal speed increased as shown in **Figure 5.18**. The sheet resistance sharply decreased from 4.36 to 1.43kΩ/□ when the withdrawal speed increased from 1.2 cm/min to 5.0 cm/min and to 0.77kΩ/□ at 12.0 cm/min. This can also be related to the increase of thickness with the increase of withdrawal speed according to the equation

(**2-3**) as shown in **Table 5-5,** which was measured by the cross-section of thin film (**Figure 5.19**), as both the sheet resistivity (*Rs*) and optical transparency (*Tr*) of thin film are related closely to the film thickness. Sheet resistivity can be expressed as: $Rs = \rho_{(t)}/t$, where $\rho_{(t)}$ is resistivity, and *t* is thickness of thin film. The sheet resistance decreased with the increase of the thickness of thin film. Optical transparency (*Tr*) can be calculated from the eqation [121]: $Tr = e^{-a \cdot t}$, where a is absorption coefficient, and *t* is thickness of thin film.

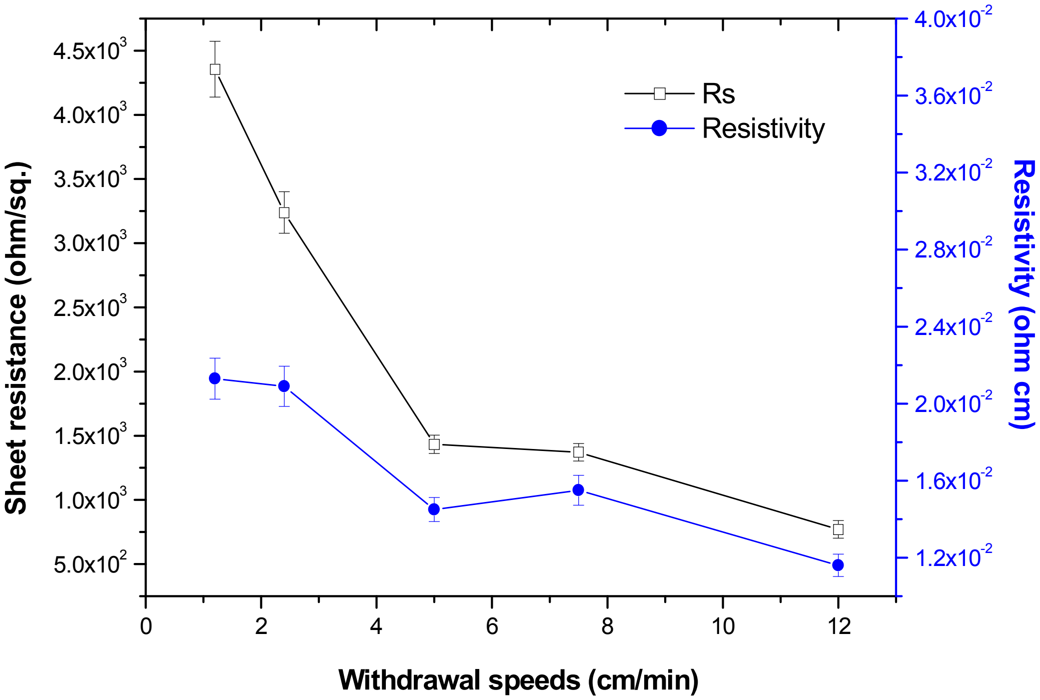

Figure 5.18 Sheet resistance and resistivity of ITO thin films prepared with different withdrawal speeds

Table 5-5 Summary of thickness of thin film varied with the withdrawal speeds

Withdrawal speeds (cm/min)	1.2	2.4	5.0	7.5	12.0
Thickness (nm)	49	86	87	113	151

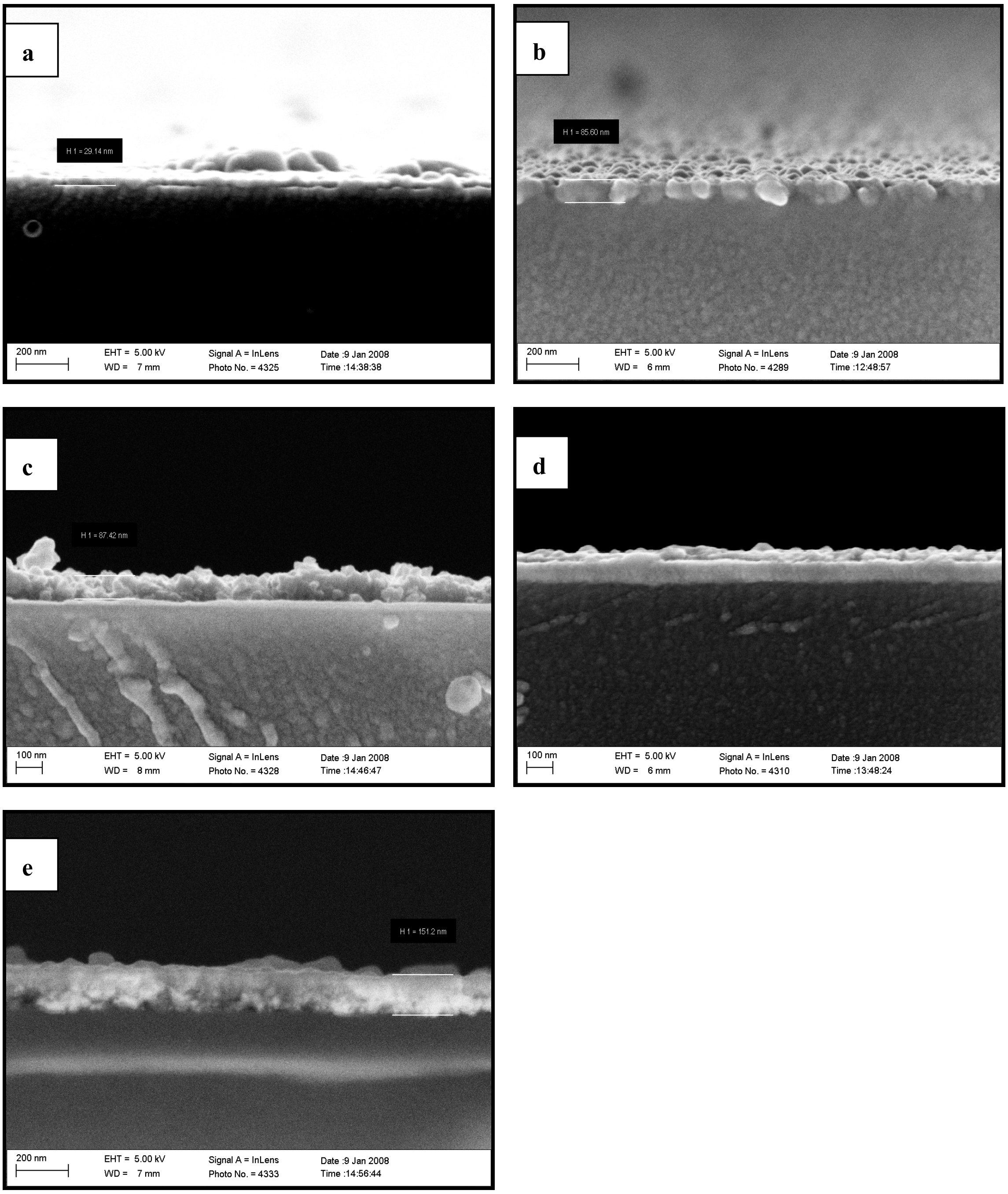

Figure 5.19 SEM cross-section images of ITO films fabricated using varying withdrawal speeds: a) 1.2 cm/min, b) 2.4 cm/min, c) 5.0 cm/min, d) 7.5 cm/min and 12 cm/min, respectively.

5.1.7 Effect of number of deposit layer

The transmittance of the multilayered ITO films versus the number of deposit layers was presented in **Figure 5.20**. The transmittance of a single layered film was 89% in the visible region and the transmittance increased to the maxium value of 90% for the 3-layered thin film. However, the transmittance was decreased to around 87.2% as the thin film was deposited with 10 layers.

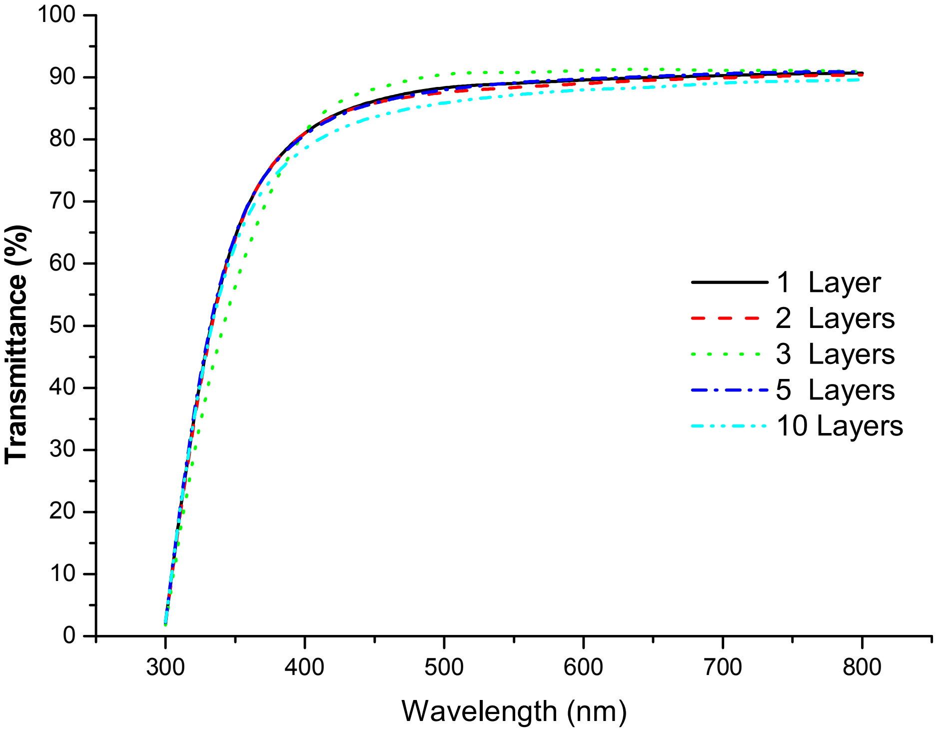

Figure 5.20 Transmittance of ITO thin films with different numbers of deposit layers

Figure 5.21 shows the variation of the ITO films sheet resistance and resistivity as a function of the number of deposit layers. It can be seen that the sheet resistance was decreased continually from 5.4 kΩ/□ for 1-layer deposition to 1.83 kΩ/□ for 10-layer deposited thin film, and the resistivity was decreased from 4.8×10^{-2} Ω•cm for 1-layered film to 3.98×10^{-2} Ω•cm for 10-layered film. This is also attributed to the increase of film thickness with the increase of number of deposit layers.

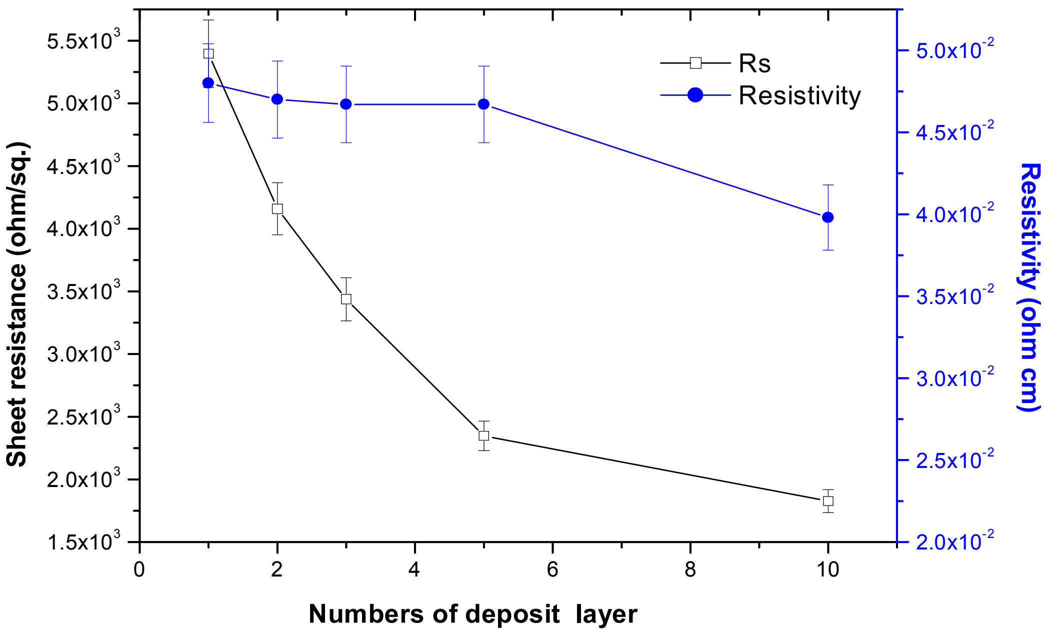

Figure 5.21 Sheet resistance and resistivity of ITO thin films with different numbers of deposit layers

The film thickness varied with the change of numbers of deposit layers was measured by the film cross-section of SEM micrographs as shown in **Figure 5.22**. The film thicknesses of 1, 2, 3, 5 and 10 layers are 89 nm, 113 nm, 136 nm, 143 nm and 218 nm, respectively (**Table 5-6**). The film thickness was increased with the increase of the number of layers. However, the thickness of 10-layered film was not as expected to be about 2 times as that of 5-layered film.

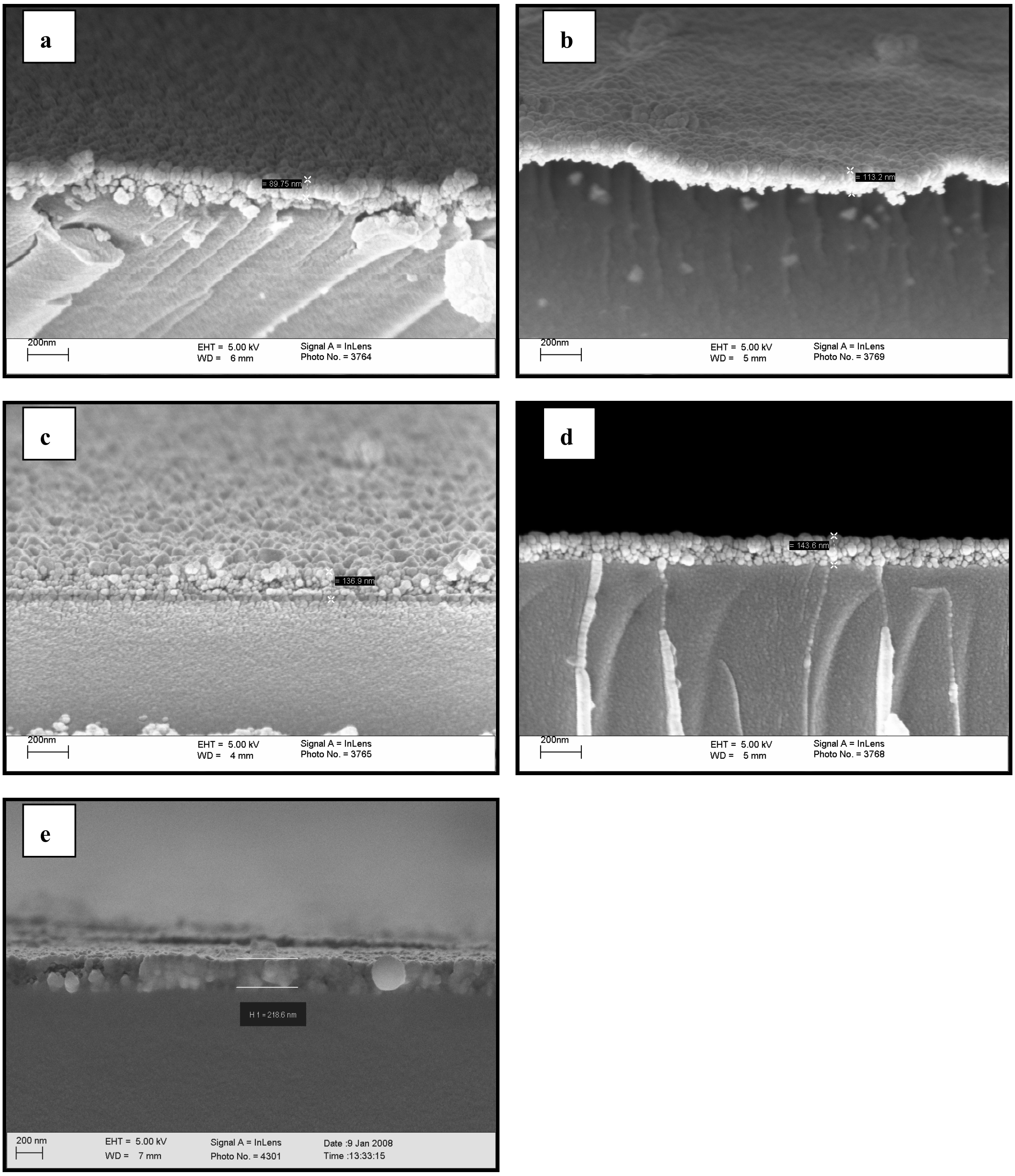

Figure 5.22 SEM micrographs of the cross-section of ITO thin film with various numbers of deposit layers: a) 1 layer, b) 2 layers, c) 3 layers, d) 5 layers and e) 10 layers.

Table 5-6 The summary of the thickness varied with the number of deposit layer

Number of deposit layer	1	2	3	5	10
Thickness (nm)	89	113	136	143	218

5.2 Fabrication of AZO thin films

5.2.1 Effect of annealing temperature

The 3-layered AZO thin films were fabricated using the concentration of 0.3 mol/L sol and the withdrawal speed of 2.4 cm/min by the dip coating method. To determine the heat treatment schedule of AZO thin films, TG-DSC analysis of the sol was carried out at the temperatures from room temperature to 550 °C at the rate of 5 °C/min. **Figure 5.23** shows a combined plot of DSC and TGA. As observed in the DSC plot several endothermic reactions took place during the heat treatment of the gel. It can be observed that a flat endothermic peak at lower temperature (at around 150 °C) was due to evaporation of water and solvents. Also, there was a sharp endothermic peak at 256.8 °C in the DSC curve and an obvious weight loss (~ 55% of the weight of sol at 270 °C) in the TG curve, which could be due to conversion of hydroxide to oxide of AZO. With the increase of the temperature, another peak was found at 320.5 °C, and, correspondingly, the weight loss was decreased to around 39% of the weight of sol at 344.4 °C and kept nearly constant over 344.4 °C, which was possibly attributed to the decomposition and elimination of the residual organic compounds.

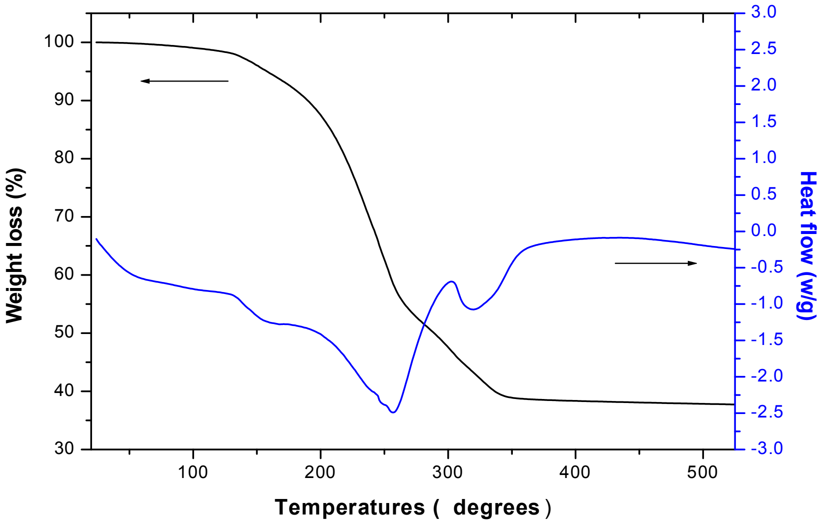

Figure 5.23 TG-DSC curves of AZO thin films

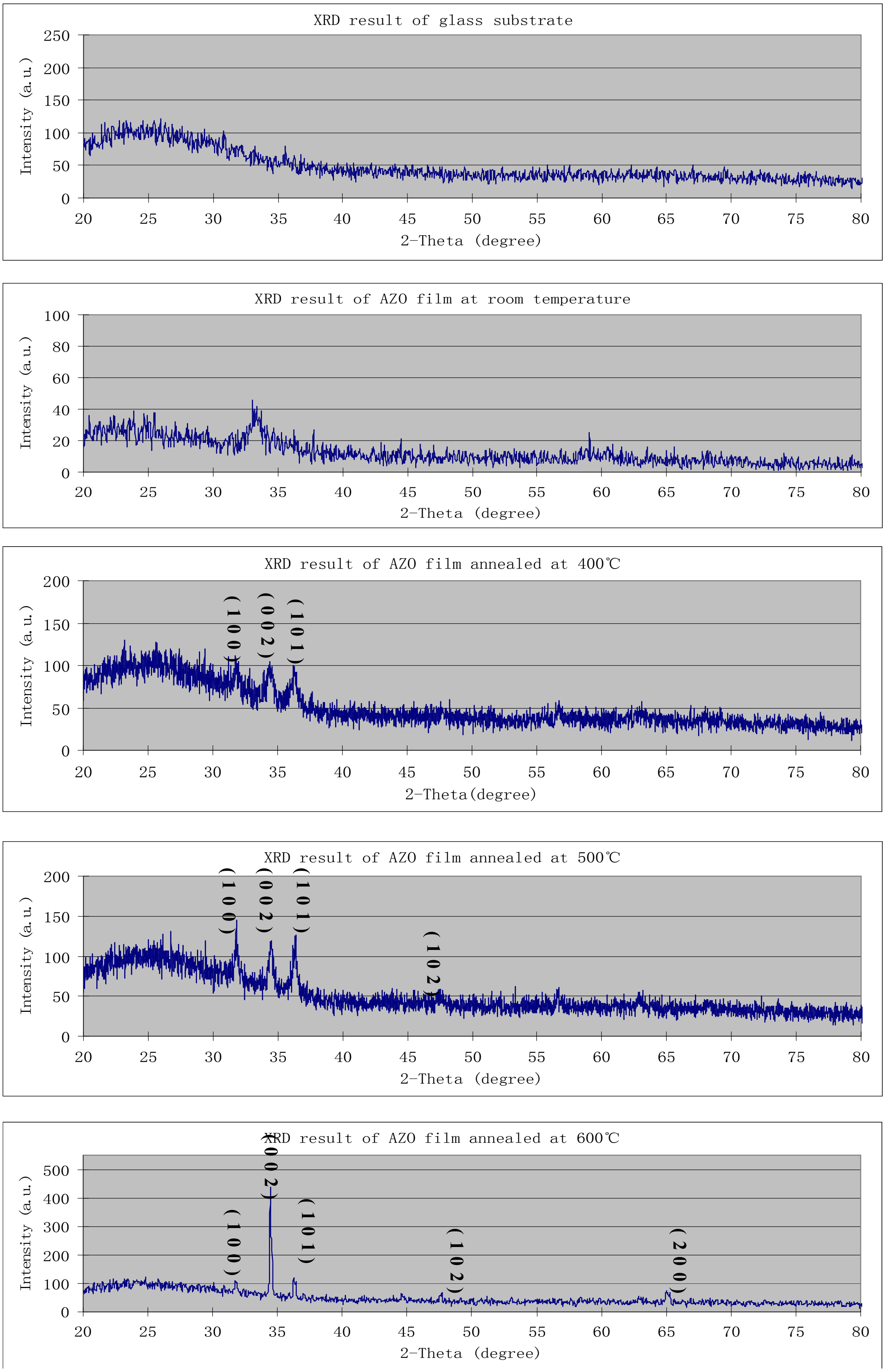

Figure 5.24 XRD results of the AZO thin films annealed at different temperatures

The crystal structures of AZO thin films with unannealed and annealed at 400 °C, 500 °C and 600 °C treated for 60 min, respectively, were detected by XRD (**Figure 5.24**). It was found that the annealing temperature played an important role in determining the crystal structure of ZnO thin films. The patterns show that the films annealed over 400 °C are polycrystalline. The intensity of the peaks was increased with the increase of annealing temperature, indicating the increase of the crystallinity of the thin films with the increase of annealing temperatures. The main peaks in the patterns could be indexed to ZnO (2θ angles are 31.77°, 34.42° and 36.25°) with hexagonal structure. No impure phases corresponding to aluminium oxide or to other aluminium compounds were detected, indicating that a solid solution of AZO was formed. The broad peaks indicate that the AZO films were composed of small nanoparticles. With the increase of the annealing temperature, the particle sizes were increased, which was also supported by the SEM micrographes of the thin films (**Figure 5.25**). The grain size varied with the annealing temperatures was summarised in **Table 5-7**.

Table 5-7 Summary of grain size varied with annealing temperatures

Temperature (°C)	400	450	500	550	600
Grain size (nm)	N/A	N/A	36	40	46

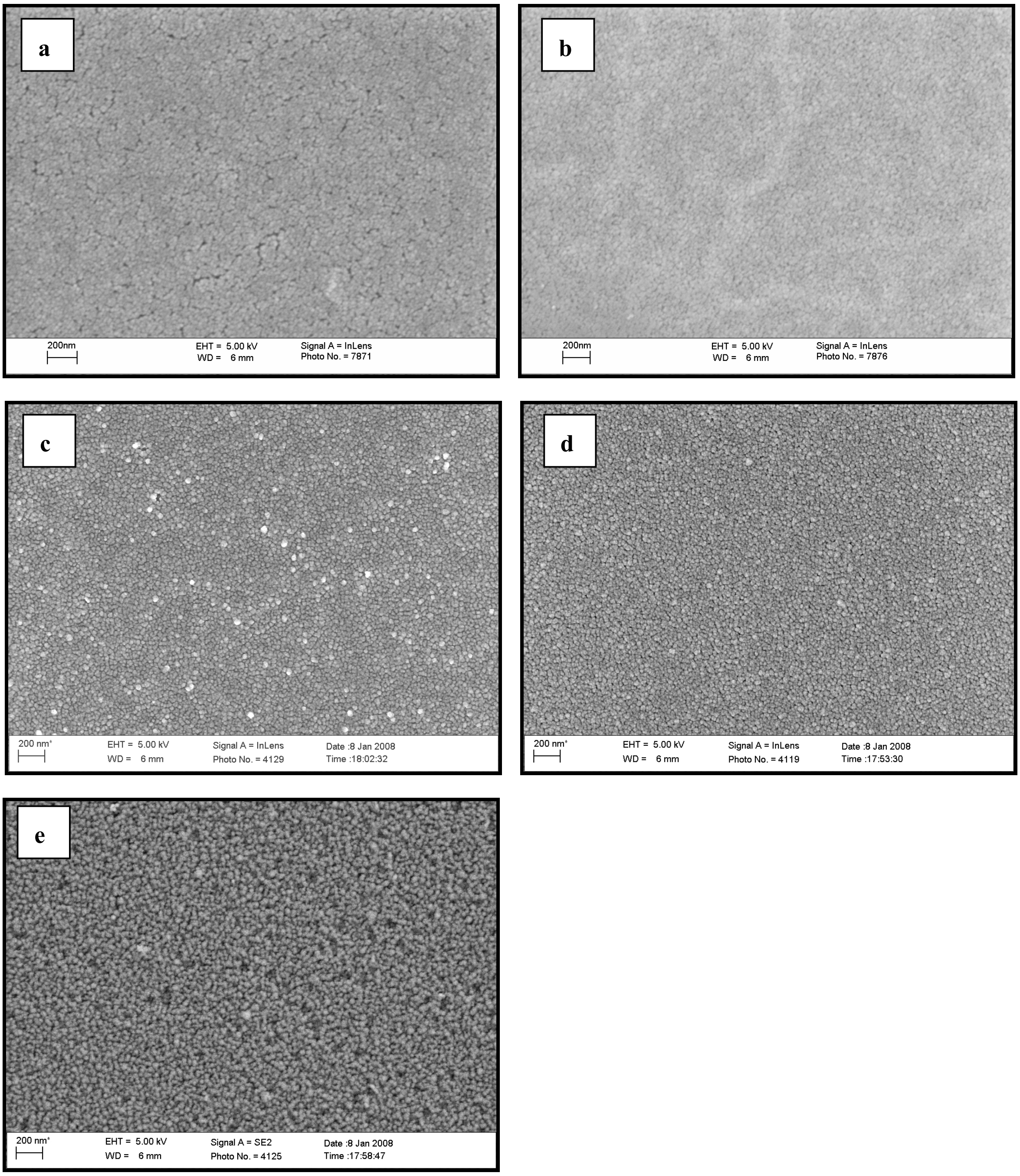

Figure 5.25 SEM micrographs of AZO thin films annealed at different temperatures: a) 400 °C, b) 450 °C, c) 500 °C, d) 550 °C and e) 600 °C.

The transmittance spectra of AZO films annealed at different temperatures were given in **Figure 5.26**. The transmittance of the film was increased from 78.4% in the visible range at 550 nm with the annealing treatment at 400 °C to around 82% when the temperatures were up to 450 °C and 500 °C where the maximum value was observed. However, the transmittance was down to 81.3% at 550 nm while annealing temperature increased to 550

°C and 600 °C. The increase in transmittance by applying the annealing treatment under 500 °C may be due to decreasing optical scattering caused by the densification of grains and the decrease of transmittance with the temperature above 500 °C could be owing to the growth of grains.

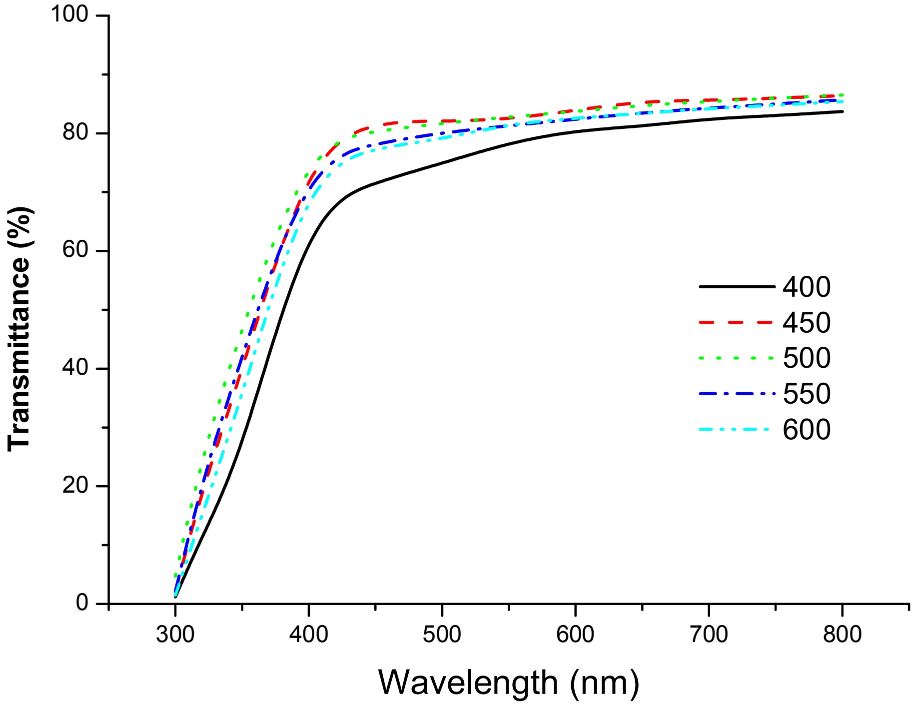

Figure 5.26 Transmittance of AZO thin films annealed at different temperatures

The sheet resistance and resistivity of thin films varied with annealing temperatures were plotted in **Figure 5.27**. The sheet resistances of thin films were 47.1 kΩ/□ and 31.9 kΩ/□ while the thin films were annealed at 400 °C and 450 °C, respectively. The lowest sheet resistance of 26.4 kΩ/□ was observed as the annealing temperature elevated to 500 °C, which was increased significantly to 89 kΩ/□ when the annealing temperature increased to 600 °C. The resistivity of the thin films with the annealing temperature showed similar trend as that of sheet resistance (**Figure 5.27**).

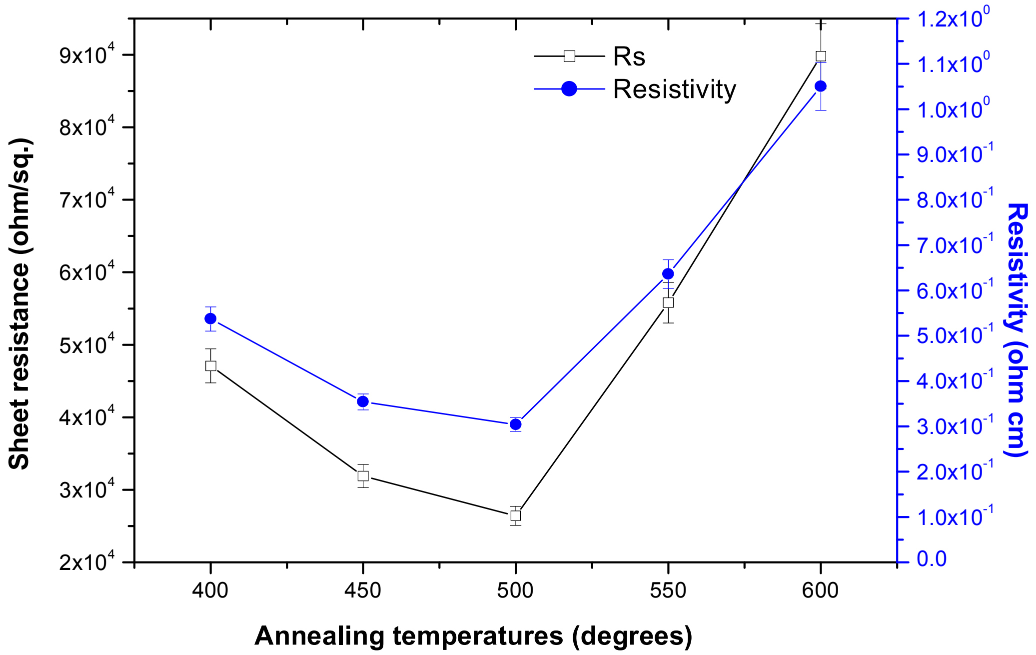

Figure 5.27 Sheet resistance and resistivity of AZO thin films annealed at different temperatures

5.2.2 Effect of annealing time

Annealing time is another important factor which affects the properties of thin film. In this section, all samples with 3 layers were prepared from 0.3 mol/L sol at the 2.4 cm/min of withdrawal speed and annealed at 500 °C for varying annealing time ranging from 30 min to 240 min. The transmittances of all sample was over 80% in the visible light range whenever the sample annealed for 30 min or 240 min (**Figure 5.28**). However, the transmittance was slightly changed with the variation of annealing time. The highest value, 84.5%, was obtained for 120 min and the lowest value of 82.1% for 30 min. On the other hand, the increase of the annealing time, from 30 min to 60 min led to a decrease in the sheet resistance from 89.5 kΩ/□ to 26.4 kΩ/□. Then the sheet resistance was increased to 79.5 kΩ/□ while annealing time prolonged to 120 min and it had little changes for further prolonging the annealing time to 240 min (**Figure 5.29**).

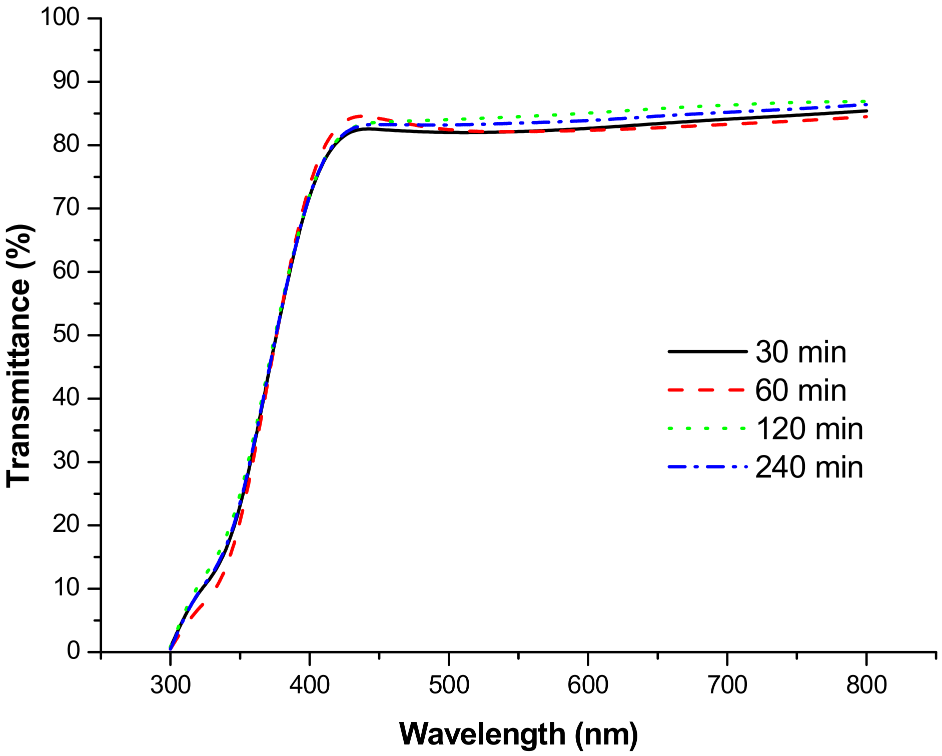

Figure 5.28 Transmittance of AZO thin films annealed for different time

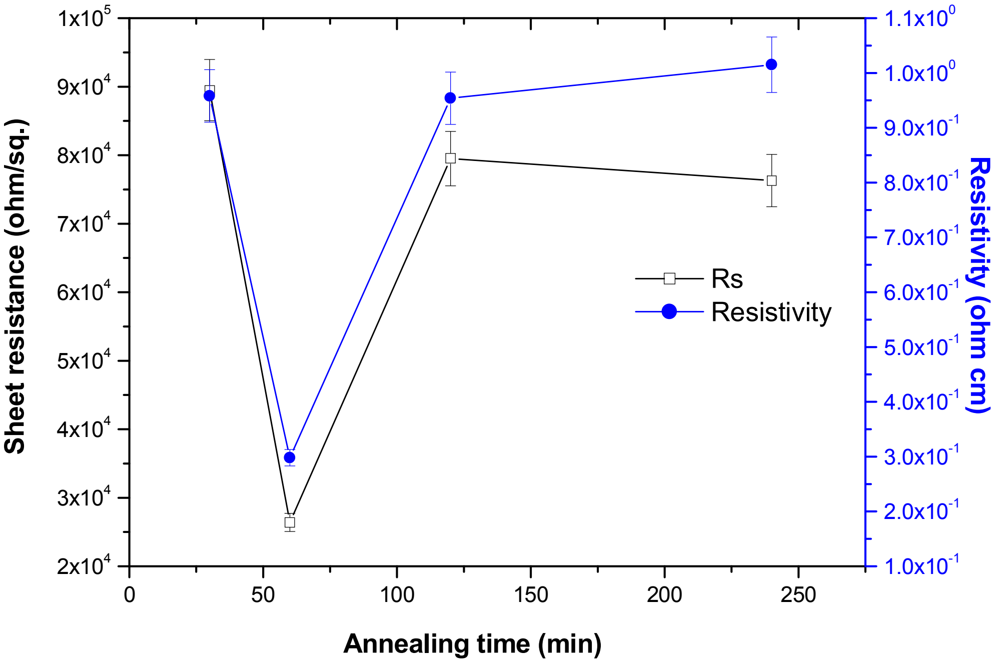

Figure 5.29 Sheet resistance and resistivity of AZO thin films annealed for different time

The grain sizes, measured from SEM images as shown in **Figure 5.30**, were increased from 32 nm to 43 nm when the annealing time was increased from 30 min to 240 min (**Table 5-8**).

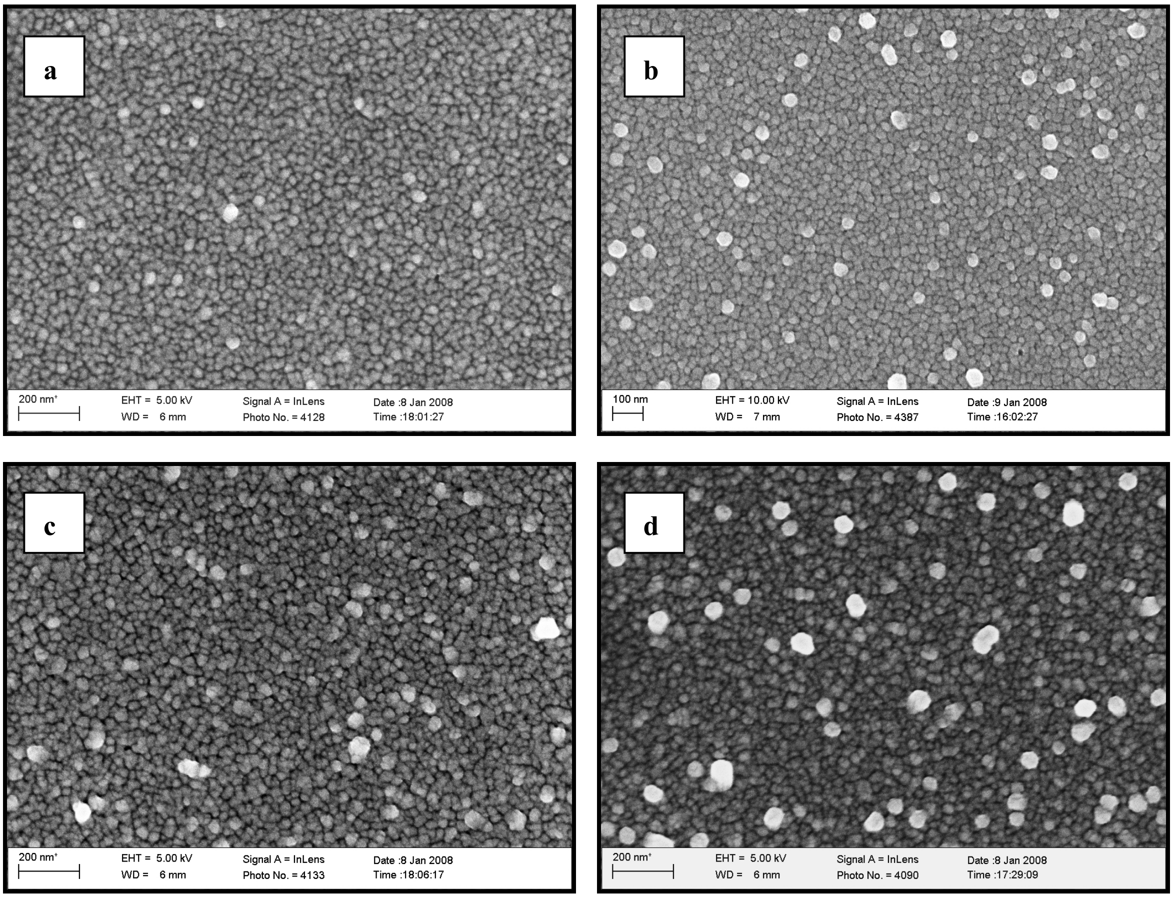

Figure 5.30 SEM micrographs of AZO films annealed at 500 °C for varying time: a) 30 min, b) 60 min, c) 120 min, d) 240 min.

Table 5-8 The summary of grain size varied with annealing time

Time (°C)	30	60	120	240
Grain size (nm)	32	36	39	43

5.2.3 Effect of starting salt concentration

In order to study the effect of sol concentration on the properties of thin film prepared by the dip coating process, the solutions of 0.1 mol/L, 0.3 mol/L, 0.6 mol/L, 1.0 mol/Land 2.0 mol/L concentration were used, and all samples were annealed at 500°C for 60 min in air. The results of transmittance, and sheet resistance and resistivity of thin films with a single layer were shown in **Figure 5.31** and **Figure 5.32**, respectively. Generally, the transmittance and sheet resistance of thin films were decreased with the increase of sol concentration. The thin film with the highest transmittance of more than 90% in the visible range and the sheet resistance of 79.6 kΩ/□ was prepared using 0.1 mol/L of sol. The transmittance was sharply decreased to 50.7% at 550 nm as the sol concentration of 2.0 mol/L was reached. However, the decrease of sheet resistance was mild. The plot showed that sheet resistance was decreased to 31.8 kΩ/□ for 1.0 mol/L and kept going a nearly level line as the sol concentration was increased to 2.0 mol/L. The resistivities of thin films, similar to the sheet resistance, were also decreased consistently with the increase of concentration. The effect of sol concentration on the properties of thin film because the higher sol concentration, with higher viscosity, which resulted in the increased thickness of thin film (**Table 5-9**). Therefore, the film thickness could be adjusted by controlling the precursor concentration.

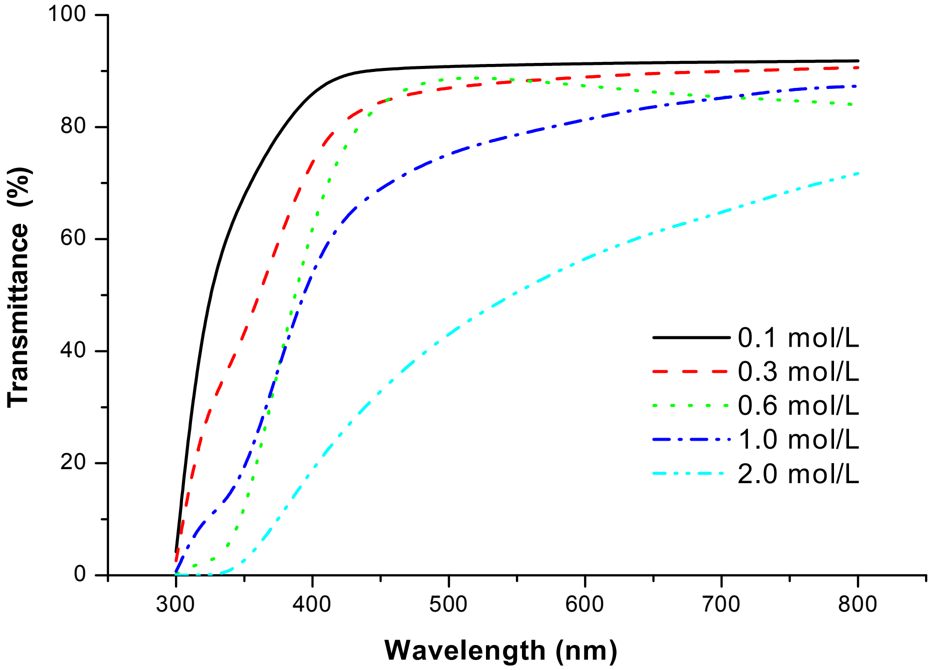

Figure 5.31 Transmittance of AZO thin films prepared using different concentrations of starting salt

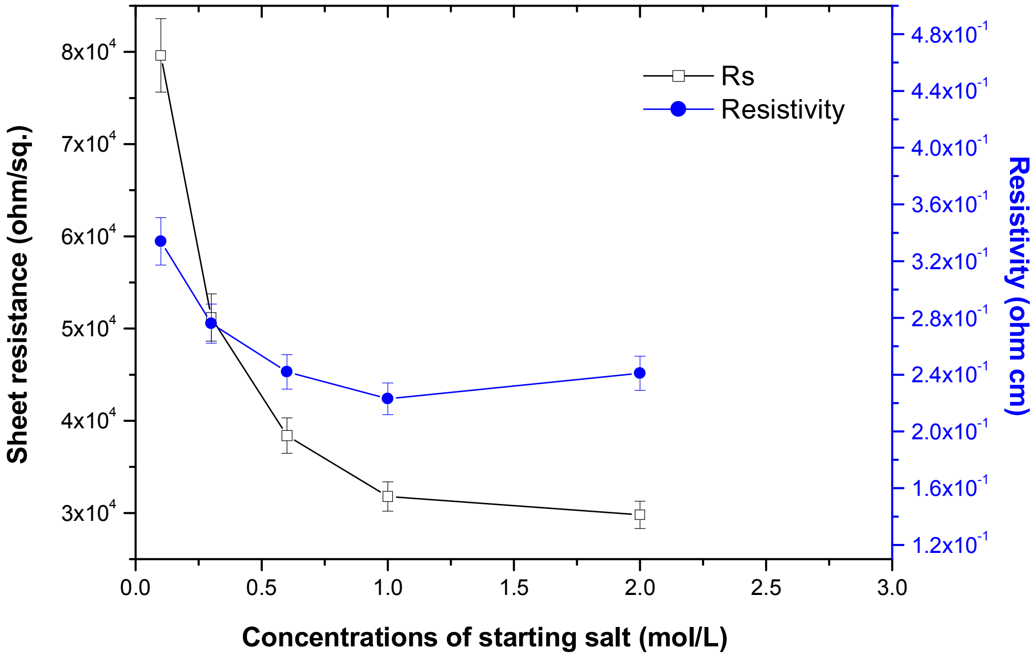

Figure 5.32 Sheet resistance and resistivity of AZO thin films prepared using different concentrations of starting salt.

Table 5-9 Thickness of AZO thin films prepared using different concentrations of starting salt

Concentration of starting salt (mol/L)	0.1	0.3	0.6	1.0	2.0
Thickness (nm)	42	54	63	70	81

5.2.4 Effect of MEA content

A comparative study of MEA effects on the transmittance and sheet resistance of AZO thin film was also investigated by comparing the deposited films from the sols prepared using various molar ratios (*r*) of MEA to Zn, which were 1/2, 1/1, 2/1 and 5/1. All samples were with 3 layers and annealed at 500 °C for 60 min. The transmittance of thin film was shown in **Figure 5.33**. The results show the thin films with high transmittance of 91.2% and 90.0% at 550 nm for r = 1/2 and 5/1, respectively. However, the sheet resistances of thin films were not detected (**Table 5-10**). The transmittance and the sheet resistance (resistivity) were 85.6% and 36.6 kΩ/□ (4.06 × 10^{-1} Ω•cm) for r = 1 and 79.6% and 9.78 ×10^{2} kΩ/□ (10.07× 10^{-1} Ω•cm) for r = 2. The surface morphologies of thin films were shown in **Figure 5.34**. The surface of thin film was tough as *r* was 0.5 (**Figure 5.34** a) and the pores located between the particles were observed while *r* was increased to 5.0 (**Figure 5.34** d).

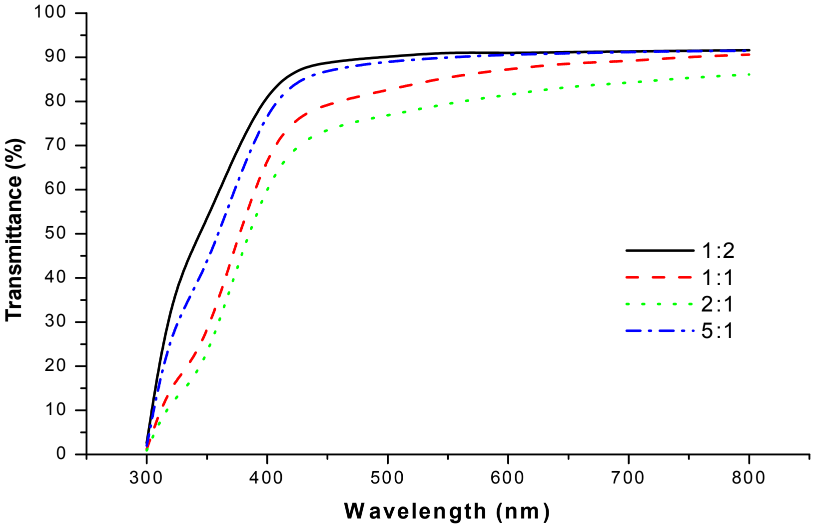

Figure 5.33 Transmittance of AZO thin films with different molar ratios of MEA to $ZnCl_2$.

Table 5-10 The variations of sheet resistance and resistivity of AZO thin films with different molar ratios of MEA to $ZnCl_2$

MEA/Zn in molar ratio	Sheet resistance (Ω/□)	Resistivity (Ω•cm)
1:2	N/A	N/A
1:1	3.66×10^{4}	4.06×10^{-1}
2:1	9.78×10^{5}	10.07×10^{-1}
5:1	N/A	N/A

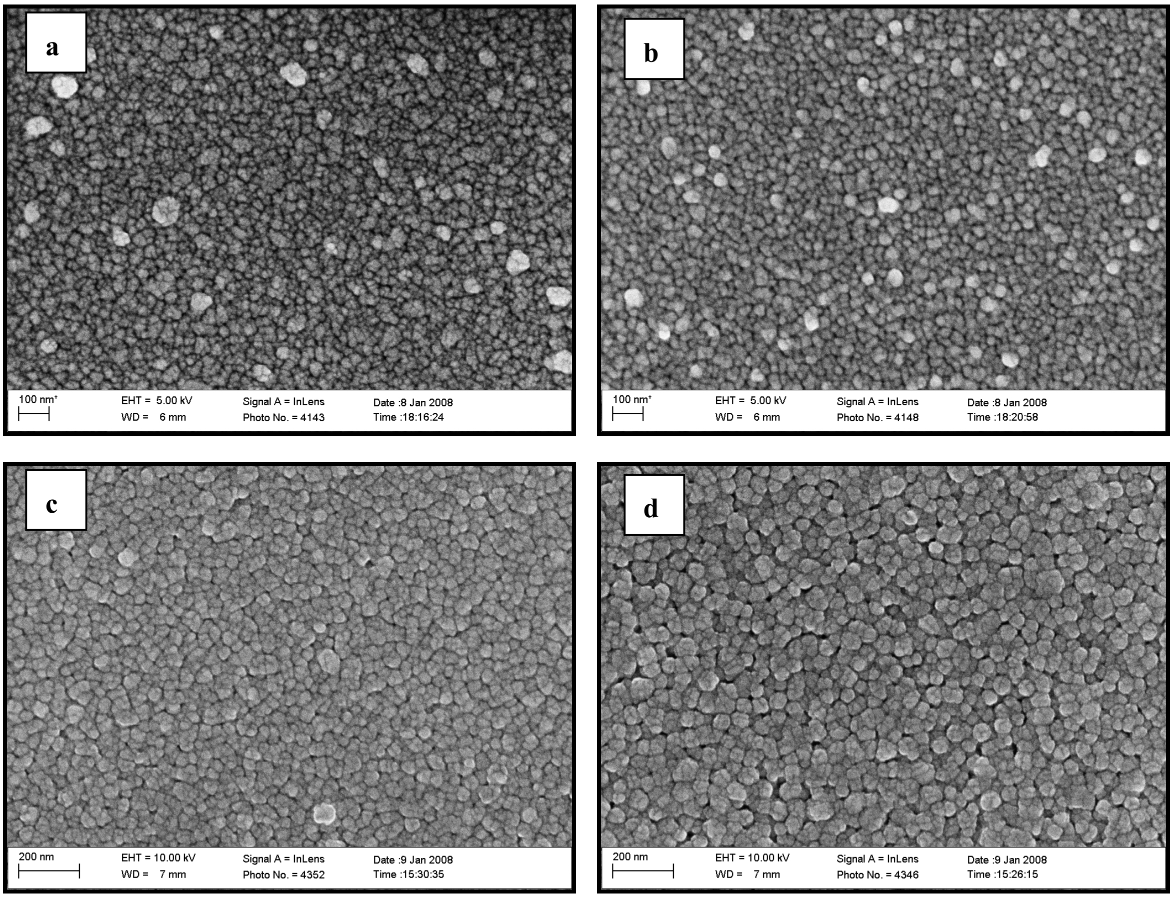

Figure 5.34 SEM micrographs of AZO thin films with varying contents of MEA (MEA/$Zn(AC)_2$ in molar ratio): a) 0.5, b) 1.0, c) 2.0 and d) 5.0, respectively.

5.2.5 Effect of dopant content

The transmittance of AZO thin film with various dopant contents was presented in **Figure 5.35**. The transmittance was 85.8% at 550 nm of wavelength for 0.5 at% of Al doped and improved to 90.7% for 1.0 at% of Al. Then, it was decreased with the increase of dopant content and the minimum value of 81.2% was obtained while the dopant content was increased up to 10.0 at%.

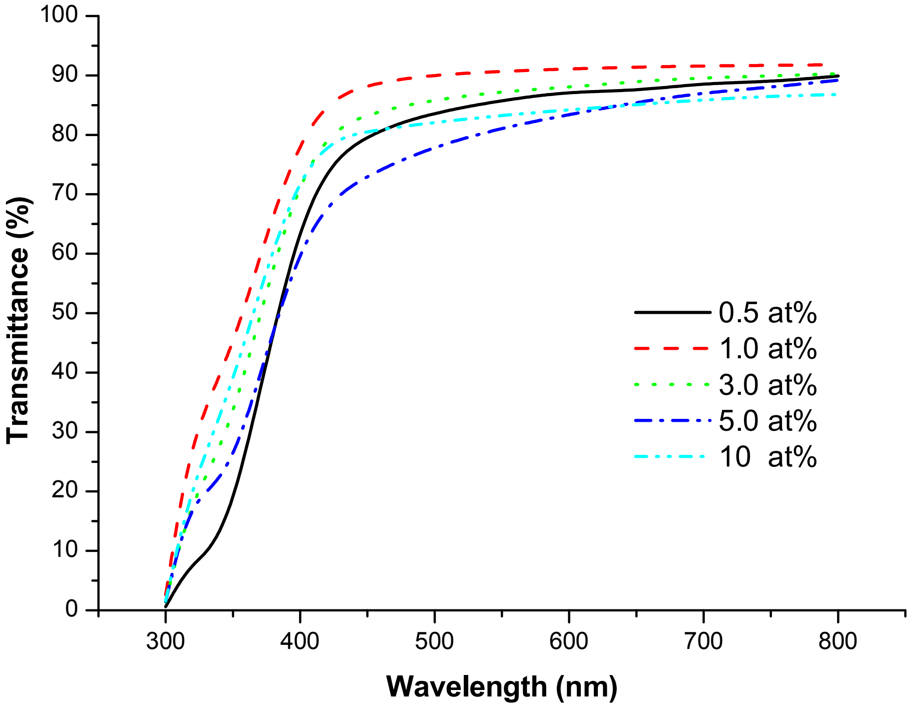

Figure 5.35 Transmittance of 3-layered AZO thin films annealed at 500 °C for 60 min using different dopant contents

The sheet resistance and resistivity variations of AZO thin films with different dopant contents were shown in **Figure 5.36**. It can be observed that the curves of the sheet resistance and the resistivity had very closed shape. The sheet resistance was first decreased from 51.2 kΩ/□ to 38.4 kΩ/□ with the increase of aluminium content which was varied from 0.5 at% to 1.0 at%. A minimum sheet resistance of 38.4 kΩ/□ was obtained at a dopant content of 1.0 at%. However, with the increase of the aluminium doping content of 3.0 at%, the sheet resistance began increasing. Then, the sheet resistance increased continuously up to 67.2 kΩ/□ for 10.0 at% of aluminium doped. The resistivity was decreased from 5.48 × 10^{-1} Ω•cm to 4.22 × 10^{-1} Ω•cm when the dopant content was increased from 0.5 at% to 1.0 at%. Then it was increased to 7.39 × 10^{-1} Ω•cm for 10.0 at% of dopant.

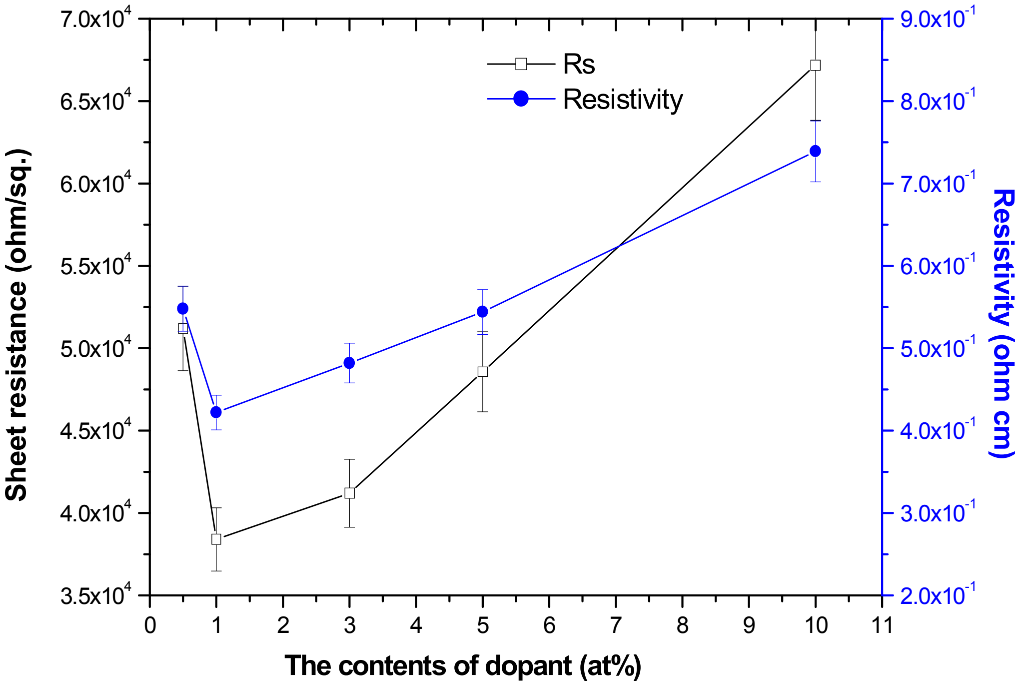

Figure 5.36 Sheet resistance and resistivity of 3-layered AZO thin films annealed at 500 °C for 60 min using different dopant contents

SEM images of AZO thin films with different contents of Al used as dopant were displayed in **Figure 5.37**. These SEM mages show that the surface morphology of the thin films was strongly dependent on the content of Al. It was shown in **Figure 5.37**, (c) that the particle size of films doped with 3.0 at% Al was somewhat larger than that of the films with other content of Al, and was also the thin film with the roughest surface. In the case of Al content less than 3.0 at%, the grain size of the film was increased with the increase of aluminium content (**Table 5-11**). However, as the aluminium content was greater than 3.0 at%, and up to 10.0 at%, the grain size was reduced with an increase in the doping content of aluminium, the microstructure of the films consisted of many round-shaped particles, and the surface became much more smooth (**Figure 5.37**(e)).

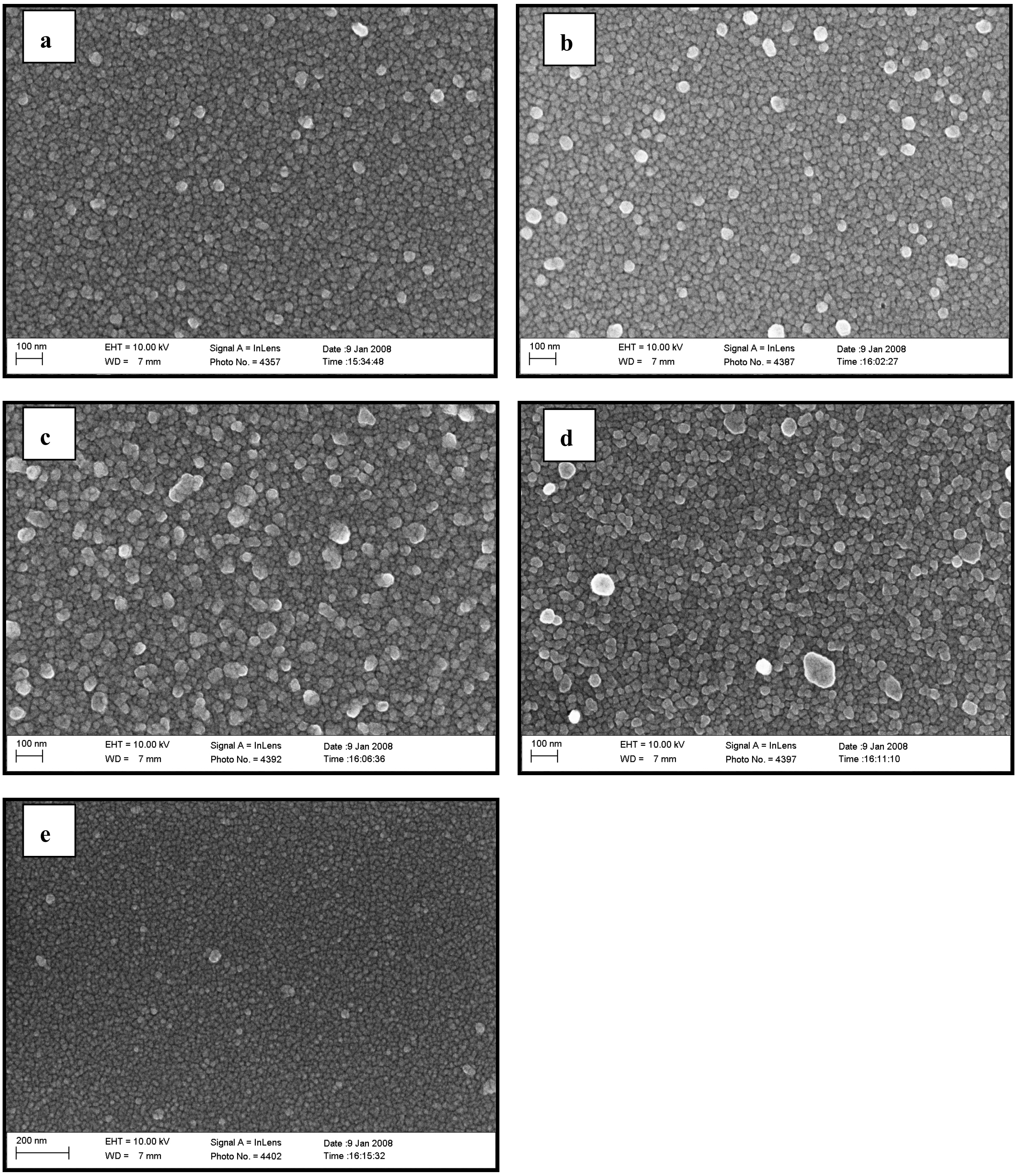

Figure 5.37 SEM micrographs of thin films with various Al contents: a) 0.5 at%, b) 1.0 at%, c) 3.0 at%, d) 5.0 at% and e) 10.0 at%, respectively.

Table 5-11 The summary of grain size varied with the content of dopant

The content of dopant (at%)	0.5	1.0	3.0	5.0	10.0
Grain size (nm)	29	36	41	35	20

5.2.6 Effect of withdrawal speed

The effect of withdrawal speed on the properties of thin films was also studied, and the transmittance varied with the withdrawal speeds was given in **Figure 5.38**. The results showed that all thin films had high transmittance which was more than 80% in visible light range. However, there were many changes of transmittance with the variations of withdrawal speed. The highest transmittance of 87.3% at 550 nm was obtained for 2.4 cm/min of withdrawal speed, which was reduced to 84.1% for the withdrawal speed of 12.0 cm/min. The variation of sheet resistance with the withdrawal speed was different from that of transmittance with the withdrawal speed (**Figure 5.39**). The sheet resistance of 38.4 kΩ/□ for 1.2 cm/min of withdrawal speed was decreased to 27.4 kΩ/□ as the withdrawal speed increased to 12.0 cm/min. Similarly, the resistivity was decreased slightly from 3.32×10^{-1} Ω•cm to 1.54×10^{-1} Ω•cm when the withdrawal speed was increased from 1.2 cm/min to 12.0 cm/min.

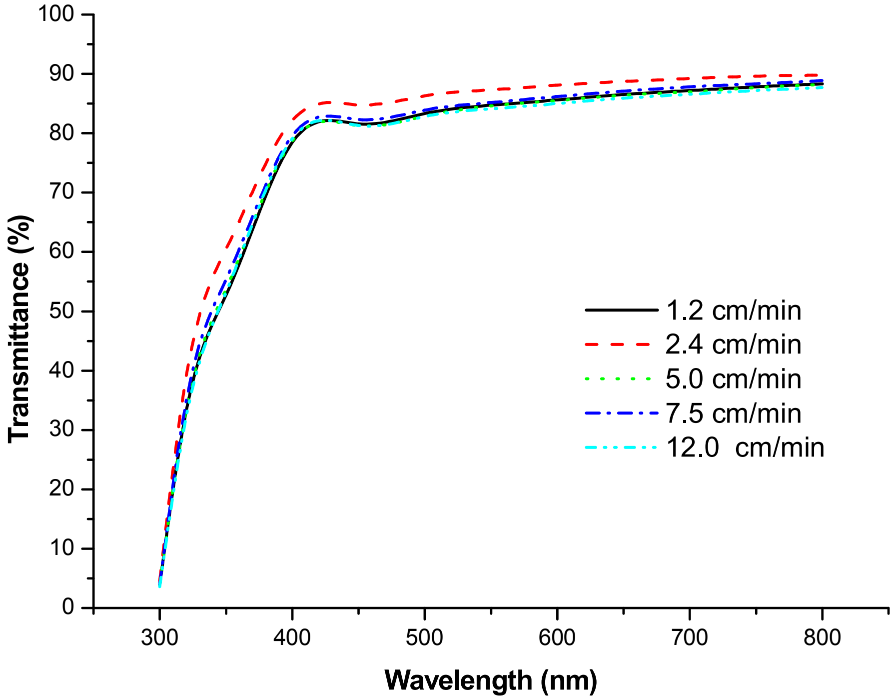

Figure 5.38 Transmittance of 1-layered AZO thin films annealed at 500 °C for 60 min using different withdrawal speeds

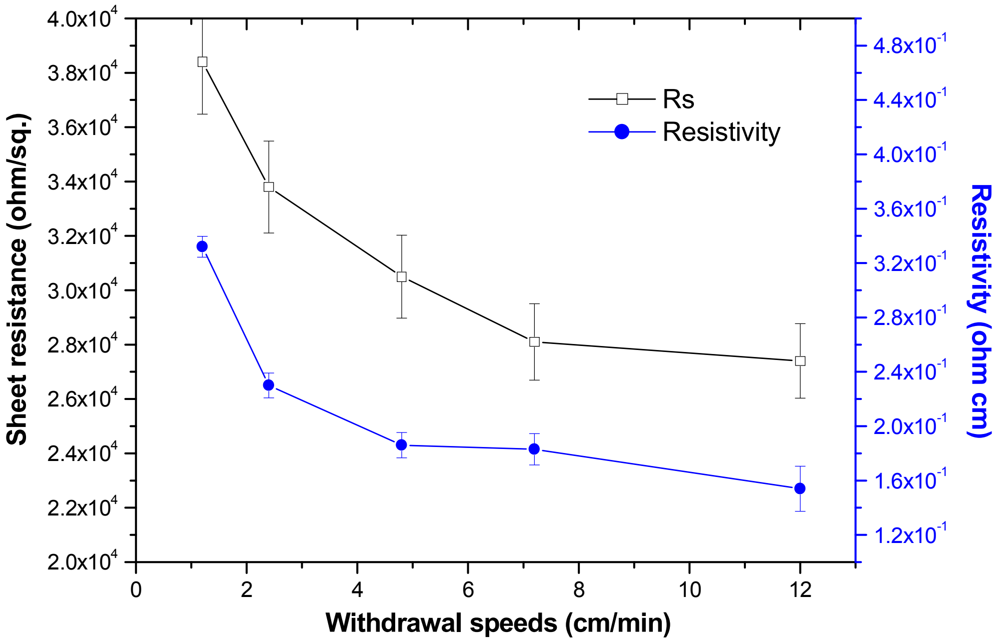

Figure 5.39 Sheet resistance and resistivity of 1-layered AZO thin films annealed at 500 °C for 60 min using different withdrawal speeds

5.2.7 Effect of the number of deposit layer

The transmittances of AZO films with the number of deposit layer varied from 1 to 10 were given in **Figure 5.40**. The results indicate that the transmittance was decreased while the number of film layers was increasing in the visible region. For single-layered AZO films, the transmittance was over 90% in the whole visible light range. However, the transmittance was decreased to 86.8%, 79.4%, 78.7% and 73.1% for the film with 2 layers, 3 slayer, 5 layers and 10 layers, respectively.

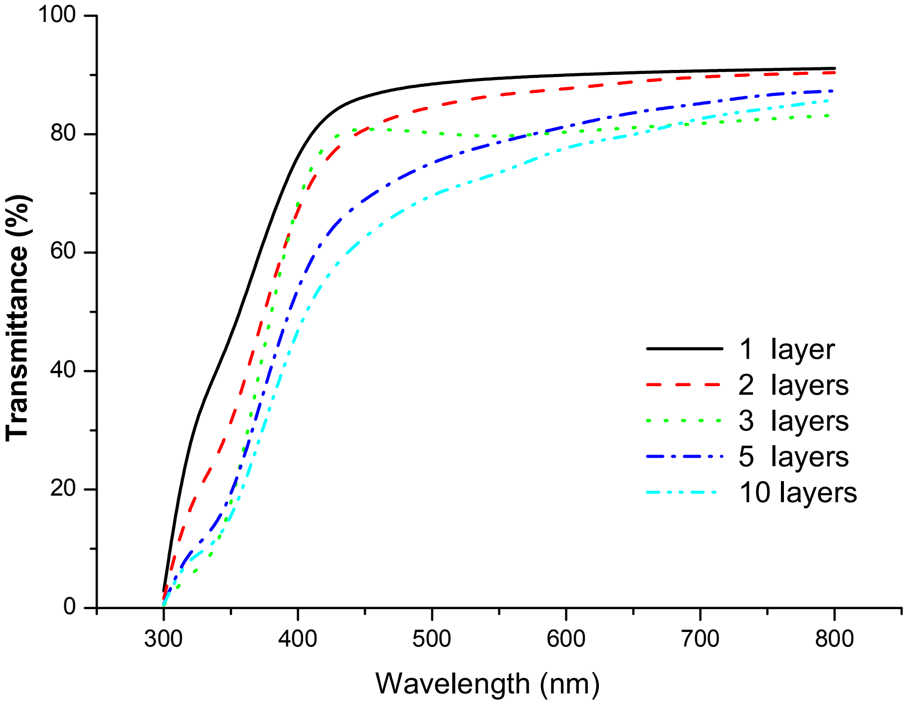

Figure 5.40 Transmittance of AZO thin films prepared with different numbers of deposit layer and annealed at 500 °C for 60 min

Sheet resistance and resistivity of the deposited AZO film were presented in **Figure 5.41**, which shows the changes in the sheet resistance and resistivity for the thin film samples fabricated with different numbers of deposit layer. A very high sheet resistance (118 kΩ/□) and resistivity (6.37×10^{-1} Ω•cm) of a single-layered film was obtained, which were reduced significantly to 46.4 kΩ/□ and 3.53×10^{-1} Ω•cm for 2- layered film, and further decreased with the increase of the number of deposit layer. The sheet resistance and resistivity of 10-layered thin film reached the minimums of 18.3 kΩ/□ and 2.8×10^{-1} Ω•cm, respectively.

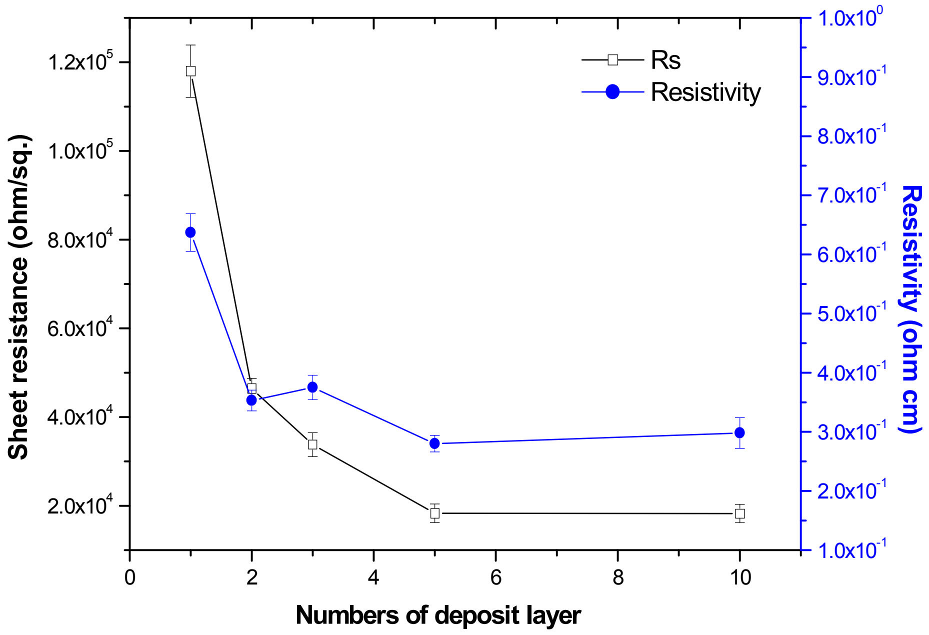

Figure 5.41 Sheet resistance of AZO thin films prepared with the number of deposit layer and annealed at 500 °C for 60 min

SEM micrographs of different layered thin films were shown in **Figure 5.42**. It can be seen that the thicknesses of the thin films were increased with the increase of the number of deposit layer, which are 54 nm, 76 nm, 111 nm, 153 nm and 284 nm for 1 layer, 2 layers, 3 layers, 5 layers and 10 layers, respectively (**Table 5-12**).

Table 5-12 The thickness of AZO thin film varied with the number of deposit layer

Number of deposit layer	1	2	3	5	10
Thickness (nm)	54	76	111	153	284

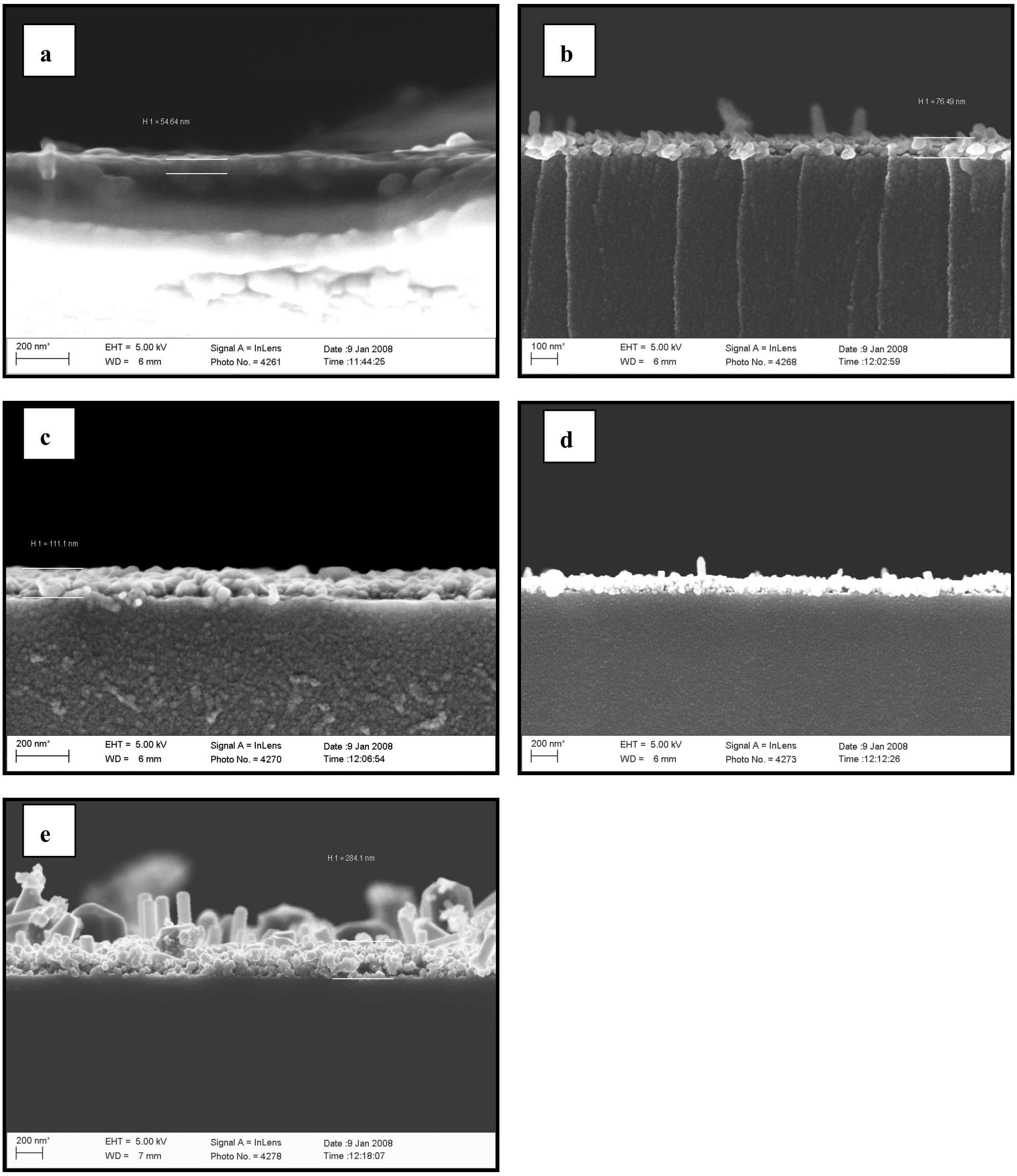

Figure 5.42 SEM micrographs of the cross-section of thin films with the number of deposit layer: a) 1 layer, b) 2 layers, c) 3 layers, d) 5 layers and e) 10 layers.

5.3 Discussion

The properties of ITO and AZO sols, heat treatment conditions and the fabrication technique are important factors which could affect the properties (optical transmittance, sheet resistance and resistivity) of thin films fabricated, which will be discussed in the following sections. As the sheet resistance of thin film varied with the fabrication conditions showed a tendency similar to that of the resistivity varied with the fabrication conditions, only will the effect of the fabrication conditions on the sheet resistance of thin films be discussed in the following sections.

5.3.1 Principle of sol-gel process

The sol-gel process is a versatile solution process for preparing inorganic oxide materials, which is particularly suitable for production of shaped materials in the form of thin film coatings, ultra-fine or spherical shaped powders [181]. Although there are many sol-gel processing technologies, the sol-gel dip coating process is almost exclusively applied for the fabrication of transparent layers, primarily for the deposition of oxide films over 1 μm in thickness on the glass as a transparent substrate with a high degree of planarity and surface quality [181, 182]. Also, the sol-gel process has been suggested as an alternative to conventional methods such as sputtering, chemical vapour deposition, and plasma spray for applying thin ceramic coatings [182]. Generally, the sol-gel process involves the transition of a system from a liquid “sol” into a solid “gel” phase, which is based on the hydrolysis and condensation reactions of metal alkoxides. Other steps such as drying and densification are also involved. The chemistry of the sol-gel process with the metal alkoxide as the precursor can be simplified as follows:

(1) Hydrolysis:

$$\text{>M-OR} + H_2O \rightarrow \text{>M-OH} + ROH \qquad (5\text{-}1)$$

(2) Condensation:

Condensation (alcohol elimination):

$$>M\text{-}OH + RO\text{-}M< \rightarrow >M\text{-}O\text{-}M< + ROH \qquad (5\text{-}2\ a)$$

Condensation (water elimination):

$$>M\text{-}OH + HO\text{-}M< \rightarrow >M\text{-}O\text{-}M< + HOH \qquad (5\text{-}2\ b)$$

where M is a metal species, such as In, Zn, Si, Al, Zr, etc., and R is an organic group, such as methyl, ethyl, isopropyl, etc..

Because of the high cost of commercial metal alkoxides, in this project, much cheaper indium and zinc salts including indium inorganic salt, indium chloride, and zinc organic salt, zinc acetate were used as the starting salts for fabricating ITO and AZO thin films. The reaction of the synthesis of indium alkoxide is as follows [183], with amine used as the catalyst.

$$InCl_3 + 3\ ROH + 3\ amine \rightarrow In(OR)_3 + 3\ amine{\cdot}HCl \qquad (5\text{-}3)$$

To form zinc alkoxide, the reaction is similar to (5-3).

$$Zn(CH_3COO)_2 + 2\ ROH + 2\ amine \rightarrow Zn(OR)_2 + 2\ amine{\cdot}CH_3COOH \qquad (5\text{-}4)$$

Hydrolysis-condensation process forms three dimensional networks in preparing alkoxide gels for TCO thin films. For the coating, firstly, the sol should be used to coat on the glass substrate before it turns to be gel. Secondly, in order to obtain dense films, drying and annealing process are the necessary steps to remove the liquid within the wet gel. In a typical sol-gel process, well prepared wet gels are dried to remove the liquid trapped within their three dimensional networks after hydrolysis-condensation reactions, which normally is carried out at moderate temperatures (< 200 °C) [181], leaving a hydroxylated metal oxide with residual organic content. The drying process usually has up to 90 vol% of shrinkage and therefore induces significant internal stress to the final dry gels. Scherer [184, 185, 186] developed a theory to explain the mechanism of the internal stress during the drying. The theory is based on the assumption of capillary pressure as the principle driving force in transporting liquid. At the stage of “constant rate period” (CRP), which means that the evaporation rate is almost constant at this stage. The drying stress at the surface of coating or plate can be expressed as:

$$\sigma_x(L) \approx \frac{L\eta_L V_E}{3D} \tag{5-5}$$

where, L is the thickness of a coatings or plate,

η_L and V_E are viscosity of liquid and its drying rate,

D is the permeability of gel.

Permeability can be estimated according to the Carman-Kozeny equation [187]:

$$D = \frac{(1-\rho)^3}{5(\rho S \rho_S)} \tag{5-6}$$

where, ρ is a relative density derived from the bulk density ρ_b divided by skeletal density ρ_S and S is the surface area.

According to the equation 5-5, which explains the important factors in stress formation during drying, the properties of the sol and the drying conditions have to be considered for fabrication of crack-free thin films. The influence of the properties of sol on the thin film is going to be discussed in a later section. Generally, the higher the temperature is, the higher the evaporation rate will be, resulting in higher drying stress, i.e., the stress in the wet coating is proportional to the drying temperature [184]. Hence, drying rate should be controlled. It is obvious that no drying, no stress generated, and no crack will occur. In the drying process, generally, the external layers tend to shrink more rapidly than the internal ones, but the internal layers do not allow them to shrink more, creating tensile stress in the external layers. Under the high drying rate, i.e., at high drying temperature, if this stress is higher than the strength of the coating layer in a particular moment, the coating layer will crack [187].

Based on Scherer's theory and some literature [188, 189, 190], the dry temperature and time were selected at 150 °C for 15 ~ 30 min, because it was observed that the surface quality of thin film fabricated was smooth and without crack under this temperature. On the other hand, up to temperature of 150 °C, the physically absorbed water molecules were evaporated from the wet film, which was supported by TG-DSC (**Figure 5.1** and **Figure 5.23**). This also means that the drying rate is suitable for drying the thin film samples prepared using the ITO and AZO sols. And also, the solvent, methoxyethanol (boiling point: 124.5 °C), and the additive, MEA (boiling point: 170 °C), can be eliminated entirely from the coating layer at 150 °C. This elimination was confirmed by FTIR spectrum as shown in **Figure 5.43**. The result is also in agreement with the result reported by Albonetti [190].

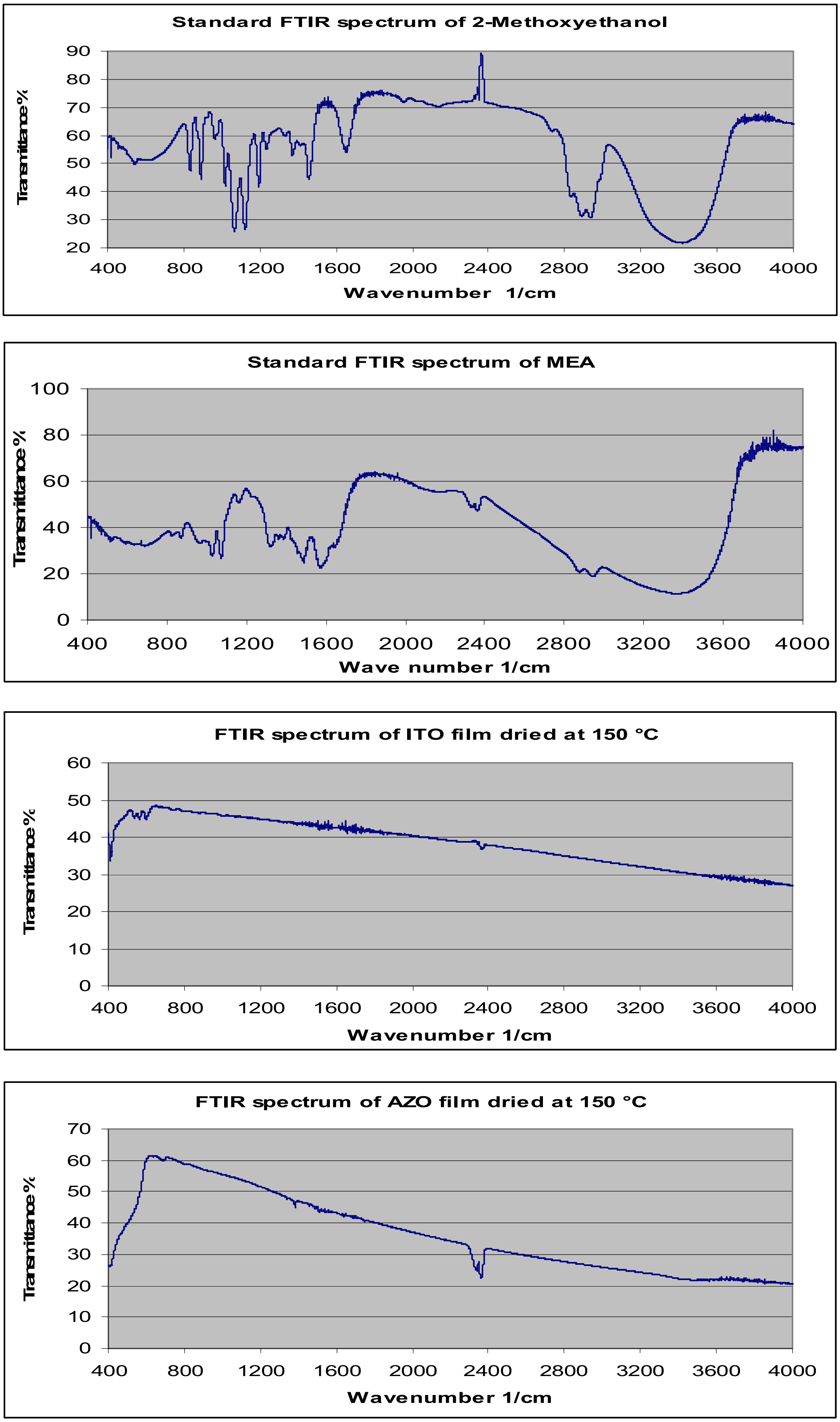

Figure 5.43 FTIR spectrums of 2-methoxyethanol, ITO and AZO films dried at 150 °C.

5.3.2 Properties of sol

5.3.2.1 Solvent and additive

The solvent property is an important factor for fabrication of good quality thin films. Normally, the solvent with low surface tension is favourable, because this will enhance the uniform flow of liquid solution over the substrate surface. Also, the solvent should have a level of volatility which ensures that drying time is short enough to avoid contamination and yet not so short as to inhibit levelling of the coating liquid on the substrate surface. Most common organic solvents are satisfactory, but alcohols are usually a much better solvent used for most sol-gel systems, because they all have low surface tension and also provide a wide selection of volatility while retaining good solubility characteristics [187]. Alcohols can also be obtained in a high degree of purity thereby minimising potential contamination problems. According to the principle mentioned above, the organic solvent, 2-methoxyethanol, was used throughout the process of fabrication of ITO and AZO thin films. Using of 2-methoxyethanol as the solvent as well as the medium was prompted because of its practical application to initiating the formation of physically and/or chemically stable transparent gels over a wide range of compositions with water. The benefit of 2-methoxyethanol is in depolymerisation, thus enhancing the solubilisation of partly formed oxo- or hydroxo-metal alkoxides. The mode of binding of 2-methoxyethanol ligand to metals is shown in structures I–VI [191]:

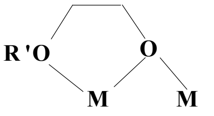

bridging-chelating

μ_2-η^2

I

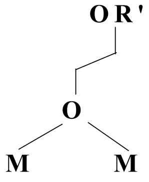

bridging

μ_2-η^1

II

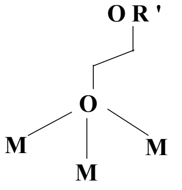

triply-bridging

μ_3-η^1

III

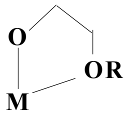

chelating

η^2

IV

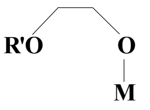

terminal

V

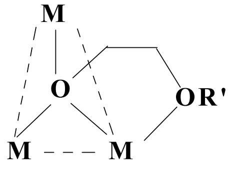

triply-bridging

μ_3-η^2

VI

It is because of these binding modes that the 2-methoxyethanol ligand finds wide use as an ancillary ligand in precursor-induced sol–gel processes. The possible reaction mechanism of zinc acetate with 2-methoxyethanol can be proposed as following [190].

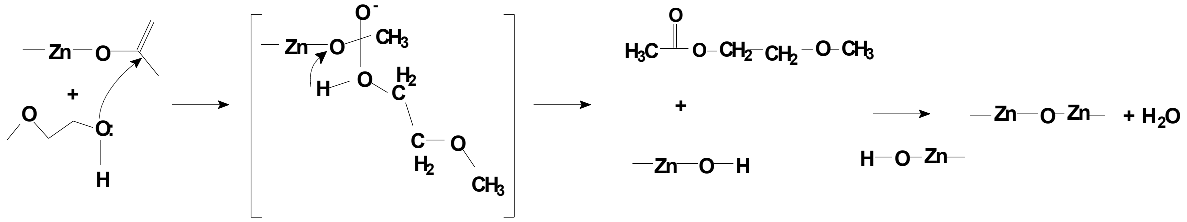

Basically, the formation of doped ZnO could be based on a hydrolytic process initiated by the OH ions that can be generated as a result of an esterification reaction of acetate ions with alcohol [192,193]. After the generation of methoxyethanol acetate, it can be assumed that the hydrolysis of zinc acetate is the first step of the overall reaction. Alcohols, in fact, provide an appropriate medium for the hydrolysis of carboxylates [194] that yield ZnO through the condensation route. Thus, the esterification of acetate with 2-methoxyethanol could lead to the release of hydroxyl groups bonded to the zinc species whose condensation lead to ZnO and water. The reaction of indium chloride with 2-methoxyethanol is presented as follows.

$$InCl_3 + 3CH_3CH_2OCH_2CH_2OH \rightarrow In(OH_3CH_2OCH_2CH_3)_3 + 3HCl \qquad (5\text{-}7)$$

Ethanolamine, commonly called monoethanolamine (MEA), is an organic chemical compound that is both a primary amine (due to an amino group in its molecule) and a primary alcohol (due to a hydroxyl group). Like other amines, monoethanolamine acts as a weak base. In this project, MEA was used as additive to prepare the stable sol in the process of fabrication of ITO and AZO thin films. Actually, MEA plays two roles in the preparation process of ITO and AZO sols: as a base and a complexing agent as well [195]. MEA used for the complexing agent, for example, it can react with zinc acetate. Firstly, zinc acetate transforms to mono acetate in 2-methoxyethanol solution as follows:

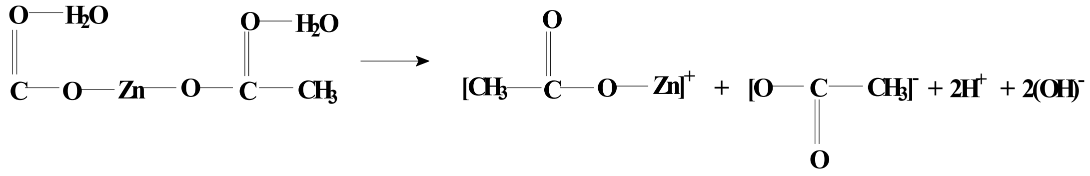

$$\mathrm{(O{-}H_2O)C(=O)\!-\!O\!-\!Zn\!-\!O\!-\!C(=O{-}H_2O)\!-\!CH_3} \longrightarrow [\mathrm{CH_3{-}C(=O){-}O{-}Zn}]^+ + [\mathrm{O{-}C(=O){-}CH_3}]^- + 2\mathrm{H}^+ + 2(\mathrm{OH})^- \quad (5\text{-}8)$$

Then, the following reaction was estimated to occur between MEA and zinc mono acetate (below) [196].

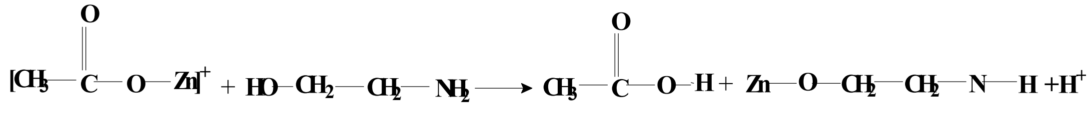

$$[\mathrm{CH_3{-}C(=O){-}O{-}Zn}]^+ + \mathrm{HO{-}CH_2{-}CH_2{-}NH_2} \longrightarrow \mathrm{CH_3{-}C(=O){-}O{-}H} + \mathrm{Zn{-}O{-}CH_2{-}CH_2{-}N{-}H} + \mathrm{H}^+ \quad (5\text{-}9)$$

On the other hand, MEA was used to modify the pH value of the sol prepared. In the case of ITO sols, while the molar ratios (*r*) of MEA to $InCl_3$ were at 0.1, 0.5, 1.0, 2.0 and 5.0, the pH values of the sols were 4, 6, 6, 7 and 8, respectively. Similar effect of MEA in AZO sols was also observed, i.e., pH values of sols increased with the increase of additional amounts of MEA. This effect can be attributed to the increase of alkaline nature of MEA in the sols. It was reported that pH value is an important factor which affects the rate of hydrolysis and condensation [187]. When pH value in solution is lower than 4, condensation rate is limited because of the lack of hydroxyl groups. With the increase of pH value, condensation rate is increased since sufficient hydroxyl groups are available for the reactions. However, under the higher pH value, e.g. pH value is higher than 11, the rate of hydrolysis becomes slow and the abundant hydroxyl groups can cause rapid termination of network growth and powder precipitates. In the current study, while *r* was 5.0, the sol was turbid and solutes were precipitated for both ITO sol and AZO sol. Also, the sheet resistance of the thin film produced was getting worse (the sheet resistance increased for ITO thin film (**Figure 5.12**) and no sheet resistance detected for AZO thin film (**Table 10**)) because there were many pores within the film, which is probably due to the evaporation of residual MEA during annealing as a high percentage of MEA was added in the process. Hence, the molar ratio of MEA to starting salt which was kept at 1.0 and the pH value of sol which was around 6 were suitable for fabricating stable ITO and AZO sols.

5.3.2.2 Concentration of starting salt

The concentration of starting salt in the sols for fabrication of thin film greatly affected the properties of thin films. The results (in **Figure 5.8, Figure 5.9**, **Figure 5.31** and **Figure 5.32**) show that, the transmittance and sheet resistance of ITO and AZO thin films reduced with the starting salt concentration increasing from 0.3 to 2.0mol/L of ITO sols and from 0.1 to 2.0mol/L of AZO sols. This maybe partially attributed to the higher viscosity of the sols with higher concentration, resulting in the increase of the thickness of the thin films. Similar results were observed by Lin, et al.[197]. Another probable reason is the growth of the grains with the increase of the concentration in the ITO thin films as observed from SEM micrographs (**Figure 5.10**), leading to chains of grains in contact and allowing more percolating paths for the current, resulting in the improvement in the conductivity of thin film. It was also found that ITO thin films were black in colour after annealing when high concentration sols (1.0 mol/L and 2.0 mol/L) were used, indicating that some carbon related organic residuals which were decomposed during annealing procedure to form free carbon were not removed fully. Thus, to achieve high transparency and low sheet resistance for ITO thin films, the concentration of starting salt should be less than 1.0 mol/L. In fact, in this project, the optimum starting salt concentrations for fabricating the colourless thin film were 0.6 mol/L and 0.3 mol/L for ITO thin films and AZO thin films, respectively.

5.3.2.3 Dopant content

Doping is the lifeblood of semiconductor materials. Doping determines the semi-conductive properties of materials and allows us to vary the conductivity from the semi-insulating through the semi-conductive to the semi-metallic range of the conductivity spectrum [198]. The species and concentration of dopants determine the conductivity type and the free carrier concentration of semi-conductors. Doping occurs when a dopant atom is in a bonding configuration that does not use all its valence electrons (n-type), or uses additional valence electrons taken from the host (p-type)[199]. Dopant incorporated into a semiconductor lattice mainly occupies substitutional lattice sites [198]. In semiconductor materials, the lattice site can be either a cation or an anion site. Which of the two sites is preferred by a dopant depends on many factors, including the valence electron correlation between dopant and host, the bond strength between the dopant atom and the surrounding host lattice, and the size of the dopant (strain effects). In this project, for ITO and AZO, they were doped with high valence elements, tin (+4) for indium (+3) and aluminum (+3) for zinc (+2), respectively, which can contribute an electron to improve the conductivity of materials. Therefore, they are both n-type semiconductor materials.

To study the effect of Sn content on the properties of ITO films, the 3-layered films with different Sn contents (1.0 at%, 3.0 at%, 5.0 at%, 10.0 at%, 15.0 at% and 20.0 at%) were fabricated using 0.6 mol/L sol and annealed at 600 °C for 60 min. The transmittance of ITO thin film was 85.8% and the sheet resistance was 19.01 kΩ/□ for 1.0 at% of tin doped. The maximum transmittance of 91.3% and the low sheet resistance of 2.52 kΩ/□ for 5.0 at.% of tin doped (**Figure 5.14** and **Figure 5.15**) can be attributed to the increase of grain size in the films (**Table 5-4**) and the decrease of the optical scattering. It can also be observed that the surface of films was become smoother with the increase of Sn content. However, the transmittance was decreased to 81.1% for tin content of 20.0 at%. This may be owing to the fact that the films with 10.0 to 20.0 at% of tin present grain boundaries, which may lead to the increased scattering of photons and decreased the transmittance of films [122].

For sheet resistance of ITO films, it is in fact widely reported that the substitution of In^{3+} with Sn^{4+} ions in the In_2O_3 n-type semiconductors causes an increase of charge carriers, electrons e^- [200], which can upgrade the conductivity of ITO materials. As shown in **Figure 5.15**, it was found that the sheet resistance of films is strongly dependent to the tin doping content. The sheet resistance of the film was decreased with increasing Sn content up to 10 at%. The sheet resistance of 10 at% Sn content ITO films showed a minimum value of 2.11kΩ/□. Then the sheet resistance was increased slightly to 9.06kΩ/□ with further increase of Sn content up to 20.0 at%. This behaviour, an initial reduction in sheet resistance with increasing Sn content followed by increasing sheet resistance at higher Sn content, is also observed by other researchers [201, 202]. The decrease of sheet resistance can be attributed to the formation of more conductive indium tin oxide solid solution, in which Sn^{4+} ions are hosted in the In_2O_3 structure. However, with the increase of Sn content, not all the Sn atoms can be substituted into the In atom sites. The Sn atoms that can not be substituted into indium sites do not behave as effective donors, probably because of Sn ions are very close to each other when the content of Sn ions is high [202]. When this occurs, one of the neighbouring Sn (+4) ions has the tendency to convert to Sn (+2). Sn (+4) ions are associated with Sn (+2) ions by electrostatic force, and this association forms a defect complex. The average electrical charge of the complex is +3. These associated Sn ions with an average charge +3 may not contribute to the electrical conduction, which resulted in the high sheet resistance at higher Sn content (more than 10.0 at%), may also be due to the very small crystals in thin films. The small crystal grains have many grain boundaries, which may behave as barriers to electron movement inside the thin film [129, 203, 204]. On the other hand, as the dopant content was more than the limit of solubility of Sn^{4+} ions in the In_2O_3, a rise in the sheet resistance occurs, possibly due to the formation of separate stable tin-oxygen at the In_2O_3 boundaries, which do not contribute to the electrical conduction. It was considered that these factors caused high sheet resistance at higher Sn content (more than 10.0 at%) in ITO thin films.

The effect of dopant content on the properties of AZO thin films was also studied and the dopant contents were varied from 0.5 at% to 10.0 at%. It was observed that the transmittance of AZO thin film (**Figure 5.35**) was 85.8% at 550 nm for 0.5 at% Al, which reached the maximum value of 90.7% for 1.0 at% Al, followed by a decrease to the minimum value of 81.2% for the Al content of 10.0 at%. This also was due to the effects of the grain size and the surface morphologies, which were observed from the micrographs of SEM shown in **Figure 5.37**.

The study of the sheet resistance of AZO films with different doping contents showed that the sheet resistance of AZO film was also dependent on the doping content of Al. For AZO film, its electrical conductivity is directly related to the number of free electrons, which can be improved by doping Al. An effective substitution of the dopant (Al) atoms in Zn sites of the ZnO structure took place according to the following equation [205]:

$$Al_2O_3 + 2Zn^{2+} \rightarrow 2Al^{3+} + 2ZnO + \tfrac{1}{2}O_2 + 2e \qquad (5\text{-}10)$$

It was observed (**Figure 5.36**) that the sheet resistance of films was decreased at a low Al doping content and reached to the lowest value of 38.4 kΩ/□ for 1.0 at% aluminium doping, and then increased with the increase of the content of aluminium more than 1.0 at%. The initial decrease in sheet resistance is attributed to the increase in dopant content as the substitution of Al^{3+}at the Zn^{2+} lattice site gives one extra electron which acts like a donor. However, at higher dopant content (>1.0 at%), because of the limited solubility of aluminum in ZnO, i.e., beyond the doping limit (0.8 at%), the doping atoms may result in some kind of neutral defects to form neutralised Al atoms. The neutralised Al atoms do not contribute to the carrier concentration and hence the amount of electrically inactive Al in the film increases. Thus when the doping level is high enough (i.e. more than 1.0 at%), more Al atoms are neutralised thereby producing a disorder in the lattice. This increases the efficiency of the scattering mechanism such as phonon and ionised scattering which in turn increases the resistivity [206]. The increase of sheet resistance with further increase in doping content may be also due to a decrease in mobility of carriers caused by segregation of dopants at the grain boundaries [100,102]. Therefore, in AZO films, aluminium is acting as an electrical dopant at low doping content but as an impurity at higher doping contents.

5.3.3 Heat treatment

The final step in fabricating a thin film is the densification or annealing of the gel coated substrate samples. Heat treatment temperature and time are the important factors that affect the densification and grain growth of thin film. In generally, the densification and grain growth are increased with the increase of temperature and time [207]. For ITO and AZO thin films, which were fabricated via sol-gel technique, the heat treatment process is with decomposition, the collapse of the the skeleton and leads to form the complete considation thin film [181]. Because gel coatings are amorphous, the dominant heat treatment mechanism is viscous flow, which is a much faster mechanism than the diffusion in crystals and this contributes to lower heat treatment temperatures in gel coatings compared to heat treatment of mineral powders [184]. Therefore, the densified ITO and AZO thin films were produced at the low temperature (at 600 °C for ITO and at 500 °C for AZO) for short time (60 min). The effects of annealing temperature and annealing time on the properties of the ITO and AZO thin films were discussed in this section.

The transmittance and the sheet resistance varied with annealing temperature for ITO and AZO films can be observed from the plots (**Figure 5.3**, **Figure 5.4**, **Figure 5.26** and **Figure 5.27**). In the case of ITO thin films, the transmittance was increased from 81.5% to 88.3% and the sheet resistance was decreased from 110 kΩ/□ to 1.33 kΩ/□ with the increase of annealing temperature. The explanation is that the crystallinity of ITO films was improved with the increase of annealing temperature, which was confirmed by XRD results of thin films shown in **Figure 5.2**. The sheet resistance of ITO thin film was decreased continuously with the increase of annealing temperature (**Figure 5.4**). It can be observed that this result indicates a correlation between the sheet resistance and the size of ITO crystallites (**Figure 5.5)**. Before annealing, the size of gel particle is more than 200 nm with round shape (**Figure 5.5**, a). Much smaller grains were formed when the film was annealed at 400 °C due to the decomposition of the gel particles, and the grain size was increased with the increase of annealing temperature up to 600 °C. The grains with unclear boundaries can be observed as the annealing temperatures were under 500 °C (**Figure 5.5**, b-e), and the grain boundaries can be well distinguished while the annealing temperature was 600 °C (**Figure 5.5**, f). Actually, the smaller the size of ITO crystallites, the higher is the sheet resistance. On the other hand, the result of TG-DSC shows that the residual organic component can not be eliminated entirely until the temperature reaches 600 °C (**Figure 5.1**). Therefore, the decrease of sheet resistance of ITO thin films with the increase of annealing temperature is resulted most likely for two reasons: one is that the high treatment temperature enhances the crystallisation of ITO thin films and decreases the effect of boundaries, resulting in the increase of electron movement inside the thin film; the other is that the residual organic compounds are burnt out step by step with the increasing temperatures, which results in producing more pores within the film.

For AZO thin films, though it was also showed that the crystallinity and grain size of the films increased with the increase of the annealing temperature (**Figure 5.24**), the trend of properties varied with annealing temperatures is different to that of ITO thin films. The transmittance and sheet resistances of AZO thin films were also improved with the increase of the temperatures from 400 °C to 500 °C. The transmittance was decreased and the sheet resistance was increased when the temperature was further raised from 500 °C to 600 °C (**Figure 5.26** and **Figure 5.27**), which could be related to the change of the grain size and surface morphology of AZO thin film (**Table 5-7**, **Figure 5.25)**. It can be seen that the annealing temperature has a great effect on film surface morphology and crystal growth. Small particles with relatively large holes and cracks were found on AZO thin film surface when the film was annealed at 400 °C. More closed-packed grain with smooth surface was observed at the annealing temperature of 500 °C. This may result in the improvement of the transmittance due to the reduction of optical scattering caused by the surface morphology and the densification of grains followed by grain growth and the reduction of grain boundary density. However, it seems more pores formed in the thin film at the temperature of 600 °C, which results in a slight decrease in transmittance. The sheet resistance which was first decreased with the increase of annealing temperature under 500 °C can be due to the growth of grains, but it was inversely proportional to the temperature increased from 500 °C to 600 °C. This could be attributed to decrease in carrier mobility by segregation of Al_2O_3 at grain boundaries [208] and more pores formed in the film.

The relationship between the properties of thin films and annealing time, which was set at 30 min, 60 min, 120 min and 240 min, respectively, at 600 °C for ITO thin films and 500 °C for AZO thin films, was investigated. The transmittances of ITO films were over 85% and the transmittances of AZO films were between 80% and 85% for annealing time ranging from 30 min to 240 min (**Figure 5.6** and **Figure 5.28**). The effect of annealing time on the transmittance of film may be due to the grain growth and the variation of surface morphology with annealing time. SEM micrographs of the surface morphologies of AZO films (in **Figure 5.30**) well matched the variation of the transmittance. Overall, the variation of sheet resistance, no inspite of ITO or AZO thin film, decreased with annealing time from 30 min to 60 min, and reached the lowest value for 60 min, then a slight increase of the sheet resistance was observed for longer annealing time (up to 240 min) (**Figure 5.7** and **Figure 5.29**). The short annealing time (for 30 min) leads to higher sheet resistance, indicating that it could still have some organic components and other residual in the thin films. However, if annealing time exceeds 60 min, increased sheet resistance may be attributed to the separation of the dopant element from the matrix to form stable oxides [131] and more pores formed by burning out the residual organic compounds [137].

5.3.4 Withdrawal speed and number of deposit layer

Withdrawal speed and the number of deposit layer are the parameters which are heavily related to the thickness of thin films, which, in turn, will affect the transmittance and conductivity of the thin films. Generally, the thickness of thin film is increased with increase of the withdrawal speed and the number of deposit layer using dip coating by sol-gel technique. The relationship between the withdrawal speed and the thickness of thin film can be expressed by the following equation by Landau and Levich [92].

$$h_0 = 0.944\frac{(\eta u_0)^{2/3}}{\sigma^{1/6}(\rho g)^{1/2}} = 0.944(Ca)^{1/6}\left(\frac{\eta u_0}{\rho g}\right)^{1/2} \qquad (2\text{-}3)$$

where,

h_o is the limiting film thickness,

u_o is the withdrawal speed,

η is the solution viscosity,

ρ is the solution density,

σ is the solution surface tension,

and Ca (= $\eta u_o/\sigma$) is a capillary number.

If the viscosity and density of sol solution are maintained constantly, the equation can be simplified to:

$$\text{Thickness} \propto [\text{withdrawal speed}]^{1/2} \qquad (2\text{-}4)$$

As shown in **Figure 5.17**, the transmittance of ITO films increased with the increase of withdrawal speeds from 1.2 cm/min to 5.0 cm/min, and decreased with the withdrawal speeds increasing up to 12 cm/min. It was also observed that the transmittance of ITO films was improved with the number of deposit layer increased from 1 layer to 3 layers, and then the transmittance was decreased as the number of deposit layer increased (**Figure 5.20**). Similar results were obtained from AZO films. The transmittance initially increased with the withdrawal speeds from 1.2 cm/min to 2.4 cm/min and then decreased with the further increase of the withdrawal speed (**Figure 5.38**). The transmittance continually decreased with the increase of the number of deposit layer (**Figure 5.40**). The initial increase of transmittance with the increased withdrawal speeds and the number of deposit layer might be due to the decrease of the pores in the thin film. For example, this can be observed from the **Figure 5.19** (a to e) showing that the surface morphologies of ITO films were becoming smoother with the increase of withdrawal speeds from 1.2 cm/min to 5.0 cm/min and becoming rougher with the further increase of withdrawal speed. Also as shown in **Figure 5.19** and **Figure 5.22**, higher sheet resistance of the monolayer film can be explained by the discontinuous nature of the film, i.e. insufficient coverage of the substrate or many pores existed and poor crystal growth. The thickness of thin films increased with the number of deposit layer can be owing to the followed coating is formed on the first one and the sol has better wetting ability on the coating than that on the substrate, which resulting in that the followed coating has more thicker thickness and much higher density [124]. The reduced sheet resistance with the increase of thickness of thin films is attributed to the improved crystallinity and increased crystalline sizes that weaken inter-crystallite boundary scattering and increase carrier lifetime, which consequently, increase the mobility for carrier with the increased thickness of thin films [209].

The transmittance decreased when the withdrawal speeds and the number of deposit layer increase due to the effect of thickness. The thickness was increased from 49 nm to 151 nm for increasing withdrawal speeds from 1.2 cm/min to 12 cm/min (**Figure 5.44**) and increased from 89 nm to 218 nm for increasing the number of deposit layer from 1 to 10 layers (**Figure 5.45**). In regard to AZO films, the thickness was from 40 nm to 121 nm for increasing withdrawal speeds from 1.2 cm/min to 12 cm/min and increased from 54 nm to 284 nm for the number of deposit layer ranging from 1 to 10 layers (**Figure 5.42**, **Figure 5.45**).

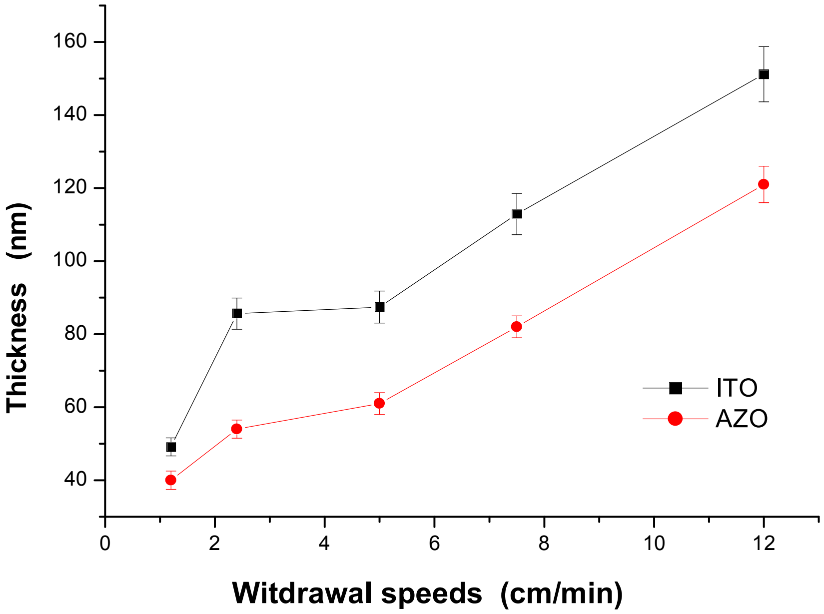

Figure 5.44 Thickness of ITO and AZO films varied with the withdrawal speeds.

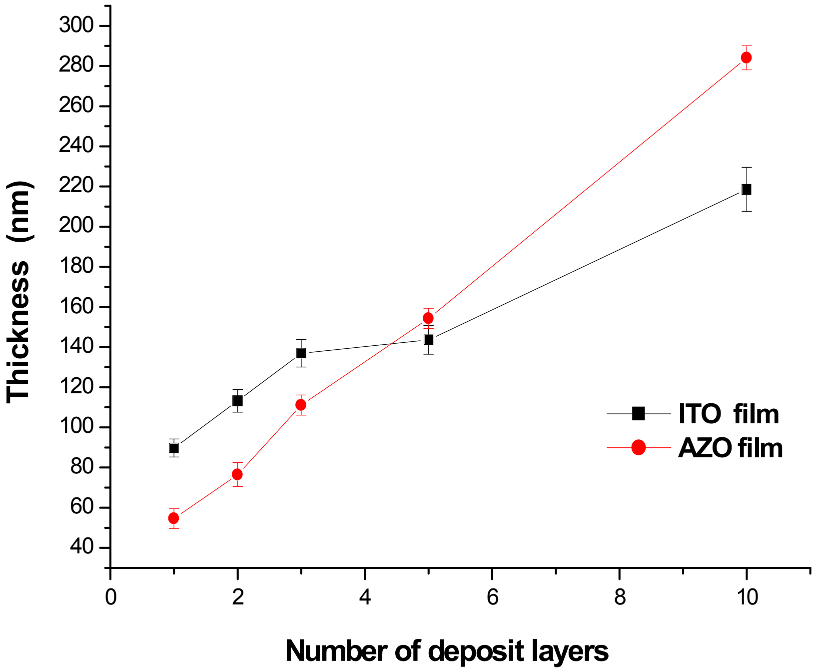

Figure 5.45 Thickness of ITO and AZO films varied with the number of deposit layer.

The effect of film thickness on the transmittance can be explained by optical physics that visible transmittance of a thin film is determined by both light absorption coefficient and the thickness of the film. No material is fully transparent in the whole optical wavelength range and hence there will always be some absorption in a certain range of the spectrum. Absorption coefficient a can be calculated from Lambert's formula [210],

$$a = \frac{1}{t}\ln(\frac{1}{Tr}) \tag{5-11}$$

where, t is the thickness of film,

Tr is optical transmittance.

Hence, optical transmittance Tr can be expressed as:

$$Tr = e^{-a \cdot t} \tag{5-12}$$

The light absorption coefficient, a, is determined by the following relation [211]:

$$a \approx (h\gamma - E_g)^{1/2} \qquad (5\text{-}13)$$

where $h\gamma$ and E_g are incident photon energy and the optical band gap, respectively.

According to equation 5-13, the absorption coefficient of film will be a constant at a certain wavelength when the films are fabricated using the same sol. Therefore, the optical transmittance is affected directly by film thicknesses theoretically. In the other words, the thicker the film, the lower the transmittance.

In the case of sheet resistances of ITO and AZO films varied with the withdrawal speeds and the number of deposit layer, the results noted that the sheet resistances were continually decreased with the increase of the withdrawal speeds and the number of deposit layer. The effect of withdrawal speed on the sheet resistance can be due to the increase of film thickness with the increase of withdrawal speed. But for the effect of the number of deposit layer on the sheet resistance, the reasons are not only the thickness but also densification. The high sheet resistance of films fabricated using low withdrawal speed and the monolayer film are possibly caused by more defects such as pores within the films, poor crystal growth[212] and thickness. How the thickness affects the sheet resistance of films is easy to explain by the relation between them. According to the equation, $Rs = \rho/t$ [213] (where ρ is the resistivity of film and t is the thickness of film), for the certain material under the same conditions, the sheet resistance is decreased with the increase of thickness.

The important reason for reduction of the sheet resistance with the number of deposit layer can also be explained by the increase of the densification of film. The increase of the density of the film with the increase in the number of layer can be attributed to two factors. First is the process of the sol filling the pores of the previously deposited layers (except for the last one). The second factor is relative to pore elimination during re-crystallisation [126]. Some researchers [214] also found that the presence of the dense inner crusts can strongly enhance the film density in multilayered film.

Chapter 6 CONCLUSIONS AND FUTURE WORK

6.1 Conclusions

This project mainly includes two parts: synthesis of powders and fabrication of thin films. Some conclusions can be drawn from the experimental results and discussion:

1. Tin oxide, zinc oxide and AZO particles with different morphologies and particle sizes were synthesised at the temperature of 200 °C for 24 hours by the hydrothermal method, but indium oxide and ITO could not obtained under the same synthesis conditions.

2. ITO and AZO thin films were successfully prepared by dipping coating using sol-gel technique. The higher of the concentration of the sol is, the lower of the sheet resistance and transmittance of thin films are. The sols with the concentrations of 0.6 mol/L of ITO and 0.3 mol/L of AZO are better for fabricating good quality ITO and AZO films.

3. XRD results revealed that ITO and AZO thin films were formed after annealing over 500 °C and 400 °C for 60 min, respectively. The grain size was increased with the increase of annealing temperature and time. ITO thin film with the maximum transmittance and the minimum sheet resistance was obtained by annealing at 600 °C for 60 min. The optimum annealing condition was at 500 °C for 60 min for fabricating of AZO thin film with the highest transmittance and the lowest sheet resistance.

4. The dopant content is closely relative to the conductivities of ITO and AZO thin

films. In regarding to ITO thin films, the sheet resistance was decreased from 19.01 kΩ/□ for 1.0 at% of tin doped to the minimum value of 2.11 kΩ/□ for 10.0 at%. Then the sheet resistance was proportionly to the tin content up to 20.0 at% owing to the limit of solubility of tin ions in the matrix of indium oxide. The transmittance was improved while the tin contents varied from 1.0 at% to 5.0 at% and then getting decrease as the tin was further doped. In regarding to AZO thin films, the lowest sheet resistance was obtained as 1.0 at% of aluminium doped as the limit of solubility of aluminium into zinc oxide is 0.8 at%. And also, the transmittance was increased firstly and reached the maximum value while the dopant content was 1.0 at%, then being reduced with further increases. The dopant contents affect the transmittance of thin films because of the influnce of dopant on the surface morphology and grain size of thin films.

5. The thickness of the thin films can be controlled by varing the withdrawal speed and the number of deposit layer, which affect the properties of the thin films.

6.2 Future work

There are several issues related to this project could be further studied:

1 In the present work, indium oxide and ITO could not be synthesised at 200 °C for 24 h by the hydrothermal method. This is because the transformation of indium hydroxide and indium tin hydroxide to their oxide needs the temperature over 250 °C [31]. However, the softening temperature of Teflon inner container of autoclave used in this project is about 230 °C to 250 °C. Hence, it is necessary to look for the autoclave can be used at the temperature over 250 °C to achieve indium oxides and ITO and to study the effect of synthesis conditions on the properties of particles.

2 In the process of transparent conducting oxide thin film formation, dopant can provide extra electrons to enhance the conductivity of thin film. On the other hand, some researchers found that it was useful to introduce the dilute hydrogen gas (95%

Ar-5% H_2) to improve the conductivity of thin film [119, 215]. The metal oxide will lose oxygen and form oxygen vacancies in the film while the film was annealed in dilute hydrogen gas atmosphere at high temperature. The oxygen vacancies can also serve as electron donors, which result in promoting the conductivity of thin film. Therefore, the further work could be done by annealing ITO and AZO thin films in dilute hydrogen gas atmosphere at different annealing temperatures and times.

References

---

1 K. Badeker, Electrical Conductivity and Thermo-Electromotive Force of Some Metallic Compounds, Ann. Phys., 22 (1907), pp749-766.

2 S. J. Limmer, S. V. Cruz, G. Z. Cao, Films and Nanorods of Transparent Conducting Oxide ITO by a Citric Acid Sol Route, Appl. Phys. A, 79 (2004), pp421– 424.

3 S. M. Rozati, T. Ganj, The Effect of Film Thickness on Physical Properties of Fluorine-Doped Indium Oxide Thin Films, Materials Science-Poland, 22 (2004), pp93-97.

4 J. C. Manifacier, Thin Metallic Oxides as Transparent Conductors, Thin Solid Films, 90 (1982), pp297-308.

5 V. M. Rotello, Nanoparticles: Building Blocks for Nanotechnology, Kluwer Academic/Plenum Publishers, New York, 2004. pp32-54.

6 J. H. Adair, Ender Suvaci, Morphological Control of Particles, Current Opinion in Colloid & Interface Science, 5 (2000), pp160-167.

7 K. L. Chopra, S. Major and D. K. Pandya, Transparent Conductors - a Status Review, Thin Solid Films, 102 (1983), pp1-46.

8 Obara Oka, Japanese patent, No.: 2006-193363.

9 R. F. Pierret, Advanced Semiconductor Fundamentals, 2nd edition, Vol. VI, Pearson Education Inc., 2003.

10 C. Rao and A. Cheetham, Science and Technology of Nanomaterials, J. Mater. Chem., 11(2001), pp 2887-2894.

11 Y. Gogotsi, Nanomateirals Handbook, 2006, Taylor & Francis Group, NW, pp1-4.

12 M. Wilson, K. Kannangara, G. Smith, M. Simmons, et al., Nanotechnology: Basic Science and Emerging Technologies, University of New South Wales Press Ltd. 2002, pp58-77.

13 Z. L. Wang, Nanowires and Nanobelts Materials, Properties and Devices-nanowires and Nanobelts of Functional Materials, 2003, Springer Science+Business Media, Inc., USA.

14 G. C. Papavassiliou, Three- and Low-dimensional Inorganic Semiconductors, J. Prog.

Solid St. Chem. Vol. 25, 1997, pp125-270.

15 P. F. Kane, G. B. Larrabee, Characterisation of Semiconductor Materials, McGRAW-HILL Book Company, 970, p1.

16 B. Sapoval, C. Herman, Physics of Semiconductors, Sringer-Verlag New York, Inc.,1995, p2.

17 B. Van Zeghbroeck, Principles of Semiconductor Devices, 2004, http://ece-www.colorado.edu/bart/book, chapter 2.

18 C. N. R Rao, A. Muller, A. K. Cheetham, The Chemistry of Nanomaterials, Volume 1, 2004, Wiley-VCH Verlag GmbH &Co. KGaA. p3.

19 G. Schmid, Clusters and Colloids: From Theory to Applications, VCH, Weinheim, 1994.

20 A. I. Kirkland, D. E. Jefferson, D. G. Duff et al., Structural Studies of Trigonal Lamellar Particles of Gold and Silver, Proc. R Soc. London Ser. A, 440 (1993), pp589-609.

21 S. Link, M. B. Mohamed, M.A. El-Sayed, Simulation of the Optical Absorption Spectra of Gold Nanorods as a Function of Their Aspect Ratio and the Effect of the Medium Dielectric Constant, J. Phys. Chem. B, 103 (1999), pp3073-3077.

22 L. Manna, E. C. Scher, A. P. Alivisatos, Synthesis of Soluble and Processable Rod-, Arrow-, Teardrop-, and Tetrapod-shaped CdSe Nanocrystal, J. Am. Chem. Soc., 122 (2000), pp12700-12706.

23 P. J. Kelly, Y. Zhou, A. Postill, A Novel Technique for the Deposition of Aluminum-Doped Zinc Oxide Films, Thin Solid Films, 426 (2003), pp111-116.

24 N. Nadaud, N. Lequeux, M. Nanot, et al. Structural Studies of Tin-Doped Indium Oxide (ITO) and $In_4Sn_3O_{12}$, Journal of Solid State Chemistry, 135 (1998), pp140-148.

25 J. Fan and J. Goodenough, X-Ray Photoemission Spectroscopy Studies of Sn-doped Indium Oxide Films, Journal of Applied Physics, 48 (8), (1977), pp3524–3531.

26 C. T. Prewitt, R. D. Shannon, D.B. Rogers, et al., C Rare Earth Oxide-corundum Transition and Crystal Chemistry of Oxides Having the Corundum Structure, Inorg.Chem., 8 (1969), pp1985-1988.

27 P. Nath and R. F. Bunshah, Preparation of In_2O_3 and Tin-Doped In_2O_3 Films by a Novel Activated Reactive Evaporation Technique, Thin Solid Films, 69 (1980), pp63 – 68.

28 O. Kluth, B. Rech, L. Houben, et al., Texture Etched ZnO:Al Coated Glass Substrates for Silicon Based Thin Film Solar Cells, Thin Solid Films, 351 (1999), pp247-253.

29 S. M. Kim, K. H. Seo, J. H. Lee, et al., Preparation and Sintering of Nanocrystalline ITO Powders with Different SnO2 Content, Journal of the European Ceramic Society, 26 (2006), pp73-80.

30 C. P. Udawatte, K. Yanagisawa, S. Nasu, Sintering of Additive Free Hydrothermally Derived Indium Tin Oxide Powders in Air, Journal of Solid State Chemistry, 154 (2000), pp444-450.

31 J. S. Lee and S. C. Choi, Solvent Efect on Synthesis of Indium Tin Oxide Nano-Powders by a Solvothermal Process, Journal of the European Ceramic Society, 25 (2005), pp3307-3314.

32 L. Gupta, A. Mansingh and P. K. Srivastava, Band Gap Narrowing and the Band Structure of Tin Doped Indium Oxide Films, Thin Solid Films, 176, 1989, pp33–44.

33 A. Mohammadi Gheidari, E. Asl Soleimani, M. Mansorhoseini, et al., Structural Properties of Indium Tin Oxide Thin Films Prepared for Application in Solar Cells, Materials Research Bulletin, 40 (2005), p1303-1307.

34 J. W. Bae, H. J. Kim, J. S. Kim, et al., Tin-Doped Indium Oxide Thin Film Deposited on Organic Substrate Using Oxygen Ion Beam Assisted Deposition, Surface and Coatings Technology, 131 (2000), pp196-200.

35 R. H. Tahar, T. Ban, Y. Ohya, et al., Tin Doped Indium Oxide Thin Films: Electrical Properties, Journal of Applied Physics, 83 (1998), pp2631-2645.

36 M. K. Jayaraj, A. Antony, M. Ramachandran, Transparent Conducting Zinc Oxide Thin Film Prepared by Off-axis RF Magnetron Sputtering, Bull. Mater. Sci., 25 (2002), pp227-230.

37 R. F. Silva, M. D. Zaniquelli, Aluminum-doped Zinc Oxide Films Prepared by an Inorganic Sol–gel route, Thin Solid Films 449 (2004) pp86–93.

38 P. Sagar, M. Kumar, R. M. Mehra, Influence of Hydrogen Incorporation in Sol-Gel Derived Aluminum Doped ZnO Thin Films, Thin Solid Films, 489 (2005), pp94–98.

39 J. Ma, F. Ji, H. L. Ma, et al., Preparation and Properties of Transparent Conducting

Zinc Oxide and Aluminum-Doped Zinc Oxide Films Prepared by Evaporating Method, Solar Energy Materials & Solar Cells, 60 (2000), pp341-348.

40 H. W. Lee, S. P. Lau, Y. G. Wang, et al., Structural, Electrical and Optical Properties of Al-doped ZnO Thin Films Prepared by Filtered Cathodic Vacuum Arc Technique, Journal of Crystal Growth, 268 (2004), pp596–601.

41 C. Granqvist, A. Hultaker, Transparent and Conducting ITO Films: New Developments and Applications, Thin Solid Films, 411 (2002), pp1-5.

42 M. J. Flynn, J. Kanicki, A. Badano, et al., High-Fidelity Electronic Display of Digital Radiographs, Radiographics, 19 (1999), pp1653-1669.

43 O. Sneh, Robert B. Clark-Phelps, A. R. Londergan, et al., Thin Film Atomic Layer Deposition Equipment for Semiconductor Processing , Thin Solid Film, 2002,402, pp248-261.

44 P. Townsend and J. Olivares, Laser Processing of Insulator Surfaces, J. Appl. Surf. Sci., 110 (1997), pp275-282.

45 T. L. Brown, S. Swaminathan, S. Chandrasekar, et al., Low-cost Manufacturing Process for Nanostructured Metals and Alloys, Mater. Res. Sci., 17 (2002), pp2484-2488.

46 N. Toshima and T. Yonezawa, Bimetallic Nanoparticles-novel Materials for Chemical and Physical Applications, New J. Chem., 22 (1998), pp 1179-1201.

47 L. L. Zhang, Preparation of Multi-component Ceramic Nanoparticles, 04019/CISM/llz, pp1-31.

48 C. N. R. Rao, A. Muller, A. K. Cheetham, The Chemical of Nanomaterials, Vol. 2, WILEY-VCH Verlag GmbH & Co. KgaA, Weinheim, 2004. p372.

49 Z Gao, Y. Z. Gao, Y. H Li, et al., Microstructure of Nanophase Indium-tin Oxide, Nanostructured Materials, 11 (5) (1999), pp611–616.

50 S. T Li, X. L. Qiao, J. G. Chen, et al, Effects of Temperature on Indium Tin Oxide Particles Synthesised by Co-precipitation, Journal of Crystal Growth, 289 (2006), pp151-156.

51 M. N. Rahaman, Ceramic Processing and Sintering, Marcel Dekker, Inc, 1995, New York.

52 K.Y. Kim, S. B. Park, Preparation and Property Control of Nano-sized Indium Tin Oxide Particle, Materials Chemistry and Physics, 86 (2004), pp210-221.

53 B. M. Patterson, K. M. Unruh, S. I. Shah, Melting and Freezing Behavior of Ultrafine Granular Metal Thin Films, Nanostruct. Mater., 1 (1992), pp65-70.

54 K. Byrappa, T. Adschiri, Hydrothermal Technology for Nanotechnology, Progress in Crystal Growth and Characterization of Materials, 53 (2007), pp117-166.

55 A. Rabenau, Angewandte Chemie International Edition in English, 24 (1998), pp1026–1040.

56 J. S. Lee, and S. C. Choi, Crystallization Behavior of Nano Ceria Powders by Hydrothermal Synthesis Using a Mixture of H_2O_2 and NH_4OH. Mater. Lett., 58 (2004), pp390–393.

57 R. R. Piticescu, C. Monty, D. Taloi, et al., Hydrothermal Synthesis of Zirconia Nanomaterials. J. Eur. Ceram. Soc., 21 (2001), pp2057–2060.

58 H. L. Zhu, K. H. Yao, Y. H. Wo, et al., Hydrothermal Synthesis of Single Crystalline $In(OH)_3$ Nanorods and Their Characterisation, Semicond. Sci. Technol., 19 (2004), pp1020–1023.

59 H. R. Xu,G. S. Zhu, H. Y. Zhou, et al. , Preparation of Monodispersed Tin-Doped Indium Oxide Powders by Hydrothermal Method, J. Am. Ceram. Soc., 88 (2005), pp986–988.

60 C. Y. Liu, H. Y. Li, W. Q. Jie, et al., Preparation of ZnO Cluster and Rod-like Whiskers Through Hydrothermal Methods, Materials Letters, 60 (2006), pp1394–1398.

61 H. Zhang, D. R. Yang, S. Z. Li, et al., Controllable Growth of ZnO Nanostructures by Citric Acid Assisted Hydrothermal Process, Materials Letters, 59 (2005), pp1696-1700.

62 T. Yoshida, M. Tochimoto, D. Schlettwein, et al., Self-assembly of Zinc Oxide Thin Films Modified with Tetrasulfonated Metallophthalocyanines by One-step Electrodeposition, Chem. Mater., 11 (1999), pp2657–2667.

63 Y. Wang, M. Li, Hydrothermal Synthesis of Single-crystalline Hexagonal Prism ZnO Nanorods, Materials Letters, 60 (2006), pp266-269.

64 J. Liu, X. Huang , J. Duan, et al., A Low-temperature Synthesis of Multiwhisker-based

Zinc Oxide Micron Crystals, Materials Letters, 59 (2005), pp 3710-3714.

65 S. C. Liufu, H. N. Xiao, Y. P. Li, Investigation of PEG Adsorption on The Surface of Zinc Oxide Nanoparticles, Powder Technology, 145 (2004), pp 20-24.

66 H. X. Zhang, J. Feng, J. Wang, et al., Preparation of ZnO Nanorods Through Wet Chemical Method, Materials Letters, 61 (2007) , pp5202–5205.

67 L. Rosenthal-Toib, K. Zohar, M. Alagem, et al., Synthesis of Stabilized Nanoparticles of Zinc Peroxide, Chemical Engineering Journal, 136 (2008), pp425–429.

68 J. D. Mu, Z. M. Liu, Y. Huang, et al, Control of ZnO Morphologies via Surfactants Assisted Route in the Subcritical Water, Journal of Crystal Growth, 280 (2005), pp126–134.

69 X. Sun, X. Chen, Z. Deng, et al., A CTAB-assisted Hydrothermal Orientation Growth of ZnO Nanorods, Materials Chemistry and Physics, 78 (2002), pp99–104.

70 P. Li, H. Liu, Y. F. Zhang, et al., Synthesis of Flower-like ZnO Microstructures via a Simple Solution Route, Materials Chemistry and Physics, 106 (2007), pp 63–69.

71 D. R. Chen, X. L. Jiao, G. Cheng, Hydrothermal Synthesis of Zinc Oxide Powders with Different Morphologies, Solid State Communications, 113 (2000), pp363–366.

72 J. P. Liu, X. T. Huang, A Low-temperature Synthesis of Ultraviolet-light-emitting ZnO Nanotubes and Tubular Whiskers, Journal of Solid State Chemistry, 179 (2006), pp 843–848.

73 H. Y. Xu, H. Wang, Y. C. Zhang, et al., Hydrothermal Synthesis of Zinc Oxide Powders with Controllable Morphology, Ceramics International, 30 (2004), pp93–97.

74 Z. K. Li, X. T. Huang, J. P. Liu, et al., Single-crystalline ZnO Nanowires on Zinc Substrate by a Simple Hydrothermal Synthesis Method, Materials Letters, 62 (2008), pp2507–2511.

75 P. Cousin, R. A. Ross, Preparation of Mixed Oxides: A Review, Materials Science and Engineering, A, 130 (1990), pp119-125.

76 B. E. Aperathitis, M. Modreanu, M. Bender, et al., Optical Characterisation of Indium-tin-oxynitride Fabricated by RF-Sputtering, Thin Solid Films, 450 (2004), pp101-104.

77 Y. Zhou, P. J. Kelly, A. Postill, et al., The Characteristics of Aluminum-Doped Zinc

Oxide Films Prepared by Pulsed Magnetron Sputtering from Powder Targets, Thin Solid Films, 447–448 (2004), pp33–39.

78 V. Sittinger, F. Ruske, W. Werner, et al., ZnO:Al Films Deposited by In-line Reactive AC Magnetron Sputtering for a-Si:H Thin Film Solar Cells, Thin Solid Films, 2005, pp2-9.

79 W. Wang, X. Diao, Z. Wang, et al., Preparation and Characterisation of High-performance Direct Current Magnetron Sputtered ZnO:Al Films, Thin Solid Films, 491 (2005), pp54–60.

80 http://www.vacgen.com/catalogue/section-16/intro.htm

81 J. G. Na, Y. R. Cho, Y. H. Kim, et al., Effects of Annealing Temperature on Microstructure and Electrical and Optical Properties of Radio-Frequency-Sputtered Tin-Doped Indium Oxide Films, J. Am Ceram. Soc., 72 [4] (1989), pp698-701.

82 E. Fortunato, P. Nunes, A. Marques, et al., Transparent, Conductive ZnO:Al Thin Film Deposited on Polymer Substrates by RF Magnetron Sputtering, Surface and Coatings Technology, 151–152 (2002), pp247–251.

83 S. H. Jeong, J. H. Boo, Influence of Target-to-substrate Distance on the Properties of AZO Films Grown by RF Magnetron Sputtering, Thin Solid Films, 447–448 (2004), pp105–110.

84 T. Tsuji, M. Hirohashi, Influence of Oxygen Partial Pressure on Transparency and Conductivity of RF Sputtered Al-doped ZnO Thin Films, Applied Surface Science, 157 (2000), pp47–51.

85 J. L. Yao, S. Hao and J. S. Wilkinson, Indium Tin Oxide Films by Sequential Evaporation, Thin Solid Films, 189 (1990), pp227–233.

86 N. Balasubramanian and A. Subrahmanyam, Electrical and Optical Properties of Reactively Evaporated Indium Tin Oxide (ITO) Films-Dependence on Substrate Temperature and Tin Concentration, Journal of Physics D: Applied Physics, 22 (1989), pp206 – 209.

87 J. Dutta and S. Ray, Variations in Structural and Electrical Properties of Magnetron-Sputtered Indium Tin Oxide Films with Deposition Parameters, Thin Solid Films, 162

(1988), pp119-127.

88 T. Seto, K. Okuyama and A. Hirota, Preparation of Aluminum Doped Zinc Oxide Particles by Chemical Vapour Deposition, J. Aerosol Sci., 26 (1995), pp601-602.

89 C. J. Brinker, G. W. Scherer, Sol-gel Science, Academic Press, New York, 1990.

90 A. C. Pierre, Introduction to the Sol-gel Processing, Kluwer Academic Publishers,1998, pp1-5.

91 http://www.chemat.com/html/solgel.html.

92 C. J. Brinker, A. J. Hurd, P. R. Schunk, et al., Review of Sol-gel Thin Film Formation, Journal of Non-Crystalline Solids 147-148 (1992), pp424-436.

93 Bornside, C.W. Macosko and L. E. Scriven, Spin Coating: One-dimensional Model, J. Appl. Phys., 66 (1989), pp5185-5193.

94 R. Schwartz, T. Schneller, R. Waser, Chemical Solution Deposition of Electronic Oxide Films, C. R. Chimie, 7 (2004), pp433–461.

95 S. Sakka, Handbook of Sol-gel Science and Technology: Volume I Sol-gel Process, Kluwer Academic Publishers, 2004, London, pp60-76.

96 C. Brinker, G. Frye, A. Hurd, et al, Fundamentals of Sol-gel Dip Coating, Thin Solid Films, 201 (1991), pp97-108.

97 S. Bandyopadhyay, G. K. Paul, R. Roy, et al, Study of Structural and Electrical Properties of Grain-boundary Modified ZnO Films Prepared by Sol–gel Technique, Materials Chemistry and Physics, 74 (2002), pp83–91.

98 S. B. Majumder, M. Jain, P. S. Dobal, et al., Investigations on Solution Derived Aluminium Doped Zinc Oxide Thin Films, Materials Science and Engineering B, 103 (2003), pp16-25.

99 E. Bacaksiz, M. Parlak, M. Tomakin, et al., The Effects of Zinc Nitrate, Zinc Acetate and Zinc Chloride Precursors on Investigation of Structural and Optical Properties of ZnO Thin Films, Journal of Alloys and Compounds, 466 (2008), pp447–450.

100 J. H. Lee, B. O. Park, Transparent Conducting ZnO:Al, In and Sn Thin Films Deposited by the Sol–Gel Method, Thin Solid Films, 426 (2003), pp94–99.

101 M. Dutta, S. Mridha, D. Basak, Effect of Sol Concentration on the Properties of ZnO

Thin Films Prepared by Sol–Gel Technique, Applied Surface Science, 254 (2008), pp2743–2747.

102 P. Sagar, M. Kumar, R. M. Mehra, Influence of Hydrogen Incorporation in Sol-Gel Derived Aluminum Doped ZnO Thin Films, Thin Solid Films, 489 (2005), pp94–98.

103 R. F. Silva and M. E. Zaniquelli, Aluminum Doped zinc Oxide Films: Formation Process and Optical Pproperties, Journal of Non-Crystalline Solids, 247 (1999), pp248-253.

104 M. J. Alam and D. C. Cameron, Optical and Electrical Properties of Transparent Conductive ITO Thin Films Deposited by Sol–gel Process, Thin Solid Films, 377-378 (2000), pp 455-459.

105 E. Elangovan, A. Marques, A. Pimentel, et al., Effect of Annealing on Molybdenum Ddoped Indium Oxide Thin Films RF Sputtered at Room Temperature, Vacuum, 82 (2008), pp1489-1494.

106 J. N. Avaritsiotis, R. P. Howson, Composition and Conductivity of Fluorine-doped Conducting Indium Oxide Films Prepared by Reactive Ion Plating, Thin Solid Films, 77 (1981), pp 351-357.

107 X. Zhang , W. J. Wu, T. Tian, et al., Deposition of Transparent Conductive Mesoporous Indium Tin Oxide Thin Films by a Dip Coating Process, Materials Research Bulletin, 43 (2008), pp1016–1022.

108 M. J. Alam, D. C. Cameron, Characterisation of Transparent Conductive ITO Thin Films Deposited on Titanium Dioxide Film by a Sol-Gel Process, Surface and Coatings Technology, 142-144 (2001), pp776-780.

109 S. R. Ramanan, Dip coated ITO Thin-Films Through Sol-Gel Process Using Metal Malts, Thin Solid Films, 389(2001), pp207-212.

110 W. Tang and D. C. Cameron, Aluminum-Doped Zinc Oxide Transparent Conductors Deposited by the Sol-Gel Process, Thin Solid Films, 238 (1994), pp83-87.

111 M. Ohyama, H. Kozuka, T. Yoko, Sol-Gel Preparation of Transparent and Conductive Aluminum-Doped Zinc Oxide Films with Highly Preferential Crystal Orientation, J. Am. Ceram. Soc. 81 (1998), pp1622-1632.

112 E. Shigeno, K. Shimizu, S. Seki, et al., Formation of Indium-Tin-Oxide Films by Dip Coating Process Using Indium Dipropionate Monohydroxide, Thin Solid Films, 411 (2002), pp56-59.

113 W. Chen, J. Wang, M. R. Wang, Influence of Doping Concentration on the Properties of ZnO:Mn Thin Films by Sol-Gel Method, Vacuum, 81 (2007), pp894-898.

114 X. T. Hao, J. Ma, D. H. Zhang, et al., Thickness Dependence of Structural, Optical and Electrical Properties of ZnO:Al Films Prepared on Flexible Substrates, Applied Surface Science, 189(2002), pp 18-23.

115 H. Gómez-Pozos, A. Maldonado, M. Olvera, Effect of the [Al/Zn] Ratio in the Starting Solution and Deposition Temperature on the Physical Properties of Sprayed ZnO:Al Thin Films, Materials Letters, 61 (2007), pp1460-1464.

116 S. Y. Kuo, W. C. Chen, F. I. Lai, et al., Effects of Doping Concentration and Annealing Temperature on Properties of Highly-Oriented Al-Doped ZnO Films, Journal of Crystal Growth, 287 (2006), pp78–84.

117 R. B. Tahar, Structural and Electrical Properties of Aluminum-Doped Zinc Oxide Films Prepared by Sol–Gel Process, Journal of the European Ceramic Society, 25 (2005), pp3301–3306.

118 S. Bandyopadhyay, G. K. Paul, S. K. Sen, Study of Optical Properties of Sol–Gel Derived Films of ZnO, Solar Energy Materials & solar Cells, 71 (2002), pp103–113.

119 R. Ota, S. Seki, Y. Sawada, et al., Indium-Tin-Oxide Films Prepared by Dip Coating Using an Ethanol Solution of Indium Chloride and Tin Chloride, Surface and Coatings Technology, 169-170 (2003), pp521-524.

120 S. S. Park, J. D. Mackenzie, Sol-Gel-Derived Tin Oxide Thin Films, Thin Solid Films, 258 (1995), pp268-273.

121 R. D. Tarey and T. A. Raju, A Method for the Deposition of Transparent Conducting Thin Films of Tin Oxide, Thin Solid Films, 128 (1985), pp181-189.

122 K. M. Lin, P. Tsai, Growth Mechanism and Characterization of ZnO: Al Multi-layered Thin Films by Sol–Gel Technique, Thin Solid Films, 515 (2007), pp 8601–8604.

123 S. S. Park, J. D. Mackenzie, Sol-Gel-Derived Tin Oxide Thin Films, Thin Solid Films,

258 (1995), pp268-273.

124 Z. H. Li, D. Y. Ren, Preparation of ITO Transparent Conductive Film by Sol-Gel Method, Trans. Nonferrous Met. Soci. China, 16 (2006), pp1358-1361.

125 H. M. Zhou, D. Q. Yi, Z. M. Yu, et al., Preparation of Aluminum Doped Zinc Oxide Films and the Study of Their Microstructure, Electrical and Optical Properties, Thin Solid Films, 515 (2007), pp6909–6914.

126 K. Daoudi, B. Canut, M.G. Blanchin, et al., Densification of In_2O_3:Sn Multilayered Films Elaborated by the Dip-Coating Sol–Gel Route, Thin Solid Films, 445 (2003), pp20-25.

127 G. Scherer, Sintering of Sol-Gel Films, Journal of Sol-Gel Science and Technology, 8 (1997), pp353-363.

128 S. Kang, Sintering, Linacre House, oxford, 2005, chapter 6. pp90-96.

129 M. J. Alam, D. C. Cameron, Characterisation of Transparent Conductive ITO Thin Films Deposited on Titanium Dioxide Film by a Sol-Gel Process, Surface and Coatings Technology, 142-144 (2001), pp776-780.

130 M. Gross, A. Winnacker, P. Wellmann, Electrical, Optical and Morphological Properties of Nanoparticle Indium–Tin–Oxide Layers, Thin Solid Films, 515 (2007), pp8567–8572.

131 J. Zhang, K. H. Au, Z. Q. Zhu, S. O'Shea, Sol–Gel Preparation of Poly(ethylene glycol) Doped Indium Tin Oxide Thin Films for Sensing Applications, Optical Materials, 26 (2004), pp 47–55.

132 C. Su, T. K. Sheu, Y. T. Chang, et al., Preparation of ITO Thin Films by Sol-Gel Process and Their Characterisations, Synthetic Metals, 153 (2005), pp9-12.

133 A. Beaurain, D. Luxembourg, C. Dufour, et al., Effects of Annealing Temperature and Heat-Treatment Duration on Electrical Properties of Sol-Gel Derived Indium-Tin-Oxide Thin Films, Thin Solid Films, 516 (2008), pp4102-4106.

134 A. R. Phani, M. Passacantando, S. Santucci, Synthesis and Characterisation of Zinc Aluminium Oxide Thin Films by Sol–Gel Technique, Materials Chemistry and Physics, 68 (2001), pp66–71.

135 S. Y. Kuo, W. C. Chen, F. I Lai, et al., Effects of Doping Concentration and Annealing Temperature on Properties of Highly-Oriented Al-Doped ZnO Films, Journal of Crystal Growth, 287 (2006), pp78–84.

136 S. Bandyopadhyay, G. K. Paul, S. Sen, Study of Optical Properties of Sol–Gel Derived Films of ZnO, Solar Energy Materials & solar Cells, 71 (2002), pp103–113.

137 Y. S. Kim and W. P. Tai, Electrical and Optical Properties of Al-Doped ZnO Thin Films by Sol–Gel Process, Applied Surface Science, 253 (2007), pp4911-4916.

138 J. Chen, J. Wang, F. Zhang, et al., The Effect of La Doping Concentration on the Properties of Zinc Oxide Films Prepared by the Sol-Gel Method, Journal of Crystal Growth , 310 (2008), pp2627-2632.

139 International Center for Diffraction Data, 21-1250.

140 W. J. Li, E. W. Shi, W. Z. Zhong and Z. W. Yin, Growth Mechanism and Growth Habit of Oxide Crystal, J. Crystal Growth, 203 (1999), pp186-196.

141 S. I. Hirano, Hydrothermal Processing of Ceramics, Am. Ceram. Soc. Bull., 66 (1987), pp1342-1344.

142 G. Rossetti, D. Watson, R. Newnham, J. Adair, Kinetics of the Hydrothermal Crystallization of the Perovskite Lead Titanate, J. Cryst. Growth, 116 (1992), pp251-259.

143 H. Kumazawa, T. Kagimoto, A. Kawabata, Preparation of Barium Titanate Ultra-fine Particles from Amorphous Titania by a Hydrothermal Method and Specific Dielectric Constants of Sintered Discs of the Prepared Particles, J. Mater. Sci., 31 (1996), pp2599-2602.

144 P. K. Dutta, J. R. Gregg, Hydrothermal Synthesis of Tetragonal Barium Titanate, Chem. Mater., 4 (1992), pp843-846.

145 C. H. Lu, S.Y. Lo, Lead Pyronibate Pyrochlore Nanoparticles Synthesized via Hydrothermal Processing, Mater. Res. Bull., 32 (1997), pp371-378.

146 O. Söhnel and J. Garside, Precipitation-Basic Principles and Industrial Applications, Butterworth-Heinemann Ltd, Oxford, 1992.

147 T. A. Ring, Fundamentals of Ceramic Powder Processing and Synthesis, Academic

Press, Inc., 1996.

148 H. R. Xu and L. Gao, Tetragonal Nanocrystalline Barium Titanate Powders: Preparation, Characterisation, and Dielectric Properties, J. Am. Ceram. Soc., 86 (2003), pp203–205.

149 I. Clark, T. Takeuchi, N. Ohtori, et al., Hydrothermal Synthesis and Characterisation of $BaTiO_3$ Fine Powders: Precursors, Polymorphism, and Properties, J. Mater. Chem., 9 (1999), pp83–91.

150 U. Schubert and N. Husing, Synthesis of Inorganic Materials, WILEY-VCH Verlag GmbH & Co. KGaA, 2005.

151 D. Yu, D. Wang, W. Yu, et al., Synthesis of ITO Nanowires and Nanorods with Corundum Structure by a Co-precipitation-Anneal Method, Materials Letters, 58 (2003), pp 84– 87.

152 P. Innocenzi, L. Malfatti, T. Kidchob, et al.,, Kinetics of Polycondensation Reactions during Self-assembly of Mesostructured Films Studied by in situ Infrared Spectroscopy, Chem. Rev., (2005), pp2384-2386.

153 K. H. Lii, Y. F. Huang, V. Zima, et al., Syntheses and Structures of Organically Templated Iron Phosphates, Chem. Mater., 10 (1998), pp2599-2609.

154 Z. Wang, X. F. Qian, J. Yin, et al., Aqueous Solution Fabrication of Large-Scale Arrayed Obelisk-like Zinc Oxide Nanorods with High Efficiency, J. Solid State Chem., 177 (2004), pp2144-2149.

155 J. Lu, J. Davis, P. Seaman, et al., Size and Morphology Control of Cerium-Titanium Oxide Nanoparticles Through Hydrothermal Synthesis, Ceramic Nanomaterials and Nanotechnology III, pp11-19.

156 R. Clemente, A. Macipe, J. Morales, et al., Hydroxyapatite Precipitation: A Case of Nucleation-Aggregation-Agglomeration-Growth Mechanism, Journal of the European Ceramic Society, 18 (1998), pp1351-1356.

157 G. D. Agli and G. Mascolo, Agglomeration of 3 mol% Y-TZP Powders Synthesised by Hydrothermal Treatment, J. Eur. Ceram. Soc., 21 (2001), pp29–35.

158 C. N. R Rao, A. Muller, A. K. Cheetham, Nanomaterials Chemistry, 2007, Wiley-VCH

Verlag GmbH &Co. KGaA,. pp139-142.

159 J. O. Eckert Jr., C. Hung-Houston, B. L. Gersten, et al., Kinetics and Mechanism of Hydrothermal Synthesis of Barium Titanate, Journal of American Ceramic Society, 79 (1996), pp2929-2939.

160 A. Randolph, E. White, Modelling Size Dispersion in the Prediction of Crystal Size Distribution, Chem. Eng. Sci., 32 (1997), pp1067-1076 .

161 L. Pleskach and G. Chirkova, Effect of Precipitation Conditions on the Formation Rate of Barium Sulfate Precipitates, Zhurn. Annl. Khim., 26 (1971), pp2290-2297.

162 H. Lu, C. H. Yeh, Influence of Hydrothermal Conditions on the Morphology and Particle Size of Zinc Oxide Powder, Ceramics International, 26 (2000), pp351-357.

163 D. Chulia, M. Deleuil and Y. Pourcelot, Powder Technology and Pharmaceutical Process, Elsevier Science B.V., Netherlands, 1994.

164 J. Nyvlt, I dustrial Crystallization: The State Art, 2nd edition, Verlag Chemie, Weinheim, Germany, 1982.

165 H. Zhang, D. Yang, X. Ma, et al., Synthesis of Flower-like ZnO Nanostructures by an Organic-free Hydrothermal Process, Nanotechnology, 15 (2004), pp 622-626.

166 H. Zhang, D. Yang, Y. Ji, et al., Low Temperature Synthesis of Flowerlike ZnO Nanostructures by Cetyltrimethylammonium Bromide-Assisted Hydrothermal Process J. Phys. Chem. B, 108(13) (2004), pp3955-3958.

167 L. Liao, D. Liu, J. Li, et al., Synthesis and Raman Analysis of 1D-ZnO Nanostructure via Vapor Phase Growth, Appl. Sur. Sci., 240 (2005), pp175-179.

168 J. Yang, J. Zheng, H. Zhai, et al., Low Temperature Hydrothermal Growth and Optical Properties of ZnO Nanorods, Cryst. Res. Technol., 44 (2009), pp87-91.

169 N. Fujimura, T. Nishihara, S. Goto, et al., Control of Preferred Orientation for ZnOx Films: Control of Self-texture, J. Cryst. Growth, 130 (1993), pp269–279.

170 X. Shi, M. Li, H. Yang, et al., PEG-300 Assisted Hydrothermal Synthesis of $4ZnO\cdot B_2O_3\cdot H_2O$ nanorods, Materials Research Bulletin, 42 (2007), pp 1649-1656.

171 Z. Q. Li, Y. J. Xiong, and Y. Xie, Selected-Control Synthesis of ZnO Nanowires and Nanorods via a PEG-Assisted Route, Inorg. Chem., 42 (2003), pp8105-8109.

172 J. Dobryszycki, S. Biallozor, On Some Organic Inhibitors of Zinc Corrosion in Alkaline Media, Corros. Sci., 43 (2001), pp1309-1319.

173 X. H. Liu, J. Yang, L. Wang, et al., An Improvement on Sol-Gel Method for Preparing Ultrafine and Crystallized Titania PowderMater. Sci. Eng. A, 289 (2000), pp241-245.

174 I. Chambouleyron, D. Comedi, Column III and V Elements as Substitutional Dopants in Hydrogenated Amorphous Germanium, J. Non-Cryst. Solids, 230A (1998), pp411-417.

175 S. Suwanboon, P. Amornpitoksuk, A. Haidoux, et al., Structural and Optical Properties of Undoped and Aluminium Doped Zinc Oxide Nanoparticles via Precipitation Method at Low Temperature, Journal of Alloys and Compounds, 462 (2008), pp335–339.

176 R. W. Kelsall, I. W. Hamley, M. Geoghegan, Nanoscale Science and Technology, John Wiley & Sons, 2006, pp237–281.

177 K. Jayanthi, S. Chawla, K. N. Sood, et al., Dopant Induced Morphology Changes in ZnO Nanocrystals, Appl. Surf. Sci., (2009), doi:10.1016/j.apsusc.2009.01.032.

178 M. Alfredsson, F. Corà, D. P. Dobson, et al., Dopant Control over the Crystal Morphology of Ceramic Materials, Surface Science, 601 (2007), pp4793-4800.

179 International Center for Diffraction Data, 71-2194.

180 J. Zhang, K. Au, Z. Zhu et al., Sol–Gel Preparation of Poly(ethylene glycol) Doped Indium Tin Oxide Thin Films for Sensing Applications, Optical Materials, 26 (2004), pp47–55.

181 L. C. Klein, Sol-Gel Technology for Thin Films, Fibers, Performs, Electronics, and Specialty Shapes, Noyers Publications, New Jersey, USA, 1998, pp51-52.

182 D. Satas, Coatings Technology Handbook, Marcel Dekker, Inc., New York, 1991, p655.

183 M. Epifani, M. Alvisi, L. Mirenghi, et al., Sol–Gel Processing and Characterization of Pure and Metal-Doped SnO_2 Thin Films, J. Am. Ceram. Soc., 84 (2001), pp48–54.

184 C. J. Brinnker and G. W. Scherer, Sol-Gel Science, Acad. Press, San Diego, CA, 1990.

185 G. W. Scherer, Drying Gels: VIII. Revision and Review, J. Non-Cryst. Solids, 109 (1989), pp171-182.

---

186 G. W. Scherer, Theory of Drying, J. Am. Ceram. Soc., 73 (1990), pp3-14.

187 Lisa C. Klein, Sol-Gel Optics Processing and Application, Kluwer Academic Publishers, USA, 1994.

188 T. F. Stoica, V. S. Teodorescu, M. G. Blanch, et al., Morphology, Structure and Optical Properties of Sol-Gel ITO Thin Films, Materials science and engineering, B101(2003), pp222-226.

189K. Daoudi, C. S. Sandu, V. S. Teodorescu, Rapid thermal annealing procedure for densification of sol-gel indium tin oxide thin films, Crystal Engineering, 5 (2002), pp187–193.

190 S. C. Albonetti, L. Forni, Solvothermal Synthesis and Properties Control of Doped ZnO Nanoparticles, Journal of Colloid and Interface Science, 329 (2009), pp73–80.

191 S. N. Misra, S. Shukla, and M. A. Gagnani, Neodymium(III)-Substituted Bismuth Titanate Thin Film Generation Using Metal Alkoxo, Acyloxo, and β-Diketonato Precursors Employing a Sol–Gel Route and Using 4f –4f Transition Spectra as Probes to Explore Kinetic Performance, Journal of Colloid and Interface Science 271 (2004), pp174–180.

192 X. H. Zhong, Y. Feng, Y. L. Zhang, etal., Nonhydrolytic Alcoholysis Route to Morphology-Controlled ZnO Nanocrystals, small, (7) 2007, pp1194 –1199.

193 G. Clavel, M. Willinger, D. Zitoun, et al., Solvent Dependent Shape and Magnetic Properties of Doped ZnO Nanostructures, Adv. Funct. Mater., (17) 2007, pp 3159-3169.

194 G. Rodriguez-Gattorno, P. Santiago-Jacinto, I. Rendon-Vazquez, et al., Novel Synthesis Pathway of ZnO Nanoparticles from the Spontaneous Hydrolysis of Zinc Carboxylate Salts, J. Phys. Chem. B, 107 (2003), pp12597-12604.

195 L. Znaidi, G. J. Soler Illia, R. L. E. Guennic, et al., Elaboration of ZnO Thin Films with Preferential Orientation by a Soft Chemistry Route, Journal of Sol-Gel Science and Technology, 26 (2003), pp817–821.

196 A. Y. Oral, Z. B. Bahsi, M. H. Aslan, Microstructure and Optical Properties of Nanocrystalline ZnO and ZnO:(Li or Al) Thin Films, Applied Surface Science , 253

(2007), pp4593–4598.

197 K. Lin, P. Tsai, Parametric Study on Preparation and Characterization of ZnO:Al Films by Sol–Gel Method for Solar Cells, Materials Science and Engineering B, 139 (2007), pp81–87.

198 E. F. Schubert, Doping in Ⅲ- Ⅴ Semiconductors, The Press Syndicate of the University of Cambridge, Cambridge, 1993, pp1-5.

199 R. A. Street, Amorphous Semiconductors: Doping, Encyclopedia of Materials: Science and Technology, 2008, pp 264-270.

200 G. Neri, A. Bonavita, G. Micali, et al., A Study on the Microstructure and Gas Sensing Properties of ITO Nanocrystals, Thin Solid Films, 515 (2007) , pp8637–8640.

201 D. B. Fraser, H. D. Cook, Highly Conductive, Transparent Films of Sputtered $In_{2-x}SnxO_{3-y}$, J. Electrochem. Soc., 119 (1972), pp1368-1374.

202 H. Kostlin, R. Jost, W. Lems, Optical and Electrical Properties of Doped In_2O_3 Films, Phys. Status Solidi, A 29 (1975), pp87- 93.

203 Y. Djaoued, V. H. Phong, S. Badilescu, et al, Sol-Gel-Prepared ITO Films for Electrochromic Systems, Thin Solid Films, 293 (1997), pp108-112.

204 K. Nishio, T. Sei and T. Tsuchiya, Preparation and Electrical Properties of ITO Thin Films by Dip-Coating Process, Journal of Materials Science, 31 (1996), pp1761-1766.

205 Z. Q. Xu, H. Deng, Y. Li, et al., Characteristics of Al-Doped C-Axis Orientation ZnO Thin Films by Sol-Gel Method, Materials Research Bullutin, 41 (2006), pp354-358.

206 S. Mridha, D. Basak, Aluminium Doped ZnO Films:Electrical, Optical and Photoresponse Studies, J. Phys. D: Appl. Phys., 40 (2007), pp6902–6907.

207 S. L. Kang, Sintering, Elsevier Butterworth-Heinemann, Oxford, UK, 2005, pp53-55.

208 Y. S. Kim , W. P. Tai, Electrical and Optical Properties of Al-Doped ZnO Thin Films by Sol–Gel Process, Applied Surface Science, 253 (2007), pp4911–4916.

209 H. M. Zhou, D. Q. Yi, Z. M. Yu, et al., Preparation of Aluminum Doped Zinc Oxide Films and the Study of Their Microstructure, Electrical and Optical Properties, Thin Solid Films, 515 (2007), pp6909–6914.

210 P. K. Manoj, B. Joseph, V. K. Vaidyan, et al., Preparation and Characterization of

Indium-Doped Tin Oxide Thin Films, Ceramics International, 33 (2007), pp273–278.

211 Y. Ohhata, F. Shinoki and S. Yoshida, Optical Properties of R.F. Reactive Sputtered Tin-Doped In_2O_3 Films,Thin solid films, 59 (1979), pp255-261.

212 Y. Takahashi, S. Okada, R. Tahar, et al., Dip-Coating of ITO Films, Journal of Non-Crystalline Solids, 218 (1997), pp129-134.

213 M. Yamaguchi, K. Maruta, M. Sugawara, et al., Analysis of Optimum Sheet Resistance for Integrated Electromagnetic Noise Suppressor, Magnetics Conference, 2006, pp61 – 61.

214 J. P. Chatelon, C. Terrier and J. A. Roger, Electrical and Optical Property Enhancement in Multilayered Sol-Gel-Deposited SnO_2 Films, Semicond. Sci. Technol., 14(1999), pp642–647.

215 A. De, P. K. Biswas, J. Manara, Study of Annealing Time on Sol–Gel Indium Tin Oxide Films on Glass, Materials Characterization , 58 (2007), pp 629–636.

APPENDIX

Appendix 1 TGA-DTA for $Zn(OH)_2$

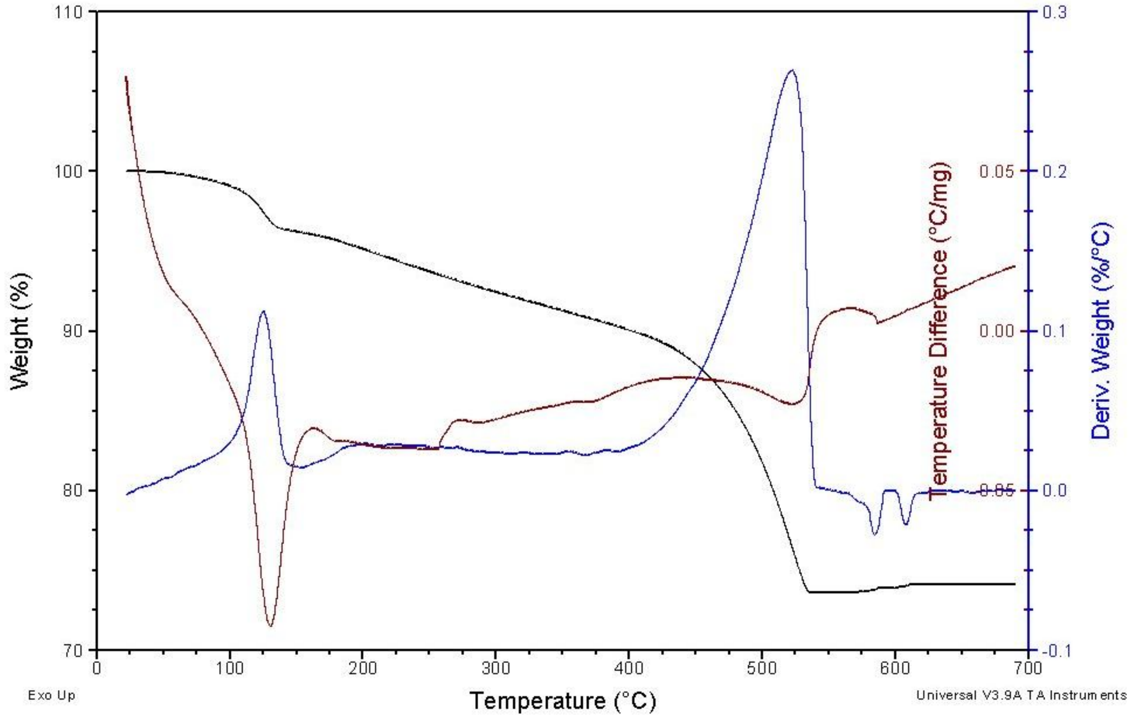

Appendix 2 Sheet resistance and resistivity of ITO thin film annealed at different temperatures varied with grain size

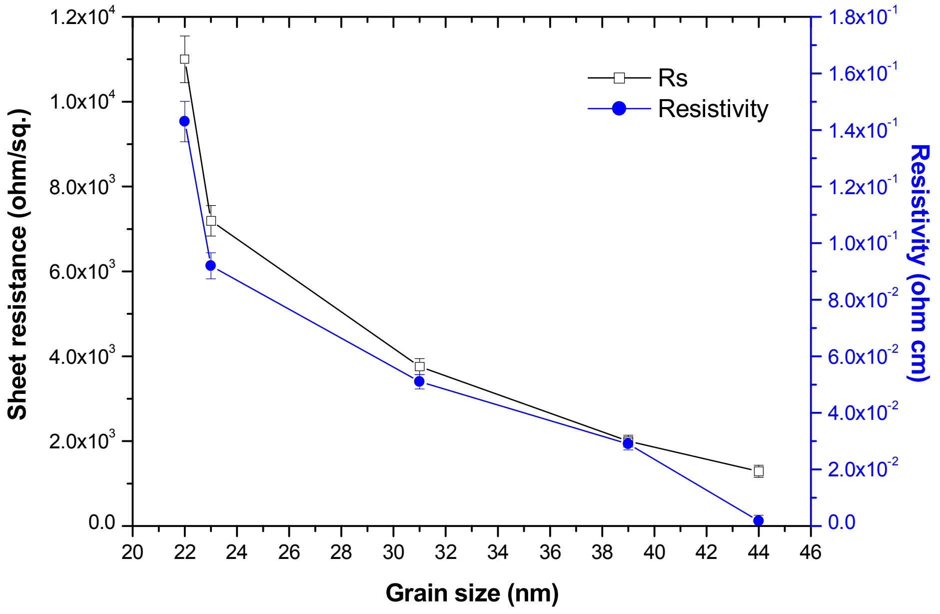

Appendix 3 Sheet resistance and resistivity of ITO thin film annealed at 600 °C for different durations varied with grain size

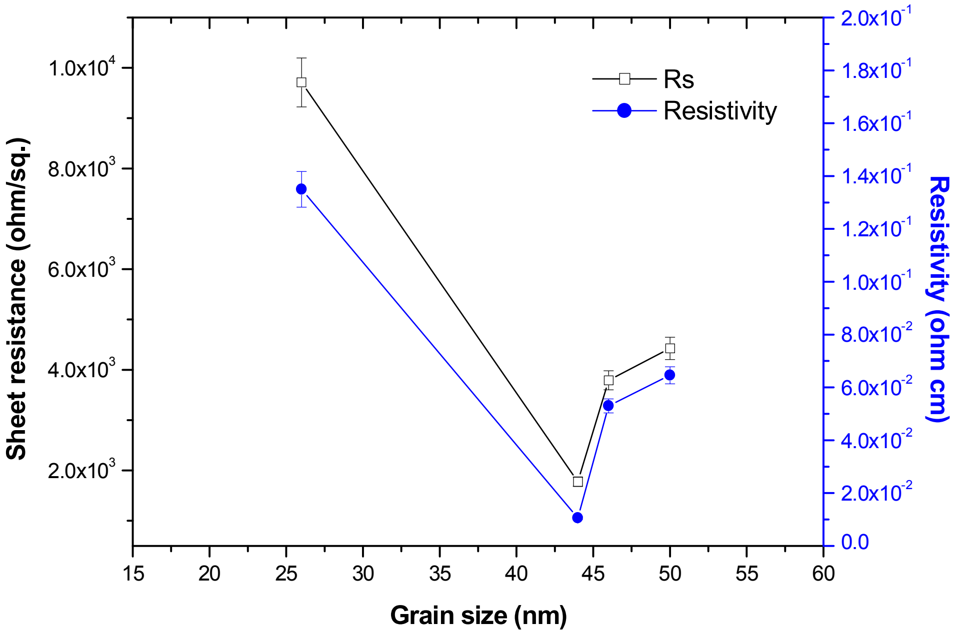

Appendix 4 Sheet resistance and resistivity of ITO thin film prepared using different concentrations of starting salt varied with thickness

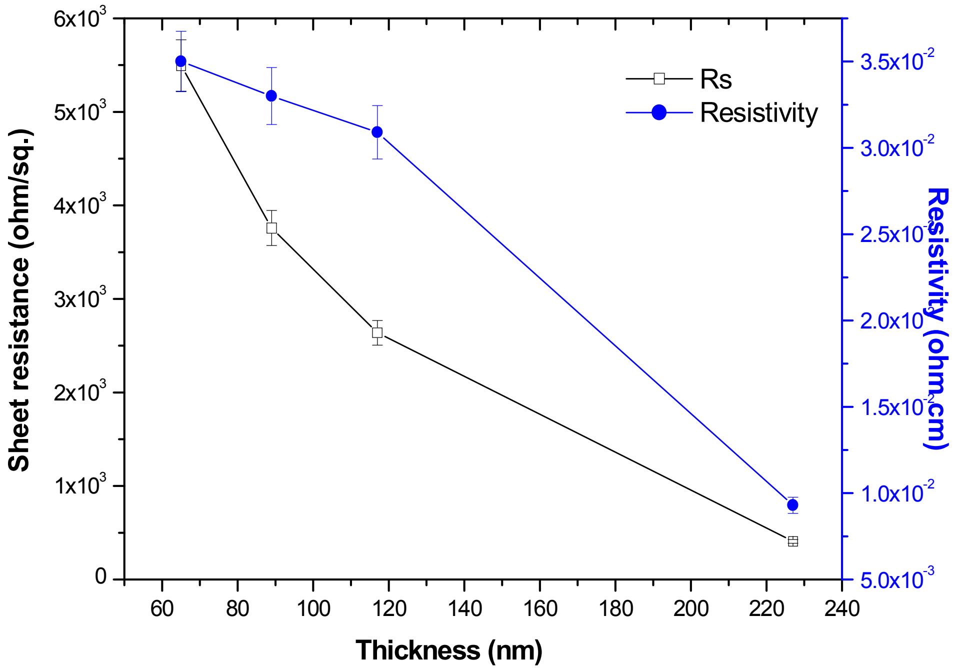

Appendix 5 Sheet resistance and resistivity of ITO thin film with different numbers of deposit layer varied with thickness

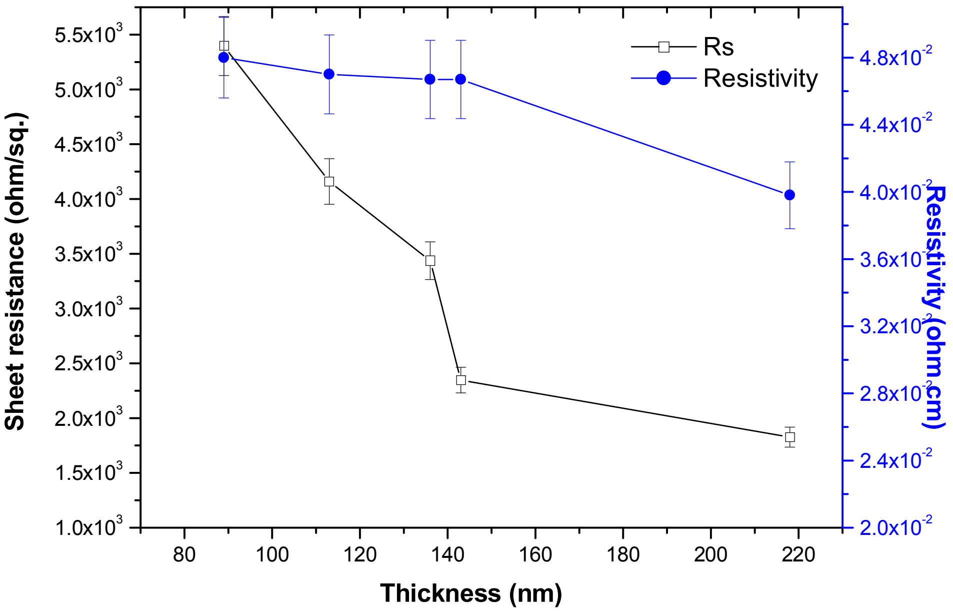

Appendix 6 Sheet resistance and resistivity of AZO thin film annealed for durations varied with thickness

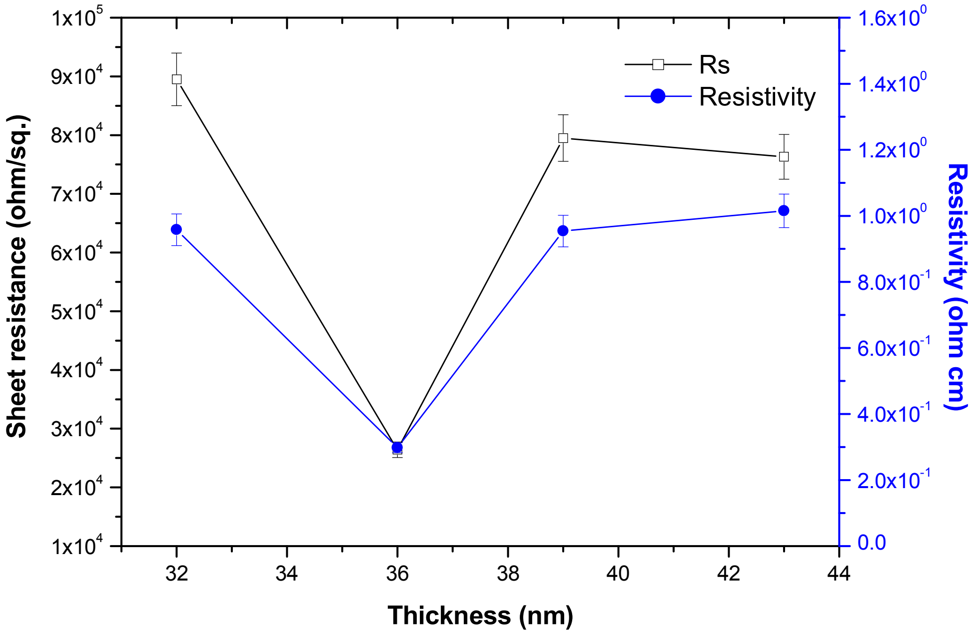

Appendix 7 Sheet resistance and resistivity of AZO thin film prepared using different concentrations of starting salt varied with thickness

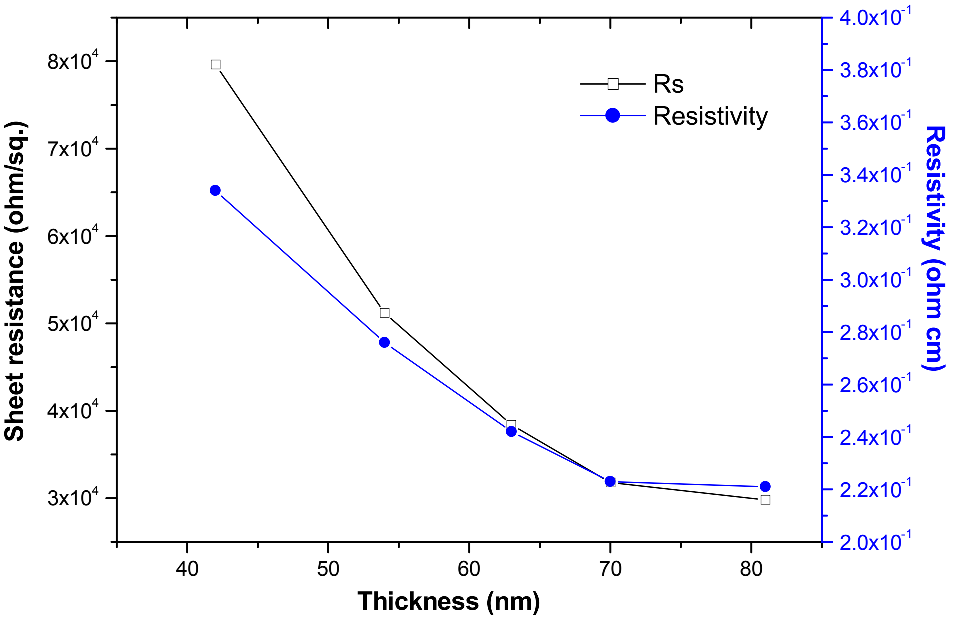

Appendix 8 Sheet resistance and resistivity of AZO thin film with different numbers of deposit layer varied with thickness

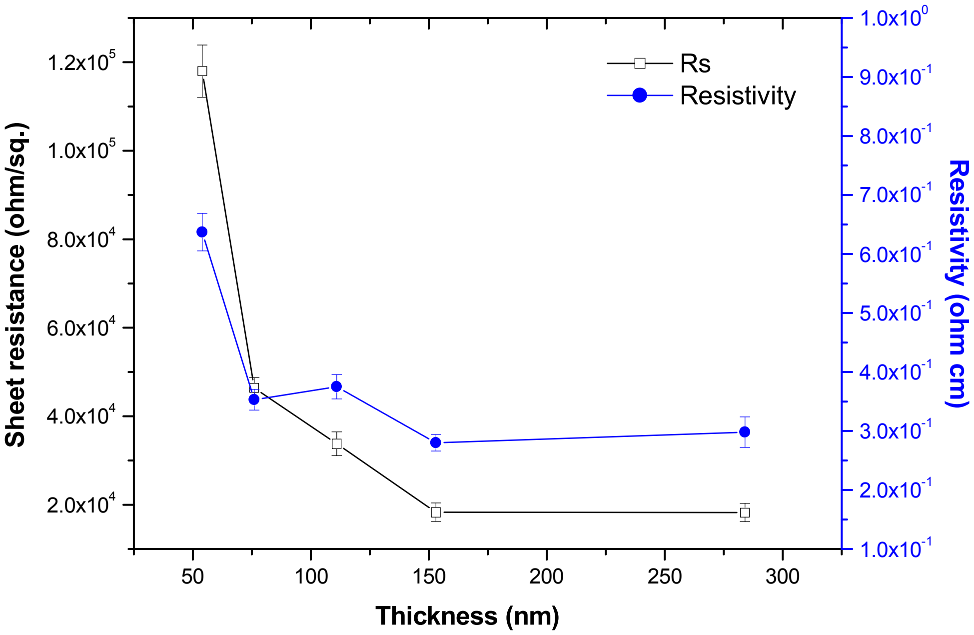

Appendix 9 Pubished paper

Dongxin Wang, Xujin Bao, Jingming Zhong, Benshuan Sun, Jianrong Zhang, Tin Oxide Nanoparticles with Controlled Morphology and Particle Size synthesised by Hydrothermal Method, *Chinese Journal of Inorganic Chemistry*, 24 (2008), pp892-896.

Abstract

Tin oxide nanoparticles with different particle sizes and morphologies were synthesised by varying the concentration, heating temperature and duration time by hydrothermal method. The particles were characterised by X-ray diffraction (XRD) and transmission electron microscopy (TEM). The TEM micrographs show that spherical, rod-like, oval and Hexagonal shaped nanoparticles with particle sizes from 10 nm to 120 nm are synthesised when the parameters of synthesis are changed. XRD patterns indicate that all of nanoparticles synthesised are with the structure of tin oxide

第 24 卷第 6 期
2008 年 6 月

无 机 化 学 学 报
CHINESE JOURNAL OF INORGANIC CHEMISTRY

Vol.24 No.6
892~896

水热合成法对纳米氧化锡粉体粒径和形貌的控制研究

王东新*,1,2 钟景明 1 孙本双 1 BAO X2 张建荣 3
(1 宁夏东方钽业股份有限公司,石嘴山 753000)
(2IPTME, Loughborough University, Loughborough, Leicestershire, LE11 3TU, UK)
(3 华东理工大学,上海 200237)

摘要： 利用氯化锡和氨水作为反应试剂,通过水热合成技术制备了近球形,棒状,椭球形,六角形等粉体形貌和粒径范围从 4 nm 至 120 nm 的纳米氧化锡粉体,并对水热合成条件对粉体的粒径和形貌的影响进行了研究。所制备的粉体的 XRD 分析结果显示,合成温度在 160 ℃以上并且合成时间在 3 h 以上,粉体全部具有氧化锡晶体结构。利用透射电镜对粉体的粒径和形貌观察发现,二氧化锡粉体的形貌和粒径可通过改变溶液的浓度,合成温度与合成时间进行有效的控制,其中合成温度与溶液浓度不仅可以控制合成粉体的粒径,而且可以控制粉体的形貌。

关键词： 氧化锡；水热合成；纳米粉体
中图分类号： TN304.21 **文献标识码：** A **文章编号：** 1001-4861(2008)06-0892-05

Tin Oxide Nanoparticles with Controlled Morphology and Particle Size by Hydrothermal Method

WANG Dong-Xin*,1,2 ZHONG Jing-Ming1 SUN Ben-Shuang1 BAO X2 ZHANG Jian-Rong3
(*1Ningxia Orient Tantalum Industry Co. Ltd., Shizuishan, Ningxia 753000*)
(*2IPTME, Loughborough University, Louhborough, Leicestershire, LE11 3TU, UK*)
(*3East China University of Science and Technology, Shanghai 200237*)

Abstract: Tin oxide nanoparticles with different particle sizes and morphologies were synthesised by varying the concentration, heating temperature and duration time by hydrothermal method. The particles were characterised by X-ray diffraction(XRD) and transmission electron microscopy(TEM). The TEM micrographs show that spherical, rod-like, oval and Hexagonal shaped nanoparticles with particle sizes from 4 nm to 120 nm are synthesised when the parameters of synthesis are changed. XRD patterns indicate that all of nanoparticles synthesised are with the structure of tin oxide.

Key words: tin oxide; hydrothermal synthesis; nanoparticle

0 引 言

纳米材料因具有量子尺寸效应，小尺寸效应和表面效应等,因而在光、电、热、磁等方面具有很多的特殊性能并得到了广泛研发[1]。氧化锡作为一种具有宽能带(E_g=3.6 eV)n 型半导体材料,是研究和应用最早的气敏材料之一[2,3]。由于其具有稳定的化学和机械性能,并兼具透明导电的特性,自 1962 年以来,氧化锡在家庭、商业和工业领域都得到了广泛的应用[4],诸如气敏探测器[5-8],电极材料[9]以及太阳能电池[10,11]等等。制备 SnO_2 纳米粉体的常用方法有液相沉淀法、微乳液法、化学气相沉积法、溶胶凝胶法和

收稿日期:2008-01-14。收修改稿日期:2008-03-07。

*通讯联系人。E-mail:wangdongxin123@hotmail.com

第一作者:王东新,男,35 岁,博士生;研究方向:纳米材料的研发与产业化。

水热合成法等。其中水热合成法与其他合成技术相比较，该方法所合成的粉体结晶度高，晶态完整，粉体粒径分布范围窄且形貌易于控制[12]。有关水热法制备 SnO_2 粉体的文献报道很多，但所合成的 SnO_2 粉体的粒径基本为 10 nm 以下，粉体的形貌特征也难以分辨[13]。在探测器制作和光化学、物理作用方面，基于 SnO_2 制造的电子设备的物化性能与其粉体的晶体结构、形貌和粒径密切相关[14,15]，因为二氧化锡材料的气敏效应是属于晶粒表面控制型的[16]。因此，有效控制所合成二氧化锡粉体的形貌和粒径具有十分重要的应用价值。虽然也有研究者利用水热法合成出了长度在 20 nm 以下的棒状 SnO_2，但其使用了有机溶剂作为辅助介质[17]。有机溶剂的使用，不仅污染环境，而且也对人体有害，为非绿色制备技术，同时对于工业生产又增加了生产成本。而本工作使用去离子水作为反应介质，通过有效控制合成温度、时间以及反应物浓度，成功制备了形貌和粒径可控的 SnO_2 纳米粉体。

1 实验部分

1.1 纳米粉体合成

试剂：$SnCl_4\cdot5H_2O$(纯度为 99.0%，如皋化学试剂厂)；质量比为 25%的氨水(Fisher Scientific, UK)；去离子水为实验室自制。

首先将不同物质的量的 $SnCl_4\cdot5H_2O$ 晶体溶于 21 mL 去离子水中配制成物质的量浓度为 0.25，0.5，1.0，2.0 和 3.0 $mol\cdot L^{-1}$ 的溶液，并利用电磁搅拌器搅拌形成均匀溶液后，滴加 25%的 $NH_3\cdot H_2O$ 至溶液的 pH=11。最后将配制的溶液转入容积为 30 mL 的反应釜内，并保持反应釜的体积填充度为 70%。将密封后的反应釜放置于温度可控的干燥箱中在不同温度(160~220 ℃)和不同处理时间(6~48 h)下合成粉体。然后自然冷却至室温并将粉体收集，用去离子水离心清洗 5~10 次，直至用 $AgNO_3$ 检测无 Cl^-。最终将粉体在 100 ℃烘干 12 h，备用。

1.2 纳米粉体表征

粉体的物相分析采用 Bruker D8 型 X 射线衍射仪进行，辐射源为铜靶(Cu $K\alpha_1$=0.154 06 nm)，扫描速率为 $0.02°\cdot s^{-1}$，2θ 角的测量范围为 10°~90°。利用 JOEL-2000FX 透射电子显微镜(TEM，加速电压 200 kV)对粉体的形貌和颗粒尺寸进行观察测定。电镜样品制备是将粉体研磨后分散于无水乙醇中，并用超声波分散 5~10 min，然后将悬浊液滴于覆有碳膜的铜网上，待酒精挥发干后，上镜观察。

2 结果与讨论

2.1 合成温度对粉体形貌和粒径的影响

反应起始溶液浓度为 0.5 $mol\cdot L^{-1}$，在不同温度水热处理 48 h 下合成粉体的 XRD 图(图 1)显示，在 160 ℃以上合成的粉体具有相同的晶体结构，各衍射峰位与标准 XRD 卡片(PDF No.41-1445)的数据基本一致，合成粉体的晶体结构为四方相 SnO_2。从 SnO_2 的衍射图上可以看出，各衍射峰随着温度的增加逐渐变得尖锐，且相对衍射强度不断提高，说明 SnO_2 粉体的结晶度随着温度的提高而逐渐增加。同时，在温度相对较低的情况下(160 ℃和 180 ℃)，晶面(110)的衍射峰半高宽较大，但当温度增加到 200 ℃以上时，相同晶面的衍射峰半高宽明显减小。根据 Scherrer 公式可以判断合成粉体的晶粒度与水热处理温度成正比变化。通过 TEM 测量的粉体粒径由 160 ℃的 6.2 nm 增长到 220 ℃的 120 nm，粉体粒径表现为随着温度的增加而增大。这是由于在合成温度相对较低的情况下(如 200 ℃以下)，SnO_2 在去离子水中的溶解度较低，晶化后不容易再次溶解，因此合成的粉体的粒径一般都小于 10 nm[18]。但随着温度的进一步提高，反应釜中的温度和压强都不断增加，为晶粒的长大提供了驱动力和能量，同时使得一些粒径较小的颗粒不断溶解，而溶解后的颗粒的直接贡献是增加了溶液中溶质的浓度，这促使了较大颗粒进一步长大，这符合 Ostwald 熟化机制[19]。从 TEM 照片(图 2)可以看到：在相对较低温度 160 ℃下，SnO_2 粉体形貌为短棒状(图 2a)，当温度升至 200 ℃时，粉体的形貌变化为分散性良好的棒状(图2c)。进一步升高

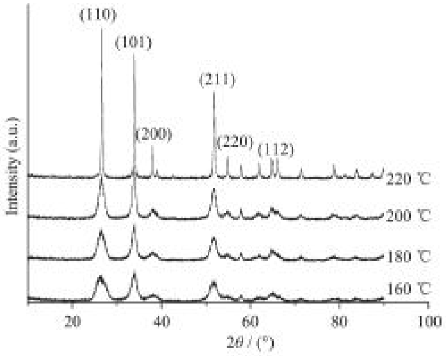

图 1 不同温度下合成粉体的 XRD 图

Fig.1 XRD results of the samples synthesised at different hydrothermal treatment temperatures

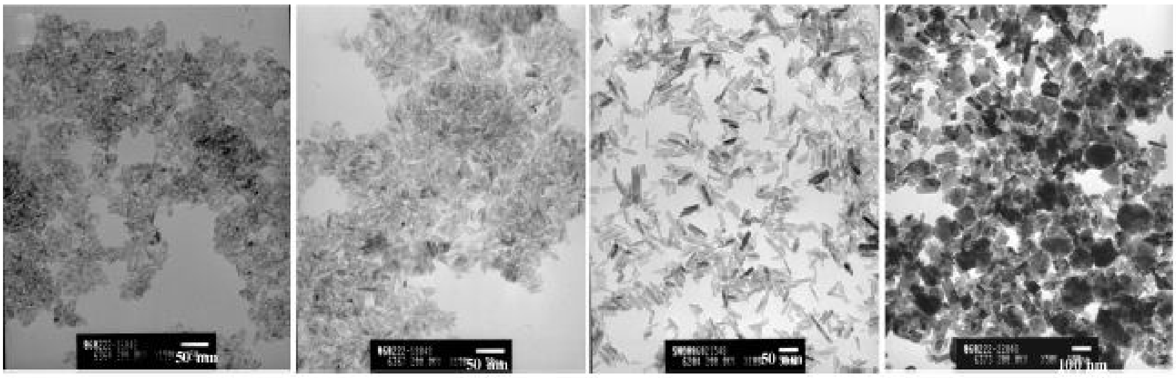

(a) 160 ℃ (b) 180 ℃ (c) 200 ℃ (d) 220 ℃

图2 不同温度下合成粉体的TEM形貌像

Fig.2 Morphologies of particles synthesised at different hydrothermal treatment temperatures

温度至220 ℃时，粉体的形貌由分散良好的棒状转化为六角形状(图2, d)。粉体形貌的改变还导致了粉体的XRD图(图1)的变化。从图中可以看到，棒状粉体的XRD普线的最强峰为(101)峰，但当粉体形貌由棒状转化为六角形状后，衍射最强峰也由(101)转变为(110)峰，说明棒状粉体在[101]晶向具有择优取向。粉体形貌在220 ℃时发生转变可能与水热过程中溶液中的NH_4^+浓度有关。有研究者发现NH_4^+在水热法合成金属氧化物过程中具有模板作用[20-22]。在温度低于200 ℃时，反应溶液中的NH_4^+浓度较大，NH_4^+能够发挥模板作用而形成棒状粉体。但当温度增加至220 ℃时，可能由于温度太高而使NH_4^+以气态NH_3逸出而导致溶液中NH_4^+浓度降低，从而弱化了其模板的作用而使合成粉体形貌发生改变。

2.2 合成时间的影响

为了研究水热处理时间对合成SnO_2粉体的形貌和粒径的影响，该实验中水热处理温度设定在200 ℃，起始溶液浓度为0.5 mol·L^{-1}，时间变化范围为6~48 h。图3是在不同处理时间下合成粉体的XRD衍射图。从图中可以看出在该实验条件下所合成的粉体均为SnO_2。通过TEM照片(图4)可以看到

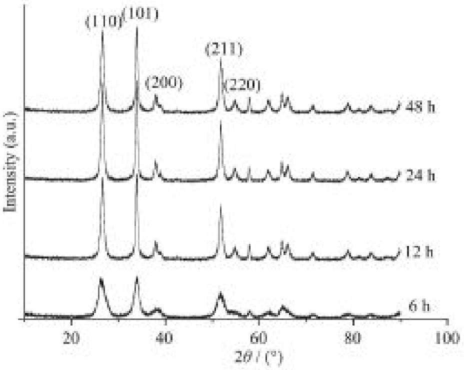

图3 不同水热处理时间合成粉体的XRD图

Fig.3 XRD patterns of the samples synthesised at 200 ℃ with different hydrothermal treatment time

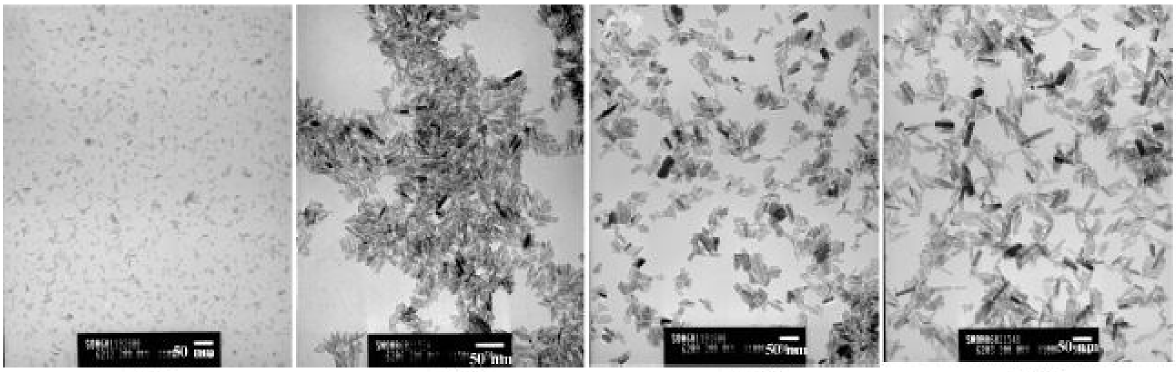

(a) 6 h (b) 12 h (c) 24 h (d) 48 h

图4 不同水热处理时间下合成粉体的形貌

Fig.4 Morphologies of tin oxide nanoparticles synthesised at 200 ℃ with different hydrothermal treatment time

在不同的水热处理时间所合成的 SnO_2 粉体具有不同粒径的棒状形貌。可见水热处理的时间仅仅影响合成粉体的粒径而不影响其形貌。但在处理时间为 6 h 时，形核的粒子没有足够的时间长大，形成粒径小于 10 nm 的纳米棒(图 4，a)。随着水热处理时间的不断延长至 48 h，SnO_2 粉体粒径也逐渐长大至 55 nm，而且粉体的表面也变得光滑(图 4，d)。这可能是由于在高温高压条件下，随着水热处理时间的延长，一些粒径较小的粒子被不断溶解而增加了溶液中可供颗粒生长的溶质的浓度，促使粒子进一步长大并且表面变得光滑。因此，通过不同的水热处理时间，可以有效控制棒状 SnO_2 粉体的粒径。

2.3　溶液浓度的影响

浓度是影响水热合成粉体粒径和形貌的另一个重要因素。合成温度和时间被设定为 200 ℃和 24 h，在反应物 $SnCl_4\cdot 5H_2O$ 的初始浓度为 0.25 $mol\cdot L^{-1}$ 时，合成的粉体是只有 4 nm 左右的近球形粒子(图 5，a)。随着反应物浓度增加至 1.0 $mol\cdot L^{-1}$，SnO_2 粉体的形貌由球形转变为棒状，粒径也增加至 30 nm 左右，该浓度下所合成粉体具有最大粒径(图 5，b)。在 $SnCl_4\cdot 5H_2O$ 浓度增加为 2.0 $mol\cdot L^{-1}$ 时，通过 TEM 照片(图 5，c)可以发现 SnO_2 粉体的粒径减小到 12 nm 左右，而且形貌也开始向椭球形转变。进一步增大反应物浓度至 3.0 $mol\cdot L^{-1}$ 时，SnO_2 粉体的形貌已经完全转化为椭球形状，但粉体的粒径不论是在长度方向还是径向都有所长大(图 5，d)。上述现象可能是因为在反应物浓度为 0.25 $mol\cdot L^{-1}$ 时，此时溶液中溶质的浓度太低，当形核完成后已经没有足够的溶质供粉体的进一步长大。在水热合成过程中形核数量与颗粒长大相互竞争，而在浓度为 1.0 $mol\cdot L^{-1}$ 的条件下可能满足了形核与颗粒长大的最佳条件，这样既保证了有一定的形核率又提供了颗粒的长大所需要的溶质浓度，合成的粉体粒径较大。当反应浓度增大为 2.0 $mol\cdot L^{-1}$，此时由于溶质浓度过大而导致成核率急剧增大，形核后溶液中尚有一定量的溶质供颗粒的进一步长大，但总体上粉体的粒径减小了，并且形貌有向椭球形转变的趋势。但进一步增大反应物至 3.0 $mol\cdot L^{-1}$ 后，由于溶液处于过饱和状态，在这种情况下可能形核与颗粒长大在短时间内都很迅速，而且溶液中又有足够的溶质成分供颗粒进一步长大，因而合成粉体的粒径又有所增加，且形貌也改变为椭球形。上述 SnO_2 粉体形貌的变化可能仍与 NH_4^+ 浓度有关系。在实验中使用 $NH_3\cdot H_2O$ 保持溶液的 pH 值为 11。在溶质浓度不断增大的情况下，相对而言，就降低了溶液中 NH_4^+浓度并降低了其作为模板的作用，导致了合成 SnO_2 粉体形貌的不断变化。可见通过控制反应物浓度就可以有效地控制合成 SnO_2 粉体的粒径和形貌。

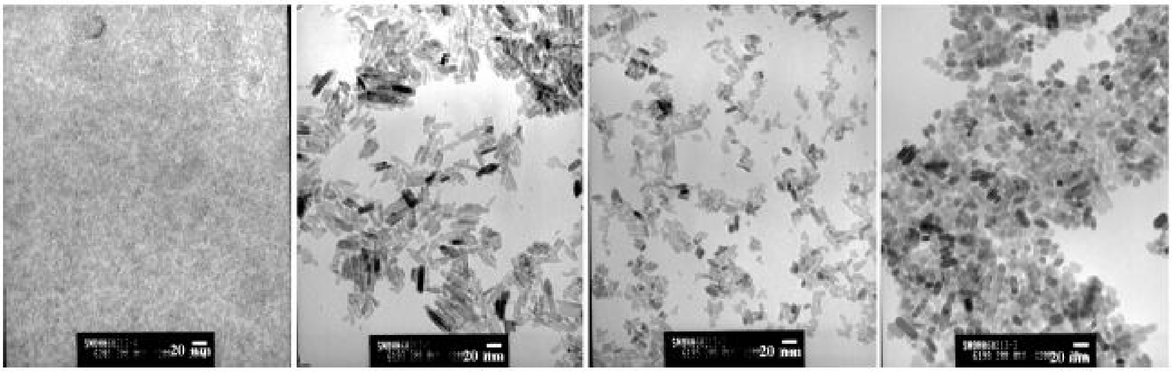

(a) 0.25 $mol\cdot L^{-1}$　(b) 1.0 $mol\cdot L^{-1}$　(c) 2.0 $mol\cdot L^{-1}$　(d) 3.0 $mol\cdot L^{-1}$

图 5　不同反应物浓度合成 SnO_2 粉体的 TEM 形貌

Fig.5　TEM micrographs of tin oxide nanoparticles synthesised using different concentrations of $SnCl_4\cdot 5H_2O$

3　结　论

水热合成温度，时间与溶液的浓度是影响合成纳米 SnO_2 粉体的形貌与粒径的重要实验参数。通过控制上述影响因素可以有效的控制纳米 SnO_2 粉体的粒径和形貌，其中合成温度与溶液的浓度不仅影响氧化锡粉体的粒径，而且影响粉体的形貌。通过控制合成温度，时间和溶液浓度，成功制备了粒径范围为 4 nm 至 120 nm 的近球形，棒状，椭球形以及六角形纳米粉体。

致谢：感谢英国 Loughborough University 与宁夏东方钽

业股份公司对此项目的技术和资金支持。

参考文献：

[1] Brirringer R, Gliter H, Klein H P, et al. *Phys. Lett.*, **1984**, **102A**(2):365~369

[2] Liu Y, Liu M L. *Adv. Funct. Mater.*, **2005**,**15**(1):57~62

[3] HOU De-Dong(侯德东), LIU Yin-Kai(刘应开). *J. Inorg. Mater.*(*Wuji Huaxue Xuebao*), **2002**,**17**(4):691~694

[4] Ihokura K, Watson J. *The Stannic Oxide Gas Sensor-Principles and Applications*. London: CRC Press, **1994**.

[5] Tamaki J, Nagaishi M, Teraoka Y, et al. *Surf. Sci.*, **1989**,**221**(1-2):183~196

[6] Wang Y L, Jiang X C, Xia Y N. *J. Am. Chem. Soc.*, **2003**, **125**(52):16176~16177

[7] Sahm T, Madler L, Gurlo A, et al. *Sensor Actuat. B*, **2004**, **98**:148~153

[8] Niranjan R S, Hwang Y K, Kim D K, et al. *Mater. Chem. Phys.*, **2005**,**92**(2):384~388

[9] Harreld J H, Sakamoto J, Dunn B. *J. Power Sources*, **2003**, **115**(1):19~26

[10]Chappel S, Zaban A. *Sol. Energ. Mat. Sol. C*, **2002**,**71**(2): 141~152

[11]Vishwakarma S R, Rahmatullah, Prasad H C. *Solid State Electron.*, **1991**,**36**:1345~1348

[12]Qian Y, Chen Q W, Chen Z Y, et al. *J. Mater. Chem.*, **1993**,**3**:203~206

[13]ZHANG Zi-Sheng (张子生), ZHANG Xiao-Jun (张晓军), WANG Wei-Wei (王伟伟), et al. *J. Synthetic Crystals* (*Rengong Jingti Xuebao*), **2006**,**35**(4):736~738

[14]Choi W, Termin A, Hoffmann M R. *J. Phys. Chem.*, **1994**,**98**(51):13669~13679

[15]Vlachos D S, Papadopoulos C A, Avaritsiotis J N. *J. Appl. Phys.*, **1996**,**80**:6050~6053

[16]CHEN You-Cun(陈有存), ZHANG Yuan-Guang(张元广). *Chinese J. Chem. Phys.* (*Huaxue Wuli Xuebao*), **2005**,**18**(6): 1015~1018

[17]Chen B, Russell, Shi M J, et al. *J. Am. Chem. Soc.*, **2004**, **126**(19):5972~5973

[18]WEI Zhi-Ren(韦志仁), LI Jun(李 军), LIU Chao(刘 超), et al. *J. Synthetic Crystals* (*Rengong Jingti Xuebao*), **2006**, **5**(1):107~109

[19]Fan W L, Zhao W, You L P, et al. *J. Solid State Chem.*, **2004**,**177**:4399~4403

[20]Soler-Illia G J de A A, Sanchez C, Lebeau B, et al. *Chem. Rev.*, **2002**,**102**(11):4093~4138

[21]Lii K H, Huang Y F, Zima V, et al. *Chem. Mater.*, **1998**,**10**: 2599~2609

[22]Wang Z, Qian X F, Yin J, et al. *J. Solid State Chem.*, **2004**, **177**(6):2144~2149

Appendix 10 Patents

Three patents were published in China shown as follows:

1 Dongxin wang, Xujin Bao, Jingming Zhong, Benshuan Sun, Synthesis of tin oxide with controlled morphology and size by hydrothermal method, published number: CN101565200A

[19] 中华人民共和国国家知识产权局

[51] Int. Cl.
C01G 19/02 (2006.01)
B82B 3/00 (2006.01)

[12] 发明专利申请公布说明书

[21] 申请号 200910117305.X

[43] 公开日 2009 年 10 月 28 日

[11] 公开号 CN 101565200A

[22] 申请日 2009.6.4
[21] 申请号 200910117305.X

[71] 申请人 西北稀有金属材料研究院
地址 753000 宁夏回族自治区石嘴山市大武口区冶金路 119 号
[72] 发明人 王东新　鲍续进　钟景明　孙本双
张　立

[74] 专利代理机构 宁夏专利服务中心
代理人 叶学军

权利要求书 1 页 说明书 8 页 附图 2 页

[54] 发明名称

粒径与形貌可控的纳米二氧化锡粉体的制备方法

[57] 摘要

本发明是一种粒径与形貌可控的纳米二氧化锡粉体的制备方法，以水溶性锡盐为原料，先加入去离子水常温下充分搅拌，再加入氨水或铵盐调整 pH =10－13，生成前驱体，将前驱体移入反应釜内，在时间 3－48 小时、温度 120－240 摄氏度内控制反应条件，反应产物用去离子水清洗 3－5 次后，在 80－100 摄氏度烘干即可得到不同粒径与形貌的纳米二氧化锡粉体。 本发明纳米 SnO_2 粉体的形貌和粒径可控，粒度变化在 3－150nm，形貌为近球形、细针状，短棒状、棒状，椭球性，六角形。

权 利 要 求 书

1、 粒径与形貌可控的纳米二氧化锡粉体的制备方法，其特征在于以水溶性锡盐为原料，先加入去离子水常温下充分搅拌，再加入氨水或铵盐调整 pH =10 -13，生成前驱体，将前驱体移入反应釜内，在时间 3-48 小时、温度 120-240 摄氏度内控制反应条件，反应产物用去离子水清洗 3-5 次后，在 80-100 摄氏度烘干即可得到不同粒径与形貌的纳米二氧化锡粉体。

2、 如权利要求 1 所述的粒径与形貌可控的纳米二氧化锡粉体的制备方法，其特征在于所述水溶性锡盐是氯化锡或硝酸锡或硫酸锡或硫酸亚锡。

3、 如权利要求 1 所述的粒径与形貌可控的纳米二氧化锡粉体的制备方法，其特征在于所述铵盐是碳酸铵或碳酸氢铵。

4、 如权利要求 1 所述的粒径与形貌可控的纳米二氧化锡粉体的制备方法，其特征在于所述水溶性锡盐的浓度为 0.25-4.0 mol/L。

粒径与形貌可控的纳米二氧化锡粉体的制备方法

技术领域：

本发明属于化学领域，涉及金属氧化物的制备方法，特别是一种粒径与形貌可控的纳米二氧化锡粉体的制备方法。

背景技术：

二氧化锡（SnO_2）作为一种具有宽能带（E_g = 3.6 eV）n 型半导体材料，是研究和应用最早的气敏材料之一。由于其具有稳定的化学和机械性能，兼具透明导电的特性，而且原材料价格低廉。自 1962 年以来，氧化锡在家庭、商业和工业领域都得到了广泛的应用，诸如气敏探测器，电极材料以及太阳能电池等等。在众多应领域中，SnO2 目前是应用在气敏元器件最多的基本原材料之一。而在探测器制作和光化学、物理作用方面，基于 SnO2 制造的电子设备的物化性能与其粉体的晶体结构、形貌和粒径密切相关，因为二氧化锡材料的气敏效应是属于晶粒表面控制型的。因此，有效控制所合成二氧化锡粉体的形貌和粒径具有十分重要的科学研究和应用价值。

制备 SnO2 纳米粉体的常用方法有液相沉淀法、微乳液法、化学气相沉积法、溶胶凝胶法和水热合成法等。其中水热合成法与其他合成技术相比较，该方法所合成的粉体结晶度高，晶态完整，粉体粒径分布范围窄且形貌易于控制。对于工业生产而言，与其他合成方法相较，水热合成法工艺相对简单，合成条件易于控制，具有较高的生产效率和较低的生产成本，合成的粉体具有单个分散的特点，且粒度分布均匀，无需进行焙烧即可获得高纯度的二氧化锡纳米粉体。

中国专利 CN101108743A 公开了一种利用沉淀法制备纳米 SnO2 粉体的方法。该方发采用可溶性锡盐为锡源，在配置成不同浓度的锡盐溶液后，需加入稀盐酸，再加如表面活性剂并在 20-80 摄氏度的恒温反应，生成前驱体。再经过过滤，去离子水洗涤，无水乙醇超声洗涤，干燥，将所得产物焙烧才可得到纳米 SnO2 粉体。该方法虽然可以制备粒度较为均匀的 SnO2 粉体，但其工艺过程

复杂，反应条件不易控制，使用的有机化学试剂很多，不仅增加了生成成本，而且也会对操作者和环境造成危害。

有关水热法制备 SnO2 粉体的文献报道很多，但所合成的 SnO2 粉体的粒径基本为 10 nm 以下，粉体的形貌特征也难以分辨。虽然也有研究者利用水热法合成出了长度在 20 nm 以下的棒状 SnO2，但其也使用了有毒有害的有机溶剂作为辅助介质（Chen B, Russell, Shi M J, et al., J. Am. Chem. Soc., 2004, 126(19):5972-5973）。此外，中国专利 CN1528671A 公开了一种利用水热合成法制备纳米 SnO2 粉体的方法。该方法的主要特征是采用锡化合物、具有络合能力的有机物为原料。具体是将锡化合物、具有络合能力的有机物溶解于水中配置成溶液，在一定温度下水热合成粒径在 2-6 nm 的 SnO2 粉体。该方法具有生成周期短，产品品质高的特点，但使用了如聚乙二醇，乙二胺，三乙醇胺，十二烷基苯磺酸钠等诸多有机试剂，且不能生产出不同粒径和形貌的粉体，不能满足不同应用的需求。

发明内容：

本发明的目的是克服现有技术缺陷，提供一种可有效控制粉体粒径与形貌的纳米二氧化锡粉体的制备方法。

本发明的目的按照下述方案实现：

粒径与形貌可控的纳米二氧化锡粉体的制备方法，以水溶性锡盐为原料，先加入去离子水常温下充分搅拌，再加入氨水或铵盐调整 pH =10-13，生成前驱体，将前驱体移入反应釜内，在时间 3-48 小时、温度 120-240℃内控制反应条件，反应产物用去离子水清洗 3-5 次后，在 80-100 摄氏度烘干即可得到不同粒径与形貌的纳米二氧化锡粉体；

所述水溶性锡盐是氯化锡或硝酸锡或硫酸锡或硫酸亚锡；

所述铵盐是碳酸铵，碳酸氢铵；

所述水溶性锡盐的浓度为 0.25～4.0 mol/L。

本发明的特点：

1. 纳米 SnO_2 粉体的形貌和粒径可控，粒度变化在 3-150 nm，形貌为近球形、细针状，短棒状、棒状，椭球性，六角形。

2. 不使用有机溶剂，避免了污染环境和有机化学试剂对人体有害，为绿色环保制备技术，是一项符合社会发展潮流的先进技术。
3. 制备工艺周期短。
4. 原材料成本低廉且容易获得。
5. 合成粉体无需焙烧处理，无需研磨，直接可获得单个分散的纳米 SnO_2 粉体，对于工业生产简化了生产工艺，减少了设备投入，降低了生产成本，非常适合大规模生产。

附图说明：

图1 为实施例4 中所制备 SnO_2 粉体的 XRD 图；

图2 为实施例4 中所制备 SnO_2 粉体的 TEM 图。

具体实施方式：

实施例 1

称取一定量的 $SnCl_4 \cdot 5H_2O$ 并溶于一定体积的去离子水中，配制成摩尔浓度为 0.5 mol/L 的溶液。用自动滴定仪滴加 25%的氨水溶液至 pH=11，将溶液转入 100 mL 的太弗龙内衬的不锈钢反应釜中，反应釜的填充度为 70%，在 120 摄氏度条件下水热处理 24 小时。产物经去离子水洗涤 3-5 次，除去酸根离子和杂质离子，在 80-100 摄氏度下烘干 3-6 小时，即可得到单个分散的白色二氧化锡粉体。颗粒的形貌为针状，粒径在 3-4 nm 左右。

实施例 2

称取一定量的 $SnCl_4 \cdot 5H_2O$ 并溶于一定体积的去离子水中，配制成摩尔浓度为 0.5 mol/L 的溶液。用自动滴定仪滴加 25%的氨水溶液至 pH=11，将溶液转入 100 mL 的太弗龙内衬的不锈钢反应釜中，反应釜的填充度为 70%，在 160 摄氏度条件下水热处理 24 小时。产物经去离子水洗涤 3-5 次，除去酸根离子和杂质离子，在 80-100 摄氏度下烘干 3-6 小时，即可得到单个分散的白色二氧化锡粉体。颗粒的形貌为短棒状，粒径在 6-7 nm 左右。

实施例 3

称取一定量的 $SnCl_4 \cdot 5H_2O$ 并溶于一定体积的去离子水中，配制成摩尔浓度为 0.5 mol/L 的溶液。用自动滴定仪滴加 25%的氨水溶液至 pH=11，将溶液转入 100 mL 的太弗龙内衬的不锈钢反应釜中，反应釜的填充度为 70%，在 180

摄氏度条件下水热处理24小时。产物经去离子水洗涤3-5次，除去酸根离子和杂质离子，在80-100摄氏度下烘干3-6小时，即可得到单个分散的白色二氧化锡粉体。颗粒的形貌为棒状，粒径在20 nm左右。

实施例 4

称取一定量的SnCl4·5H2O并溶于一定体积的去离子水中，配制成摩尔浓度为0.5 mol/L的溶液。用自动滴定仪滴加25%的氨水溶液至pH=11，将溶液转入100 mL的太弗龙内衬的不锈钢反应釜中，反应釜的填充度为70%，在200摄氏度条件下水热处理24小时。产物经去离子水洗涤3-5次，除去酸根离子和杂质离子，在80-100摄氏度下烘干3-6小时，即可得到单个分散的白色二氧化锡粉体。颗粒的形貌为棒状，粒径在55 nm左右。

实施例 5

称取一定量的SnCl4·5H2O并溶于一定体积的去离子水中，配制成摩尔浓度为0.5 mol/L的溶液。用自动滴定仪滴加25%的氨水溶液至pH=11，将溶液转入100 mL的太弗龙内衬的不锈钢反应釜中，反应釜的填充度为70%，在220摄氏度条件下水热处理24小时。产物经去离子水洗涤3-5次，除去酸根离子和杂质离子，在80-100摄氏度下烘干3-6小时，即可得到单个分散的白色二氧化锡粉体。颗粒的形貌为棒状，粒径在 120 nm左右。

实施例 6

称取一定量的SnCl4·5H2O并溶于一定体积的去离子水中，配制成摩尔浓度为0.5 mol/L的溶液。用自动滴定仪滴加25%的氨水溶液至pH=11，将溶液转入100 mL的太弗龙内衬的不锈钢反应釜中，反应釜的填充度为70%，在240摄氏度条件下水热处理24小时。产物经去离子水洗涤3-5次，除去酸根离子和杂质离子，在80-100摄氏度下烘干3-6小时，即可得到单个分散的白色二氧化锡粉体。颗粒的形貌为六角形，粒径在150 nm左右。

实施例 7

称取一定量的SnCl4·5H2O并溶于一定体积的去离子水中，配制成摩尔浓度为0.5 mol/L的溶液。用自动滴定仪滴加25%的氨水溶液至pH=11，将溶液转入100 mL的太弗龙内衬的不锈钢反应釜中，反应釜的填充度为70%，在200摄氏度条件下水热处理3小时。产物经去离子水洗涤3-5次，除去酸根离子和杂

质离子，在 80-100 摄氏度下烘干 3-6 小时，即可得到单个分散的白色二氧化锡粉体。颗粒的形貌为短棒状，粒径在 5 nm 左右。

实施例 8

称取一定量的 SnCl4·5H2O 并溶于一定体积的去离子水中，配制成摩尔浓度为 0.5 mol/L 的溶液。用自动滴定仪滴加 25%的氨水溶液至 pH=11，将溶液转入 100 mL 的太弗龙内衬的不锈钢反应釜中，反应釜的填充度为 70%，在 200 摄氏度条件下水热处理 6 小时。产物经去离子水洗涤 3-5 次，除去酸根离子和杂质离子，在 80-100 摄氏度下烘干 3-6 小时，即可得到单个分散的白色二氧化锡粉体。颗粒的形貌为棒状，粒径在 10 nm 左右。

实施例 9

称取一定量的 SnCl4·5H2O 并溶于一定体积的去离子水中，配制成摩尔浓度为 0.5 mol/L 的溶液。用自动滴定仪滴加 25%的氨水溶液至 pH=11，将溶液转入 100 mL 的太弗龙内衬的不锈钢反应釜中，反应釜的填充度为 70%，在 200 摄氏度条件下水热处理 12 小时。产物经去离子水洗涤 3-5 次，除去酸根离子和杂质离子，在 80-100 摄氏度下烘干 3-6 小时，即可得到单个分散的白色二氧化锡粉体。颗粒的形貌为棒状，粒径在 25 nm 左右。

实施例 10

称取一定量的 SnCl4·5H2O 并溶于一定体积的去离子水中，配制成摩尔浓度为 0.5 mol/L 的溶液。用自动滴定仪滴加 25%的氨水溶液至 pH=11，将溶液转入 100 mL 的太弗龙内衬的不锈钢反应釜中，反应釜的填充度为 70%，在 200 摄氏度条件下水热处理 48 小时。产物经去离子水洗涤 3-5 次，除去酸根离子和杂质离子，在 80-100 摄氏度下烘干 3-6 小时，即可得到单个分散的白色二氧化锡粉体。颗粒的形貌为棒状，粒径在 80 nm 左右。

实施例 11

称取一定量的 SnCl4·5H2O 并溶于一定体积的去离子水中，配制成摩尔浓度为 0.25 mol/L 的溶液。用自动滴定仪滴加 25%的氨水溶液至 pH=11，将溶液转入 100 mL 的太弗龙内衬的不锈钢反应釜中，反应釜的填充度为 70%，在 200 摄氏度条件下水热处理 24 小时。产物经去离子水洗涤 3-5 次，除去酸根离子和

杂质离子，在 80-100 摄氏度下烘干 3-6 小时，即可得到单个分散的白色二氧化锡粉体。颗粒的形貌为针状，粒径在 3-4 nm 左右。

实施例 12

称取一定量的 $SnCl_4 \cdot 5H_2O$ 并溶于一定体积的去离子水中，配制成摩尔浓度为 1.0 mol/L 的溶液。用自动滴定仪滴加 25%的氨水溶液至 pH=11，将溶液转入 100 mL 的太弗龙内衬的不锈钢反应釜中，反应釜的填充度为 70%，在 200 摄氏度条件下水热处理 24 小时。产物经去离子水洗涤 3-5 次，除去酸根离子和杂质离子，在 80-100 摄氏度下烘干 3-6 小时，即可得到单个分散的白色二氧化锡粉体。颗粒的形貌为棒状，粒径在 30 nm 左右。

实施例 13

称取一定量的 $SnCl_4 \cdot 5H_2O$ 并溶于一定体积的去离子水中，配制成摩尔浓度为 2.0 mol/L 的溶液。用自动滴定仪滴加 25%的氨水溶液至 pH=11，将溶液转入 100 mL 的太弗龙内衬的不锈钢反应釜中，反应釜的填充度为 70%，在 200 摄氏度条件下水热处理 24 小时。产物经去离子水洗涤 3-5 次，除去酸根离子和杂质离子，在 80-100 摄氏度下烘干 3-6 小时，即可得到单个分散的白色二氧化锡粉体。颗粒的形貌为棒状，粒径在 60 nm 左右。

实施例 14

称取一定量的 $SnCl_4 \cdot 5H_2O$ 并溶于一定体积的去离子水中，配制成摩尔浓度为 3.0 mol/L 的溶液。用自动滴定仪滴加 25%的氨水溶液至 pH=11，将溶液转入 100 mL 的太弗龙内衬的不锈钢反应釜中，反应釜的填充度为 70%，在 200 摄氏度条件下水热处理 24 小时。产物经去离子水洗涤 3-5 次，除去酸根离子和杂质离子，在 80-100 摄氏度下烘干 3-6 小时，即可得到单个分散的白色二氧化锡粉体。颗粒的形貌为棒状与短棒状混合体，粒径在 50 nm 左右。

实施例 15

称取一定量的 $SnCl_4 \cdot 5H_2O$ 并溶于一定体积的去离子水中，配制成摩尔浓度为 4.0 mol/L 的溶液。用自动滴定仪滴加 25%的氨水溶液至 pH=11，将溶液转入 100 mL 的太弗龙内衬的不锈钢反应釜中，反应釜的填充度为 70%，在 200 摄氏度条件下水热处理 24 小时。产物经去离子水洗涤 3-5 次，除去酸根离子和

杂质离子，在 80-100 摄氏度下烘干 3-6 小时，即可得到单个分散的白色二氧化锡粉体。颗粒的形貌为椭球形，粒径在 35 nm 左右。

实施例 16

称取一定量的 Sn(NO3)4 并溶于一定体积的去离子水中，配制成摩尔浓度为 0.5 mol/L 的溶液。用自动滴定仪滴加 25%的氨水溶液至 pH=11，将溶液转入 100 mL 的太弗龙内衬的不锈钢反应釜中，反应釜的填充度为 70%，在 200 摄氏度条件下水热处理 24 小时。产物经去离子水洗涤 3-5 次，除去酸根离子和杂质离子，在 80-100 摄氏度下烘干 3-6 小时，即可得到单个分散的白色二氧化锡粉体。颗粒的形貌为近球形，粒径在 15 nm 左右。

实施例 17

称取一定量的 Sn(SO4)2 并溶于一定体积的去离子水中，配制成摩尔浓度为 0.5 mol/L 的溶液。用自动滴定仪滴加 25%的氨水溶液至 pH=10，将溶液转入 100 mL 的太弗龙内衬的不锈钢反应釜中，反应釜的填充度为 70%，在 200 摄氏度条件下水热处理 24 小时。产物经去离子水洗涤 3-5 次，除去酸根离子和杂质离子，在 80-100 摄氏度下烘干 3-6 小时，即可得到单个分散的白色二氧化锡粉体。颗粒的形貌为近球形，粒径在 5-7 nm 左右。

实施例 18

称取一定量的硫酸亚锡并溶于一定体积的去离子水中，配制成摩尔浓度为 0.5 mol/L 的溶液。用自动滴定仪滴加 25%的氨水溶液至 pH=12，将溶液转入 100 mL 的太弗龙内衬的不锈钢反应釜中，反应釜的填充度为 70%，在 200 摄氏度条件下水热处理 24 小时。产物经去离子水洗涤 3-5 次，除去酸根离子和杂质离子，在 80-100 摄氏度下烘干 3-6 小时，即可得到单个分散的白色二氧化锡粉体。颗粒的形貌为近球形，粒径在 10 nm 左右。

实施例 19

称取一定量的 SnCl4·5H2O 并溶于一定体积的去离子水中，配制成摩尔浓度为 0.5 mol/L 的溶液。用自动滴定仪滴加 0.5 mol/L 的碳酸铵溶液至 pH=13，将溶液转入 100 mL 的太弗龙内衬的不锈钢反应釜中，反应釜的填充度为 70%，在 200 摄氏度条件下水热处理 24 小时。产物经去离子水洗涤 3-5 次，除去酸根

离子和杂质离子，在 80-100 摄氏度下烘干 3-6 小时，即可得到单个分散的白色二氧化锡粉体。颗粒的形貌为棒状，粒径在 40 nm 左右。

实施例 20

称取一定量的 SnCl4·5H2O 并溶于一定体积的去离子水中，配制成摩尔浓度为 0.5 mol/L 的溶液。用自动滴定仪滴加 0.5 mol/L 的碳酸氢铵溶液至 pH=11，将溶液转入 100 mL 的太弗龙内衬的不锈钢反应釜中，反应釜的填充度为 70%，在 200 摄氏度条件下水热处理 24 小时。产物经去离子水洗涤 3-5 次，除去酸根离子和杂质离子，在 80-100 摄氏度下烘干 3-6 小时，即可得到单个分散的白色二氧化锡粉体。颗粒的形貌为棒状，粒径在 30 nm 左右。

---

2 Dongxin wang, Xujin Bao, Jingming Zhong, Benshuan Sun, Synthesis of aluminium doped zinc oxide by hydrothermal method, published number:CN101665237A

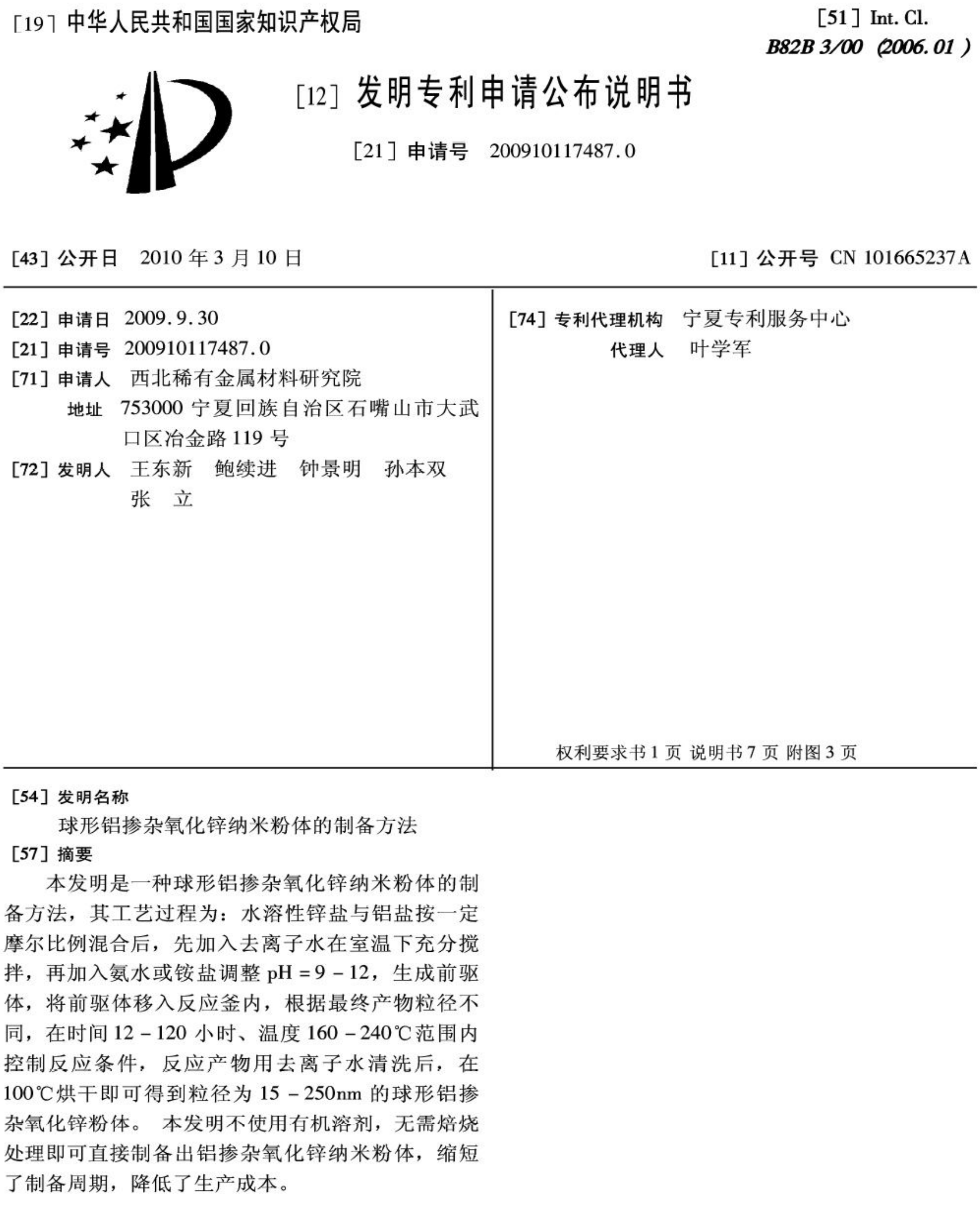

[19] 中华人民共和国国家知识产权局

[51] Int. Cl.
B82B 3/00 (2006.01)

[12] 发明专利申请公布说明书

[21] 申请号 200910117487.0

[43] 公开日 2010 年 3 月 10 日

[11] 公开号 CN 101665237A

[22] 申请日 2009.9.30
[21] 申请号 200910117487.0
[71] 申请人 西北稀有金属材料研究院
地址 753000 宁夏回族自治区石嘴山市大武口区冶金路 119 号
[72] 发明人 王东新　鲍续进　钟景明　孙本双　张　立

[74] 专利代理机构 宁夏专利服务中心
代理人 叶学军

权利要求书 1 页 说明书 7 页 附图 3 页

[54] 发明名称

球形铝掺杂氧化锌纳米粉体的制备方法

[57] 摘要

本发明是一种球形铝掺杂氧化锌纳米粉体的制备方法，其工艺过程为：水溶性锌盐与铝盐按一定摩尔比例混合后，先加入去离子水在室温下充分搅拌，再加入氨水或铵盐调整 pH = 9 - 12，生成前驱体，将前驱体移入反应釜内，根据最终产物粒径不同，在时间 12 - 120 小时、温度 160 - 240℃范围内控制反应条件，反应产物用去离子水清洗后，在 100℃烘干即可得到粒径为 15 - 250nm 的球形铝掺杂氧化锌粉体。本发明不使用有机溶剂，无需焙烧处理即可直接制备出铝掺杂氧化锌纳米粉体，缩短了制备周期，降低了生产成本。

权 利 要 求 书

1、　一种球形铝掺杂氧化锌纳米粉体的制备方法，其工艺过程为：水溶性锌盐与铝盐按一定摩尔比例混合后，先加入去离子水在室温下充分搅拌，再加入氨水或铵盐调整 pH =9-12，生成前驱体，将前驱体移入反应釜内，根据最终产物粒径不同，在时间 12-120 小时、温度 160-240℃范围内控制反应条件，反应产物用去离子水清洗后，在 100℃烘干即可得到不同粒径的球形纳米铝掺杂氧化锌粉体。

2、　如权利要求 1 所述的球形铝掺杂氧化锌纳米粉体的制备方法，其特征在于所述水溶性锌盐是氯化锌或硝酸锌或硫酸锌。

3、　如权利要求 1 所述的球形铝掺杂氧化锌纳米粉体的制备方法，其特征在于所述水溶性铝盐是氯化铝或硝酸铝或硫酸铝。

4、　如权利要求 1 所述的球形铝掺杂氧化锌纳米粉体的制备方法，其特征在于所述铵盐是碳酸氢铵。

5、　如权利要求 1 所述的球形铝掺杂氧化锌纳米粉体的制备方法，其特征在于所述水溶性锌盐的浓度为 0.1～2.0 mol/L。

6、　如权利要求 1 所述的球形铝掺杂氧化锌纳米粉体的制备方法，其特征在于所述水溶性铝中铝的含量在 0.5-10.0 at%。

球形铝掺杂氧化锌纳米粉体的制备方法

技术领域：

本发明属于无机化学领域，也属于光电功能材料领域，涉及透明导电金属氧化物的制备方法，特别是一种球形铝掺杂氧化锌纳米粉体的制备方法。

背景技术：

透明导电氧化物半导体材料由于其特殊的光学，电学特性， 已经被广泛应用于很多领域，如 LCD,OLED,TPD,以及太阳能电池等方面。在透明导电氧化物家族中，锡掺杂氧化铟是目前技术发展和应用最为成熟的材料，但由于其原材料稀有，价格较高，且有毒有害等缺点，限制了其应用和发展。铝掺杂氧化锌（AZO）作为一种透明导电的 n 型半导体材料，由于其具有稳定的化学和机械性能，兼具透明导电的特性，而且原材料丰富且价格低廉，无毒无污染等优点，被认为是最具潜力的透明导电材料之一，而且也被认为是最有可能替代锡掺杂氧化铟的材料，因此在近年来吸引了众多研究者的兴趣并得到了很大发展。

目前制备铝掺杂氧化锌粉体的方法有共沉淀法，热蒸发法，化学气相沉积法和水热合成法等。其中水热合成法与其他合成技术相比较，该方法所合成的粉体结晶度高，晶态完整，粉体粒径分布范围窄且形貌易于控制。对于工业生产而言，与其他合成方法相较，水热合成法工艺相对简单，合成条件易于控制，具有较高的生产效率和较低的生产成本，合成的粉体具有单个分散的特点，且粒度分布均匀，无需进行焙烧即可获得高纯度的铝掺杂氧化锌纳米粉体。

中国专利 CN101274775A 公开了一种利用溶剂热合成法制备铝掺杂氧化锌纳米粉体的方法。该方发采用醋酸锌为锌源，硝酸铝、硫酸铝或氯化铝为掺杂剂，利用有机溶剂配置成浓度为 0.01-0.5 mol/L 的先驱体溶液后，再在温度为 120-220 摄氏度下反应 2-144 小时。再经过去离子水及无水乙醇洗涤，干燥，将所得产物在 400-700 摄氏度，氢气气氛下焙烧 1-4 小时才可得到铝掺杂氧化锌纳米粉体。该方法虽然可以制备不同粒度粒度的近球形铝掺杂氧化锌粉体，但其工艺过程相对较为复杂。其存在两个方面的不足：一是使用了有机化学试剂，如

甲醇，乙醇和一缩二乙二醇，不仅增加了生产成本，而且也会对操作者和环境造成危害和污染；其二是该方法所合成的粉体必须经过在氢气气氛下烧结才能得到不同粒径的铝掺杂氧化锌纳米粉体。而烧结粉体不仅需要增加工业成本，也增加了制备周期。同时烧结法制备的粉体具有易团聚，粒径不易控制等弊端。

除上述专利外，有关水热法制备铝掺杂氧化锌粉体的文献报道并不多见，目前报道较多是利用共沉淀法。聂登攀等研究者（聂登攀等，中国科学 B辑:化学，2008，38 （7）：584-588）将一定比例的 $Al_2(SO_4)_3 \cdot 18H_2O$ 和 $ZnSO_4 \cdot 7H_2O$ 混合溶液与一定浓度的氨水溶液反应，将所沉淀的前驱物在1000-1200摄氏度煅烧而得到铝掺杂氧化锌粉体。该方法虽然制备除了粒度分布较为均匀，晶粒发育良好的近球形铝掺杂氧化锌粉体，但粉体的粒度较大（0.5-1 微米之间），不能满足不同应用的需求，特别是纳米领域的应用要求。

发明内容：

本发明的目的是克服现有技术不足，提供一种方法简单，成本低廉的合成铝掺杂氧化锌纳米粉体的方法。

本发明的目的按照下述方案实现：

一种球形铝掺杂氧化锌纳米粉体的制备方法，其工艺过程为：水溶性锌盐与铝盐按一定摩尔比例混合后，先加入去离子水在室温下充分搅拌，再加入氨水或铵盐调整 pH =9-12，生成前驱体，将前驱体移入反应釜内，根据最终产物粒径不同，在时间 12-120 小时、温度 160-240℃范围内控制反应条件，反应产物用去离子水清洗后，在100℃烘干即可得到粒径为15-250 nm的球形铝掺杂氧化锌粉体；

所述水溶性锌盐是氯化锌或硝酸锌或硫酸锌；

所述水溶性铝盐是氯化铝或硝酸铝或硫酸铝；

所述铵盐是碳酸氢铵；

所述水溶性锌盐的浓度为 0.1～2.0 mol/L；

所述水溶性铝中铝的含量在 0.5-10.0 at%。

本发明与现有技术相比具有以下的特点：

1、 纳米铝掺杂氧化锌粉体的形貌为球形，粒度变化在15-250 nm。

2、　不使用有机溶剂，避免了污染环境和有机化学试剂对人体的危害，为绿色环保制备技术。

3、　制备工艺简单且周期短。

4、　原材料丰富，成本低廉。

5、　合成粉体无需焙烧处理，无需研磨，直接可获得单个分散的纳米铝掺杂氧化锌粉体，对于工业生产简化了生产工艺，减少了设备投入，降低了生产成本，适合大规模生产。

附图说明：

图1 为实施例1 中所制备铝掺杂氧化锌粉体的XRD图。

图2 为实施例1 中所制备铝掺杂氧化锌粉体的TEM图。

图3 为实施例6 中所制备铝掺杂氧化锌粉体的TEM图。

具体实施方式：

实施例 1

称取一定量的氯化锌并溶于一定体积的去离子水中，配制成摩尔浓度为0.25 mol/L 的溶液。再加入一定量的氯化铝，使 Al 离子与锌离子的摩尔比为0.5%，在室温下充分搅拌溶解后，用自动滴定仪滴加 25%（w）的氨水溶液至pH=11，将溶液转入100 mL 的太弗龙内衬的不锈钢反应釜中，反应釜的填充度为70%，在200摄氏度条件下水热处理24小时。产物经去离子水洗涤约5次，除去酸根离子和杂质离子，在100摄氏度下烘干6-12小时，即可得到单个分散的白色铝掺杂氧化锌粉体。颗粒的形貌为球形，粒径在150-200 nm 左右。

实施例 2

称取一定量的氯化锌并溶于一定体积的去离子水中，配制成摩尔浓度为0.25 mol/L 的溶液。再加入一定量的氯化铝，使 Al 离子与锌离子的摩尔比为1.0%，在室温下充分搅拌溶解后，用自动滴定仪滴加 25%（w）的氨水溶液至pH=11，将溶液转入100 mL 的太弗龙内衬的不锈钢反应釜中，反应釜的填充度为70%，在200摄氏度条件下水热处理24小时。产物经去离子水洗涤约5次，除去酸根离子和杂质离子，在100摄氏度下烘干6-12小时，即可得到单个分散的白色铝掺杂氧化锌粉体。颗粒的形貌为球形，粒径在120 nm 左右。

实施例 3

称取一定量的氯化锌并溶于一定体积的去离子水中，配制成摩尔浓度为0.25 mol/L 的溶液。再加入一定量的氯化铝，使 Al 离子与锌离子的摩尔比为2.0%，在室温下充分搅拌溶解后，用自动滴定仪滴加 25%（w）的氨水溶液至pH=11，将溶液转入 100 mL 的太弗龙内衬的不锈钢反应釜中，反应釜的填充度为 70%，在 200 摄氏度条件下水热处理 24 小时。产物经去离子水洗涤约 5 次，除去酸根离子和杂质离子，在 100 摄氏度下烘干 6-12 小时，即可得到单个分散的白色铝掺杂氧化锌粉体。颗粒的形貌为球形，粒径在 100 nm 左右。

实施例 4

称取一定量的氯化锌并溶于一定体积的去离子水中，配制成摩尔浓度为0.25 mol/L 的溶液。再加入一定量的氯化铝，使 Al 离子与锌离子的摩尔比为3.0%，在室温下充分搅拌溶解后，用自动滴定仪滴加 25%（w）的氨水溶液至pH=11，将溶液转入 100 mL 的太弗龙内衬的不锈钢反应釜中，反应釜的填充度为 70%，在 200 摄氏度条件下水热处理 24 小时。产物经去离子水洗涤约 5 次，除去酸根离子和杂质离子，在 100 摄氏度下烘干 6-12 小时，即可得到单个分散的白色铝掺杂氧化锌粉体。颗粒的形貌为球形，粒径在 90 nm 左右。

实施例 5

称取一定量的氯化锌并溶于一定体积的去离子水中，配制成摩尔浓度为0.25 mol/L 的溶液。再加入一定量的氯化铝，使 Al 离子与锌离子的摩尔比为5.0%，在室温下充分搅拌溶解后，用自动滴定仪滴加 25%（w）的氨水溶液至pH=11，将溶液转入 100 mL 的太弗龙内衬的不锈钢反应釜中，反应釜的填充度为 70%，在 200 摄氏度条件下水热处理 24 小时。产物经去离子水洗涤约 5 次，除去酸根离子和杂质离子，在 100 摄氏度下烘干 6-12 小时，即可得到单个分散的白色铝掺杂氧化锌粉体。颗粒的形貌为球形，粒径在 70-80 nm 左右。

实施例 6

称取一定量的氯化锌并溶于一定体积的去离子水中，配制成摩尔浓度为0.25 mol/L 的溶液。再加入一定量的氯化铝，使 Al 离子与锌离子的摩尔比为10.0%，在室温下充分搅拌溶解后，用自动滴定仪滴加 25%（w）的氨水溶液至pH=11，将溶液转入 100 mL 的太弗龙内衬的不锈钢反应釜中，反应釜的填充度为 70%，在 200 摄氏度条件下水热处理 24 小时。产物经去离子水洗涤约 5 次，

除去酸根离子和杂质离子，在 100 摄氏度下烘干 6-12 小时，即可得到单个分散的白色铝掺杂氧化锌粉体。颗粒的形貌为球形，粒径在 40-50 nm 左右。

实施例 7

称取一定量的氯化锌并溶于一定体积的去离子水中，配制成摩尔浓度为 0.1 mol/L 的溶液。再加入一定量的硝酸铝，使 Al 离子与锌离子的摩尔比为 1.0%，在室温下充分搅拌溶解后，用自动滴定仪滴加 25%（w）的氨水溶液至 pH=11，将溶液转入 100 mL 的太弗龙内衬的不锈钢反应釜中，反应釜的填充度为 70%，在 160 摄氏度条件下水热处理 12 小时。产物经去离子水洗涤约 5 次，除去酸根离子和杂质离子，在 100 摄氏度下烘干 6-12 小时，即可得到单个分散的白色铝掺杂氧化锌粉体。颗粒的形貌为球形，粒径在 15 nm 左右。

实施例 8

称取一定量的氯化锌并溶于一定体积的去离子水中，配制成摩尔浓度为 0.1 mol/L 的溶液。再加入一定量的硝酸铝，使 Al 离子与锌离子的摩尔比为 1.0%，在室温下充分搅拌溶解后，用自动滴定仪滴加 25%（w）的氨水溶液至 pH=10，将溶液转入 100 mL 的太弗龙内衬的不锈钢反应釜中，反应釜的填充度为 70%，在 200 摄氏度条件下水热处理 24 小时。产物经去离子水洗涤约 5 次，除去酸根离子和杂质离子，在 100 摄氏度下烘干 6-12 小时，即可得到单个分散的白色铝掺杂氧化锌粉体。颗粒的形貌为球形，粒径在 30 nm 左右。

实施例 9

称取一定量的硫酸锌并溶于一定体积的去离子水中，配制成摩尔浓度为 0.25 mol/L 的溶液。再加入一定量的硫酸铝，使 Al 离子与锌离子的摩尔比为 1.0%，在室温下充分搅拌溶解后，用自动滴定仪滴加 25%（w）的氨水溶液至 pH=11，将溶液转入 100 mL 的太弗龙内衬的不锈钢反应釜中，反应釜的填充度为 70%，在 200 摄氏度条件下水热处理 24 小时。产物经去离子水洗涤约 5 次，除去酸根离子和杂质离子，在 100 摄氏度下烘干 6-12 小时，即可得到单个分散的白色铝掺杂氧化锌粉体。颗粒的形貌为球形，粒径在 70 nm 左右。

实施例 10

称取一定量的硝酸锌并溶于一定体积的去离子水中，配制成摩尔浓度为 0.25 mol/L 的溶液。再加入一定量的硝酸铝，使 Al 离子与锌离子的摩尔比为

1.0%，在室温下充分搅拌溶解后，用自动滴定仪滴加 25%（w）的氨水溶液至 pH=11，将溶液转入 100 mL 的太弗龙内衬的不锈钢反应釜中，反应釜的填充度为 70%，在 200 摄氏度条件下水热处理 24 小时。产物经去离子水洗涤约 5 次，除去酸根离子和杂质离子，在 100 摄氏度下烘干 6-12 小时，即可得到单个分散的白色铝掺杂氧化锌粉体。颗粒的形貌为球形，粒径在 80-90 nm 左右。

实施例 11

称取一定量的氯化锌并溶于一定体积的去离子水中，配制成摩尔浓度为 1.0 mol/L 的溶液。再加入一定量的氯化铝，使 Al 离子与锌离子的摩尔比为 1.0%，在室温下充分搅拌溶解后，用自动滴定仪滴加 25%（w）的氨水溶液至 pH=12，将溶液转入 100 mL 的太弗龙内衬的不锈钢反应釜中，反应釜的填充度为 70%，在 200 摄氏度条件下水热处理 24 小时。产物经去离子水洗涤约 5 次，除去酸根离子和杂质离子，在 100 摄氏度下烘干 6-12 小时，即可得到单个分散的白色铝掺杂氧化锌粉体。颗粒的形貌为球形，粒径在 120-140 nm 左右。

实施例 12

称取一定量的氯化锌并溶于一定体积的去离子水中，配制成摩尔浓度为 2.0mol/L 的溶液。再加入一定量的氯化铝，使 Al 离子与锌离子的摩尔比为 1.0%，在室温下充分搅拌溶解后，用自动滴定仪滴加 25%（w）的氨水溶液至 pH=11，将溶液转入 100 mL 的太弗龙内衬的不锈钢反应釜中，反应釜的填充度为 70%，在 200 摄氏度条件下水热处理 24 小时。产物经去离子水洗涤约 5 次，除去酸根离子和杂质离子，在 100 摄氏度下烘干 6-12 小时，即可得到单个分散的白色铝掺杂氧化锌粉体。颗粒的形貌为球形，粒径在 120 nm 左右。

实施例 13

称取一定量的氯化锌并溶于一定体积的去离子水中，配制成摩尔浓度为 0.25 mol/L 的溶液。再加入一定量的氯化铝，使 Al 离子与锌离子的摩尔比为 1.0%，在室温下充分搅拌溶解后，用自动滴定仪滴加 25%（w）的氨水溶液至 pH=9，将溶液转入 100 mL 的太弗龙内衬的不锈钢反应釜中，反应釜的填充度为 70%，在 200 摄氏度条件下水热处理 24 小时。产物经去离子水洗涤约 5 次，除去酸根离子和杂质离子，在 100 摄氏度下烘干 6-12 小时，即可得到单个分散的白色铝掺杂氧化锌粉体。颗粒的形貌为球形，粒径在 50-60 nm 左右。

实施例 14

称取一定量的氯化锌并溶于一定体积的去离子水中，配制成摩尔浓度为 0.25 mol/L 的溶液。再加入一定量的氯化铝，使 Al 离子与锌离子的摩尔比为 1.0%，在室温下充分搅拌溶解后，用自动滴定仪滴加 25%（w）的氨水溶液至 pH=11，将溶液转入 100 mL 的太弗龙内衬的不锈钢反应釜中，反应釜的填充度为 70%，在 240 摄氏度条件下水热处理 48 小时。产物经去离子水洗涤约 5 次，除去酸根离子和杂质离子，在 100 摄氏度下烘干 6-12 小时，即可得到单个分散的白色铝掺杂氧化锌粉体。颗粒的形貌为球形，粒径在 200 nm 左右。

实施例 15

称取一定量的氯化锌并溶于一定体积的去离子水中，配制成摩尔浓度为 0.25 mol/L 的溶液。再加入一定量的氯化铝，使 Al 离子与锌离子的摩尔比为 1.0%，在室温下充分搅拌溶解后，用自动滴定仪滴加 25%（w）的氨水溶液至 pH=11，将溶液转入 100 mL 的太弗龙内衬的不锈钢反应釜中，反应釜的填充度为 70%，在 240 摄氏度条件下水热处 120 小时。产物经去离子水洗涤约 5 次，除去酸根离子和杂质离子，在 100 摄氏度下烘干 6-12 小时，即可得到单个分散的白色铝掺杂氧化锌粉体。颗粒的形貌为球形，粒径在 240-250 nm 左右。

实施例 16

称取一定量的氯化锌并溶于一定体积的去离子水中，配制成摩尔浓度为 0.25 mol/L 的溶液。再加入一定量的氯化铝，使 Al 离子与锌离子的摩尔比为 1.0%，在室温下充分搅拌溶解后，用自动滴定仪滴加 25%（w）的碳酸氢铵溶液至 pH=11，将溶液转入 100 mL 的太弗龙内衬的不锈钢反应釜中，反应釜的填充度为 70%，在 200 摄氏度条件下水热处理 24 小时。产物经去离子水洗涤约 5 次，除去酸根离子和杂质离子，在 100 摄氏度下烘干 6-12 小时，即可得到单个分散的白色铝掺杂氧化锌粉体。颗粒的形貌为球形，粒径在 110 nm 左右。

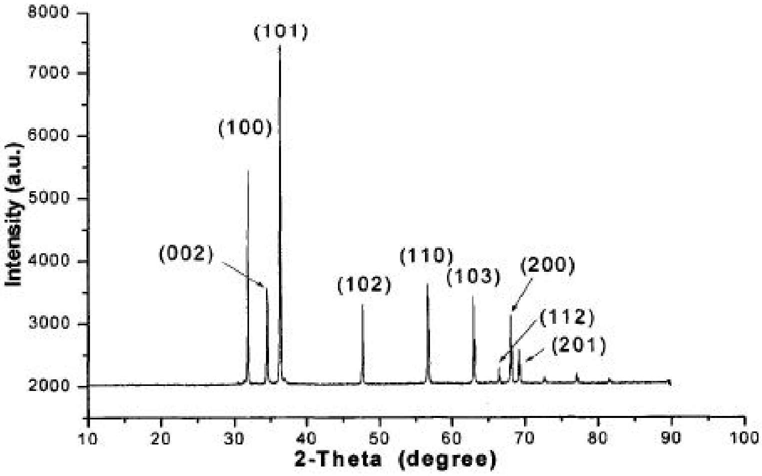
8000
7000
6000
5000
4000
3000
2000
Intensity (a.u.)
10
20
30
40
50
60
70
80
90
100
2-Theta (degree)
(101)
(100)
(002)
(102)
(110)
(103)
(200)
(112)
(201)

图 1

图 2

3 Dongxin wang, Xujin Bao, Jingming Zhong, Benshuan Sun, Synthesis of disc-like zinc oxide by hydrothermal method, published number:CN101767813A

（19）中华人民共和国国家知识产权局

（12）发明专利申请

（10）申请公布号 CN 101767813 A
（43）申请公布日 2010.07.07

（21）申请号 201010046303.9

（22）申请日 2010.01.07

（71）申请人 西北稀有金属材料研究院
地址 753000 宁夏回族自治区石嘴山市大武口区冶金路 119 号

（72）发明人 王东新 鲍续进 钟景明 孙本双 张立

（74）专利代理机构 宁夏专利服务中心 64100
代理人 叶学军

（51）Int. Cl.
C01G 9/02（2006.01）
B82B 3/00（2006.01）

权利要求书 1 页 说明书 5 页 附图 1 页

（54）发明名称

一种片状纳米氧化锌粉体的制备方法

（57）摘要

本发明是一种片状纳米氧化锌粉体的制备方法，采用以下制备步骤：1）配制水溶性锌盐溶液；2）在室温和搅拌下，滴加氨水或铵盐至溶液的 pH ＝ 11，再加入溶质重量 0.1% -0.6% 的 PEG，最后将配制的溶液转入反应釜内。3）反应釜内物料在密闭条件下进行水热处理，处理温度为 160-240 摄氏度，时间为 3-24 小时。4）产物用去离子水清洗后烘干，即可得到白色片状纳米二氧化锌粉体。合成粉体无需焙烧处理，无需研磨，直接可获得单个分散的纳米氧化锌粉体，对于工业生产简化了生产工艺，减少了设备投入，降低了生产成本，非常适合大规模生产。

CN 101767813 A

1. 一种片状纳米氧化锌粉体的制备方法，采用以下制备步骤：

1) 配制水溶性锌盐溶液；

2) 在室温和搅拌下，滴加氨水或铵盐至溶液的 pH = 11，再加入溶质重量 0.1%-0.6% 的 PEG，最后将配制的溶液转入反应釜内。

3) 反应釜内物料在密闭条件下进行水热处理，处理温度为 160-240 摄氏度，时间为 3-24 小时。

4) 产物用去离子水清洗后烘干，即可得到白色片状纳米二氧化锌粉体。

2. 如权利要求 1 所述的片状纳米氧化锌粉体的制备方法，其特征在于上述配制水溶性锌盐溶液的可溶性锌盐为氯化锌、硝酸锌或硫酸锌，铵盐为碳酸铵或碳酸氢铵，配制溶液的摩尔浓度为 0.1-1.0 $molL^{-1}$。

一种片状纳米氧化锌粉体的制备方法

技术领域：

[0001] 本发明属于金属氧化物制备技术领域，还涉及纳米半导体材料技术，特别是一种片状纳米氧化锌粉体的制备方法。

背景技术：

[0002] 纳米氧化锌可以作为一种新型高功能高附加值的具有宽能带（$E_g = 3.2$ eV）n型的半导体材料。纳米氧化锌由于晶粒的细微化和形貌的控制而导致其表面电子结构和晶体结构发生变化，产生了宏观物体所不具有的表面效应、量子尺寸效应、体积效应、宏观隧道效应等特点。研究发现，纳米氧化锌具备常规块体材料所不具备的光、电、磁、热、敏感等性能，产品活性高，具有抗红外、紫外和杀菌的功能，已被广泛应用于压敏电阻、压电材料、化妆品、气体传感器、变阻器、吸湿离子传导温度计、磁性材料、紫外线屏蔽材料、图像记录材料、高效催化剂和光催化剂等。在众多应用中，氧化锌气敏半导体元件是一种新型且具有广泛市场的气敏半导体元件，其电阻值随着所在环境可燃气体浓度的变化而变化，具有对多种气体敏感且灵敏度高、性能稳定、环境适应性强等诸多优点。而基于这一特性的电子设备的物化性能与其粉体的晶体结构、形貌和粒径密切相关。因此，有效控制所合成氧化锌粉体的形貌和粒径具有十分重要的科学研究和应用价值。由于纳米氧化锌一系列的优异的特性和广泛的应用前景，研发可控制粒径和形貌的纳米氧化锌的制备技术已成为当今众多研究人员的焦点。

[0003] 目前，制备氧化锌纳米粉体的方法和专利很多，常用方法有液相沉淀法、微乳液法、化学气相沉积法、溶胶凝胶法和水热合成法等。其中水热合成法与其它合成技术相比较，该方法所合成的粉体结晶度高，晶态完整，粉体粒径分布范围窄且形貌易于控制。对于工业生产而言，与其它合成方法相较，水热合成法工艺相对简单，合成条件易于控制，具有较高的生产效率和较低的生产成本，合成的粉体具有单个分散的特点，且粒度分布均匀，通过控制合成条件并无需进行焙烧即可获得高纯度的纳米氧化锌粉体。

[0004] 中国专利CN1562762，CN1686819A分别公开了一种利用水热法制备纳米氧化锌粉体的方法。该方发采用醋酸锌和硝酸锌为锌源，以氢氧化锂为沉淀剂，成功制备了单分散的纳米氧化锌粉体，但都使用了无水乙醇或甲醇，聚六烯吡咯烷酮等有毒有害且成本较高的有机溶剂，增加了工业化生产成本以及对环境的污染。此外合成的粉体形貌也不能有效控制。中国专利CN1396117，CN1415545公开了利用沉淀法制备纳米氧化锌。该类方法是在可溶性锌盐溶液中加入碳酸盐，碳酸氢铵，氨水等沉淀剂，生成碳酸锌粉体，在经过高温煅烧而得到粒径在10-40纳米的粉体。该类方法制备的氧化锌粉体的工艺过程较多，反应条件不易控制，使用的有机化学试剂很多，而且合成粉体易团聚，分散性差，形貌难以控制，不能满足各种应用的要求，限制了其应用领域。

[0005] 一种尺寸可控的纳米氧化锌颗粒的制备方法被中国专利CN1626446所公布。该方法将聚合物螯合剂与乙醇混合后，然后将氯化锌溶液加入该混合溶液中并搅拌混合均匀，再滴加碱溶液，在50到110度搅拌反应0.5-5小时。最后通过干燥得到氧化锌粉体。该方

法不仅工艺复杂，而且成本较高，所得分体易团聚。此外，中国专利 CN155040A 公布了一种均匀尺寸的纳米氧化锌分体的制备方法。该方法为了解决行核时间不同与生长速度的影响而导致的颗粒尺寸不均问题，大量加入了溴甲苯，溴苯酚等有机溶剂。这些溶剂毒性大，成本较高，对生产和环境都不利。

[0006] 聚乙二醇，PEG，英文名 ：polyethylene glycol

[0007] 化学结构 ：HO(CH2CH2O)nH，由环氧乙烷聚合而成，是一种非离子表面活性剂。

发明内容 ：

[0008] 本发明的目的是克服现有技术之不足，提供一种片状纳米氧化锌粉体的制备方法。本发明的目的按照下述方案实现 ：

[0009] 一种片状纳米氧化锌粉体的制备方法，采用以下制备步骤 ：

[0010] 1) 配制水溶性锌盐溶液 ；

[0011] 2) 在室温和搅拌下，滴加氨水或铵盐至溶液的 pH ＝ 11，再加入溶质重量 0.1％ -0.6％的 PEG，最后将配制的溶液转入反应釜内。

[0012] 3) 反应釜内物料在密闭条件下进行水热处理，处理温度为 160-240 摄氏度，时间为 3-24 小时。

[0013] 4) 产物用去离子水清洗后烘干，即可得到白色片状纳米二氧化锌粉体 ；

[0014] 上述配制水溶性锌盐溶液的可溶性锌盐为氯化锌、硝酸锌或硫酸锌，铵盐为碳酸铵或碳酸氢铵，配制溶液的摩尔浓度为 0.1-1.0$\mathrm{molL^{-1}}$。

[0015] 本发明的特点 ：

[0016] 1) 纳米氧化锌粉体的形貌为片状，粒度变化在 10-200 纳米。

[0017] 2) 不使用有毒有害的机溶剂，避免了污染环境和有机化学试剂对人体的危害，属于绿色环保制备技术。

[0018] 3) 制备工艺周期短。

[0019] 4) 原材料成本低廉且容易获得。

[0020] 5) 合成粉体无需焙烧处理，无需研磨，直接可获得单个分散的纳米氧化锌粉体，对于工业生产简化了生产工艺，减少了设备投入，降低了生产成本，非常适合大规模生产。

附图说明 ：

[0021] 图 1 为实施例 13 中所制备氧化锌粉体的 XRD 图 ；

[0022] 图 2 为实施例 13 中所制备氧化锌粉体的 SEM 图。

具体实施方式 ：

[0023] 实施例 1

[0024] 将一定量的氯化锌并溶于一定体积的去离子水中，配制成摩尔浓度为 0.1mol/L 的溶液，并加入 0.2wt％溶质重量的 PEG 8000。用自动滴定仪滴加 25％的氨水溶液至 pH ＝ 11，将溶液转入 100 mL 的太弗龙内衬的不锈钢反应釜中，使反应釜的填充度为 70％，在 200 摄氏度条件下水热处理 24 小时。产物经去离子水洗涤约 5 次左右，以便除去酸根离子和杂质离子，在 100 摄氏度下烘干约 12 小时，即可得到单个分散的白色片状二氧化锌粉体。粒

径在80纳米左右。

[0025] 实施例2

[0026] 将一定量的氯化锌并溶于一定体积的去离子水中，配制成摩尔浓度为0.5mol/L的溶液，并加入0.2 wt%溶质重量的PEG 8000。用自动滴定仪滴加25%的氨水溶液至pH＝11，将溶液转入100 mL的太弗龙内衬的不锈钢反应釜中，使反应釜的填充度为70%，在200摄氏度条件下水热处理24小时。产物经去离子水洗涤约5次左右，以便除去酸根离子和杂质离子，在100摄氏度下烘干约12小时，即可得到单个分散的白色片状二氧化锌粉体。粒径在60-70纳米。

[0027] 实施例3

[0028] 将一定量的氯化锌并溶于一定体积的去离子水中，配制成摩尔浓度为1.0mol/L的溶液，并加入0.2 wt%溶质重量的PEG 8000。用自动滴定仪滴加25%的氨水溶液至pH＝11，将溶液转入100 mL的太弗龙内衬的不锈钢反应釜中，使反应釜的填充度为70%，在200摄氏度条件下水热处理24小时。产物经去离子水洗涤约5次左右，以便除去酸根离子和杂质离子，在1 00摄氏度下烘干约12小时，即可得到单个分散的白色片状二氧化锌粉体。粒径在40纳米左右。

[0029] 实施例4

[0030] 将一定量的硝酸锌并溶于一定体积的去离子水中，配制成摩尔浓度为0.1mol/L的溶液，并加入0.2 wt%溶质重量的PEG 8000。用自动滴定仪滴加25%的氨水溶液至pH＝11，将溶液转入100 mL的太弗龙内衬的不锈钢反应釜中，使反应釜的填充度为70%，在200摄氏度条件下水热处理24小时。产物经去离子水洗涤约5次左右，以便除去酸根离子和杂质离子，在100摄氏度下烘干约12小时，即可得到单个分散的白色片状二氧化锌粉体。粒径在60纳米左右。

[0031] 实施例5

[0032] 将一定量的硫酸锌并溶于一定体积的去离子水中，配制成摩尔浓度为0.1mol/L的溶液，并加入0.2 wt%溶质重量的PEG 8000。用自动滴定仪滴加25%的氨水溶液至pH＝11，将溶液转入100 mL的太弗龙内衬的不锈钢反应釜中，使反应釜的填充度为70%，在200摄氏度条件下水热处理24小时。产物经去离子水洗涤约5次左右，以便除去酸根离子和杂质离子，在100摄氏度下烘干约12小时，即可得到单个分散的白色片状二氧化锌粉体。粒径在30-50纳米。

[0033] 实施例6

[0034] 将一定量的氯化锌并溶于一定体积的去离子水中，配制成摩尔浓度为0.1mol/L的溶液，并加入0.2 wt%溶质重量的PEG 3400。用自动滴定仪滴加25%的氨水溶液至pH＝11，将溶液转入100 mL的太弗龙内衬的不锈钢反应釜中，使反应釜的填充度为70%，在200摄氏度条件下水热处理24小时。产物经去离子水洗涤约5次左右，以便除去酸根离子和杂质离子，在100摄氏度下烘干约12小时，即可得到单个分散的白色片状二氧化锌粉体。粒径在120-140纳米。

[0035] 实施例7

[0036] 将一定量的氯化锌并溶于一定体积的去离子水中，配制成摩尔浓度为0.1mol/L的溶液，并加入0.2 wt%溶质重量的PEG 10000。用自动滴定仪滴加25%的氨水溶液至pH

＝11，将溶液转入 100 mL 的太弗龙内衬的不锈钢反应釜中，使反应釜的填充度为 70%，在 200 摄氏度条件下水热处理 24 小时。产物经去离子水洗涤约 5 次左右，以便除去酸根离子和杂质离子，在 100 摄氏度下烘干约 12 小时，即可得到单个分散的白色片状二氧化锌粉体。粒径在 20 纳米左右。

[0037] 实施例 8

[0038] 将一定量的氯化锌并溶于一定体积的去离子水中，配制成摩尔浓度为 0.1mol/L 的溶液，并加入 0.1 wt%溶质重量的 PEG 8000。用自动滴定仪滴加 25%的氨水溶液至 pH＝11，将溶液转入 100 mL 的太弗龙内衬的不锈钢反应釜中，使反应釜的填充度为 70%，在 200 摄氏度条件下水热处理 24 小时。产物经去离子水洗涤约 5 次左右，以便除去酸根离子和杂质离子，在 100 摄氏度下烘干约 12 小时，即可得到单个分散的白色片状二氧化锌粉体。粒径在 100 纳米左右。

[0039] 实施例 9

[0040] 将一定量的氯化锌并溶于一定体积的去离子水中，配制成摩尔浓度为 0.1mol/L 的溶液，并加入 0.4 wt%溶质重量的 PEG 8000。用自动滴定仪滴加 25%的氨水溶液至 pH＝11，将溶液转入 100 mL 的太弗龙内衬的不锈钢反应釜中，使反应釜的填充度为 70%，在 200 摄氏度条件下水热处理 24 小时。产物经去离子水洗涤约 5 次左右，以便除去酸根离子和杂质离子，在 100 摄氏度下烘干约 12 小时，即可得到单个分散的白色片状二氧化锌粉体。粒径在 50 纳米左右。

[0041] 实施例 10

[0042] 将一定量的氯化锌并溶于一定体积的去离子水中，配制成摩尔浓度为 0.1mol/L 的溶液，并加入 0.6 wt%溶质重量的 PEG 8000。用自动滴定仪滴加 25%的氨水溶液至 pH＝11，将溶液转入 100mL 的太弗龙内衬的不锈钢反应釜中，使反应釜的填充度为 70%，在 200 摄氏度条件下水热处理 24 小时。产物经去离子水洗涤约 5 次左右，以便除去酸根离子和杂质离子，在 100 摄氏度下烘干约 12 小时，即可得到单个分散的白色片状二氧化锌粉体。粒径在 40-50 纳米左右。

[0043] 实施例 11

[0044] 将一定量的氯化锌并溶于一定体积的去离子水中，配制成摩尔浓度为 0.1mol/L 的溶液，并加入 0.2 wt%溶质重量的 PEG 8000。用自动滴定仪滴加 25%的氨水溶液至 pH＝11，将溶液转入 100 mL 的太弗龙内衬的不锈钢反应釜中，使反应釜的填充度为 70%，在 160 摄氏度条件下水热处理 3 小时。产物经去离子水洗涤约 5 次左右，以便除去酸根离子和杂质离子，在 100 摄氏度下烘干约 12 小时，即可得到单个分散的白色片状二氧化锌粉体。粒径在 10-20 纳米。

[0045] 实施例 12

[0046] 将一定量的氯化锌并溶于一定体积的去离子水中，配制成摩尔浓度为 0.1mol/L 的溶液，并加入 0.2 wt%溶质重量的 PEG 8000。用自动滴定仪滴加 25%的氨水溶液至 pH＝11，将溶液转入 100mL 的太弗龙内衬的不锈钢反应釜中，使反应釜的填充度为 70%，在 200 摄氏度条件下水热处理 6 小时。产物经去离子水洗涤约 5 次左右，以便除去酸根离子和杂质离子，在 100 摄氏度下烘干约 12 小时，即可得到单个分散的白色片状二氧化锌粉体。粒径在 30-50 纳米。

[0047] 实施例 13

[0048] 将一定量的氯化锌并溶于一定体积的去离子水中，配制成摩尔浓度为 0.1mol/L 的溶液，并加入 0.2 wt％溶质重量的 PEG 8000。用自动滴定仪滴加 25％的氨水溶液至 pH ＝ 11，将溶液转入 100 mL 的太弗龙内衬的不锈钢反应釜中，使反应釜的填充度为 70％，在 240 摄氏度条件下水热处理 24 小时。产物经去离子水洗涤约 5 次左右，以便除去酸根离子和杂质离子，在 100 摄氏度下烘干约 12 小时，即可得到单个分散的白色片状二氧化锌粉体。粒径在 180-200 纳米。

[0049] 实施例 14

[0050] 将一定量的氯化锌并溶于一定体积的去离子水中，配制成摩尔浓度为 1.0mol/L 的溶液，并加入 0.2 wt％溶质重量的 PEG 8000。用自动滴定仪滴加 25％的碳酸铵溶液至 pH ＝ 11，将溶液转入 100 mL 的太弗龙内衬的不锈钢反应釜中，使反应釜的填充度为 70％，在 200 摄氏度条件下水热处理 24 小时。产物经去离子水洗涤约 5 次左右，以便除去酸根离子和杂质离子，在 100 摄氏度下烘干约 12 小时，即可得到单个分散的白色片状二氧化锌粉体。粒径在 70-80 纳米。

[0051] 实施例 15

[0052] 将一定量的氯化锌并溶于一定体积的去离子水中，配制成摩尔浓度为 1.0mol/L 的溶液，并加入 0.2 wt％溶质重量的 PEG 8000。用自动滴定仪滴加 25％的碳酸氢铵溶液至 pH ＝ 11，将溶液转入 100 mL 的太弗龙内衬的不锈钢反应釜中，使反应釜的填充度为 70％，在 200 摄氏度条件下水热处理 24 小时。产物经去离子水洗涤约 5 次左右，以便除去酸根离子和杂质离子，在 100 摄氏度下烘干约 12 小时，即可得到单个分散的白色片状二氧化锌粉体。粒径在 70 纳米左右。

[0053] 实施例 16

[0054] 将一定量的氯化锌并溶于一定体积的去离子水中，配制成摩尔浓度为 1.0mol/L 的溶液，并加入 0.2 wt％溶质重量的 PEG 8000。用自动滴定仪滴加 25％的碳酸氢铵溶液至 pH ＝ 11，将溶液转入 100 mL 的太弗龙内衬的不锈钢反应釜中，使反应釜的填充度为 70％，在 180 摄氏度条件下水热处理 24 小时。产物经去离子水洗涤约 5 次左右，以便除去酸根离子和杂质离子，在 100 摄氏度下烘干约 12 小时，即可得到单个分散的白色片状二氧化锌粉体。粒径在 60-70 纳米。

[0055] 实施例 17

[0056] 将一定量的氯化锌并溶于一定体积的去离子水中，配制成摩尔浓度为 1.0mol/L 的溶液，并加入 0.2 wt％溶质重量的 PEG 8000。用自动滴定仪滴加 25％的碳酸铵溶液至 pH ＝ 11，将溶液转入 100 mL 的太弗龙内衬的不锈钢反应釜中，使反应釜的填充度为 70％，在 220 摄氏度条件下水热处理 24 小时。产物经去离子水洗涤约 5 次左右，以便除去酸根离子和杂质离子，在 100 摄氏度下烘干约 12 小时，即可得到单个分散的白色片状二氧化锌粉体。粒径在 80 纳米左右。

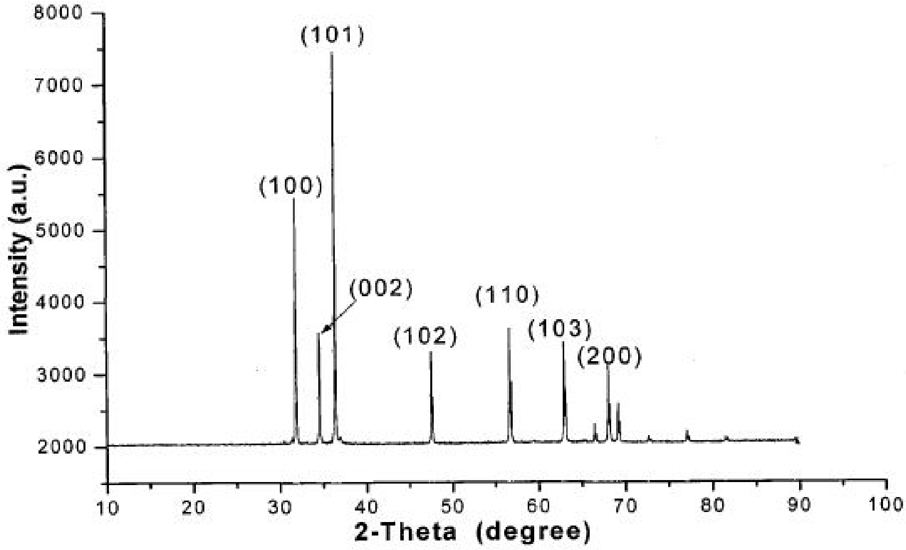
8000
7000
6000
5000
4000
3000
2000
Intensity (a.u.)
(101)
(100)
(002)
(110)
(102)
(103)
(200)
10
20
30
40
50
60
70
80
90
100
2-Theta (degree)

图 1

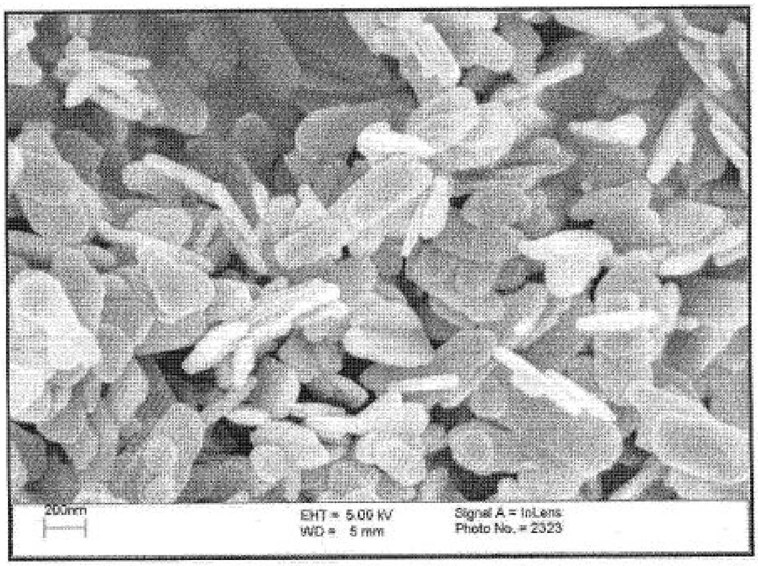
200nm
EHT = 5.00 kV
WD = 5 mm
Signal A = InLens
Photo No. = 2323

图 2